Vector Magnetometry with RF-driven Zeeman Rabi Oscillations in Hot Atomic Vapor

by

Thanmay Sunil Menon

B.S., Indian Institute of Science, 2020

M.S., University of Colorado Boulder, 2024

A thesis submitted to the
Faculty of the Graduate School of the
University of Colorado in partial fulfillment
of the requirements for the degree of
Doctor of Philosophy
Department of Physics
2026

Committee Members:
Cindy Regal, Chair
Svenja Knappe
James K. Thompson
Murray Holland
Shuo Sun

Menon, Thanmay Sunil (PhD, Physics)

Vector Magnetometry with RF-driven Zeeman Rabi Oscillations in Hot Atomic Vapor

Thesis directed by Prof. Cindy Regal

In this thesis, I present a novel approach for atomic vector magnetometry based on RF-driven Zeeman Rabi oscillations in hot ^{87}Rb vapor. I describe a theoretical framework for understanding atomic spin dynamics in the presence of static and oscillating magnetic fields, including the effects of optical pumping and relaxation processes. I then develop a Floquet-based model that describes the angular dependence of the measured Rabi frequencies. The model accounts for corrections beyond the rotating wave approximation, and incorporates heading-error systematics that arise from the nonlinear Zeeman effect. I then describe the implementation of this method in a single-optical-axis configuration using a microfabricated vapor cell. A calibration protocol based on controlled rotations of an applied magnetic field is used to determine a set of resonant RF polarization ellipses. These polarization ellipses drive Rabi oscillations between adjacent Zeeman sublevels in the ground state hyperfine manifolds of ^{87}Rb. Combined with the theoretical model, I show how the measured Zeeman Rabi frequencies can be used to determine an unknown magnetic field direction, while Larmor precession measurements yield the field magnitude. This method enables vector measurements with high angular accuracy and sensitivity across the full angular range without deadzones. I extend this platform by applying resonant microwave fields using a combination of alumina resonator and loop antennas, allowing access to hyperfine Rabi oscillations, and additional Zeeman Rabi oscillations. I further identify key limitations of this approach arising from calibration drifts and residual systematics, and discuss potential strategies for improving performance. This work lays the groundwork for compact and calibrated vector magnetic field sensors with high accuracy, without requiring multiple optical axes or cumbersome mechanical rotations.

Acknowledgements

There are far more people who have contributed to this journey than I can properly thank here, and far too little space to do justice to all of them. I would like to thank my advisor, Cindy Regal, for her support and guidance throughout my PhD. I joined her group during the uncertainty of the COVID times, and I am grateful for how she helped me find my place in the lab during that time. Her mentorship and encouragement have been invaluable to me over the years. I am also grateful to Svenja Knappe for her mentorship, insightful discussions, and for letting us use her lab space over the past couple of years.

I would like to thank Chris Kiehl, who helped me get started on this project and navigate the early stages of my time at JILA. I am especially grateful for his sharp physics intuition and sense of humor, particularly during the times when we found ourselves stuck. I am also thankful to Dawson and Michaela for all their help in moving the setup across campus and for the many discussions that helped me better understand the experiment.

I am grateful to Pooja, Aritra, and Arindam for making Boulder feel like home. I will always remember our trips to the Rockies and beyond, and the many dinners we shared. I would also like to thank Willa and Aaron for all the coffees and dinners together, and for taking such great pictures at my proposal, even though it was far too cold and snowy for September.

Finally I would like to thank my parents for their constant love, and for encouraging me even from afar. Above all, I am deeply grateful to my wife, Kristina, for her patience and support, and for the countless things she has done for me while I pursued my graduate studies and wrote this thesis. I hope to repay that debt over the rest of our lives.

Contents

Chapter

1 Introduction **1**

1.1 Alkali Atoms for Magnetometry . . . 3

1.2 OPM Operation . . . 6

1.3 Vector OPMs . . . 8

1.3.1 Vector References in OPMs . . . 8

1.3.2 Reference Calibration . . . 10

1.3.3 Mathematical Modeling of Atomic Signals . . . 13

1.3.4 Vector Deadzones . . . 14

1.4 Zeeman Rabi oscillations for Vector Magnetometry . . . 15

1.5 Thesis Outline . . . 22

1.6 Publications . . . 24

1.7 Presentations . . . 25

2 Theoretical Background **26**

2.1 Atomic Spin Dynamics . . . 26

2.1.1 Density Matrix . . . 27

2.1.2 Coherent Spin Dynamics in a DC Magnetic Field . . . 31

2.2 Relaxation Mechanisms . . . 38

2.2.1 Spin-Exchange Collisions . . . 39

2.2.2 Spin-Destruction Collisions 40
2.2.3 Collisions with Vapor Cell Wall 41
2.3 Optical Pumping 43
2.3.1 Synchronous Optical Pumping 45
2.4 Measuring Spin Polarization via Faraday Rotation 46

3 RF-driven Zeeman Rabi Dynamics **50**
3.1 RF-driven Zeeman Interaction Hamiltonian 52
3.2 Rotating Wave Approximation 55
3.3 Bloch-Siegert Systematics 58
3.4 Floquet Formalism and Bloch-Siegert Corrections 61
3.4.1 Floquet Description of Two-Level Systems 62
3.4.2 Floquet Description of Multilevel Zeeman Dynamics 66
3.5 Nonlinear Zeeman Systematics in Rabi Dynamics 71

4 Apparatus for Zeeman Rabi Vector Magnetometry **79**
4.1 Overview of the Experimental Setup 79
4.2 Microfabricated Vapor cell 81
4.3 Magnetic field Generation and Control 86
4.3.1 DC Magnetic field System 87
4.3.2 RF PE Generation 96
4.4 Extraction of Rabi and Larmor Frequencies 107

5 Vector Magnetometry with Zeeman Rabi oscillations **111**
5.1 Experiment Sequence 112
5.2 PE Calibration 114
5.3 Vector Magnetometry 120
5.4 Systematic Effects and Technical Limitations 128

5.4.1 Residual Modeling Systematics 129
5.4.2 Systematics from Technical Drifts 132

6 Microwave Delivery and Control Using Alumina Resonator **137**
6.1 Alumina Resonator Context 137
6.2 Excitation of Resonator Modes with Loop antennas 140
6.3 Driving Hyperfine Rabi Oscillations 142
6.4 σ^- Zeeman Rabi Measurements via Microwave Population Transfer 145

7 Conclusion **149**
7.1 Prospects for π-driven Rabi oscillations 151
7.2 Comparison and Outlook for Vector Magnetometry Techniques 154
7.3 Applications beyond Vector Magnetometry 159

Bibliography **162**

Tables

Table

2.1 Cross-sections and corresponding collision rates associated with dominant relaxation processes in hot ^{87}Rb vapor . . . 42

4.1 DC coil system parameters . . . 89
4.2 RF coil system parameters . . . 98

5.1 Nominal calibration parameters . . . 117
5.2 Calibration parameter errors . . . 117
5.3 Angular accuracy budget . . . 128

7.1 Comparison of performance across several vector OPMs . . . 156

Figures

Figure

1.1 Typical OPM operation 6

1.2 Zeeman Rabi oscillations in ^{87}Rb 16

1.3 Angular sensitivity variations 17

1.4 Interleaved calibration and sensing 18

2.1 Level structure showing D_1 and D_2 transitions in ^{87}Rb 27

2.2 Larmor spin precession 33

2.3 Simulation of Larmor amplitudes for several magnetic field directions 37

2.4 Optical pumping on the D_1 line of ^{87}Rb 43

2.5 Comparison of D_1 absorption for ^{87}Rb vapor cells 45

3.1 RF-driven Zeeman Rabi oscillations in ^{87}Rb 53

3.2 Rabi oscillations described in the rotating frame 56

3.3 Deviation of the Rabi frequency from the rotating wave approximation . . . 60

3.4 Floquet quasienergy spectrum for a driven two-level system 66

3.5 Floquet quasienergy spectrum of RF-driven Zeeman Rabi dynamics in $F = 2$ manifold. 69

3.6 Comparison between Floquet quasienergies and direct time-domain simulation 71

3.7 Origin of dynamic heading error systematic in Zeeman Rabi measurements. . 75

3.8 Dynamic heading error measurements 76

4.1 Schematic of the experimental setup 82
4.2 Examples of Faraday rotation signals probing atomic spin dynamics 83
4.3 Microfabricated ^{87}Rb vapor cell 84
4.4 Optical heating of the vapor cell 85
4.5 First generation DC coil system 87
4.6 Second generation DC coil system 88
4.7 Scalar calibration of the DC coil system 90
4.8 Circuit diagram of the homebuilt DC current controller 94
4.9 Homebuilt DC controller characterization 95
4.10 Twinleaf controller characterization 97
4.11 RF coil system 99
4.12 RF controller circuit diagram 100
4.13 Schematic of RF signal conditioning 103
4.14 Angular dependence of Rabi frequencies 105
4.15 Measurements of Rabi frequency noise and drifts 106
4.16 Extraction of Rabi frequencies from Faraday rotation measurements 107
4.17 Extraction of the magnetic field strength from Larmor precession measurements 109

5.1 Experiment timing sequence 113
5.2 Measurement sequence 115
5.3 Nominal calibration residuals for the six polarization ellipses 119
5.4 Angular accuracy and relative angular error measurements 122
5.5 Angular noise density measurements 125
5.6 Dynamic heading error systematics beyond the time-independent model . . . 130
5.7 Dynamic heading error systematics beyond the time-independent model . . . 131
5.8 Effect of measurement delay on Rabi frequency drift and vector performance 133
5.9 RF amplitude dependence of vector accuracy 135

6.1 Compact alumina resonator for microwave delivery 139

6.2 S_{11} measurements for the Alumina resonator-loop antenna system 141

6.3 Loop antenna system coupled to the alumina resonator 142

6.4 Hyperfine Rabi oscillations excited with alumina resonator 143

6.5 Comparison of Rabi coherences in copper cavity and alumina resonator . . . 144

6.6 Measurement of σ^--driven Zeeman Rabi oscillations 146

7.1 Driving two-photon Zeeman Rabi oscillations 152

Chapter 1

Introduction

Few physical quantities are measured across as distinct length scales as magnetic fields. Measurements of magnetic fields are used to investigate phenomena ranging from atomic and condensed matter physics to planetary and space science. Due to the effects of the magnetic field on electrical currents, magnetic moments, and the trajectories of charged particles, measurements of the magnetic field are key to understanding a variety of physical processes that may otherwise be inaccessible. Magnetometry therefore plays a crucial role across many scientific disciplines and technological applications.

Measurements of the Earth's magnetic field are widely used in geophysics and navigation. Variations in the geomagnetic field can reveal the presence of buried metallic objects, mineral deposits, and clues about the dynamics of the planet's interior [1–3]. These spatial variations are also used in magnetic anomaly navigation (MAGNAV), where maps of the Earth's magnetic field are used as a reference for navigation in environments where GPS-based positioning may be unavailable due to signal interference or jamming [4, 5].

Magnetic field sensing is also important to many experiments in fundamental physics. Precise control and detection of magnetic fields enable sensitive probes of atomic and nuclear spin systems, which are widely used to investigate fundamental interactions. High sensitivity magnetometers have been employed in experiments that search for physics beyond the Standard Model, including measurements of permanent electric dipole moments, investigations of parity violation and searches for exotic spin-dependent forces [6–10]. These experiments often require magnetic field measurements with extremely high stability and sensitivity, motivating advances in magnetometer performance [11].

Beyond fundamental physics, sensitive magnetometers also enable biomedical measurements of extremely weak magnetic fields generated by electrical activity in the human body. Electrical currents associated with neural and cardiac activity produce magnetic fields at the outside of the body that are many orders of magnitude smaller than the Earth's magnetic field. Techniques such as magnetoencephlography (MEG) and magnetocardiography (MCG) detect the magnetic fields associated with these currents, providing a non-invasive probe for studying brain and heart function [12–22].

The diversity of these applications illustrates the broad impact of magnetic field sensing. Different applications place different demands on magnetic sensors, including high sensitivity and accuracy, long-term stability, compact size, weight, and power. In many cases, it is not enough to measure only the magnitude of the magnetic field. Instead, accurate determination of the field direction is also required to extract useful information from the measurement [23–27].

Over the past several decades, a wide range of magnetometer technologies have been developed to meet these requirements. These include superconducting quantum interference devices (SQUIDs) [28], fluxgate magnetometers [29], nitrogen vacancy-center magnetometers [30], Hall effect-based magnetometers [31] and optically pumped magnetometers (OPMs) [32]. Fluxgate magnetometers are widely used for vector magnetic field measurements because of their compact form and long-term stability, offering mrad-level angular accuracies. However, their sensitivity ($\sim$ pT/$\sqrt{\text{Hz}}$) is limited and their performance can be influenced by hysteresis effects associated with the magnetic core. SQUIDs offer exceptionally high sensitivities ($\sim$ fT/$\sqrt{\text{Hz}}$) but require cryogenic temperatures, which significantly increases the complexity of the system and challenges deployment. Hall effect-based sensors provide compact and low cost solutions, although their sensitivity ($\sim$ μT/$\sqrt{\text{Hz}}$) is substantially lower than that of other precision technologies. NV-center magnetometers enable measurements with high spatial resolution and operate under ambient conditions, but extending their sensitivity ($\sim \mathrm{nT}/\sqrt{\mathrm{Hz}} - \mu\mathrm{T}/\sqrt{\mathrm{Hz}}$) to larger sensing volumes remains an ongoing challenge.

OPMs have attracted significant interest because they can achieve extremely high sensitivity in a compact package, while operating without any cryogenic cooling [33]. They exploit the coherent interaction between magnetic fields and atomic spins. Because atomic energy levels are fundamentally linked to magnetic fields through the Zeeman interaction, measurements of atomic spin dynamics can provide extremely precise measurements of magnetic field strength. Among the various atomic systems employed for magnetic field measurements, alkali atoms are especially attractive because they combine a simple level structure with optical control, and practical implementation in compact vapor cells.

1.1 Alkali Atoms for Magnetometry

Alkali atoms have been central to the development of atomic physics research for more than a century. The sensitivity of alkali energy levels to magnetic fields has been recognized since early atomic physics studies, such as Pieter Zeeman's 1896 observation of magnetic-field-induced broadening of sodium D lines [34]. Alkali atoms continue to be widely used because their outer electron configuration contains a single valence electron. As a result, their electron structure is comparatively simple, while still exhibiting hyperfine structure and Zeeman shifts that are essential for precision measurements and coherent control.

The relative simplicity of the alkali level structure is especially valuable for magnetometry, where one seeks to prepare a spin polarization and monitor its subsequent evolution in a magnetic field. This state preparation is commonly achieved through optical pumping [35], in which resonant polarized light selectively drives transitions from some Zeeman sublevels more strongly than others, thereby redistributing population and generating a spin-polarized ensemble. After state preparation, the spin polarization evolves under the influence of the magnetic field through the Zeeman interaction. The evolution can often be monitored optically, allowing the magnetic field to be inferred from changes to the atomic populations and coherences in the ground state density matrix. Hence, alkali atom measurements can often be described using straightforward density matrix models that connect the measured optical signals to the underlying spin dynamics. Furthermore, many alkali optical transitions used for optical pumping and readout are accessible in the visible or near-infrared wavelengths. These wavelengths are conveniently addressed with commercial diode lasers that offer narrow linewidth operation and continuous frequency tuning.

The late Arthur Schawlow, 1981 Nobel laureate in physics once said, “Never measure anything but frequency!” [36]. One of the major advantages of atomic systems is that the magnetic field can often be inferred from frequency measurements rather than from absolute signal amplitudes. Through the Zeeman interaction, the magnetic field sets characteristic frequencies for the spin dynamics, such as the Larmor precession frequency or the resonance frequencies of driven spin transitions. Frequencies can be measured very precisely against ultra-stable oscillators, and are generally less sensitive to fluctuations in optical power, detector gain, and spurious reflections compared to amplitude measurements.

For highly sensitive magnetic field measurements, one benefits from measuring an ensemble of atoms that share the same magnetic environment, rather than just a single alkali atom. If the number density is n and the sensing volume is V, then the number of atoms than sense the magnetic field is

$$N = nV$$

The detected optical signal results from the collective response of many spins. Because the signal increases with atom number, N, while the atomic shot noise scales as $\sqrt{N}$, the magnetic field sensitivity, δB improves as the ensemble gets larger as:

$$\delta B \propto \frac{1}{\sqrt{N}} \tag{1.1}$$

In alkali magnetometers, such ensembles are most commonly realized as atomic vapors. Borosilicate glass cells provide stable containment of alkali vapors, and their vapor density can be tuned through temperature control. For instance, the vapor pressure of rubidium is given by

$$\log_{10} p_{\mathrm{Rb}} = 2.881 + 4.312 - \frac{4040}{T} \tag{1.2}$$

where p_{Rb} is the vapor pressure in Torr, and T is the temperature in K [37]. Eq. (1.2) is only valid above the melting point of ^{87}Rb at 39.3°C (312.45 K). From the ideal gas law, the number of ^{87}Rb atoms is then given by

$$N = \frac{p_{\mathrm{Rb}} V}{k_B T}$$

where k_B is the Boltzmann constant. Buffer gases, such as N_2, He, Ne, etc., are frequently added to reduce diffusion to the walls and reduce collisional relaxation [38, 39]. Alternatively, anti-relaxation wall coatings are used to reduce spin depolarization during wall collisions [40, 41]. Together, these engineering choices set key magnetometer parameters such as coherence times, resonance linewidth, and optical pumping efficiency [42, 43]. Recently, alkali vapor cells have been manufactured using silicon-wafer-based microfabrication techniques [42, 44–46]. In these approaches, cavities are etched into silicon wafers and sealed with glass windows, and the alkali atoms and buffer gas are introduced during manufacturing [47, 48]. Batch processing enables many cells to be produced in parallel from a single wafer with uniform dimensions and optical access, reducing costs and improving reliability.

These features together make alkali atoms, specifically alkali vapors, an attractive platform for magnetometry. Optical pumping can be used to prepare a spin-polarized ensemble whose evolution is sensitive to the magnetic field, and this evolution can be detected optically through changes in transmitted intensity or polarization. Measurements of these spin dynamics form the basis for a wide range of OPMs.

1.2 OPM Operation

The basic operating principle of an OPM is the measurement of Zeeman shifts in an atom. When an external magnetic field is applied, the magnetic sublevels of the atomic ground state are shifted in energy. Measurement of these shifts provides a direct measurement of the magnetic field strength. Different OPMs use different experimental schemes, but they all generally rely on the same connection between magnetic fields and Zeeman interaction.

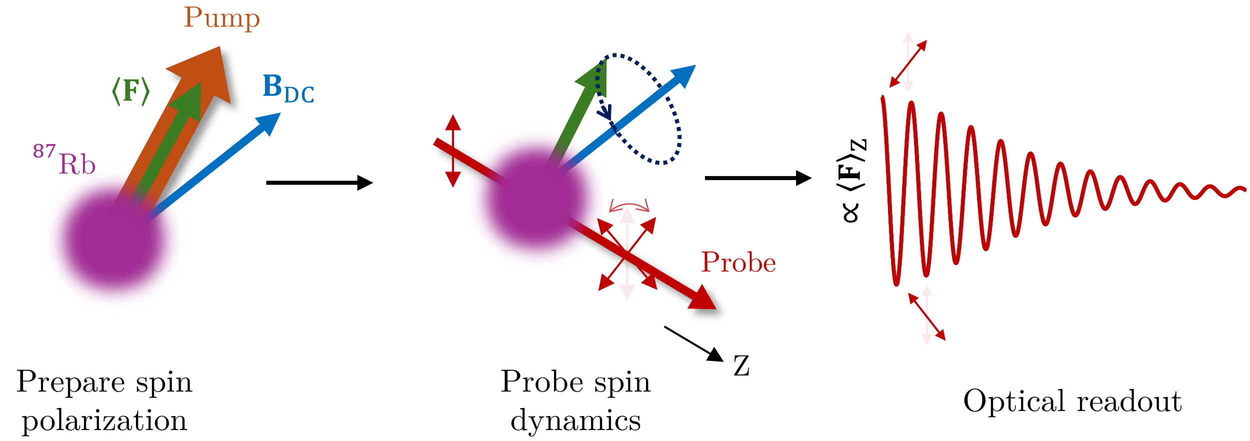

Figure 1.1: Typical OPM operation. A spin-polarized atomic state is prepared using a pump laser. The atomic state evolves in the ambient field and the resulting spin dynamics is then measured optically. The magnetic field strength is then obtained from the frequency of the measured signal.

A common approach is based on the free precession of a polarized atomic ensemble (Fig. 1.1). After the atoms are prepared in a polarized state, they precess freely about the magnetic field at the Larmor precession frequency, ν_L, which reflects the Zeeman splitting [11, 32]. The precession frequency is given by

$$\nu_L = \gamma \mathrm{B}_{\mathrm{DC}}$$

where γ is the gyromagnetic ratio. By measuring the time-dependent signal associated with this precession, the magnetic field is obtained from the measured frequency.

Another class of measurements is based on driven resonances. In these methods, the atomic spins are excited by an external drive rather than being allowed to evolve freely. The drive generally consists of an oscillating magnetic field or modulation of the optical pumping light. When the drive frequency approaches a transition frequency set by the Zeeman splitting, the atomic response becomes resonant and is detected optically. The center of this resonance therefore determines the magnetic field strength.

Examples of this approach include M_x and M_z techniques [49–51], in which a transverse oscillating magnetic field drives the spin polarization on resonance, and the resulting response is measured optically. In the Bell-Bloom method, periodic modulation of the optical pumping light excites the atomic spins, and produces a resonance when the modulation frequency is resonant with the Zeeman splitting [52–55]. Similarly, microwave fields drive transitions between the ground state hyperfine manifolds [56]. In this case, the magnetic field is inferred from the frequencies of several hyperfine transitions. The Zeeman interaction shifts each sublevel in proportion to its magnetic quantum number, which leads to different shifts for different transitions. Comparing these shifts then allows the Zeeman splitting, and hence the magnetic field strength to be determined. Similar ideas are also exploited in optical schemes based on Raman excitation of hyperfine resonances [46, 57, 58].

In all of these approaches, the magnetic field is obtained from frequencies primarily defined by the Zeeman interaction. The Zeeman splitting, however, depends only on the magnitude of the magnetic field and not on its direction. As a result, the OPMs described above function as scalar magnetometers providing precise measurements of the scalar value of the magnetic field. Determination of the full vector magnetic field therefore requires additional information in the form of an external vector reference with respect to which the magnetic field is measured.

1.3 Vector OPMs

In vector magnetometry, the goal is to determine the orientation of the magnetic field relative to a set of known spatial directions. This is accomplished by coupling the atomic spin dynamics to an external 3D reference frame and measuring how the atomic signal depends on the orientation of the field with respect to this frame. The measured signals are then compared with a theoretical model that relates the atomic observables to the magnetic field, allowing the field direction to be determined.

Accurate knowledge of the magnetic field direction is useful in many applications, including geophysics, space science and magnetic navigation. In geophysical surveys, the orientation of the measured magnetic field relative to the Earth's field provides important information about subsurface structures and mineral deposits. Small angular errors can therefore lead to incorrect interpretation of the magnetic anomalies used to infer geological features [59–61]. In space science, vector magnetometers are used to study planetary magnetospheres and plasma dynamics. Accurate measurements of the magnetic field direction are required to reconstruct the current systems from planetary models and determine the orientation of the magnetic field lines [26, 27, 62, 63]. In magnetic anomaly navigation, measurements of the local magnetic field are compared with geomagnetic anomaly reference maps to estimate position without external navigation signals [4, 5]. Conventional approaches have relied on scalar measurements of the local magnetic field. However, in Ref. [64], it has been shown that vector measurements can provide additional independent constraint, which can improve the position estimate and also provide information about the platform orientation.

1.3.1 Vector References in OPMs

A variety of techniques have been explored to establish such reference frames in vector OPMs. A common approach is based on coil-generated magnetic fields. In these methods, known modulation fields are applied along two or more axes through a coil system, and the field direction is reconstructed from the resulting atomic signals. Coil-based references are especially useful because coil fields provide a simple laboratory reference and can be integrated naturally with feedback and closed-loop operation [60, 65–67]. These coil systems are also well suited to miniaturization, for instance through planar coil geometries enabled by printed circuit fabrication [68]. In several implementations, a scalar OPM is within a coil system that generates rotating or multi-tone modulation fields, and the transverse field components are inferred from the closed-loop compensation currents required to null the signal [66, 67, 69]. Another prominent example is the Helium SWARM magnetometer, which uses coil modulations to measure the vector components from the amplitudes of the modulations in the Larmor precession signal [70, 71]. In a related method, modulation fields applied by a coil system drive spin alignment dynamics, and the field direction is inferred from the amplitude of the resulting Voigt effect signal [72]. More recent work combines Larmor precession measurements with controlled rotating field protocols to define vector axes through the rotation plane [73].

Another approach seeks to avoid reliance on mechanically defined or current-driven references entirely by using optical fields to define the vector reference. In this approach, several experiments use multiple intersecting laser beams together with optical modulations to define a 3D reference inside the vapor cell, and determine the field direction from differences in the measured atomic signals along different beam directions [74–78]. Other optical methods recover vector information from scalar magnetometer signals. Ref. [79] showed that steady-state transmission of a probe beam in a Bell-Bloom scalar magnetometer depends on the polar angle between the magnetic field and the probe beam, and additional angular information can be obtained from a light-shift-induced effective magnetic field generated by the frequency modulation of the probe beam. Optical polarization offers another route to defining a 3D reference. Examples include tilt-dependent nonlinear magneto-optical rotation (NMOR) measurements [80] and electromagnetically-induced transparency (EIT) measurements in linearly polarized bichromatic fields, where the EIT resonance amplitudes vary with the magnetic field orientation [81–85]. Related work has combined beam propagation direction and polarization to determine the magnetic field orientation from absorption measurements of transient alignment precession amplitudes in rubidium vapor [86].

Additional approaches establish the vector reference through external electromagnetic field structure. Resonant microwave fields driving Rabi oscillations between hyperfine manifolds provide a reference through the spatial structure of a polarization ellipse (PE) [87]. In other systems, a strong bias magnetic field is used to define a preferred axis for the vector measurement [88].

Although these approaches differ in implementation, they all establish vector information by coupling the atomic spin dynamics to a known spatial reference. Their performance is therefore limited by how well those references are defined and how accurately the measured atomic signals can be related to the magnetic field orientation. In practice, references are often vulnerable to environmental drifts, beam pointing errors, and misalignments in the coil system in the experimental hardware. These effects can introduce errors in the inferred field direction, degrade long-term stability, and limit the angular accuracy of the vector measurement. Therefore, careful calibration of the vector reference is required to establish an accurate relationship between the measured atomic signals and the true magnetic field orientation.

1.3.2 Reference Calibration

The accuracy of a vector magnetometer depends strongly on the stability of the reference frame with respect to which the magnetic field is measured. In practice, this reference frame is often affected by imperfect alignment, thermal drifts and other slow changes in the apparatus. Calibration procedures are therefore needed to determine the orientation of the vector reference. The resulting calibration parameters can be used to correct systematic offsets, misalignments, and scale factors in the reference model. Periodic recalibration is often required because slow drifts in the apparatus can gradually degrade the accuracy of the reference over time.

One common calibration strategy uses measurements taken at several known magnetic field orientations. The measured magnetometer signals are compared with the known direction, and the calibration parameters are optimized until the model accurately reproduces the observed signals. In Ref. [87], Kiehl *et. al* used this approach to calibrate the microwave PE references by measuring Rabi frequencies driven by resonant microwave fields for several known magnetic field orientations. The reported angular accuracy after calibration was 460 μrad. In another example of this calibration approach based on vector EIT [89], ground state EIT resonances were measured for several known magnetic field orientations, and the resulting amplitudes were used in a machine learning algorithm to establish the relationship between magnetic field direction and the light polarization axes. The work reported an angular accuracy of 1° (17 mrad) after calibration.

Another calibration approach uses controlled rotations of the sensor in a known magnetic field orientation. This method was employed by the He SWARM vector magnetometer, which uses the coil modulation technique. Here, the field direction is inferred from the amplitudes of applied low-frequency modulation signals in the Larmor precession of metastable ^{4}He. Metastable ^{4}He is an attractive sensing platform because its zero nuclear spin leads to a fairly simple level structure. In this system, the reported pre-calibration angular accuracy was 300 μrad, which was improved to approximately 10 μrad after calibration using known physical sensor rotations in a stable magnetic field. This calibration approach is particularly relevant for coil modulation techniques, as calibration via field rotation can be challenging. This is because in vector magnetometers that rely on low-frequency coil modulations, the modulation amplitudes remain small compared to the measured magnetic field strength ($\sim$ 50 μT) to reduce systematics from harmonics associated with the modulation signal. In this regime however, fluctuations in the modulation fields can lead to amplified errors in the inferred field direction. Fluctuations in the applied coil fields are effectively scaled by a factor B/a, where B and a are the magnetic field strength and modulation amplitude, respectively.

Under geomagnetic fields, where $B \sim 50\,\mu\mathrm{T}$ and $a \sim 50$ nT, even small fluctuations in the coil fields can lead to appreciable errors in the inferred direction. This amplification makes calibration procedures based on controlled magnetic field rotations difficult to implement with high accuracy.

Calibration based on sensor rotation can therefore offer a high angular accuracy, as demonstrated for the SWARM magnetometer, but this approach is mechanically more complex and is generally more time-consuming. On the other hand, calibration based on controlled rotations of the magnetic field can often be implemented rapidly using a triaxial coil system. For both approaches, it is important that experimental drifts remain small during the calibration time, $\mathbf{C}_t$. During this interval, the reference magnetic fields and the apparatus must remain sufficiently stable so that the calibration procedure accurately captures the relationship between the vector reference and measured atomic signals. If the calibration interval is long, slow variations in magnetic fields, optical alignment, or electronics can degrade the accuracy of the calibration.

Once the vector reference has been calibrated, the measured magnetic field can be expressed in an absolute coordinate system by determining the sensor orientation with respect to a global frame such as an Earth-fixed or an inertial celestial frame. This is especially useful for space missions mapping planetary magnetic fields [26] and in GPS-denied magnetic navigation applications [4]. In practice, this is often achieved using nonmagnetic theodolites [90] or star trackers [27]. A star tracker infers the sensor orientation by imaging the surrounding star field and matching the star pattern to a catalog, hence providing a transformation between the sensor frame and an absolute inertial frame. In laboratory settings, optical components such as prisms can be rigidly attached to the sensor to define a reference direction, although spatial separation between the reference component and the vapor cell can introduce errors. Referencing optical beams directly at the vapor cell can reduce these effects. For instance, the RANBA (Rabi Amplitude Nulling for measuring Beam Attitude) technique determines the probe beam orientation within the magnetometer frame by finding the magnetic field direction for which the Rabi amplitude is nulled, and can be combined with optical beam tracking to link this reference to an absolute coordinate system [91].

1.3.3 Mathematical Modeling of Atomic Signals

In addition to the stability of the reference frame, the accuracy of a vector magnetometer also depends on how accurately the measurements can be mapped to the magnetic field orientation. The atomic signals that are measured in an OPM are not direct measurements of the magnetic field direction. Instead, they arise from the evolution of atomic spin polarization under the combined influence of the magnetic field, optical pumping, relaxation processes and external driving fields. As a result, the magnetic field direction must be inferred through a mathematical model that describes how these physical processes map the magnetic field orientation to the measured atomic signal.

Theoretical models of these signals are typically based on density matrix descriptions of the atomic ground state. These models incorporate the relevant interactions, including the Zeeman interaction with the magnetic field, optical pumping by resonant light, and relaxation arising from collisions. By solving the equations governing the density matrix evolution, one can predict how the atomic signals depend on the magnetic field.

The inferred field direction therefore depends on the accuracy of this theoretical mapping between the atomic signals and the magnetic field orientation. Even if the vector reference is well-defined, inaccuracies in the model can introduce systematic errors in the measured field direction. Such errors may arise from neglected physical effects or approximations in the theoretical description, or incomplete knowledge of experimental parameters such as optical polarization, vapor cell temperature or buffer gas pressure. Theoretical models are combined with calibration measurements to determine unknown experimental parameters, and improving the modeling of atomic dynamics can therefore translate directly into improvements in the angular accuracy of the magnetometer.

1.3.4 Vector Deadzones

A fundamental challenge in many vector magnetometers is the presence of angular regions where the magnetometer signal vanishes. These regions are commonly referred to as "deadzones" [92, 93]. Deadzones arise because the atomic signals used for inferring field direction typically depend on the projection of atomic polarization onto a measurement axis defined by the probe beam. If the atomic spin dynamics evolve in a direction that is orthogonal to this projection, the measured signal can approach zero. They also arise when the measured signal remains nonzero but becomes insensitive to changes in the magnetic field direction, which reduces angular sensitivity and can prevent reliable determination of the magnetic field direction. Avoiding these deadzones is therefore essential for practical vector magnetometry.

Several approaches have been developed to eliminate such deadzones. One common approach combines measurements from multiple sensing axes or probe beam directions so that at least one measurement remains sensitive for every magnetic field orientation [74, 75]. Because each measurement depends on a different projection of the magnetic field, the combined measurement provides angular information across the full solid angle. Another approach avoids deadzones by rotating the sensor or the magnetic field so that the measurement does not remain in a direction with vanishing sensitivity [65]. While these techniques can remove deadzones, they increase the complexity of the sensor. The addition of multiple optical axes or mechanical rotation stages introduces further sources of systematic error, including sensitivity to optical alignment and mechanical stability.

These challenges have motivated efforts to achieve deadzone-free vector operation in single-optical-axis configurations. Such configurations are especially attractive because they allow compact and portable implementations, which is important for many practical applications. Several experimental strategies have been explored in this context. One approach uses an additional large bias magnetic field orthogonal to the optical axis defining a preferred quantization axis, regardless of the direction of the unknown magnetic field [88]. Another NMOR-based approach uses machine learning algorithms to correct the orientation dependence of the measured atomic signals [85]. Although these methods can improve vector performance, they also introduce additional complexity through the need for strong magnetic fields or additional computational overhead. These factors motivate magnetometer designs that achieve inherently deadzone-free vector operation.

1.4 Zeeman Rabi oscillations for Vector Magnetometry

In this thesis, I investigate vector magnetometry based on Rabi oscillations between adjacent Zeeman sublevels in the ground state hyperfine manifolds of ^{87}Rb. The Rabi oscillations are driven by RF fields that are resonant with the Zeeman splitting. The angular dependence of the resulting Rabi frequencies provides information about the field direction, while the magnitude of the field is determined independently from measurements of the Larmor precession frequency (Fig. 1.2a).

The DC magnetic field, $\mathbf{B}_{\mathrm{DC}}$ defines the quantization axis for the atom, and therefore determines the $\sigma^{\pm}$, π polarization components of the applied RF field. In the ground state hyperfine structure of ^{87}Rb, the σ^{+} and σ^{-} components drive transitions in the $F = 2$ and $F = 1$ manifolds, respectively, as a result of the magnetic dipole selection rules. These transitions cause atomic populations to coherently oscillate between the adjacent Zeeman sublevels, i.e., Rabi oscillations at frequencies $\Omega_{\sigma+}$ and $\Omega_{\sigma-}$ (Fig. 1.2a). The Rabi frequencies, $\Omega_{\sigma\pm}$, depend on the magnetic field direction through the projection of the PE associated with the RF field onto the $\sigma^{\pm}$ polarization axes (Fig. 1.2b). If the direction of the DC magnetic field is described by the polar angle, β and azimuthal angle, α,

$$\Omega_{\sigma\pm}^{(\alpha,\beta)} \approx \frac{\mu_{\sigma\pm}(\mathcal{B}_{RF})_{\sigma\pm}^{(\alpha,\beta)}}{h}$$

where $\mu_{\sigma\pm}$ is the magnetic transition dipole moment for $\sigma^{\pm}$ transitions and $(\mathcal{B}_{RF})_{\sigma\pm}^{(\alpha,\beta)}$ is the

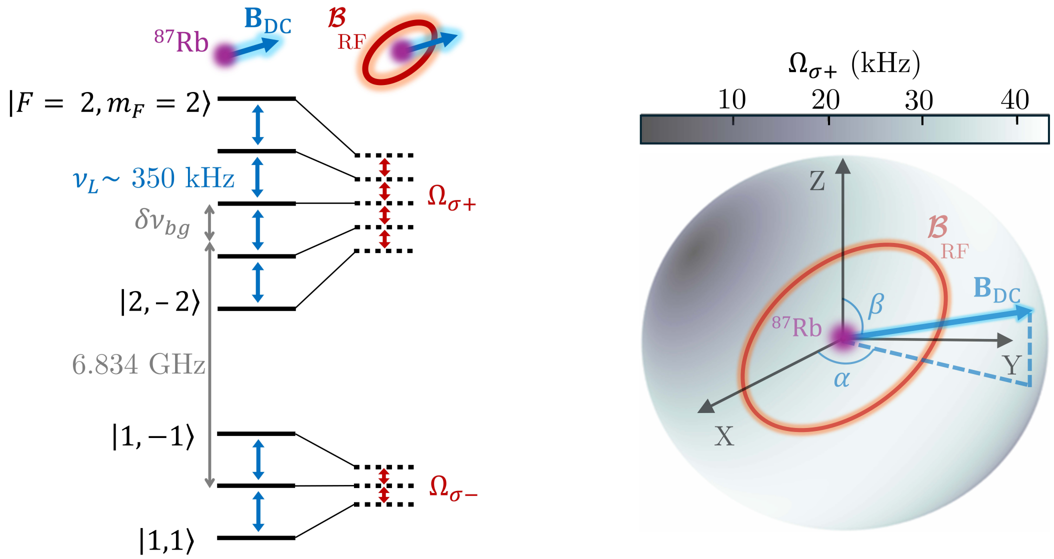

(a) (b)

Figure 1.2: Zeeman Rabi oscillations in ^{87}Rb. (a) In a 50 μT DC field, ^{87}Rb spins precess at ν_L (blue arrows). A resonant RF field with PE, $\boldsymbol{\mathcal{B}}_{\mathrm{RF}}$ drives Rabi oscillations (red arrows) between the rotating frame dressed states (dotted lines). (b) Angular dependence of $\Omega_{\sigma+}$ versus DC field direction represented by (α, β). $\langle \mathbf{F} \rangle$ denotes the spin polarization.

direction-dependent projection of the RF field onto the corresponding polarization axes.

Optical pumping and measurement of the atomic spin dynamics are performed using two co-propagating laser beams. A pump laser at 795 nm resonant with the D_1 transition in ^{87}Rb prepares the spin polarization. RF fields subsequently drive Rabi oscillations of this polarization. The resulting spin dynamics are measured with a probe laser at 780 nm that is about 100 GHz blue-detuned from the D_2 transition. Because the probe light is far from resonance, its interaction with the atoms is primarily dispersive, and therefore produces only a small perturbation of the spin dynamics [94]. The probe beam measures the atomic polarization through Faraday rotation of its linear polarization. The pump and probe beams propagate along the same direction through the microfabricated vapor cell containing the ^{87}Rb atoms. As a result, this configuration defines a single-optical-axis for the experiment.

Similar to coil modulation techniques, our approach relies on a coil-based vector reference. The resonant PEs are produced by driving a compact triaxial coil system, consisting of three nominally orthogonal coil pairs with RF currents of controlled amplitude, frequency and phase. This approach also combines naturally with the microfabricated vapor cell and miniaturized coils in a single-optical-axis configuration, and therefore provides a practical route to a compact and portable vector magnetometer that can be adapted to other OPM systems.

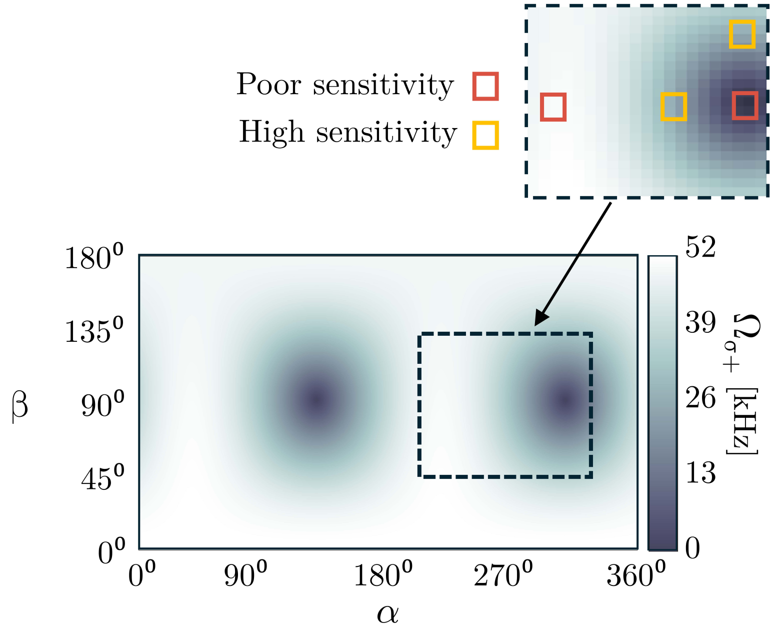

Figure 1.3: Variations in vector sensitivity are determined by the angular gradient of the Rabi frequency. Angular dependence of the Rabi frequency for an example PE is shown. Outset: Expanded view of the dashed region, where red squares indicate a few directions with weak angular gradients, and yellow squares indicate directions with stronger gradients.

By varying the RF currents applied to the coils, a series of PEs can be generated to drive Rabi oscillations with distinct angular dependencies. This angular structure plays a central role in determining the performance of the vector magnetometer. Magnetic field directions that yield higher Rabi frequencies exhibit lower fractional systematic errors, as the resonant σ^+ couplings dominate over other off-resonant systematics. By utilizing multiple PEs with complementary Rabi frequency dependencies, angular regions exhibiting smaller Rabi frequencies in one PE are balanced by regions that show large Rabi frequencies in another, thereby improving the overall accuracy of the vector magnetometer. Likewise, the vector sensitivity is similarly governed by the angular gradient of the Rabi frequency. As this gradient is non-uniform across the full solid angle, each PE exhibits distinct regions of varying sensitivity. Combining measurements from multiple PEs thus compensates for these variations, improving the overall angular resolution at all orientations and ensuring deadzone-free vector performance despite a single-optical-axis configuration.

To establish the orientation of each PE, we use a calibration protocol based on controlled DC magnetic field rotations with a separate stable DC coil system. This approach reduces the effect of long-term drift by repeatedly referencing the PE orientation to the most recent calibration (Fig. 1.4). In principle, the apparatus can be recalibrated as often as needed, so the long-term stability is set primarily by the drifts in the RF system accumulated over the calibration time, $\mathbf{C}_t$. Furthermore, the measurement itself is based on RF excitation at resonance with the Zeeman splitting, ν_L, which suppresses the influence of low-frequency off-resonant technical noise. Because the method relies only on frequency measurements, it takes advantage of the high signal-to-noise ratio and the long-term accuracy that can be achieved when referenced to stable oscillators, as discussed in Sec. 1.1.

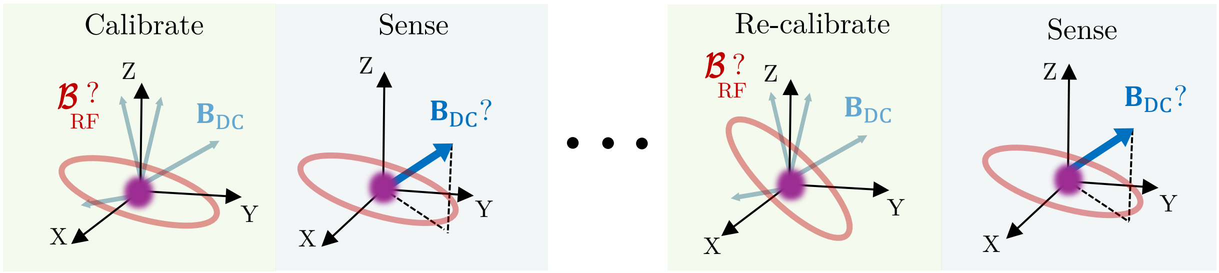

Figure 1.4: PEs are calibrated using Rabi frequencies measured at multiple known magnetic field directions. After calibration, the orientation of an unknown magnetic field is determined by measuring Rabi frequencies driven using the calibrated PEs. To mitigate drifts, the PEs are recalibrated, and the recalibrated PEs are used for subsequent vector measurements.

The calibration methods used to determine the PE are also relevant for a broader class of applications, such as RF circuit imaging and RF communication with alkali vapor cells. Related work has demonstrated atom-based sensing of electromagnetic fields [95–100], but much of this literature has focused on microwave and higher frequency fields, typically in the GHz range and above. Low-frequency measurements present a different set of challenges. As this thesis will show, low-frequency RF fields produce systematic effects that are not usually dominant for higher frequency fields. These effects therefore motivate the development of methods tailored specifically to low-frequency RF sensing.

As mentioned earlier, angular accuracy of our magnetometer depends not only on the stability of the vector reference but also on how accurately the measured Rabi frequencies are mapped to the magnetic field direction. Achieving angular accuracies at the μrad-level requires a detailed model that connects the RF-driven atomic dynamics to the magnetic field direction, which requires calculating the Rabi frequencies with sub-Hertz accuracy. The interaction between the atomic spins and the RF field is described by a Hamiltonian that includes both the static magnetic field and the oscillating RF magnetic field. In many similar treatments, this interaction is simplified using the Rotating Wave Approximation (RWA), which neglects rapidly oscillating terms in the interaction. This approximation is often valid when the Rabi frequency is much smaller than the frequency of the interrogating field.

However, in our experiment, the Rabi frequencies are appreciable compared to the RF frequencies (350 kHz for 50 μT geomagnetic fields). As a result, the counter-rotating components of the RF field produce measurable shifts in the transition frequencies. These shifts are known as Bloch-Siegert shifts, and lead to corresponding shifts in the Rabi frequencies as well. To describe these effects, we use a Floquet formalism [101, 102] that treats the periodic Hamiltonian without relying on the RWA. The Floquet treatment accounts for the full time-dependence of the field and therefore includes the effects of counter-rotating components. This approach allows accurate calculation of the full angular dependence of the Rabi frequencies and naturally incorporates systematic effects like the Bloch-Siegert shifts.

Additionally, we also observe and account for a dependence of the Rabi frequencies on the phase of the RF field with respect to the optical pumping sequence used to prepare the spin polarization. This effect is closely related to the static heading error systematic well-known in scalar OPMs, where the measured Larmor precession frequency depends on the orientation of the magnetic field relative to the optically pumped spin polarization [56, 103, 104]. The static heading error originates from the nonlinear Zeeman effect, which makes the Zeeman sublevel spacings unequal and changes the relative contribution of the Zeeman coherences that contribute to the measured precession signal. A related effect appears in our vector magnetometer because the measured Rabi frequencies are determined by the RF-driven spin dynamics in the same nonlinear Zeeman structure. The unequal Zeeman splittings modify the driven evolution of the atomic coherences, and introduce an additional dependence of the Rabi frequency on the RF phase because the measured atomic signal includes interference between coherences associated with Larmor precession, and those driven by the RF field. By analogy with a related effect identified in Ref. [73], we refer to this systematic as the dynamic heading error.

The motivation for the present work originates from earlier studies in our group on vector measurements with microwave-driven Rabi oscillations between hyperfine manifolds that we mentioned earlier [87]. In that experiment, resonant microwave PEs drove Rabi oscillations between $\sigma^{\pm}, \pi$ hyperfine transitions in the ground state ^{87}Rb and the corresponding Rabi frequencies were used to find the direction of an unknown magnetic field. Because multiple, independent transitions were available to measure the field direction, this approach also enables tracking of slow drifts in the microwave amplitudes, and self-calibration of the microwave PEs from Rabi measurements alone [105], yielding sub-milliradian angular accuracies [87]. Because each hyperfine transition couples a pair of individual Zeeman sublevels, this approach also allows measurement of the magnetic field strength while avoiding static heading error systematics [56, 105]. Despite these advantages, the experimental implementation required a copper microwave cavity to generate microwave PEs, which added complexity and made miniaturization challenging. To mitigate deadzones in the plane orthogonal to the probe beam axis, this experiment combined simultaneous measurements of the Larmor precession with Stark shift measurements of Rabi frequency. However, the performance of the magnetometer degraded significantly in this regime.

These limitations motivated the search for a vector measurement technique that could offer improved performance with a simpler experimental implementation. Zeeman Rabi oscillations are driven using a simple Helmholtz coil system and offer inherently deadzone-free vector operation. Furthermore, they also experience weaker spin-exchange decoherence, resulting in coherence times approximately twice ($\sim$ 1 ms) those of hyperfine Rabi oscillations [106]. A promising long-term direction is a hybrid instrument that combines RF and microwave capabilities to realize an integrated vector-scalar magnetometer with minimal heading error.

The performance of the magnetometer was evaluated by comparing the measured magnetic field direction with known field orientations generated by a calibrated DC coil system. The coil fields were independently calibrated through Larmor spin precession measurements, which provide an accurate determination of the magnetic field magnitude and direction. Vector measurements were then performed over a wide range of applied test magnetic field orientations over the full solid angle. The resulting measurements yielded a mean angular accuracy of ≈ 80 μrad (0.004°). This result exceeds the performance reported for vector OPMs that operate with a single optical axis and without mechanical sensor rotation [87, 89].

In addition to the mean angular accuracy, the angular noise was benchmarked from repeated measurements of the field direction. The magnetometer exhibited a mean angular noise density of 22 $\mu\text{rad}/\sqrt{\text{Hz}}$ ($0.4\ \text{nT}/\sqrt{\text{Hz}}$), with a lowest measured value of 8 $\mu\text{rad}/\sqrt{\text{Hz}}$. These values are comparable to or better than those reported for other high accuracy vector magnetometers [70, 83, 87]. The current performance is primarily limited by slow technical drifts in the apparatus that occur during the calibration interval. Additional limitations arise from residual systematic errors in the model that describes the angular dependence of the measured Rabi frequencies.

1.5 Thesis Outline

I began my PhD working on vector magnetometry based on microwave-driven hyperfine transitions in a microfabricated vapor cell enclosed in a copper microwave cavity. I worked on this system for a little over two years and during that time, Chris Kiehl and I developed methods to generate and calibrate microwave PEs through controlled magnetic field rotations, and established measurement protocols to extract vector information from Rabi frequency measurements. The results of these experiments are presented in Refs. [56, 87]. Through this work, I came to appreciate that the key challenge was not only generating resonant microwave fields but also keeping the system stable over time in the presence of slow drifts.

At the time, we also considered whether similar ideas could be applied to Zeeman transitions. These transitions appeared less favorable because of additional effects such as Bloch-Siegert shifts and nonlinear Zeeman splitting. Compared with the relatively simple structure of hyperfine transitions, the Zeeman system appeared more complicated. As hyperfine transitions are driven between two Zeeman sublevels (across hyperfine manifolds), it avoids complications associated with unresolved nonlinear Zeeman splittings, and the microwave frequencies involved makes the simple RWA accurate [87]. However, as the microwave system developed, its practical limitations became more apparent, which led me to revisit the Zeeman approach. The alumina resonator discussed later in the thesis represents an intermediate step in this effort, where I explored ways to reduce eddy current transients associated with the copper cavity in an attempt to reduce the microwave PE calibration time.

The central part of my thesis is the development of an RF-driven Zeeman vector magnetometry platform that retains many of the advantages of Rabi-based vector measurements, while reducing sensitivity to slow drifts and overall experimental complexity. Towards this goal, I developed the corresponding measurement and calibration protocols, including generation of RF PEs with a triaxial coil system, developing models that translate the measured Rabi frequencies to magnetic field direction, aond methods to account for the dominant sources of systematics.

The vector magnetometry method and results presented in the thesis form the basis of a manuscript, submitted for peer review [107]. This thesis also includes many components that extend beyond the paper, including a more complete treatment of two-level and multi-level Floquet modeling, a more detailed analysis of systematic effects and calibration protocols, and an expanded discussion of the experimental design and apparatus. This thesis is organized as follows:

Chapter 2 introduces the theoretical framework required to describe atomic spin dynamics in OPMs. The interaction of atomic ensembles with static and oscillating magnetic fields is developed, including the Zeeman interaction, optical pumping processes, and relaxation mechanisms. This chapter establishes the foundation for understanding both scalar and vector magnetometry.

Chapter 3 focuses on RF-driven Zeeman Rabi dynamics. It presents the interaction Hamiltonian describing the coupling between atomic spins and oscillating magnetic fields, and discusses commonly used approximations such as the RWA. I then extend this framework by introducing a Floquet-based description together with a heading error model to account for systematic effects that are not accounted for within the standard treatment, including Bloch-Siegert shifts and nonlinear Zeeman effects. Using Floquet methods in this context along with the heading error model constitute key contributions in this work.

Chapter 4 describes the experimental apparatus used in this work. This includes the design and operation of the microfabricated alkali vapor cell, and associated optical systems for spin preparation and readout. The implementation of the DC and RF magnetic field generation systems is discussed in detail, followed by signal processing techniques used to extract Larmor precession and Rabi frequencies from the measured signals.

Chapter 5 presents the implementation of vector magnetometry using Zeeman Rabi oscillations. It describes the measurement protocol, calibration approach and data analysis techniques, and presents a detailed evaluation of performance metrics such as angular accuracy and sensitivity. The impact of systematic errors and experimental limitations are discussed.

Chapter 6 explores the use of microwave resonators for simultaneous measurements of multiple Zeeman Rabi and hyperfine Rabi transitions. This chapter highlights potential pathways for improving performance and integrating additional sensing capabilities.

Chapter 7 concludes the thesis with a summary of the main results and an outlook for future improvements. Possible extensions to other atomic species and sensing protocols are discussed.

1.6 Publications

Related to this thesis

- **T. S. Menon**, C. Kiehl, D. P. Hewatt, M. Ellmeier, S. Knappe, C. A. Regal, Accurate vector magnetometry via Zeeman Rabi oscillations, arXiv:2603.08594, submitted (2026)

Other publications related to magnetometry

- C. Kiehl, **T. S. Menon**, S. Knappe, T. Thiele, C. A. Regal, Accurate vector optically pumped magnetometer with microwave-driven Rabi frequency measurements, Optica 12 77 (2025)

- C. Kiehl, **T. S. Menon**, D. P. Hewatt, S. Knappe, T. Thiele, C. A. Regal, Correcting heading errors in optically pumped magnetometers through microwave interrogation, Physical Review Applied 22, 014005 (2024)

- D. P. Hewatt, M. Ellmeier, C. Kiehl, **T. S. Menon**, J. W. Pollock, C. A. Regal, S. Knappe, Investigating the hyperfine systematic error and relative phase in low-spin-polarization alkali-metal free-induction-decay magnetometers, Physical Review A 111, 033106 (2025)

1.7 Presentations

- Accurate vector magnetometry in alkali vapor cell via Floquet modeling of Zeeman Rabi oscillations, APS DAMOP Meeting 2025, June 2025 (Poster)

- Vector magnetometry in alkali vapor cell using Radio Frequency Rabi oscillations, Hot Vapor Workshop, October 2024 (Poster)

- Accurate vector magnetometry in alkali vapor cell using hyperfine spectroscopy, NSF Site Visit for QSEnSE, June 2024 (Talk)

- Vector magnetometry in alkali vapor cell using Radio Frequency Rabi oscillations, APS DAMOP Meeting 2024, June 2024 (Talk)

- Reference calibration for vector magnetometry using Rabi oscillations, Workshop on Optically Pumped Magnetometers, August 2023 (Poster)

- Rabi vector magnetometry in hot vapor cell, Workshop on Optically Pumped Magnetometers, August 2022 (Talk)

Chapter 2

Theoretical Background

This chapter introduces the theoretical framework used throughout the thesis to describe optically pumped magnetometry in an alkali vapor cell. The goal of this chapter is to develop a physical picture of the magnetometry platform presented in this dissertation, in which an atomic ensemble is prepared by optical pumping, evolves under the influence of DC and RF magnetic fields, and is interrogated optically to measure the spin dynamics. Description of RF-driven Rabi dynamics is deferred to the next chapter to allow a more detailed and dedicated discussion. The chapter begins by developing a density matrix description of spin dynamics, including the ground state Hamiltonian, Larmor precession, and the emergence of the nonlinear Zeeman effect at geomagnetic fields. The dominant decoherence mechanisms are identified and incorporated into the model through relaxation operators that represent collision processes. The chapter concludes by describing the methods used to create spin polarization and to detect its evolution, establishing the link between the theoretical description and the measured signals used in later chapters. Throughout the remainder of the dissertation, I focus on ^{87}Rb which forms the basis of the experimental platform studied here.

2.1 Atomic Spin Dynamics

Fig. 2.1 shows the level structure of ^{87}Rb, including the ground state and the first excited states that are relevant for optical pumping and probing of spins. In the ground state, the sole electron in the valence shell occupies the 5s orbital, with orbital angular momentum, $L = 0$. With electron spin $S = 1/2$, the total electron angular momentum is $J = L + S = 1/2$, yielding the ground state term symbol $^2S_{\frac{1}{2}}$. The first excited states arise from the 5p orbital where $L = 1$. Spin-orbit coupling described by an interaction proportional to $\mathbf{L} \cdot \mathbf{S}$ lifts the degeneracy of this orbital and produces the fine structure levels $^2P_{\frac{1}{2}}$ and $^2P_{\frac{3}{2}}$. Optical transitions from $^2S_{\frac{1}{2}}$ to these excited states yield the D_1 and D_2 lines at 795 nm and 780 nm, respectively. Because ^{87}Rb possesses a nuclear spin, $I = 3/2$, the hyperfine interaction, $\propto \mathbf{I} \cdot \mathbf{J}$ couples the electron and nuclear spin. This coupling splits the ground state manifold into two hyperfine levels, $F = I + J = 1, 2$. When a DC magnetic field is applied, each hyperfine level further separates into Zeeman sublevels with magnetic quantum numbers, $m_F = -F, -(F-1)..., F$.

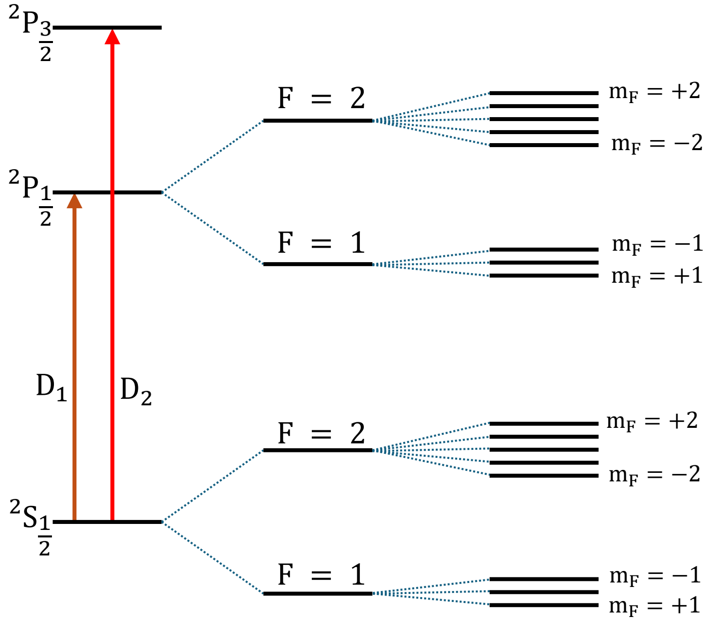

Figure 2.1: Level structure showing D_1 and D_2 transitions in ^{87}Rb

2.1.1 Density Matrix

A central theme in quantum sensing with alkali vapor cells is that the measured signal is an average over a large number of atoms. A rubidium vapor cell heated to 100°C contains

10^{12} atoms per cm^3. Each atom experiences frequent random collisions with other atoms, the buffer gas, and the cell wall. These processes lead to relaxation and redistribution of populations and coherences among internal states. Hence the ensemble cannot be described by a single coherent wavefunction. The density matrix formalism provides a systematic description of such mixed states, while also incorporating relaxation and optical pumping processes. Additionally, optical probing techniques often measure macroscopic observables that typically depend on ensemble-averaged spin polarization rather than on the state of an individual atom.

We describe the atomic state by the density matrix, ρ, given by

$$\rho = \sum_i p_i \left|\psi_i\right\rangle \left\langle\psi_i\right| \tag{2.1}$$

where p_i are probabilities associated with the states, $|\psi_i\rangle$, with $p_i \geq 0$ and $\sum_i p_i = 1$. By definition, ρ is hermitian and positive semi-definite, and it is normalized so that $\mathrm{Tr}\,(\rho) = 1$, where $\mathrm{Tr}\,(...)$ denotes the trace operation.

Expectation values of physical observables follow directly from ρ. For an operator A associated with an observable,

$$\langle A\rangle = \mathrm{Tr}\,(\rho A) \tag{2.2}$$

This expression forms a bridge between atomic parameters and macroscopic observables, and will be used extensively to connect spin polarization to optical rotation signals.

Throughout this dissertation, ρ in the ground state manifold of $^{87}\mathrm{Rb}$ is expressed in the coupled basis states, $|F, m_F\rangle$ with $F = 1, 2$ and $m_F = -F, ..., F$. The matrix elements of ρ have a physical interpretation. The diagonal elements, $\langle\psi_i|\,\rho\,|\psi_i\rangle$ correspond to populations in the respective basis states, while off-diagonal elements $\langle\psi_i|\,\rho\,|\psi_j\rangle$ with $i \neq j$ are coherences and describe phase relations between basis states. In the ground state manifold, it is often useful to separate cohernces within a hyperfine manifold from coherences between manifolds.

Radiofrequency (RF) fields that are resonant with Zeeman splittings, for instance, primarily drive coherences within hyperfine manifolds. Microwaves tuned to the hyperfine splitting drive coherences between the $F = 1$ and $F = 2$ manifolds. Decoherence mechanisms can couple differently to these coherences, so that one type of coherence can decay more rapidly than the other.

The coherent time evolution of the density matrix in the presence of a Hamiltonian, H is given by the quantum Liouville equation [108].

$$\dot{\rho} = -\frac{i}{\hbar}[H, \rho] \tag{2.3}$$

where $\dot{\rho} = d\rho/dt$ and $[H, \rho] = H\rho - \rho H$ denotes the commutator of H and ρ. The explicit form of the Hamiltonian is introduced in the next section.

Often spin dynamics are described more naturally in a rotating reference frame than in the laboratory frame. For instance, an applied RF field oscillating at a frequency ω in the laboratory frame can appear stationary in a frame rotating at the same ω about an appropriate axis. Here, the co-rotating component of the field appears as a time-independent term in the Hamiltonian, which can be interpreted as an effective stationary magnetic field experienced by the spin. In this picture, Rabi oscillations driven by the RF field correspond to precession about this effective stationary field in the rotating frame.

Rotation of a state vector, $|\psi\rangle$, about an axis $\mathbf{a}$ by an angle θ is given by

$$\begin{aligned} |\psi_{\text{rot}}\rangle &= U_a(\theta)\,|\psi\rangle \\ U_a(\theta) &= \exp(-i\theta\,\mathbf{F}\cdot\mathbf{a}) \end{aligned} \tag{2.4}$$

where $\mathbf{F}$ is the angular momentum operator. Conversely, if the laboratory frame were instead rotated by θ about the same axis, the resulting state in the new frame is $|\psi_{\text{rot}}\rangle = U_a^{\dagger}(\theta)\,|\psi\rangle$.

For a frame rotating at frequency ω about an axis $\mathbf{a}$, from Eq. (2.1), the density matrix, ρ, transforms as

$$\rho_{\text{rot}} = U_a^\dagger(\omega t)\,\rho\,U_a(\omega t) \tag{2.5}$$

We can derive the transformation of the Hamiltonian, H, in this frame through Eq. (2.3). First we evaluate the time derivative of ρ_{rot} from Eq. (2.5)

$$\begin{aligned}\dot{\rho}_{\text{rot}} &= \frac{d\left(U_a^\dagger(\omega t)\,\rho\,U_a(\omega t)\right)}{dt}\\ &= \dot{U}_a^\dagger(\omega t)\rho\,U_a(\omega t) + U_a^\dagger(\omega t)\,\dot{\rho}\,U_a(\omega t) + U_a^\dagger(\omega t)\rho\,\dot{U}_a(\omega t)\end{aligned}$$

Substituting $\rho = U_a(\omega t)\,\rho_{\text{rot}}\,U_a^\dagger(\omega t)$ and using $U_a(\omega t)U_a^\dagger(\omega t) = \mathbb{I}$, where $\mathbb{I}$ is the identity operator

$$\dot{\rho}_{\text{rot}} = \dot{U}_a^\dagger(\omega t)U_a(\omega t)\rho_{\text{rot}} + U_a^\dagger(\omega t)\,\dot{\rho}\,U_a(\omega t) + \rho_{\text{rot}}\,U_a^\dagger(\omega t)\dot{U}_a(\omega t)$$

Since $\frac{d}{dt}\left(U_a(\omega t)U_a^\dagger(\omega t)\right) = 0$, $\dot{U}_a^\dagger(\omega t)U_a(\omega t) = -U_a^\dagger(\omega t)\dot{U}_a(\omega t)$. Therefore,

$$\dot{\rho}_{\text{rot}} = U_a^\dagger(\omega t)\,\dot{\rho}\,U_a(\omega t) + [\rho_{\text{rot}}, U_a^\dagger(\omega t)\dot{U}_a(\omega t)]$$

Substituting Eq. (2.3),

$$\dot{\rho}_{\text{rot}} = \frac{-i}{\hbar}U_a^\dagger(\omega t)\,[H,\rho]\,U_a(\omega t) + [\rho_{\text{rot}}, U_a^\dagger(\omega t)\dot{U}_a(\omega t)] \tag{2.6}$$

We can simplify $U_a^\dagger(\omega t)\,[H,\rho]\,U_a(\omega t)$ and rewrite it in terms of ρ_{rot} using Eq. (2.5),

$$\begin{aligned}U_a^\dagger(\omega t)\,[H,\rho]\,U_a(\omega t) &= U_a^\dagger(\omega t)\,[H,\ U_a(\omega t)\,\rho_{\text{rot}}\,U_a^\dagger(\omega t)]\,U_a(\omega t)\\ &= [U_a^\dagger(\omega t)HU_a(\omega t), \rho_{\text{rot}}]\end{aligned}$$

Substituting this equation in Eq. 2.6,

$$\begin{aligned}\dot{\rho}_{\mathrm{rot}} &= \frac{-i}{\hbar}[U_a^{\dagger}(\omega t) H U_a(\omega t), \rho_{\mathrm{rot}}] + [\rho_{\mathrm{rot}}, U_a^{\dagger}(\omega t)\dot{U}_a(\omega t)] \\ &= \frac{-i}{\hbar}[H_{\mathrm{rot}}, \rho_{\mathrm{rot}}]\end{aligned}$$

where

$$\begin{aligned}H_{\mathrm{rot}} &= U_a^{\dagger}(\omega t) H U_a(\omega t) - i\hbar U_a^{\dagger}(\omega t)\dot{U}_a(\omega t) \\ &= U_a^{\dagger}(\omega t) H U_a(\omega t) - \hbar\omega\left(\mathbf{F}\cdot\mathbf{a}\right) \qquad (2.7)\end{aligned}$$

Here we used $\dot{U}_a(\omega t) = -i\omega\left(\mathbf{F}\cdot\mathbf{a}\right)U_a(\omega t)$, which follows from Eq. (2.4). As discussed in the next section, the additional term has the same structure as a Zeeman interaction with a DC magnetic field oriented along **a**. Transforming to the rotating frame therefore effectively introduces a pseudo-magnetic field along the axis of rotation.

2.1.2 Coherent Spin Dynamics in a DC Magnetic Field

Neglecting collisional relaxation, the spin dynamics in the ground state of ^{87}Rb in the presence of a DC magnetic field and buffer gas are governed by a Hamiltonian, H_0, given by

$$\begin{aligned}H_0 &= H_{\mathrm{hfs}} + H_Z \qquad (2.8) \\ H_{\mathrm{hfs}} &= \left(A_{\mathrm{hfs}} + h\frac{\delta\nu_{bg}}{2}\right)\mathbf{I}\cdot\mathbf{S} \\ H_Z &= \mu_B\left(g_S\mathbf{S} + g_I\mathbf{I}\right)\cdot\mathbf{B}_{\mathrm{DC}}\end{aligned}$$

Here H_{hfs} describes hyperfine coupling in the ground state. Here A_{hfs} denotes the hyperfine coupling constant, while collisions between the buffer gas and rubidium atoms produce a collisional shift, $\delta\nu_{bg}$, between hyperfine manifolds. H_Z describes the Zeeman interaction between electron and nuclear spins with the applied DC magnetic field. μ_B

denotes the Bohr magneton, and g_s and g_I are the electron and nuclear Landé g-factors, respectively . As a result of hyperfine coupling, it is far more convenient to work in the coupled basis $\{|F = I + S, m_F\rangle\}$. The scalar product in the hyperfine coupling term can be expressed as

$$\mathbf{I} \cdot \mathbf{S} = \frac{\mathbf{F}^2 - \mathbf{I}^2 - \mathbf{S}^2}{2} \tag{2.9}$$

Eq. (2.9) diagonalizes H_{hfs} in the $\{|F = I + S, m_F\rangle\}$ basis.

$$H_{\text{hfs}} = \frac{1}{2}\left(A_{\text{hfs}} + h\frac{\delta\nu_{bg}}{2}\right)\left(F(F+1) - I(I+1) - S(S+1)\right)|F, m_F\rangle\langle F, m_F| \tag{2.10}$$

The Zeeman interaction, H_Z is not diagonal in this basis as $[H_Z, \mathbf{F}^2] \neq 0$. In the weak field regime, when $\mu_B \mathrm{B}_{\text{DC}} \ll \Delta E_{\text{hfs}}$, where ΔE_{hfs} is the hyperfine splitting. As a result, H_Z can be treated as a perturbation on the $\{|F = I + S, m_F\rangle\}$ states within each hyperfine manifold. With the quantization axis chosen along $\mathbf{B}_{\text{DC}}$, the first-order Zeeman shift is given by,

$$\begin{aligned}
\Delta E^{(1)}_{F,m_F} &= \langle \mu_B \mathrm{B}_{\text{DC}} \left(g_s S_z + g_I I_z\right)\rangle \\
&= \mu_B \mathrm{B}_{\text{DC}} \langle g_F F_z \rangle \\
&= \mu_B \mathrm{B}_{\text{DC}} g_F m_F
\end{aligned}$$

which defines an effective landé g-factor, g_F for each manifold. g_F is given by

$$\begin{aligned}
g_F \langle \mathbf{F} \rangle &= \langle g_s \mathbf{S} + g_I \mathbf{I} \rangle \\
g_F \left\langle \mathbf{F^2} \right\rangle &= \langle g_s \mathbf{S} \cdot \mathbf{F} + g_I \mathbf{I} \cdot \mathbf{F} \rangle \\
g_F F(F+1) &= \left\langle g_s(S^2 + \mathbf{I} \cdot \mathbf{S}) + g_I(I^2 + \mathbf{I} \cdot \mathbf{S}) \right\rangle
\end{aligned} \tag{2.11}$$

Substituting Eq. (2.9), we obtain

$$g_F = \frac{g_s[S(S+1)+F(F+1)-I(I+1)]+g_I[I(I+1)+F(F+1)-S(S+1)]}{2F(F+1)} \tag{2.12}$$

For the ^{87}Rb ground state, this expression yields $g_F \approx 0.4998$ for $F = 2$ and $g_F \approx -0.5018$ for $F = 1$. The opposite signs of g_F reverse the ordering of Zeeman sub-levels in the two hyperfine manifolds, as shown in Fig. 2.1. As discussed in the next chapter, this reversal also determines which polarization component of an RF field, tuned near the Zeeman splitting, couples most strongly to each manifold. The ground state Hamiltonian also governs Larmor precession in the prescence of a DC magnetic field. As illustrated in Fig. 2.2a, the average atomic spin polarization, $\langle \mathbf{F} \rangle$ undergoes precession at the Larmor frequency, ν_L about $\mathbf{B}_{\mathrm{DC}}$, oriented at polar angle β and azimuthal angle α. We consider the

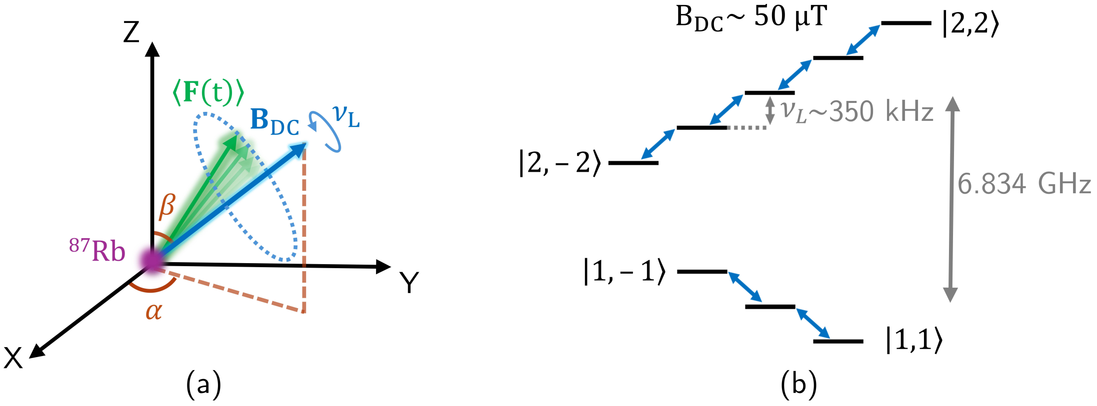

Figure 2.2: Larmor spin precession. (a) Average spin polarization, $\langle \mathbf{F}(\mathrm{t}) \rangle$ precesses around the magnetic field, $\mathbf{B}_{\mathrm{DC}}$ at the Larmor frequency, ν_L. The direction of $\mathbf{B}_{\mathrm{DC}}$ is defined by the polar angle, β and azimuthal angle, α in the laboratory frame. (b) Larmor precession corresponds to coherent evolution between Zeeman sublevels within each manifold at the Zeeman frequency.

evolution of the average spin using Eqs. (2.2) and (2.3)

$$\begin{aligned}\frac{d\langle\mathbf{F}\rangle}{dt} &= \mathrm{Tr}(\dot{\rho}\mathbf{F})\\ &= -\frac{i}{\hbar}\,\mathrm{Tr}([H_0,\rho]\mathbf{F})\\ &= \frac{i}{\hbar}\,\mathrm{Tr}(\rho[H_0,\mathbf{F}])\\ &= \frac{i}{\hbar}\mu_B \mathrm{B}_{\mathrm{DC}} g_F\,\mathrm{Tr}(\rho[F_z,\mathbf{F}])\end{aligned}$$

Evaluating the commutator using spin commutation relations, $[F_z, F_x] = iF_y$ and $[F_y, F_z] = iF_x$.

$$\begin{aligned}\frac{d\langle\mathbf{F}\rangle}{dt} &= -\frac{\mu_B g_F \mathrm{B}_{\mathrm{DC}}}{\hbar}\,\mathrm{Tr}(\rho(F_y\hat{x} - F_x\hat{y}))\\ &= -\frac{\mu_B g_F \mathrm{B}_{\mathrm{DC}}}{\hbar}\,\langle\mathbf{F}\rangle\times\hat{z}\\ &= -\frac{\mu_B g_F}{\hbar}\,\langle\mathbf{F}\rangle\times\mathbf{B}_{\mathrm{DC}}\end{aligned} \tag{2.13}$$

This equation describes the precession of the spin polarization about the applied field, $\mathbf{B}_{\mathrm{DC}}$ at the Larmor frequency, $\gamma\mathrm{B}_{\mathrm{DC}}$, where γ is the gyromagnetic ratio, $\mu_B g_F/h$. Thus the opposite signs of g_F in the two manifolds imply opposite precession directions for $F = 1$ and $F = 2$.

The first-order Zeeman effect, therefore, results in states that vary linearly with m_F across the manifold. This linear dependence produces a set of equally spaced sublevels, and the precession of spin polarization is characterized by a single Larmor frequency within each manifold (Fig. 2.2b). In many magnetometry contexts, this description is often sufficient, particularly for zero-field OPMs, when the DC magnetic field is near zero. First-order treatment is also adequate for those magnetometers based on atoms with zero nuclear spin, as in metastable ^{4}He [109], where the ground state lacks hyperfine structure and the Zeeman structure remains linear over a broad range of fields.

At geomagnetic field strengths ($\mathrm{B_{DC}} \sim 50\,\mu\mathrm{T}$), however, this is no longer true. The mixing of the hyperfine manifolds through the Zeeman interaction contributes to measurable shifts for the $\{|F, m_F\rangle\}$ basis that are nonlinear in m_F. These shifts break the symmetry of the Zeeman sublevels, and lead to unequal adjacent transition frequencies, an effect commonly referred to nonlinear Zeeman effect. We can estimate the quadratic contributions to the Zeeman shifts by computing the second-order corrections to the energies of $\{|F, m_F\rangle\}$ states.

From time-independent perturbation theory, the second-order Zeeman shifts are given by,

$$\begin{aligned}
\Delta E^{(2)}_{F,m_F} &= \sum_{F\neq F'} \frac{|\langle F', m_F|H_Z|F, m_F\rangle|^2}{E^{(0)}_F - E^{(0)}_{F'}} \\
&= \frac{\left|\left\langle I+\frac{1}{2}, m_F\middle|H_Z\middle|I-\frac{1}{2}, m_F\right\rangle\right|^2}{E^{(0)}_F - E^{(0)}_{F'}}
\end{aligned} \tag{2.14}$$

The matrix element is diagonal in m_F as $F_z = S_z + I_z$ commutes with S_z and I_z. To evaluate $\langle F', m_F|H_Z|F, m_F\rangle$, it is helpful to express the coupled basis $\{|F, m_F\rangle\}$ in the uncoupled basis $\{|I, m_I\rangle\, |S, m_S\rangle\}$ following Clebsch-Gordon expansions for $|F, m_F\rangle$

$$\left|F = \frac{3}{2} \pm \frac{1}{2}, m_F\right\rangle = c_\pm \left|\frac{3}{2}, m_F - \frac{1}{2}\right\rangle \left|\frac{1}{2}, +\frac{1}{2}\right\rangle \pm c_\mp \left|\frac{3}{2}, m_F + \frac{1}{2}\right\rangle \left|\frac{1}{2}, -\frac{1}{2}\right\rangle$$

$$c_\pm(m_F) = \sqrt{\frac{\frac{3}{2} \pm m_F + \frac{1}{2}}{2\frac{3}{2} + 1}}$$

These expansions give the intermanifold matrix elements,

$$\langle 2, m_F|S_z|1, m_F\rangle = c_-(m_F)c_+(m_F)$$

$$\langle 2, m_F|I_z|1, m_F\rangle = -c_-(m_F)c_+(m_F)$$

Subsituting these results in Eq. (2.14) yields the second-order Zeeman shifts,

$$\begin{aligned}\Delta E^{(2)}_{F=\frac{3}{2}\pm\frac{1}{2},m_F} &= \pm\mu_B^2 \mathrm{B}_{\mathrm{DC}}^2 \frac{\left|(g_s - g_I)c_-(m_F)c_+(m_F)\right|^2}{\Delta E_{\mathrm{hfs}}} \\ &= \pm\mu_B^2 \mathrm{B}_{\mathrm{DC}}^2 \frac{(g_s - g_I)^2}{2\Delta E_{\mathrm{hfs}}}\left(\frac{1}{2} - \frac{m_F^2}{8}\right)\end{aligned} \qquad (2.15)$$

which shows the quadratic dependence on the magnetic field and a characteristic m_F-dependent shift of the Zeeman transition frequencies. For 50 μT, the second-order correction results in $\sim h \times 35\,\mathrm{Hz}$ variation in energy between adjacent Zeeman splittings, which is significant at the level of precision that OPMs typically measure. An exact treatment of the ground state eigenenergies of H_0 is given by the Breit-Rabi formula [37, 110]

$$E_{F=\frac{3}{2}\pm\frac{1}{2},m_F} = g_I \mu_B m_F \mathrm{B}_{\mathrm{DC}} \pm \frac{\Delta E_{\mathrm{hfs}}}{2}\left(1 + m_F\eta + \eta^2\right)^{1/2} \qquad (2.16)$$

where $\eta = (g_s - g_I)\mu_B \mathrm{B}_{\mathrm{DC}}/\Delta E_{\mathrm{hfs}}$. We can confirm this formula reproduces the first and second-order Zeeman shifts obtained from perturbation theory by expanding the square root to second order in η .

$$\left(1 + m_F\eta + \eta^2\right)^{1/2} \approx 1 + \frac{m_F}{2}\eta + \left(\frac{1}{2} - \frac{m_F^2}{8}\right)\eta^2$$

$$E_{F=\frac{3}{2}\pm\frac{1}{2},m_F} \approx \pm\frac{\Delta E_{\mathrm{hfs}}}{2} + \underbrace{g_I \mu_B m_F \mathrm{B}_{\mathrm{DC}} \pm \frac{(g_s - g_I)\mu_B \mathrm{B}_{\mathrm{DC}} m_F}{4}}_{\Delta E^{(1)}_{F,m_F} = g_F \mu_B \mathrm{B}_{\mathrm{DC}} m_F} \underbrace{\pm\, \mu_B^2 \mathrm{B}_{\mathrm{DC}}^2 \frac{(g_s - g_I)^2}{2\Delta E_{\mathrm{hfs}}}\left(\frac{1}{2} - \frac{m_F^2}{8}\right)}_{\Delta E^{(2)}_{F,m_F}}$$

As a result of the nonlinear Zeeman effect, the $\Delta m_F = \pm 1$ adjacent Zeeman coherences in the two manifolds evolve at slightly different frequencies. Therefore the collective spin polarization does not precess at a single frequency. Instead, the measured Larmor precession contains multiple, closely spaced Larmor frequencies. The relative contributions of these components are determined by the initial density matrix expressed in the basis defined by the magnetic field. If the magnetic field is tilted by an angle, β relative to the initial spin polarization $\langle \mathbf{F}(\mathrm{t}=0)\rangle$, then the initial density matrix, ρ_0 is not an eigenstate of H_0. In the $\{|F, m_F\rangle\}$ basis quantized along $\mathbf{B}_{\mathrm{DC}}$, ρ_0 contains coherences between adjacent Zeeman sublevels, $\langle F, m_F|\rho_0|F, m_F-1\rangle$. The magnitude of each coherence, and therefore the amplitude of the corresponding Larmor component, is determined by the transverse spin projection in the plane spanned by F_x and F_y. In Fig. 2.3, the atoms are prepared with an initial spin polarization $\langle \mathbf{F}(\mathrm{t}=0)\rangle$ aligned with the laboratory Z axis, and the polarization is subsequently measured along the same axis during free precession about $\mathbf{B}_{\mathrm{DC}}$. This figure shows the Fourier transform of a simulated Larmor precession signal at fixed magnetic field strength with progressively decreasing T_2 at various polar angles. We will discuss the physical mechanisms that determine T_2 in the next section. At $\beta = 90°$, the polarization is purely transverse with respect to $\mathbf{B}_{\mathrm{DC}}$, and as a result adjacent coherences contribute with equal weights (Fig. 2.3a). When T_2 is long, the individual components can be resolved, and when T_2 is short, they merge into a single broadened peak, but in both cases, the symmetry of the amplitudes prevents any shifts in the Larmor peak. In contrast, for $\beta = 30°$ (Fig. 2.3b)

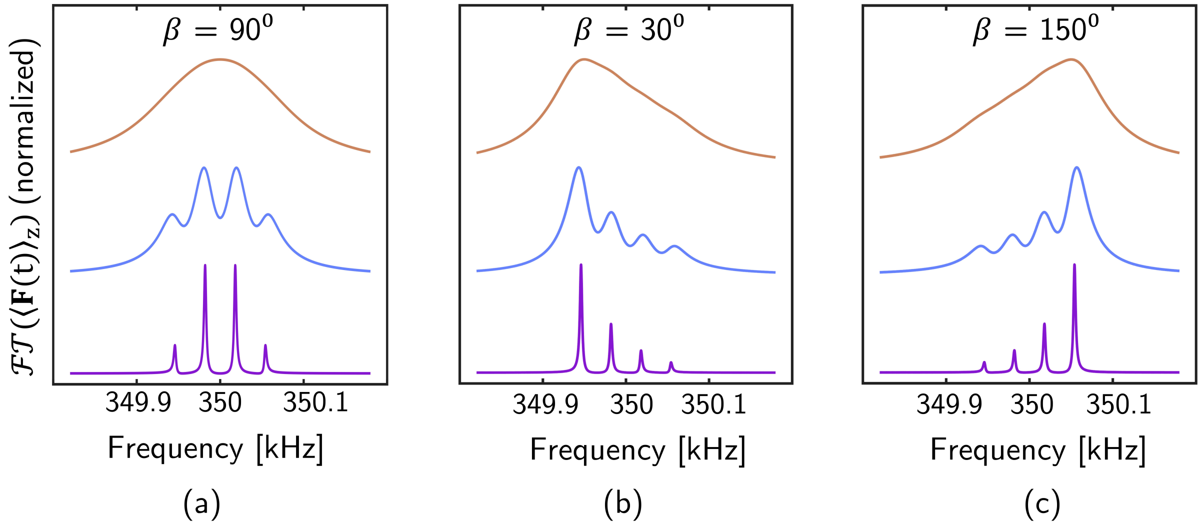

Figure 2.3: Simulation of Larmor amplitudes for several magnetic field directions. Normalized Fourier transform of spin polarization component along the laboratory Z-axis, $\langle \mathbf{F}(\mathrm{t})\rangle$, for pumping rate of 1 MHz depicting Larmor peaks at $T_2 =$ 100 ms (purple), 10 ms (blue), 4 ms (orange) for 50 μT magnetic fields pointed along polar angles (a) $\beta = 90°$, (b) $\beta = 30°$ and (c) $\beta = 150°$.

and 150° (Fig. 2.3c), the initial polarization includes a longitudinal component parallel or anti-parallel to $\mathbf{B}_{\mathrm{DC}}$. This longitudinal projection changes the distribution of population among Zeeman sublevels and breaks the symmetry between positive and negative m_F, producing unequal amplitudes for the coherences that contribute to the measured precession. The resulting asymmetric superposition yields a small shift in the measured Larmor peak, on the order of ~ 36 Hz, corresponding to ~ 5 nT, even though the magnetic field magnitude remains unchanged. This orientation-dependent shift of the inferred Larmor frequency due to the nonlinear Zeeman effect is commonly known as heading error [56, 103, 104, 111]. In the remainder of this dissertation, we will refer to this effect as static heading error to distinguish it from a separate heading error that affects Zeeman Rabi measurements, also arising from the nonlinear Zeeman effect.

2.2 Relaxation Mechanisms

The coherent spin evolution driven by the ground state Hamiltonian is realistically accompanied by non-unitary dynamics that reduce spin polarization and destroy quantum coherence. Relaxation can be included in the quantum Liouville equation in Eq. 2.3 by adding non-unitary terms that represent irreversible processes such as collisions, diffusion and dephasing.

$$\dot{\rho} = -\frac{i}{\hbar}[H, \rho] + \sum_j \mathcal{L}_j(\rho) \tag{2.17}$$

where each $\mathcal{L}_j(\rho)$ is a superoperator that corresponds to a distinct physical process that contributes to the damping of populations and coherences. In an alkali vapor cell, these processes arise primarily from collisions between the different atomic species [112]. Here we will identify the dominant relaxation mechanisms affecting coherent spin dynamics in a buffer gas environment.

2.2.1 Spin-Exchange Collisions

Rubidium vapor cells used for magnetometry are typically operated at high temperatures to increase rubidium density and improve signal-to-noise ratio. In a dense rubidium vapor, collisions between rubidium atoms occur frequently on the timescale of spin precession. The primary collisional interaction between rubidium atoms is spin-exchange. When two rubidium atoms approach closely, overlap of their electron wavefunctions leads to an effective contact interaction that couples the electron spins. The collision effectively interchanges the electron spins of the atoms while conserving the total spin. As the $\{|F, m_F\rangle\}$ basis is defined by the hyperfine coupling between the electron and nuclear spins, the exchange of the electron spins results in the coupling of the hyperfine manifolds and redistribution of populations and coherences within the ground state density matrix.

While the net spin is conserved, spin-exchange collisions degrade transverse spin coherence. Because of differences in the effective Landé g-factor g_F, the Zeeman coherences $\langle F, m_F|\rho_0|F, m_F - 1\rangle$ precess at slightly different frequencies and in opposite directions in the two hyperfine manifolds. Spin-exchange couples hyperfine and Zeeman coherences and redistributes phase information among components, effectively mixing phase evolution occurring at multiple frequencies. The measured spin polarization, $\langle \mathbf{F}(\mathrm{t})\rangle$ is an average over many atoms whose phases have repeatedly been mixed, which yields an effective decay of transverse coherence. This decay is especially pronounced for coherences driven across hyperfine manifolds, such as for microwave-driven Rabi oscillations [87, 106]. Mixing of phase relationships driven across hyperfine manifolds results in a smaller coherence time, ($T_2 \sim 0.4$ ms) compared to Larmor precession or Zeeman Rabi oscillations where coherences evolve within a hyperfine manifold ($T_2 \sim 1$ ms).

Additionally, spin-exchange collisions can also lead to shifts in the eigenenergies. As spin-exchange collisions couple the electron spins of the colliding atoms, each spin of the colliding pair briefly precesses in the effective magnetic field of the other, and the accumulated phase shifts from numerous spin-exchange collisions can give rise to a systematic shift of the Larmor frequency.

We can capture these effects in our master equation (Eq. (2.17)) through the spin-exchange superoperator, $\mathcal{L}_{se}(\rho)$ [113, 114]

$$\mathcal{L}_{se}(\rho) = \Gamma_{\text{se}} \left(\varphi_n \left(1 + 4\langle \mathbf{S} \rangle \cdot \mathbf{S}\right) - \rho \right) + \frac{\delta E_{\text{se}} \left[\langle \mathbf{S} \rangle \cdot \mathbf{S}, \rho \right]}{i\hbar} \tag{2.18}$$

The first term represents decoherence due to spin-exchange collisions while, the second term accounts for the spin-exchange frequency shift. Here φ_n is the nuclear part of the density matrix given by $\varphi_n = \rho/4 + \mathbf{S} \cdot \rho \mathbf{S}$ with $\text{Tr}\left(\varphi_n \mathbf{S}\right) = 0$. $\Gamma_{\text{se}} = \sigma_{se} n_{\text{Rb}} v_r$ denotes the rate of spin-exchange collisions where σ_{se} denotes the spin-exchange cross-section, n_{Rb} is the rubidium number density and v_r denotes the mean relative velocity. The spin-exchange frequency shift is parametrized by $\delta E_{\text{se}}/\hbar = \lambda_{se} n_{\text{Rb}} v_r$, where λ_{se} denotes the spin-exchange frequency shift cross-section. Values of λ_{se}, σ_{se}, and Γ_{se} for the parameters used in our work are listed in Table 2.1.

2.2.2 Spin-Destruction Collisions

Spin-destruction collisions are depolarizing collisions that randomize the electron spin of the rubidium atoms and thereby reduce the ground state polarization of the ensemble. They fundamentally differ from spin-exchange collisions because the electron spin polarization of the colliding pair is not conserved, and therefore the resulting dynamics cannot be interpreted purely as a redistribution of spin within the ensemble. In vapor cells filled with buffer gas, spin-destruction arises through rubidium-rubidium collisions and collisions between rubidium atoms and the buffer gas species. As spin-destruction collisions reduce spin polarization, rather than merely dephasing it, these collisions contribute to both longitudinal as well as transverse relaxation.

In the density matrix formalism, the effect of spin-destruction collisions is included in the master equation (Eq. (2.17)) through the relaxation superoperator, $\mathcal{L}_{sd}$ [115].

$$\mathcal{L}_{sd} = \Gamma_{\text{sd}} \left(\varphi_n - \rho\right) \tag{2.19}$$

This form represents relaxation of the density matrix, ρ towards φ_n at a rate Γ_{sd}. Here $\Gamma_{\text{sd}} = \Gamma_{\text{sd}}^{\text{Rb}-\text{Rb}} + \Gamma_{\text{sd}}^{\text{Rb}-\text{N}_2}$, where $\Gamma_{\text{sd}}^{\text{Rb}-\text{Rb}} = n_{\text{Rb}} v_r \sigma_{\text{sd}}^{\text{Rb}-\text{Rb}}$ and $\Gamma_{\text{sd}}^{\text{Rb}-\text{N}_2} = n_{\text{N}_2} v_r \sigma_{\text{sd}}^{\text{Rb}-\text{N}_2}$ are the spin-destruction rates associated with Rb-Rb and Rb-N_2 collisions, respectively. $\mathcal{L}_{sd}$ describes depolarization of the electron spin, relaxing the ensemble towards a state described by a nuclear density matrix with an unpolarized electron spin. The cross-sections and relaxation rates associated with spin destruction collisions are given in Table 2.1.

2.2.3 Collisions with Vapor Cell Wall

The boundaries of a vapor cell also cause relaxation because interactions with the cell wall destroy ground state polarization When a polarized alkali atom reaches the surface, it experiences large, rapidly varying electric and magnetic fields resulting from the atomic distribution at the cell wall surface, which effectively scrambles the atomic spin. In a buffer gas-filled vapor cell, frequent collisions between rubidium and buffer gas atoms randomize the atomic velocity, and strongly suppress collisions with the cell wall. Repeated buffer gas collisions cause the spin polarization to spread diffusively according to the equation [106, 111, 116, 117],

$$\frac{\partial P}{\partial t} = D\nabla^2 P,\ P|_{\text{wall}} = 0 \tag{2.20}$$

where $P(x, y, z, t)$ denotes the polarization density. The diffusion constant, D is inversely proportional to the buffer gas pressure, p_{bg} and is given by $D = \frac{D_0 p_0}{p_{bg}}$, where $p_0 = 760$ Torr or 1 atm. Here collisions with the wall are treated as perfectly depolarizing. For a rectangular chamber of dimensions x_c, y_c, z_c, the solution to Eq. (2.20) is a sum of diffusion eigenmodes of the form

$$P(x,y,z,t) = \sum_{i,j,k} A_{ijk} \sin\left(\frac{i\pi x}{x_c}\right) \sin\left(\frac{i\pi y}{y_c}\right) \sin\left(\frac{i\pi z}{z_c}\right) e^{-\gamma_{ijk} t}$$
$$\gamma_{ijk} = D\pi^2 \left(\frac{i^2}{x_c^2} + \frac{j^2}{y_c^2} + \frac{k^2}{z_c^2}\right) \tag{2.21}$$

where the coefficients, A_{ijk} are determined by the spatial profile of the initial spin polarization, $P(x,y,z,0)$. In practice, the decay due to the wall collisions is often dominated by the fundamental eigenmode, yielding an effective relaxation rate of γ_{111} in Eq. (2.21).

In the master equation, the effect of wall collisions on the density matrix evolution is represented by the superoperator, $\mathcal{L}_{wc}$

$$\mathcal{L}_{wc} = \Gamma_{\mathrm{wc}}(\rho_{eq} - \rho)$$
$$\Gamma_{\mathrm{wc}} = \frac{D_0 p_0 \pi^2}{p_{bg}} \left(\frac{1}{x_c^2} + \frac{1}{y_c^2} + \frac{1}{z_c^2}\right) \tag{2.22}$$

where ρ_{eq} is the equilibrium density matrix with vanishing coherences and equal populations across the ground state Zeeman sublevels. The values of D_0 and Γ_{wc} for a N_2 buffer gas pressure of 350 Torr and a vapor cell temperature of 100°C are given in Table 2.1 below.

Collision	Cross-section (10^{-18} m^2)	Γ (s^{-1})
(Rb-Rb)$_{se}$	σ_{se} =1.9 [118]	3.9×10^3
	λ_{se} = 0.69 [114]	1.4×10^3
(Rb-Rb)$_{sd}$	1.77×10^{-4}[115]	4
(Rb-N$_2$)$_{sd}$	1.44×10^{-8} [119]	80
Wall	$D_0p_0 = 0.017$ m^2 Torr [120]	220

Table 2.1: Cross-sections and corresponding collision rates associated with dominant relaxation processes in hot ^{87}Rb vapor. Collision rates, Γ are evaluated for a vapor temperature of 100°C, N_2 buffer gas pressure of 350 Torr, and cell size of $3 \times 3 \times 2$ mm^3.

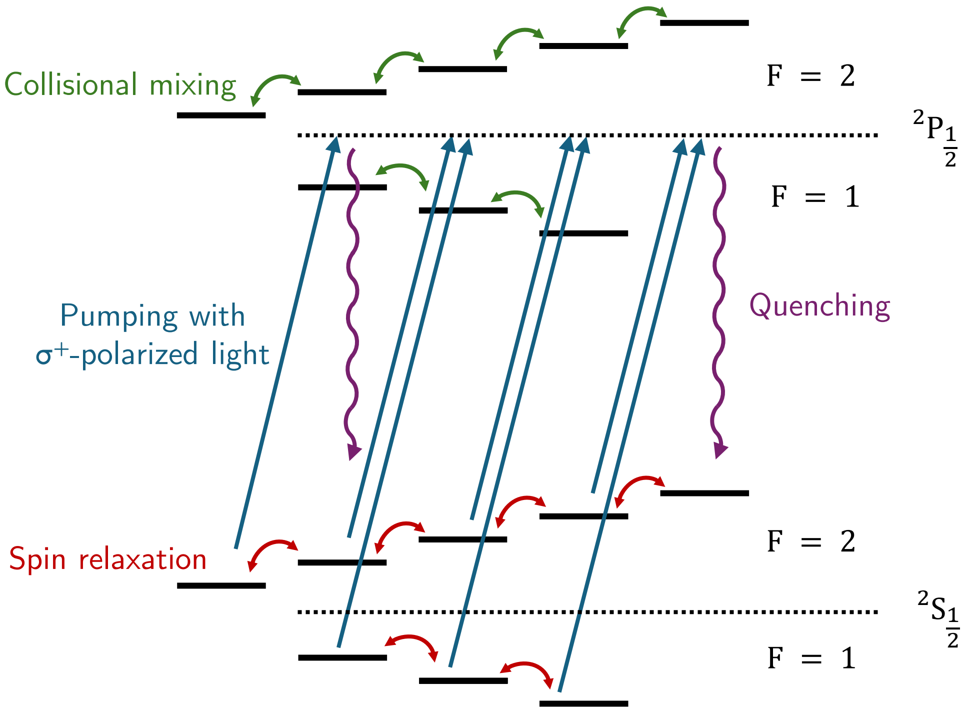

Figure 2.4: Optical pumping on the D_1 line of ^{87}Rb. Resonant σ^+ light drives $\Delta m_F = +1$ transitions from the ground state Zeeman sublevels, excluding the stretched dark state $|2, 2\rangle$. Buffer gas collisions mix the excited state hyperfine manifolds and enable rapid quenching to the ground state. Spin relaxation slowly redistributes population among the ground state Zeeman sublevels.

2.3 Optical Pumping

Optical pumping prepares the atoms in a polarized ground state by transferring photon angular momentum to the atoms through resonant absorption. With σ^+-polarized pump light, $\Delta m_F = +1$ transitions are driven more strongly, and thus population is progressively moved into stretched Zeeman sublevels that are weakly coupled to the pump. In this work, we apply σ^+-polarized light resonant with the D_1 transition to pump atoms into the stretched state $|2, 2\rangle$ [121].

Fig. 2.4 illustrates the optical pumping process in ^{87}Rb. The collisions between ^{87}Rb and N_2 buffer gas broaden and shifts the optical absorption lineshape by several GHz, as shown in Fig. 2.5, making the use of a repumper laser unnecessary to excite population out of $F = 1$. After excitation to the ${}^2P_{\frac{1}{2}}$ state, the buffer gas atoms also promote collisional mixing among the excited state Zeeman sublevels, effectively equalizing the populations in the excited state. Furthermore, in optically thick vapors, polarization can be strongly reduced by radiation trapping, where resonant fluorescence from spontaneous decay is reabsorbed and reemitted multiple times, exposing atoms to randomly polarized light. N_2 reduces radiation trapping by providing a nonradiative decay pathway that transfers excitation energy into molecular rotational and vibrational modes [122]. Ground state spin polarization continuously builds up through repeated optical cycles until it is limited by relaxation mechanisms that repopulate Zeeman levels that absorb pump light. This balance between pumping and relaxation determines the maximum achievable steady-state polarization.

Optical pumping can be incorporated into the Liouville master equation (Eq. (2.17)) with the following superoperator, $\mathcal{L}_{op}$ [111, 113]

$$\mathcal{L}_{op} = R_{OP}(\varphi_n(1 + 2s\hat{k} \cdot \mathbf{S}) - \rho) \tag{2.23}$$

where R_{OP} is the pumping rate, $\hat{k}$ is the propagation direction for the pump beam, and $s \in (-1, +1)$ is the mean photon spin, where $s = +1$ indicates a pure σ^+-polarized pump beam. R_{OP} determines the rate at which the pump light drives absorption-emission cycles that transfer angular momentum to the atoms, and hence controls how quickly ρ is driven towards the pumped state. When the pump beam is tuned to D_1 resonance, R_{OP} is given by

$$R_{OP} = \frac{P_{\text{pump}}}{E_{ph}} \frac{2cr_e f_{\text{D1}}}{A_b \Gamma_{\text{D1}}} \tag{2.24}$$

Here P_{pump}, E_{ph}, and A_b are the optical power, photon energy and cross-sectional area of the pump beam, respectively [123]. The remaining factors express the resonant coupling strength in terms of the oscillator strength, f_{D1}, and linewidth, Γ_{D1}, with r_e, the classical electron radius.

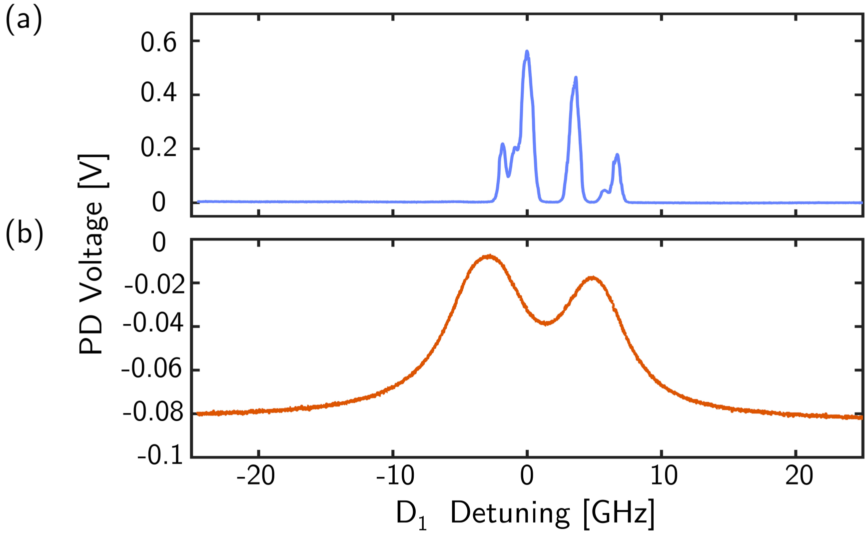

Figure 2.5: Transmission spectra on the ^{87}Rb D$_1$ line measured in (a) conventional glass-blown vapor cell and (b) microfabricated vapor cell filled with 180 Torr N$_2$ buffer gas. The temperature of both cells is maintained at 110°C and the D$_1$ detuning is measured relative to $F = 2 \leftrightarrow F' = 2$ resonance in the glass-blown vapor cell.

2.3.1 Synchronous Optical Pumping

Optical pumping is often implemented continuously to maintain a steady-state polarization, but it can also be modulated in time to amplify the precessing spin coherently. In synchronous optical pumping (SOP), a pump parameter associated with R_{OP} is modulated at a frequency related to the Larmor frequency. The modulated pump parameter commonly includes pump frequency [124], amplitude [80, 125], or pump polarization [126]. This modulation creates a sequence of spin polarization ”kicks” that occur in phase with the Larmor precession. When the modulation matches the Larmor frequency, the kicks are applied at the same spin angle on each cycle, so the successive angular momentum transfers add coherently. In this work, we use SOP with modulation of the optical power at the Larmor frequency using an Acousto-optic modulator, as described in Chapter 4. In the master equation, SOP can be modeled through Eq. (2.23) by allowing R_{OP} to depend explicitly on time. For instance, for a square-wave amplitude modulation applied to the pump beam, $R_{OP}(t)$ is given by

$$R_{OP}(t) = \begin{cases} R_{OP,\max} & \mathrm{mod}(t, 1/\nu_L) \leq d/\nu_L \\ 0 & \text{Otherwise} \end{cases} \tag{2.25}$$

Here d denotes the duty cycle associated with the square wave modulation of frequency, ν_L, while $R_{OP,\max}$ is the pumping rate during the "on" interval.

2.4 Measuring Spin Polarization via Faraday Rotation

A spin-polarized alkali vapor acts as a magneto-optical medium that is birefringent for σ^+-polarized and σ^--polarized light. The refractive index for σ^+ light differs from that for σ^- light when the populations of Zeeman sublevels are unequal [110, 127]. Linearly polarized light can be viewed as an equal superposition of σ^+ and σ^- components with respect to its propagation axis. As the two circular components acquire different phases, the polarization plane rotates. This rotation, which results from spin polarization in the alkali vapor, is known as Faraday rotation.

For a linearly polarized probe beam of frequency, ν propagating along $\hat{k}$ through a cell of length l, the Faraday rotation is given by [106, 127]

$$\theta_f = \frac{\pi \nu l}{c}(n_+(\nu) - n_-(\nu)) \tag{2.26}$$

Here $n_\pm$ are refractive indices for $\sigma^\pm$-polarized light. In a dilute vapor, they may be written in terms of the bulk atomic polarizability, $\chi^\pm$, as

$$n_\pm(\nu) = \sqrt{1 + \chi^\pm(\nu)} \approx 1 + \frac{\chi^\pm(\nu)}{2} \tag{2.27}$$

The polarizabilities $\chi^{\pm}$ can be expressed as a weighted sum over the Zeeman sublevels,

$$\begin{aligned}\chi^{\pm} &= \sum_{F,m_F} \langle F, m_F|\rho|F, m_F\rangle\, \chi^{\pm}_{F,m_F} \\ &= \sum_{F,m_F} \langle F, m_F|\rho|F, m_F\rangle \left(\frac{n_{Rb}}{\epsilon_0 h} \sum_{F',m'_F} |\langle F, m_F|er_{\pm}|F', m'_F\rangle|^2 D(\nu-\nu_0) \right) \qquad (2.28)\end{aligned}$$

where $\langle F, m_F|\rho|F, m_F\rangle$, are the Zeeman sublevel populations and $\langle F, m_F|er_{\pm}|F', m'_F\rangle$ are the transition dipole matrix elements. $D(\nu-\nu_0) = (\nu-\nu_0)/[(\nu-\nu_0)^2 + \Gamma^2]$ denotes the dispersive lineshape for the transition $|F, m_F\rangle \leftrightarrow |F', m'_F\rangle$ with linewidth, Γ which includes pressure broadening from buffer gas, and resonance frequency, ν_0. The dipole matrix elements can be simplified using the Wigner-Eckart theorem,

$$|\langle F, m_F|er_{\pm}|F', m'_F\rangle|^2 = (2F+1)|\langle F\|e\mathbf{r}\|F'\rangle|^2 \begin{pmatrix} F' & 1 & F \\ m'_F & \pm 1 & -m_F \end{pmatrix}^2$$

where the reduced matrix element, $\langle F\|e\mathbf{r}\|F'\rangle$ may be written as [37]

$$|\langle F\|e\mathbf{r}\|F'\rangle|^2 = |\langle J\|e\mathbf{r}\|J'\rangle|^2 (2F'+1)(2J+1) \begin{Bmatrix} J & J' & 1 \\ F' & F & I \end{Bmatrix}^2$$

Here $|\langle J\|e\mathbf{r}\|J'\rangle|^2 = 3h\epsilon_0 c^2 r_e f_{\text{osc}}/2\pi\nu_0$ with f_{osc} denoting the oscillator strength of the transition. We use a linearly polarized probe beam far-detuned from the D_2 transition to monitor spin polarization. Substituting these expressions in Eq. (2.26) yields,

$$\theta_f = \frac{3cr_e f_{D2} n_{Rb} l}{2I+1} \sum_{F,F',m_F} \langle F, m_F|\rho|F, m_F\rangle\,(2F+1)(2F'+1)(2J+1) \begin{Bmatrix} J & J' & 1 \\ F' & F & I \end{Bmatrix}^2$$
$$\times \left[D(\nu-\nu_{0,-}) \begin{pmatrix} F' & 1 & I-\frac{1}{2} \\ m_F+1 & -1 & -m_F \end{pmatrix}^2 - D(\nu-\nu_{0,+}) \begin{pmatrix} F' & 1 & I+\frac{1}{2} \\ m_F-1 & +1 & -m_F \end{pmatrix}^2 \right] \tag{2.29}$$

where $\nu_{0,\pm}$ denotes the transition frequency for excitation from $F = I \pm \frac{1}{2}$ manifolds. As our probe detuning, $\Delta \sim 100$ GHz $\gg |\nu_{0,+} - \nu_{0,-}|$, $D(\nu-\nu_{0,+}) \sim D(\nu-\nu_{0,-})$. This approximation simplifies Eq. (2.29) to give,

$$\theta_f \approx \frac{cr_e f_{D2} n_{Rb} l}{2(2I+1)} D(\nu-\nu_{D_2}) \begin{cases} m_F & F=2 \\ -m_F & F=1 \end{cases} \tag{2.30}$$

The m_F-dependence in this equation means that Faraday rotation is proportional to spin projection as $\theta_f \propto (\langle F=2\rangle)_z - (\langle F=1\rangle)_z$, where z is assumed to be the propagation direction for the probe beam. For a time-dependent density matrix, $\rho(t)$, it is useful to express the Faraday rotation in operator form, so that the measured signal follows directly from the state evolution. In this representation, $\theta_f(t) = \mathrm{Tr}\left(\rho(t)\Theta_f\right)$, where Θ_f is given by

$$\Theta_f = D(\nu-\nu_{D_2}) \frac{cr_e f_{D2} n_{Rb} l}{2(2I+1)} \left(\mathbb{P}_2 F_z \mathbb{P}_2^\dagger - \mathbb{P}_1 F_z \mathbb{P}_1^\dagger \right) \tag{2.31}$$

Here $\mathbb{P}_F$ denotes the projection operator associated with the hyperfine manifold, F.

Faraday rotation provides a nearly non-destructive measurement of the spin polarization as the probe is far-detuned from optical resonance and hence the measurement is dominated by dispersion rather than absorption. The probe acquires a polarization rotation through the birefringence set primarily by the real part of the atomic polarizabilty, while the scattering probability is governed by the imaginary part, and is therfore suppressed by operating at large detuning and low probe powers [128]. In this regime, the probe interaction is quantum nondemolition with respect to the spin component along the probe axis [129]. The remaining back-action arises from residual absorption, which produces optical pumping and scattering, and from AC Stark shifts. These effects can be reduced by increasing detuning and optimizing the probe polarization and optical power. As a result, Faraday rotation allows continuous monitoring of spin dynamics, with minimal perturbation of the atomic state.

Chapter 3

RF-driven Zeeman Rabi Dynamics

In the previous chapter, we developed the theoretical framework for describing spin dynamics based on free-evolution in a DC magnetic field. We established the density matrix formalism, derived the ground state Hamiltonian, including hyperfine and Zeeman interactions, and incorporated the dominant relaxation and optical pumping processes. Here, we extend that framework to include coherent driving by an applied RF field.

RF-driven Zeeman Rabi oscillations form the central process underlying the vector magnetometry technique developed in this dissertation. An accurate determination of magnetic field direction based on Zeeman Rabi oscillations relies fundamentally on a precise theoretical description of the RF-DC magnetic field interaction. In this approach, the direction of the magnetic field is not measured directly, but inferred from the angular dependence of the Rabi frequencies. The DC magnetic field defines the quantization axis, and the applied RF field decomposes into σ^+, σ^-, and π components relative to this axis. Rabi oscillations driven by these components therefore encode information about the magnetic field direction through the Rabi frequencies. The theoretical model that maps field orientation to Rabi frequency thus functions as the transfer function for the vector measurements. Extracting vector information with high accuracy therefore requires an accurate mapping between magnetic field direction and measured Rabi frequencies.

In the weak-driving limit and under near-resonant conditions, the rotating wave approximation provides an intuitive picture in which Rabi oscillations correspond to precession about an effective transverse magnetic field in a rotating frame. However, at geomagnetic field strengths and for finite RF amplitudes, additional effects become significant. Counter-rotating terms, Bloch-Siegert shifts, nonlinear Zeeman structure, and multi-level couplings introduce measurable corrections to the idealized two-level Rabi frequency from the rotating wave approximation.

The same theoretical model also underpins the calibration procedure that extracts the parameters of the RF polarization ellipse (PE) through Rabi frequency measurements. This connection between modeling and calibration makes theoretical accuracy especially important. If the model is incomplete, the calibration may compensate by adjusting the fitted ellipse parameters in a way that reproduces the measurements, thus introducing a systematic bias. Because these parameters define the mapping between the measured Rabi frequencies and the magnetic field direction, the bias propagates directly into the reconstructed vector measurement. At the tens of μrad level, even discrepancies of a few Hz in the predicted Rabi frequency can lead to systematic errors in the inferred direction.

Thus, the performance of the vector magnetometer ultimately depends on how accurately the Rabi frequencies can be modeled. We begin by constructing the full RF-driven atomic Hamiltonian and expressing the applied field in the spherical basis defined by the DC magnetic field. This decomposition of the RF field isolates the components that couple specific Zeeman sublevels and clarifies how the PE determines the relative strengths of $\Delta m_F = \pm 1$ transitions. Sec. 3.2 then introduces a rotating frame description and applies the rotating wave approximation to obtain closed form expressions for the Rabi frequencies. We then describe the contributions of the counter-rotating terms neglected by this approximation that lead to Bloch-Siegert shifts. We then introduce a Floquet-based formalism to capture the full time dependence of the periodic drive and account for higher-order corrections beyond the rotating wave approximation. Finally, we extend this model to include the nonlinear Zeeman effect, which introduces additional orientation and RF phase-dependent distortions of the Rabi frequency.

3.1 RF-driven Zeeman Interaction Hamiltonian

We model the influence of an applied RF field, $\boldsymbol{\mathcal{B}}_{\mathrm{RF}}(t)$, on the ground state dynamics by adding a time-dependent Zeeman interaction to the DC Hamiltonian [108, 130]. The total Hamiltonian is

$$H_{\mathrm{tot}}(t) = H_0 + H_{RF}(t) \tag{3.1}$$

where

$$H_{RF}(t) = \mu_B(g_s\mathbf{S} + g_I I) \cdot \boldsymbol{\mathcal{B}}_{\mathrm{RF}}(t)$$

Here H_0 is the DC magnetic field Hamiltonian given in Eq. (2.8). The time-dependent RF field can be expressed as $\boldsymbol{\mathcal{B}}_{\mathrm{RF}}(\mathrm{t}) = \Re\left(\boldsymbol{\mathcal{B}}_0 e^{i\omega_{RF}t}\right)$ with the complex amplitude $\boldsymbol{\mathcal{B}}_0 = \sum \left(\boldsymbol{\mathcal{B}}_0\right)_j e^{i\phi_j}\,\hat{j},\ j \in \{x, y, z\}$, expressed in the laboratory frame. The parameters $\{(\mathcal{B}_0)_x$, $(\mathcal{B}_0)_y$, $(\mathcal{B}_0)_z$, ϕ_x, ϕ_y, $\phi_z\}$ specify the polarization of the RF field in the cell and determine the corresponding PE as illustrated in Fig. 3.1.

When ω_{RF} is tuned to the Zeeman transition frequency, the RF field couples adjacent Zeeman sublevels determined by the DC magnetic field and drive Rabi oscillations between them within the hyperfine manifolds (Fig. 3.1a). As H_0 captures the time-independent part of the Hamiltonian, we continue to define the quantization axis to be along $\mathbf{B}_{\mathrm{DC}}$, and work in the coupled angular momentum $\{|F, m_F\rangle\}$ basis. In this basis,

$$H_{RF}(t) = \mu_B g_F \mathbf{F} \cdot \boldsymbol{\mathcal{B}}_{\mathrm{RF}}(t) \tag{3.2}$$

To map the RF polarization ellipse to specific Zeeman transitions in ^{87}Rb, we decompose the applied RF field into its spherical components defined in the atomic frame. We use

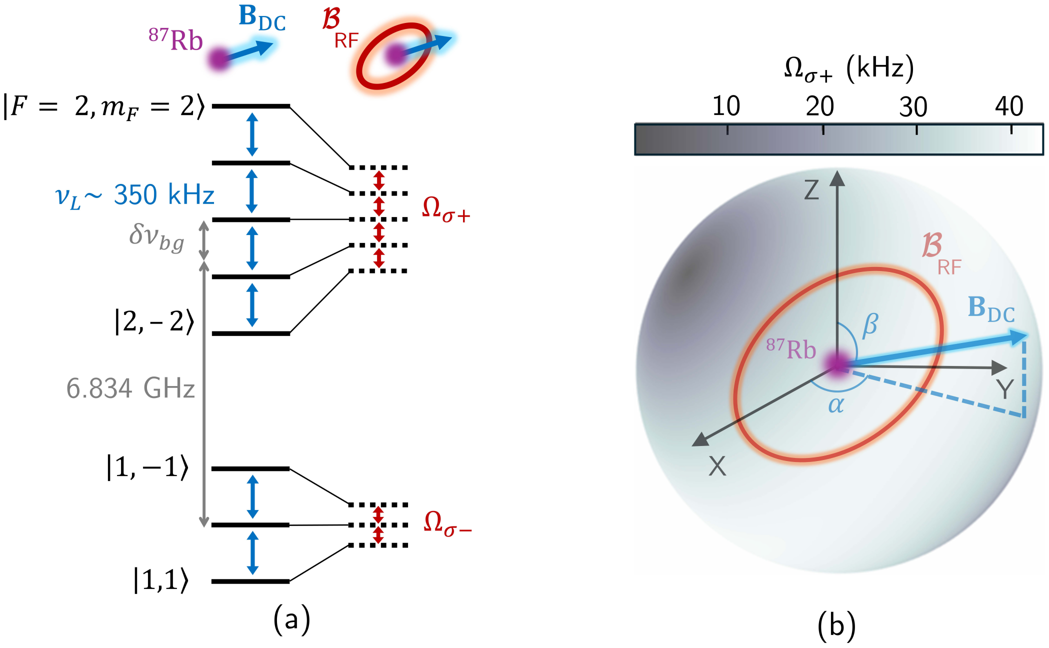

Figure 3.1: RF-driven Zeeman Rabi oscillations in ^{87}Rb. (a) Resonant PE drives Rabi oscillations between Zeeman sublevels within each hyperfine manifold. Because of opposite signs of the Landé g-factor, g_F in the two manifolds, the Zeeman transitions couple to the σ^+ and σ^- polarization components of the RF field in the $F=2$ and $F=1$ hyperfine manifolds, respectively. (b) The resulting σ^+-driven Rabi frequency, $\Omega_{\sigma+}$ depends systematically on the magnetic field direction, (α, β), defined with respect to the X-Y-Z laboratory frame.

the spherical unit vectors [87, 105, 130]

$$\hat{\epsilon}_{\sigma\pm} = \frac{\mp(\hat{x}_a \pm i\hat{y}_a)}{\sqrt{2}}$$

$$\hat{\epsilon}_{\pi} = \hat{z}_a \tag{3.3}$$

where $\hat{z}_a = \mathbf{B}_{\mathrm{DC}}/\mathrm{B}_{\mathrm{DC}}$ defines the quantization axis, and $\hat{x}_a, \hat{y}_a$ span the plane orthogonal to the quantization axis in the atomic frame (Fig. 3.2). For a DC field direction (α, β) in the laboratory frame, the RF amplitude $\boldsymbol{\mathcal{B}}_0$ is projected onto the atomic frame as

$$(\mathcal{B}_0)_{\sigma\pm,\pi} = (R_y(-\beta) R_z(-\alpha)\, \boldsymbol{\mathcal{B}}_0) \cdot \hat{\epsilon}^*_{\sigma\pm,\pi}$$

Here $\hat{\epsilon}^*_{\sigma\pm,\pi}$ denotes the complex conjugate of $\hat{\epsilon}_{\sigma\pm}$, R_y and R_z are rotation matrices about Y and Z axes in the laboratory frame, and $(\mathcal{B}_0)_{\sigma\pm,\pi}$ are PE components aligned with the $\sigma^\pm$ and π atomic polarization basis. In the $\{|F, m_F\rangle\}$ basis, Eq. (3.2) can be written as

$$H_{RF}(t) = \frac{\mu_B g_F}{2\sqrt{2}} \Big(F_+ \left(\mathcal{B}_0\right)_{\sigma+} + F_- \left(\mathcal{B}_0\right)_{\sigma-} + \sqrt{2} F_z \left(\mathcal{B}_0\right)_{\pi} \Big) e^{-i\omega_{RF} t} + h.c. \tag{3.4}$$

where $F_\pm = F_x \pm iF_y$, $h.c.$ denotes the Hermitian conjugate. This ladder operator form is useful because it makes the role of each polarization component term explicit. We identify the relevant couplings by transforming to the interaction picture with respect to H_0:

$$H_{\mathrm{RF,I}} = e^{iH_0 t/\hbar} H_{\mathrm{RF}}(t) e^{-iH_0 t/\hbar} \tag{3.5}$$

Evaluating the dipole matrix element $\langle F, m_F' | H_{\mathrm{RF,I}} | F, m_F \rangle$ in this picture,

$$\begin{aligned} \langle F, m_F' | H_{\mathrm{RF,I}} | F, m_F \rangle &= \frac{\mu_B g_F}{2\sqrt{2}} \langle F, m_F' | \Big(F_+ \left(\mathcal{B}_0\right)_{\sigma+} + F_- \left(\mathcal{B}_0\right)_{\sigma-} \\ &\quad + \sqrt{2} F_z \left(\mathcal{B}_0\right)_{\pi} \Big) \exp\left(i \left[\frac{\mu_B g_F \mathrm{B}_{\mathrm{DC}}}{\hbar} (m_F' - m_F) - \omega_{RF} \right] t \right) + h.c \, | F, m_F \rangle \\ &= \frac{\mu_B g_F}{2\sqrt{2}} \Bigg(\langle F, m_F + 1 | F_+ | F, m_F \rangle \left(\mathcal{B}_0\right)_{\sigma+} e^{i\left(\frac{\mu_B g_F \mathrm{B}_{\mathrm{DC}}}{\hbar} - \omega_{RF}\right)t} \\ &\qquad + \langle F, m_F - 1 | F_- | F, m_F \rangle \left(\mathcal{B}_0\right)_{\sigma-} e^{i\left(-\frac{\mu_B g_F \mathrm{B}_{\mathrm{DC}}}{\hbar} - \omega_{RF}\right)t} \\ &\qquad + \sqrt{2} m_F \left(\mathcal{B}_0\right)_{\pi} e^{-i\omega_{RF} t} \Bigg) + h.c. \end{aligned} \tag{3.6}$$

As $g_F > 0$ for $F = 2$ and $g_F < 0$ for $F = 1$, Zeeman transitions in $F = 2$ and $F = 1$ couple only to the σ^+ and σ^- components of the resonant RF field, respectively.

Eq. (3.6) shows how the RF PE determines the $\Delta m_F = \pm 1$ Rabi couplings through $(\mathcal{B}_0)_{\sigma\pm}$ components, while the remaining components contribute primarily through off-resonant driving and level shifts [101, 131, 132]. While the resulting time-dependent Hamiltonian is exact, it is not yet in a form that yields Rabi frequencies. In the following section, we introduce the rotating wave approximation (RWA), which retains the resonant terms and derives the corresponding Rabi frequencies. We then identify the systematics introduced by this approximation, including residual couplings from neglected counter-rotating and off-resonant components that become relevant outside the weak driving limit.

3.2 Rotating Wave Approximation

To eliminate time dependence, we go into a frame that is rotating at ω_{RF} around $\mathbf{B}_{\mathrm{DC}}$, according to the unitary matrix, $U_{\mathrm{rot}} = \exp(-i\omega_{RF} t F_z)$ consistent with Eq. (2.4) [133]. We continue to work in the atomic frame where the quantization axis points along the DC magnetic field. Transforming into the rotating frame, the total Hamiltonian, $H_{\mathrm{tot}}(t)$ becomes H_{rot} (Eq. (2.7)), where

$$\begin{aligned} H_{\mathrm{rot}} &= U_a^{\dagger}(\omega t) H_{\mathrm{tot}} U_a(\omega t) - i\hbar\omega_{RF} F_z \\ &= e^{i\omega_{RF} t F_z} H_0 e^{-i\omega_{RF} t F_z} + e^{i\omega_{RF} t F_z} H_{RF} e^{-i\omega_{RF} t F_z} - \hbar\omega_{RF} F_z \end{aligned} \tag{3.7}$$

The first term is unchanged as $[H_0, F_z] = [H_{\mathrm{hfs}} + \mu_B g_F \mathrm{B}_{\mathrm{DC}} F_z, F_z] = 0$, and therefore

$$e^{i\omega_{RF} t F_z} H_0 e^{-i\omega_{RF} t F_z} = H_0 \tag{3.8}$$

The RF term is evaluated using the ladder operator form of H_{RF} given by Eq. (3.4),

$$\begin{aligned} e^{i\omega_{RF} t F_z} H_{RF} e^{-i\omega_{RF} t F_z} = e^{i\omega_{RF} t F_z} \Bigg[\frac{\mu_B g_F}{2\sqrt{2}} \Bigg(& F_+ \left(\mathcal{B}_0\right)_{\sigma+} + F_- \left(\mathcal{B}_0\right)_{\sigma-} \\ & + \sqrt{2} F_z \left(\mathcal{B}_0\right)_{\pi} \Bigg) e^{-i\omega_{RF} t} + h.c. \Bigg] e^{-i\omega_{RF} t F_z} \end{aligned}$$

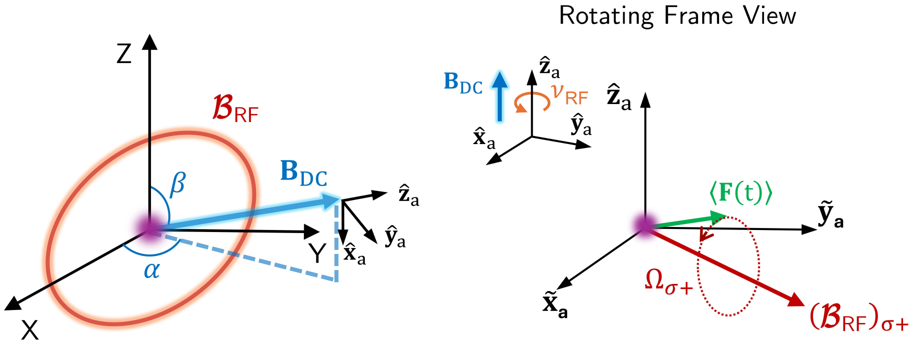

(a) (b)

Figure 3.2: Rabi oscillations described in the rotating frame. (a) $\hat{x}_a - \hat{y}_a - \hat{z}_a$ defines the atomic frame coordinate system with $\hat{z}_a$ oriented along DC magnetic field. (b) Transforming to a frame rotating at $\nu_{RF} = \omega_{RF}/2\pi$ about $\mathbf{B}_{\text{DC}}$ yields the $\tilde{x}_a - \tilde{y}_a - \hat{z}_a$ coordinate system. In this frame, Rabi oscillations reduce to spin precession about the σ^+ polarization component of the RF field, $(\boldsymbol{\mathcal{B}}_{\text{RF}})_{\sigma+}$.

$$\begin{aligned} &= \frac{\mu_B g_F}{2\sqrt{2}} \Big(e^{i\omega_{RF} t F_z} F_+ e^{-i\omega_{RF} t F_z} \left(\mathcal{B}_0\right)_{\sigma+} + e^{i\omega_{RF} t F_z} F_- e^{-i\omega_{RF} t F_z} \left(\mathcal{B}_0\right)_{\sigma-} \\ &+ \sqrt{2} e^{i\omega_{RF} t F_z} F_z e^{-i\omega_{RF} t F_z} \left(\mathcal{B}_0\right)_{\pi} \Big) e^{-i\omega_{RF} t} + e^{i\omega_{RF} t F_z} (h.c.) e^{i\omega_{RF} t F_z} \end{aligned} \tag{3.9}$$

To simplify Eq. (3.9) further, we use the commutation relations, $[F_z, F_\pm] = \mp\hbar F_\pm$ together with the Baker-Campbell-Hausdorff lemma [134],

$$\begin{aligned} e^{i\omega_{RF} t F_z} F_\pm e^{-i\omega_{RF} t F_z} &= F_\pm + [i\omega_{RF} t F_z, F_\pm] + \frac{1}{2!}[i\omega_{RF} t F_z, [i\omega_{RF} t F_z, F_\pm]] + \dots \\ &= F_\pm + i\omega_{RF} t [F_z, F_\pm] + \frac{1}{2!}(i\omega_{RF} t)^2 [F_z, [F_z, F_\pm]] + \dots \\ &= (1 + i\omega_{RF} t(\mp\hbar) + \frac{1}{2!}(i\omega_{RF} t)^2 (\mp\hbar)^2 + \dots) F_\pm \\ &= F_\pm e^{\mp i\omega_{RF} t} \end{aligned}$$

Substituting these expressions in Eq. (3.9),

$$e^{i\omega_{RF}tF_z}H_{RF}e^{-i\omega_{RF}tF_z} = \frac{\mu_B g_F}{2\sqrt{2}}\left(F_+\left(\mathcal{B}_0\right)_{\sigma+} + F_-e^{-i2\omega_{RF}t}\left(\mathcal{B}_0\right)_{\sigma-} + \sqrt{2}F_z e^{-i\omega_{RF}t}\left(\mathcal{B}_0\right)_{\pi}\right) + h.c. \tag{3.10}$$

Therefore, the co-rotating component becomes stationary in this frame, wheareas the residual terms oscillate at ω_{RF} and $2\omega_{RF}$. The RWA retains only the stationary contribution, and neglects the rapidly oscillatory terms [130]. The resulting effective Hamiltonian, $H_{\text{rot}} \approx H_{\text{RWA}}$ is

$$H_{\text{RWA}} = H_{\text{hfs}} + \frac{\mu_B g_F}{2\sqrt{2}}F_+\left(\mathcal{B}_0\right)_{\sigma+} + \frac{\mu_B g_F}{2\sqrt{2}}F_-\left(\mathcal{B}_0\right)^*_{\sigma+} + \mu_B g_F \mathrm{B}_{\mathrm{DC}}F_z - \hbar\omega_{RF}F_z \tag{3.11}$$

Expressing $\left(\mathcal{B}_0\right)_{\sigma+} = |\left(\mathcal{B}_0\right)_{\sigma+}|e^{i\xi}$ and defining the gyromagnetic ratio, $\gamma \equiv \mu_B g_F/\hbar$, we write,

$$H_{\text{RWA}} = H_{\text{hfs}} + \mu_B g_F \frac{|\left(\mathcal{B}_0\right)_{\sigma+}|}{\sqrt{2}}\left(\frac{F_+e^{i\xi} + F_-e^{-i\xi}}{2}\right) + \mu_B g_F\left(\mathrm{B}_{\mathrm{DC}} - \frac{\omega_{RF}}{\gamma}\right)F_z$$

Here $(F_+e^{i\xi} + F_-e^{-i\xi})/2$ is a superposition of F_x and F_y. As a result, this form is equivalent to a Zeeman interaction with an effective DC field, $\mathbf{B}_{\text{rot}}$ in the rotating frame,

$$\mathbf{B}_{\text{rot}} = \frac{|\left(\mathcal{B}_0\right)_{\sigma+}|}{\sqrt{2}}\,\hat{r} + \left(\mathrm{B}_{\mathrm{DC}} - \frac{\omega_{RF}}{\gamma}\right)\hat{z}$$

where $\hat{r}$ is a unit vector in the transverse $\tilde{x}'_a$-$\tilde{y}'_a$ plane such that, $\hat{r}\cdot\mathbf{F} = (F_+e^{i\xi} + F_-e^{-i\xi})/2$. The spin precesses about $\mathbf{B}_{\text{rot}}$, at the effective Rabi frequency,

$$\begin{aligned}\Omega_{\sigma+} &= \frac{\mu_B g_F}{h}\mathrm{B}_{\mathrm{rot}} \\ &= \frac{\mu_B g_F}{h}\sqrt{\left(\frac{|\left(\mathcal{B}_0\right)_{\sigma+}|}{\sqrt{2}}\right)^2 + \left(\mathrm{B}_{\mathrm{DC}} - \frac{\omega_{RF}}{\gamma}\right)^2}\end{aligned} \tag{3.12}$$

which reduces near resonance to, $\Omega_{\sigma+} \approx \mu_B g_F|\left(\mathcal{B}_0\right)_{\sigma+}|/h\sqrt{2}$. For ^{87}Rb, the effective coupling constant here, $\mu_B g_F/h\sqrt{2}$, is approximately ≈ 5 Hz/nT. Similarly, $\Omega_{\sigma-}$ under the RWA can be calculated in a similar fashion by rotating in the opposite sense with the unitary operator, $U_{\text{rot}} = \exp(i\omega_{RF}tF_z)$ to obtain $\Omega_{\sigma-} \approx \mu_B g_F |\left(\mathcal{B}_0\right)_{\sigma-}|/h\sqrt{2}$, near resonance.

3.3 Bloch-Siegert Systematics

The RWA provides an accurate description when the drive is weak and near resonant, so that terms oscillating at ω_{RF} and $2\omega_{RF}$ average to a negligible effect. As a result, this approximation requires $\Omega_{\sigma\pm}/\nu_L \ll 1$. As the RF amplitude increases, the neglected counter-rotating terms induce an AC Zeeman shift that modifies the dressed state energies, shifting the apparent resonance frequency and introducing a small bias in the Rabi frequency. The shifts in the dressed state energies resulting from counter-rotating terms are known as Bloch-Siegert shifts [131, 132]. These effects therefore represent a systematic error in $\Omega_{\sigma+}$ and when translating measured Rabi frequencies into field direction [135, 136].

We can obtain an estimate for Bloch-Siegert shifts by looking at an isolated two-level transition in the presence of a far-detuned field. Consider a two-level system with a Hamiltonian,

$$H = \frac{\hbar\omega_0}{2}\sigma_z + \frac{\hbar\Omega}{2}\frac{\sigma_x + i\sigma_y}{2}e^{-i\omega_{RF}t} + h.c.$$

where, $\sigma_j, j \in \{x, y, z\}$ are the Pauli operators. Applying the RWA, $\sigma_x + i\sigma_y \rightarrow (\sigma_x + i\sigma_y)e^{i\omega_{RF}t}$. As a result, H reduces to H_{rot}, where

$$\begin{aligned} H_{\text{rot}} &= \frac{\hbar\Delta}{2}\sigma_z + \frac{\hbar\Omega}{2}\frac{\sigma_x + i\sigma_y}{2} + h.c. \\ &= \frac{\hbar\Delta}{2}\sigma_z + \frac{\hbar\Omega}{2}\sigma_x \end{aligned}$$

Here $\Delta \equiv \omega_0 - \omega_{RF}$. The resulting dressed state energies are given by the eigenvalues of

H_{rot}, $\epsilon_\pm$

$$\epsilon_\pm = \pm\sqrt{\left(\frac{\Delta}{2}\right)^2 + \left(\frac{\Omega}{2}\right)^2} \tag{3.13}$$

For a far-detuned field, $\Delta \gg \Omega$ and thus the dressed energies in Eq. (3.13) can be simplified using the Taylor approximation.

$$\begin{aligned}\epsilon_\pm &\approx \pm\frac{\Delta}{2}\left(1 + \frac{\Omega^2}{2\Delta^2}\right)\\ &= \pm\frac{\Delta}{2} \pm \frac{\Omega^2}{4\Delta}\end{aligned}$$

Thus the presence of a far-detuned field results in a net effective AC Stark shift of magnitude, $\Omega^2/2\Delta$ to the energy levels of the two-level system.

From this simple estimate, the Bloch-Siegert shifts from counter-rotating terms at frequency $2\omega_{RF}$ in the rotating frame are

$$\begin{aligned}\delta\omega_{BS} &= \frac{\Omega^2}{2(\omega_0 + \omega_{RF})}\\ &\approx \frac{\Omega^2}{4\omega_{RF}}\end{aligned} \tag{3.14}$$

In the multi-level Zeeman structure of ^{87}Rb, the relevant shift is polarization-dependent. This dependence can be appreciated in Eq. (3.10) as the counter-rotating contribution is proportional to $(\mathcal{B}_0)_{\sigma-}$. Residual opposite handed components enchance the counter-rotating coupling and increase the Bloch-Siegert shift. Furthermore, the RF field couples multiple adjacent transitions with matrix elements determined by the Clebsch-Gordan coefficients and with detunings that can differ due to nonlinear Zeeman splittings. The counter-rotating contribution therefore produces a sum of AC Stark shifts whose magnitude depends on the specific $|F, m_F\rangle \leftrightarrow |F, m_F \pm 1\rangle$ transition, the spherical decomposition of the PE and on the direction of the DC magnetic field. We can estimate the impact of the Bloch-Siegert

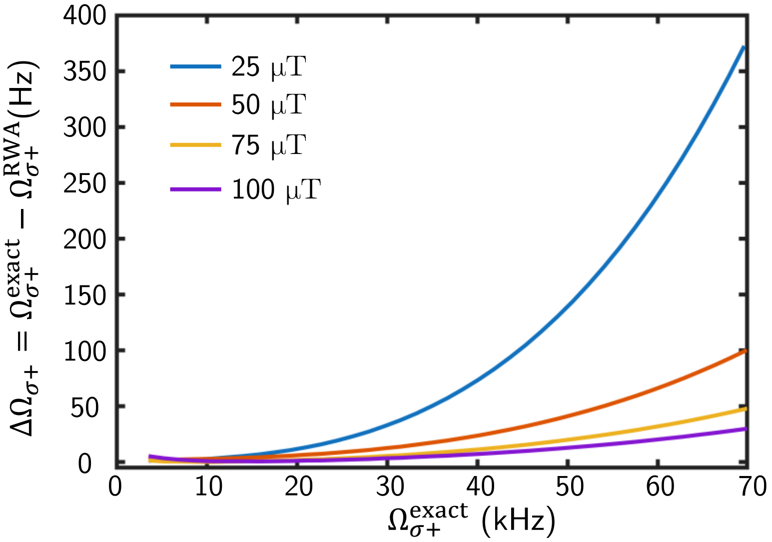

Figure 3.3: Deviation of the Rabi frequency from RWA prediction. $\Omega_{\sigma+}^{exact}$ denotes the Rabi frequency evaluated from numerical integration of the full time-dependent Hamiltonian, H_{tot} for $\boldsymbol{\mathcal{B}}_{\mathrm{RF}} \sim \mathcal{B}_0 \cos(\omega_{RF} t)\hat{x}$ for a DC magnetic field oriented along the laboratory Z axis ($\beta = 0$). The difference, $\Delta\Omega_{\sigma+}$ between the exact and RWA predictions is plotted as a function of $\Omega_{\sigma+}^{exact}$ at various magnetic field strengths.

shifts on the Rabi frequency, $\Omega_{\sigma+}$ using Eq. (3.14). When the RF field is resonant with a Zeeman transition, the Bloch-Siegert shifts to the Zeeman levels result in a detuning, $\Delta \approx \delta\omega_{BS} \sim \Omega_{\sigma-}^2/4\omega_{RF}$. Assuming a detuning dependence similar to a two-level Rabi system,

$$\begin{aligned} \Omega'_{\sigma+} &= \sqrt{\Omega_{\sigma+}^2 + \Delta^2} \\ &= \sqrt{\Omega_{\sigma+}^2 + \left(\frac{\Omega_{\sigma-}^2}{4\omega_{RF}}\right)^2} \\ &\approx \Omega_{\sigma+} + \frac{\Omega_{\sigma-}^4}{32\omega_{RF}\Omega_{\sigma+}^2} \end{aligned} \tag{3.15}$$

where the approximation only holds when $\delta\omega_{BS} \ll \Omega_{\sigma+}$. For $\Omega_{\sigma\pm} = 50$ kHz and $\omega_{RF} = 350$ kHz, the estimated Rabi frequency shift from Eq. (3.15) evaluates to $\sim$ 32 Hz. We can also evaluate the effects of the Bloch-Siegert shifts more rigourously by numerically solving the full time-dependent Hamiltonian, $H(t)$ from Eq. (3.1) and comparing the Rabi frequency, $\Omega_{\sigma+}^{\text{exact}}$ to the rotating wave prediction, $\Omega_{\sigma+}^{\text{RWA}}$ from Eq. (3.12). Fig. 3.3 plots $\Delta\Omega_{\sigma+}$ $= \Omega_{\sigma+}^{\text{Exact}} - \Omega_{\sigma+}^{\text{RWA}}$ as a function of $\Omega_{\sigma+}^{\text{Exact}}$ for four different magnetic field strengths - 25 μT, 50 μT, 75 μT and 100 μT, with RF fields tuned to their respective resonances. $\Delta\Omega_{\sigma+}$ rises rapidly as the Rabi frequency is increased, and reaches $\sim$ 100 Hz systematics for 70 kHz Rabi frequencies at 50 μT. The systematic error also increases as the magnetic field strengths, and thereby the resonant RF frequencies, decrease, consistent with Eq. (3.15) above. These estimates and simulations show how the Bloch-Siegert shifts represent a significant beyond-RWA systematic in modeling our RF interaction. In the next section, we introduce methods that go beyond the rotating wave approximation and incorporate the counter-rotating effects explicitly, providing a route to suppress their systematic effects.

3.4 Floquet Formalism and Bloch-Siegert Corrections

Floquet formalism provides a systematic framework for treating dynamics under a Hamiltonian that is periodic in time, $H(t+T) = H(t)$ [101, 102, 137, 138]. This approach retains the full Hamiltonian and maps the problem to a time-independent eigenvalue equation. Here the periodic driving field is incorportated by working in an expanded Hilbert space that includes Fourier harmonics of the field. The key idea is to represent the time dependence through a Fourier expansion at the driving frequency and to solve for eigenmodes that are periodic in time. The corresponding quasienergies define an effective spectrum for the driven system, similar to an energy spectrum for a time-independent Hamiltonian. Counter-rotating terms that are neglected under the RWA are treated on the same footing as co-rotating terms in the resulting Floquet Hamiltonian, appearing as additional coupling between Fourier components. Their influence on the quasienergy spectrum produces the Bloch-Siegert shifts and they appear as a modification of splitting between dressed state energies that determine the Rabi frequencies. As a result, Floquet theory therefore yields a unified description of both near resonant dynamics and dominant systematic corrections arising from counter-rotating and off-resonant couplings.

3.4.1 Floquet Description of Two-Level Systems

We first develop the Floquet framework for a driven two-level system and then extend the formalism to the multi-level Zeeman structure. For a periodic Hamiltonian, $H(t+T) = H(t)$, with period $T = 2\pi/\omega_{RF}$, Floquet theory provides a general form for the solutions of the Schrodinger equation [139],

$$i\hbar\frac{\partial \left|\psi(t)\right\rangle}{\partial t} = H(t)\left|\psi(t)\right\rangle \tag{3.16}$$

has solutions of the form

$$\begin{aligned}\left|\psi(t)\right\rangle &= e^{-iqt/\hbar}\left|\chi(t)\right\rangle \\ \left|\chi(t+T)\right\rangle &= \left|\chi(t)\right\rangle\end{aligned}$$

Here q is referred to as the associated quasienergy of $\left|\chi(t)\right\rangle$. Substituting this expression into Eq. (3.16) yields the Floquet eigenvalue equation,

$$i\hbar\frac{\partial \left|\chi(t)\right\rangle}{\partial t} = H(t)\left|\chi(t)\right\rangle - q\left|\chi(t)\right\rangle \tag{3.17}$$

Eq. (3.17) can be transformed into a time-independent matrix problem by working in the Fourier basis at the driving frequency. Therefore, to obtain an explicit matrix representation, we expand both $H(t)$ and $\chi(t)$ in Fourier harmonics of ω_{RF},

$$H(t) = \sum_{n=-\infty}^{+\infty} H^{(n)} e^{in\omega_{RF}t}, \quad \left|\chi(t)\right\rangle = \sum_{n=-\infty}^{+\infty} \left|\chi^{(n)}\right\rangle e^{in\omega_{RF}t} \tag{3.18}$$

where $H^{(n)}$ and $\chi^{(n)}$ are the amplitudes of the corresponding Fourier components given by,

$$H^{(n)} = \frac{1}{T}\int_0^T H(t)e^{-in\omega_{RF}t}dt, \quad \left|\chi^{(n)}\right\rangle = \frac{1}{T}\int_0^T \left|\chi(t)\right\rangle e^{-in\omega_{RF}t}dt$$

For a pure sinusoidal driving field, $H^{(n)} = 0$ for $|n| > 1$, leaving only $H^{(\pm 1)}$ and the DC term, $H^{(0)}$. Using Eq. (3.18) in Eq. (3.17) and matching Fourier components yields the coupled equation,

$$\sum_{m=-\infty}^{+\infty} \left(H^{(n-m)} + n\hbar\omega_{RF}\delta_{m,n}\right) \left|\chi^{(m)}\right\rangle = q \left|\chi^{(n)}\right\rangle \tag{3.19}$$

Eq. (3.19) is a time-independent eigenvalue problem in the expanded Hilbert space, $|\alpha\rangle \otimes |m\rangle$, where $|\alpha\rangle$ denotes atomic basis states in the absence of the periodic interaction, while $n \in \mathbb{Z}$, spanning from $-\infty$ to ∞, is the Fourier harmonic index corresponding to the n^{th} Fourier component of $|\chi(t)\rangle$ at frequency ω_{RF}.

If $\widetilde{H}$ denotes the Floquet Hamiltonian in the expanded basis, $\{|\alpha\rangle \otimes |m\rangle\}$,

$$\langle \alpha'; n'|\widetilde{H}|\alpha, n\rangle = \langle \alpha'|H^{(n'-n)}|\alpha\rangle + n\hbar\omega_{RF}\delta_{n',n}\delta_{\alpha,\alpha'} \tag{3.20}$$

The term proportional to $n\hbar\omega_{RF}$ produces a ladder of diagonal blocks shifted by integer multiples of $\hbar\omega_{RF}$. As a result, quasienergies, q are defined modulo $\hbar\omega_{RF}$, which reflects the fact that shifting the Fourier index by an integer corresponds to the same physical solution expressed in a different Fourier harmonic block. This structure will be used below to identify the resonant blocks that reproduce the RWA and those that incorporate the Bloch-Siegert shifts. The resulting quasienergy spectrum, $q_{\alpha;n}$ is obtained by solving the eigenvalue equation for $\widetilde{H}$,

$$\sum_{\alpha''}\sum_{n''} \langle \alpha'; n'|\widetilde{H}|\alpha'', n''\rangle \langle \alpha''; n''|q_{\alpha;n}\rangle = q_{\alpha;n} \langle \alpha'; n'|q_{\alpha;n}\rangle \tag{3.21}$$

with eigenstates $\langle \alpha'; n'|q_{\alpha;n}\rangle = \left\langle \alpha' \middle| \chi_{\alpha}^{(n'-n)} \right\rangle$.

To illustrate the block structure explicitly, consider the Hamiltonian, $H(t)$ describing a two-level system,

$$H(t) = E_e \left|e\right\rangle \left\langle e\right| + E_g \left|g\right\rangle \left\langle g\right| + \hbar(2\Omega \cos \omega_{RF} t)(\left|g\right\rangle \left\langle e\right| + \left|e\right\rangle \left\langle g\right|) \tag{3.22}$$

As the only non-zero terms in the Fourier expansion of $H(t)$ are $H^{(0)}$, $H^{(\pm 1)}$, the only non-zero matrix elements in $\widetilde{H}$ are $\langle \alpha'; n \pm 1|\widetilde{H}|\alpha, n\rangle$ and $\langle \alpha; n|\widetilde{H}|\alpha, n\rangle$. The form of the Floquet Hamiltonian matrix for $H(t)$, $\widetilde{H}$ is shown in Eq. (3.23) below [101].

$$\begin{array}{c|cccccccccc|}
 & \cdots & \langle e;-2| & \langle g;-1| & \langle e;-1| & \langle g;0| & \langle e;0| & \langle g;+1| & \langle e;+1| & \langle g;+2| & \cdots \\
\vdots & \ddots & \vdots & \vdots & \vdots & \vdots & \vdots & \vdots & \vdots & \vdots & \iddots \\
|e;-2\rangle & \cdots & E_e - 2\omega_{RF} & \Omega & 0 & 0 & 0 & 0 & 0 & 0 & \cdots \\
|g;-1\rangle & \cdots & \Omega & E_g - \omega_{RF} & 0 & 0 & \Omega & 0 & 0 & 0 & \cdots \\
|e;-1\rangle & \cdots & 0 & 0 & E_e - \omega_{RF} & \Omega & 0 & 0 & 0 & 0 & \cdots \\
|g;0\rangle & \cdots & 0 & 0 & \Omega & E_g & 0 & 0 & \Omega & 0 & \cdots \\
|e;0\rangle & \cdots & 0 & \Omega & 0 & 0 & E_e & \Omega & 0 & 0 & \cdots \\
|g;+1\rangle & \cdots & 0 & 0 & 0 & 0 & \Omega & E_g + \omega_{RF} & 0 & 0 & \cdots \\
|e;+1\rangle & \cdots & 0 & 0 & 0 & \Omega & 0 & 0 & E_e + \omega_{RF} & \Omega & \cdots \\
|g;+2\rangle & \cdots & 0 & 0 & 0 & 0 & 0 & 0 & \Omega & E_g + 2\omega_{RF} & \cdots \\
\vdots & \iddots & \vdots & \vdots & \vdots & \vdots & \vdots & \vdots & \vdots & \vdots & \ddots
\end{array} \tag{3.23}$$

The Floquet matrix provides a direct comparison between the Hamiltonian under the RWA and the full driven dynamics. Under the rotating frame transformation, $U =$

$\exp\{(-i\omega_{RF} t \left|e\right\rangle \left\langle e\right|)\}$, the resulting Hamiltonian, H_{RWA} is given by

$$H_{\text{RWA}} = (E_e - \hbar\omega_{RF}) \left|e\right\rangle \left\langle e\right| + E_g \left|g\right\rangle \left\langle g\right| + \hbar\Omega(\left|g\right\rangle \left\langle e\right| + \left|e\right\rangle \left\langle g\right|), \tag{3.24}$$

with the resonance condition satisfied when $\hbar\omega_{RF} = E_e - E_g$. The Floquet matrix contains repeated 2×2 submatrices addressing the transition $|g;n\rangle \leftrightarrow |e;n-1\rangle$ that reproduce H_{RWA}. These submatrices provide a direct interpretation of the RWA as a projection of the full Floquet Hamiltonian onto a near resonant block.

The Floquet Hamiltonian goes beyond this approximation by retaining the couplings between the near resonant block and the remaining Fourier blocks. In Eq. (3.23), $|g;n\rangle$ is coupled not only to $|e;n-1\rangle$ but also to $|e;n+1\rangle$, which represents the $2\omega_{RF}$ couter-rotating terms neglected under the RWA. Even though these couplings are far-detuned, they shift the eigenvalues of the resonant dressed states through off-resonant mixing. This shift is inherently amplitude-dependent as the mixing between off-resonant Fourier blocks scales with Ω ($\langle e;n+1|\widetilde{H}|g;n\rangle$ and $\langle g;n|\widetilde{H}|e;n+1\rangle$ in Eq. (3.23)). In the weak driving regime, the shifts can be interpreted as a second-order correction due to off-resonant blocks. These shifts move the center of the avoided crossing, and therefore shift the apparent resonance frequency, leading to Bloch-Siegert shifts in the Floquet description.

The Floquet framework also naturally incorporates multi-photon resonances because in the expanded Hilbert space, each bare atomic state, $|\alpha\rangle$ is transformed into a ladder of states, $|\alpha;n\rangle$, whose energies are shifted by $n\hbar\omega_{RF}$ [138]. Resonances occur whenever two such shifted levels become nearly degenerate, i.e., $E_e - E_g \approx m\hbar\omega_{RF}$, which corresponds to a m-photon resonance. In the quasienergy spectrum, this appears as a sequence of avoided crossings between different Fourier blocks. For a sinusoidal driving field, the Floquet Hamiltonian couples only neighbouring Fourier blocks through $H^{(\pm 1)}$. As a result, an m-photon resonance arises through higher-order processes that couple $|\alpha;n\rangle$ to $|\alpha';n-m\rangle$ through m successive nearest-neighbour couplings. The resulting avoided crossing gap sets the effective dressed state splitting and therefore determines the corresponding multi-photon Rabi frequency.

3.4.2 Floquet Description of Multilevel Zeeman Dynamics

Fig. 3.4 shows the quasienergy spectrum for the two-level Hamiltonian in Eq. (3.22), where $\omega_0 = (E_e - E_g)/\hbar$. The spectrum is plotted for Floquet harmonic indices, $n = -2, -1 \ldots 2$. The dominant avoided crossing occurs at $\omega_{RF} \approx \omega_0$ corresponding to single-photon resonance. Additional avoided crossings at $\omega_{RF} \approx \omega_0/2$ and $\omega_{RF} \approx \omega_0/3$, indicating two-photon and three-photon resonances, respectively.

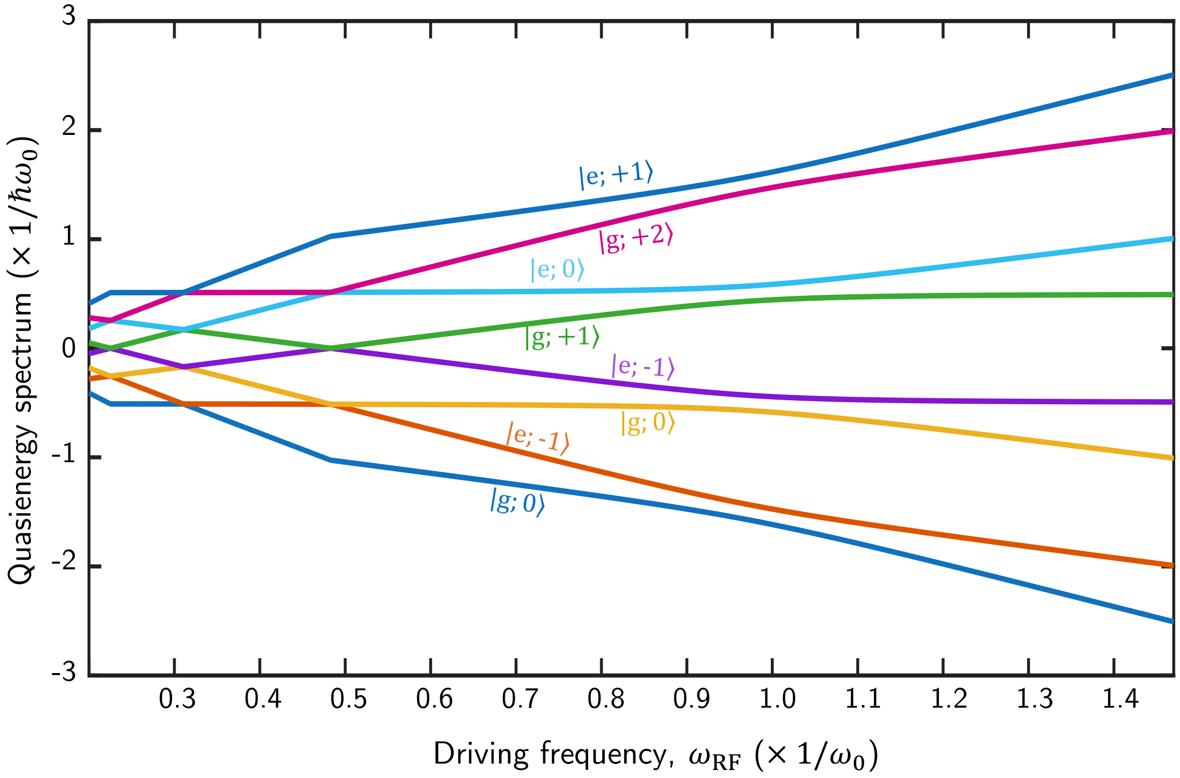

Figure 3.4: Quasienergy spectrum obtained from the Floquet Hamiltonian of a periodically driven two-level system. As the driving frequency, ω_{RF} is varied, avoided crossings emerge at $\omega_{RF} \approx \omega_0$, as well as subharmonics $\approx \omega_0/2$ and $\approx \omega_0/3$ corresponding to multi-photon resonances. Far from resonance, Floquet states $|\alpha; n\rangle$ and $|\alpha; n+1\rangle$ are separated by $\hbar\omega_{RF}$.

The Floquet framework developed for the two-level system generalizes conveniently to the multilevel Zeeman structure of ^{87}Rb by replacing the states, $|g\rangle$ and $|e\rangle$ with the $\{|F, m_F\rangle\}$ basis. Because the applied RF field only drives transitions within the hyperfine manifolds, it is convenient to decompose the total Hamiltonian, $H_{\text{tot}}(t)$ in Eq. (3.1) into contributions from the two manifolds. We define $H_F(t)$ as the projection of the H_{tot} onto the subspace of hyperfine manifold F, so that

$$H_{\text{tot}}(t) = H_{F^+}(t) + H_{F^-}(t),$$

where F^+ and F^- denote $F = 2$ and $F = 1$, respectively. $H_F(t) = \mathbb{P}_F H_{\text{tot}} \mathbb{P}_F^\dagger$, where $\mathbb{P}_F$ is the projection operator associated with each hyperfine manifold. Separating this out between the manifolds helps us define the Floquet matrix for each manifold separately, simplifying the calculation of the Rabi frequencies.

As in the two-level case, to incorporate the periodic structure of the Hamiltonian, we construct the Floquet Hamiltonian, $\widetilde{H}_F$ in the expanded Hilbert space, $|F, m_F\rangle \otimes |n\rangle$, where $n \in \mathbb{Z}$ labels Fourier harmonics of ω_{RF}. Thus, like Eq. (3.20), the matrix elements follow from the Fourier decomposition of $\widetilde{H}_F$ and take the form,

$$\langle F, m_F'; n'|\widetilde{H}_F|F, m_F; n\rangle = \langle F, m_F'|H_F^{(n'-n)}|F, m_F\rangle + n\hbar\omega\, \delta_{m_F', m_F}\delta_{n', n} \tag{3.25}$$

Here $H_F^{(m)}$ denotes the amplitude of $e^{im\omega_{RF}t}$ in the Fourier expansion of H_F. The RF-dressed states are then obtained by diagonalizing $\widetilde{H}_F$. Writing the Floquet states as $|q_{F,m_F;n}\rangle$ with associated quasienergies, $q_{F,m_F;n}$, the eigenvalue equation becomes,

$$\sum_{m_F''}\sum_{n''}\langle F, m_F'; n'|\widetilde{H}_F|F, m_F''; n''\rangle\langle F, m_F''; n''|q_{F,m_F;n}\rangle = q_{F,m_F;n}\langle F, m_F'; n'|q_{F,m_F;n}\rangle,$$

where $\langle F, m_F'; n'|q_{F,m_F;n}\rangle = \left\langle F, m_F' \middle| \chi_{F,m_F}^{(n'-n)} \right\rangle$.

Eq. (3.26) shows the explicit matrix representation of $\widetilde{H}_F$ implied by Eq. (3.25), revealing the block ladder structure along the Fourier index, and how the RF field couples neighboring Fourier blocks through $H_F^{(\pm1)}$.

$$\widetilde{H}_F = \begin{pmatrix} \ddots & \vdots & \vdots & \vdots & \vdots & \vdots & \iddots \\ \cdots & H_F^{(0)} - 2\hbar\omega_{RF}\mathbb{I} & H_F^{(1)} & 0 & 0 & 0 & \cdots \\ \cdots & H_F^{(-1)} & H_F^{(0)} - \hbar\omega_{RF}\mathbb{I} & H_F^{(1)} & 0 & 0 & \cdots \\ \cdots & 0 & H_F^{(-1)} & H_F^{(0)} & H_F^{(1)} & 0 & \cdots \\ \cdots & 0 & 0 & H_F^{(-1)} & H_F^{(0)} + \hbar\omega_{RF}\mathbb{I} & H_F^{(1)} & \cdots \\ \cdots & 0 & 0 & 0 & H_F^{(-1)} & H_F^{(0)} + 2\hbar\omega_{RF}\mathbb{I} & \cdots \\ \iddots & \vdots & \vdots & \vdots & \vdots & \vdots & \ddots \end{pmatrix} \tag{3.26}$$

Here $\mathbb{I}$ denotes the identity operator of size $(2F+1) \times (2F+1)$. The diagonal blocks are given by $H_F^{(0)}$ shifted by multiples of $\hbar\omega_{RF}$, while the off-diagonal blocks are set by $H_F^{(\pm1)}$. $\widetilde{H}_F$ contains the near-resonant couplings, $|F, m_F; n\rangle \leftrightarrow |F, m_F \mp 1; n \pm 1\rangle$ that reproduce the RWA, as well as off-resonant couplings $|F, m_F; n\rangle \leftrightarrow |F, m_F \pm 1; n \pm 1\rangle$, the latter being responsible for Bloch-Siegert effects.

To obtain the Rabi frequencies from the Floquet model, we first compute the quasienergy spectrum and then identify the relevant dressed state splittings. Numerically, the quasienergy spectrum is obtained by diagonalizing the Floquet Hamiltonian, $\widetilde{H}_F$. However, the Floquet Hamiltonian is infinite dimensional because the Fourier index spans all integers, so numer-

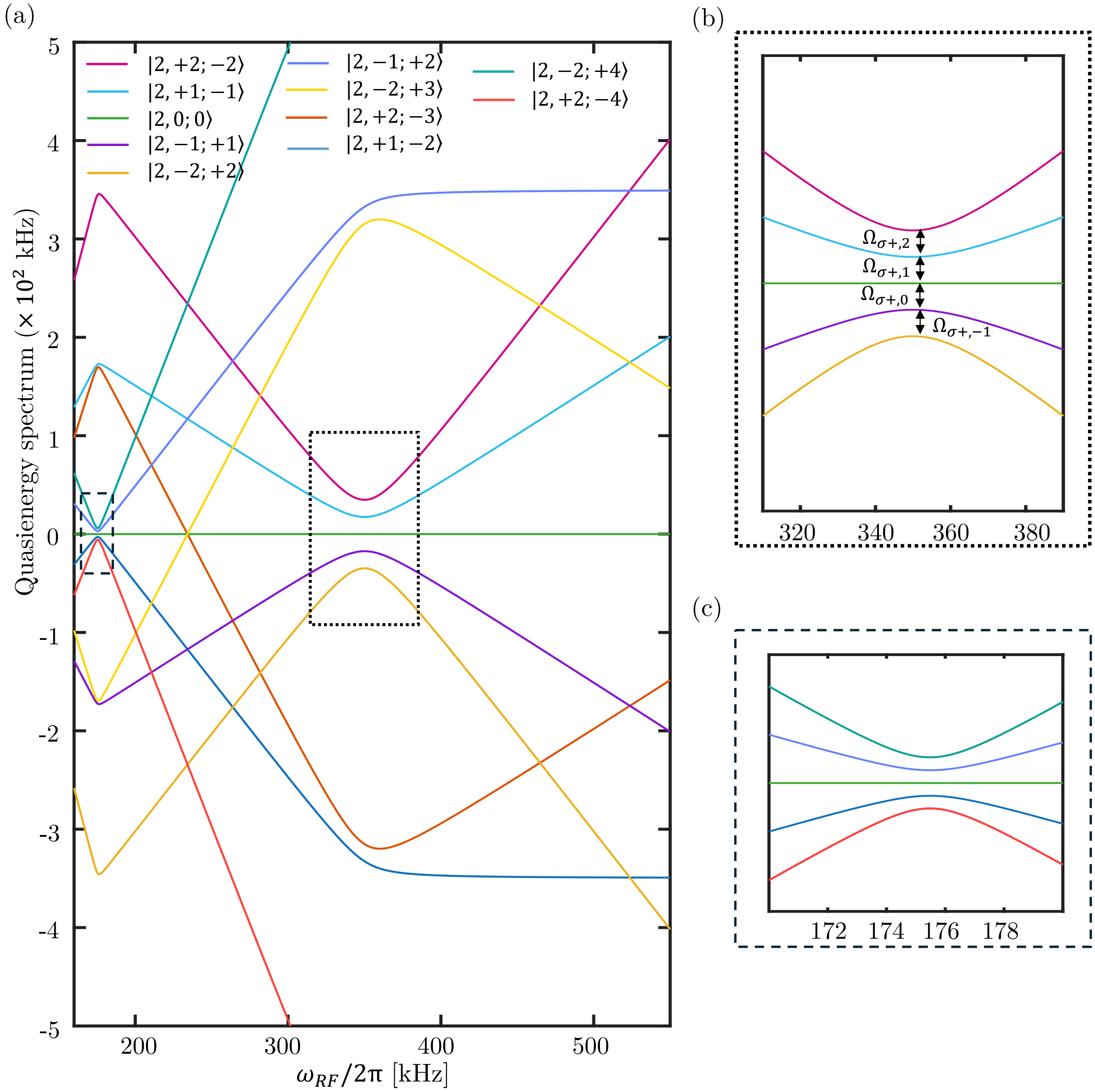

Figure 3.5: Floquet quasienergy spectrum of RF-driven Zeeman Rabi dynamics in $F = 2$ manifold. (a) Quasienergies are computed for a DC field $\mathrm{B}_{\mathrm{DC}} = 50\,\mu\mathrm{T}$ pointing along $(\alpha, \beta) = (0°, 60°)$ in the laboratory frame. As the driving frequency, ω_{RF} is varied, avoided crossings appear near $\omega_{RF}/2\pi \approx \nu_L \approx 350$ kHz (b), and near $\nu_L/2 \approx 175$ kHz (c). Additional Floquet state quasienergies intersect without avoided crossings when the coupling is forbidden by selection rules. Dressed state splittings in (b) yield the Rabi frequencies, $\Omega_{\sigma+,m}$. Far from resonance, Floquet states $|2, m_F; n\rangle$ and $|2, m_F; n+1\rangle$ are separated by $\hbar\omega_{RF}$.

ical evaluation of the spectrum requires truncation to $-n_{\max} \leq n \leq n_{\max}$. The appropriate choice of $n_{\max}$ depends on the strength of off-resonant couplings, including multi-photon transitions that mix distant Fourier blocks into the Floquet states. The contribution of these higher-order couplings scales as, $(\mu_B \mathcal{B}_0/\hbar\omega_{RF})^{m-1}$ [140], for an m-photon transition. For the parameters relevant to the measurements discussed throughout the rest of the dissertation, we find that retaining harmonics from $n = -5$ to $n = +5$ is sufficient.

Fig. 3.5 shows the quasienergy spectrum of $\widetilde{H}_F$ for the $F = 2$ hyperfine manifold in the presence of a 50 μT DC field oriented at, $(\alpha, \beta) = (0, 60°)$, driven by the RF field, $\boldsymbol{\mathcal{B}}_{\mathrm{RF}} = 10\,\mu\mathrm{T}\,\cos(\omega_{RF} t)$. As $\omega_{RF}/2\pi \approx \nu_L$, the five Floquet states associated with adjacent Zeeman sublevels form avoided crossings, that correspond to the driven Zeeman transitions, $|F^+, m_F - 1\rangle \leftrightarrow |F^+, m_F\rangle$ for $m_F = 2, 1, 0, -1$. The Rabi frequencies are obtained from the quasienergy differences between the dressed states at the avoided crossing (Fig. 3.5b). $\Omega_{\sigma\pm,m}$ denotes the Rabi frequency for the Zeeman transition $|F^\pm, m \pm 1\rangle \leftrightarrow |F^\pm, m\rangle$. In the full infinite-dimensional Floquet Hamiltonian, any group of avoided crossings yields the same splittings because of the periodicity of the quasienergy spectrum modulo $\hbar\omega_{RF}$. For a truncated Floquet Hamiltonian, boundary effects can perturb the outermost blocks, so we extract Rabi frequencies from splittings that are well separated from the truncation edges. One convenient choice is to pick the Floquet states lying near the center of the truncated matrix, yielding Rabi frequencies given by,

$$\Omega_{\sigma\pm,m} = \frac{q_{F^\pm,m;-m} - q_{F^\pm,(m-1);-(m-1)}}{h} \tag{3.27}$$

Because the Floquet Hamiltonian retains the counter-rotating and off-resonant terms, the resulting Rabi frequencies include the Bloch-Siegert corrections. As a result, the Floquet prediction reproduces the Rabi frequency obtained from direct numerical calculation with the full Hamiltonian, H_{tot} in Eq. (3.1). Across the range of DC magnetic fields and RF amplitudes explored in Fig. 3.6, the difference remains within 1 Hz.

The quasienergy spectrum in Fig. 3.5c further shows multi-photon resonances near

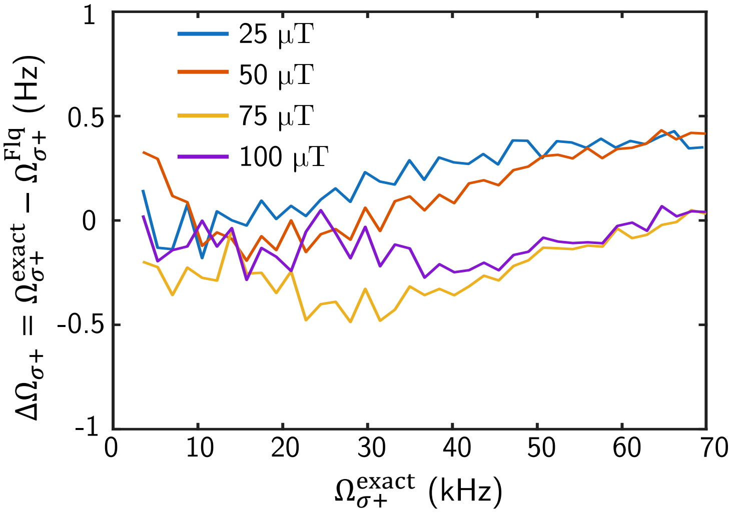

Figure 3.6: Comparison between Floquet quasienergies and direct time-domain simulation. $\Delta\Omega_{\sigma+}$ quantifies the difference between Floquet prediction and numerical integration of H_{tot} for a DC field oriented at $(\alpha, \beta) = (0°, 60°)$ at various magnetic field strengths. The small residual deviations confirm the accuracy of the Floquet description.

$\omega_{RF}/2\pi \approx \nu_L/2$. Angular momentum selection rules constrain the allowed two-photon pathways in the $F = 2$ manifold. The lowest order two-photon process that couples adjacent Zeeman sublevels combines a π transition with a σ^+ transition, leading to a net angular momentum transfer of $\hbar$ and exciting $\Delta m_F = 1$ Zeeman transitions. The Floquet approach captures these resonances as avoided crossings between Floquet states, and the corresponding gaps reflect the effective two-photon Rabi frequencies. The dependence of these two photon couplings on the π component of the RF field offers a route to infer π-driven Rabi dynamics, which is not accessible through single photon Zeeman transitions in either manifold.

3.5 Nonlinear Zeeman Systematics in Rabi Dynamics

The nonlinear Zeeman effect slightly modifies the spacing between Zeeman sublevels within each hyperfine manifold. In Sec. 2.1.2, we showed that these corrections cause adjacent Zeeman coherences to evolve at slightly different frequencies, so that the ensemble spin polarization, $\langle \mathbf{F}(\mathrm{t}) \rangle$ does not precess at a single Larmor frequency. The resulting superposition of the nearby frequencies leads to an orientation-dependent shift, referred to as static heading error when the spin polarization signal is reduced to a single effective frequency.

The same underlying level structure also influences RF-driven dynamics, and therefore the observed Rabi frequencies. In the absence of non-linear Zeeman shifts, all allowed $|F^{\pm}, m \pm 1\rangle \leftrightarrow |F^{\pm}, m\rangle$ transitions within a manifold are resonant at the same Zeeman transition frequency, and the quasienergy spectrum exhibits a single relevant dressed state splitting. When nonlinear Zeeman shifts are present, each adjacent Zeeman transition has a slightly different resonance frequency. Driving the atoms with a single applied ω_{RF} therefore produces a distribution of detunings, resulting in a set of corresponding dressed state splittings and the inferred $\Omega_{\sigma\pm,m}$ from Eq. (3.27). The separation between adjacent $\Omega_{\sigma\pm,m}$, on the order of tens of Hz, depends on both the PE structure as well as the DC magnetic field strength. In hot ^{87}Rb vapor, as in the static heading error case, these splittings are not individually resolved as the coherence time is limited by relaxation and collisions. The measured Rabi signal is therefore a weighted combination of overlapping contributions whose relative weights depend on the DC field orientation and RF field parameters as we discuss below. Variations in these weights distort the Rabi lineshape, giving rise to a systematic we refer to as the dynamic heading error, in analogy with related effects described in Ref. [73].

The dynamic heading error originates from an interplay between the driven Rabi dynamics and the spin state prepared by optical pumping, so it is convenient to describe the systematics in the context of the pumping protocol used. Fig. 3.7 illustrates the physical origin of this error in the rotating frame. As discussed in Sec. 2.3, the experiment primarily employs a synchronous pumping protocol where atoms are pumped to the stretched state, $|2, 2\rangle$. State preparation is achieved using resonant σ^{+}-polarized light, applied as a train of pulses, phase-locked to the RF oscillator. During the pumping interval, the RF field is turned off at the atoms to prevent Rabi oscillations while the spin polarization is being established. In Fig. 3.7, the relative phase between the pump pulse train and the RF waveform is varied. If Δt denotes the time between the end of a pump pulse and the nearest peak of the RF waveform, then the corresponding phase is $\phi_0 = \omega_{RF}\Delta t$. In Fig. 3.7a, Fig. 3.7c and Fig. 3.7e, ϕ_0 takes the values, 90°, 0° and 180° respectively. These values determine the effective RF phase at the start of probe sequence when the RF fields begin to drive coherent Rabi oscillations. In a frame rotating at $\omega_{RF}/2\pi$ about $\mathbf{B}_{\mathrm{DC}}$, variation in the initial RF phase manifests as a spatial rotation of the stationary σ^+ polarization component of the RF field. We can show this using a simple classical derivation.

Consider the RF field,

$$\boldsymbol{\mathcal{B}}_{\mathrm{RF}}(t) = \Re\left(\boldsymbol{\mathcal{B}}_0 e^{-i(\omega_{RF}t+\phi)}\right) \tag{3.28}$$

where ϕ is an initial phase offset applied to the RF field.

The transformation to a rotating frame can be described by the Euler-Rodrigues formula [141]. The rotation of a vector, $\mathbf{v}$ by angle θ about an axis $\hat{b}$ is given by

$$\mathbf{v}' = \mathbf{v}\cos(\theta) + (\hat{b}\times\mathbf{v})\sin(\theta) + \hat{b}(\hat{b}\cdot\mathbf{v})(1-\cos(\theta)) \tag{3.29}$$

The rotating frame is defined by rotation about an axis defined by $\hat{b} = \mathbf{B}_{\mathrm{DC}}/\mathrm{B}_{\mathrm{DC}}$ at angular frequency ω_{RF}. Here we focus on the σ^+ polarization component of $\boldsymbol{\mathcal{B}}_{\mathrm{RF}}(t)$

$$(\boldsymbol{\mathcal{B}}_{\mathrm{RF}}(t))_{\sigma+} = \left(\boldsymbol{\mathcal{B}}_{\mathrm{RF}}(t)\cdot\hat{\epsilon}^*_{\sigma+}\right)\,\hat{\epsilon}_{\sigma+}$$

where both $\boldsymbol{\mathcal{B}}(t)$ and $\hat{\epsilon}_{\sigma+}$ are expressed in the laboratory frame. Transforming to a frame rotating at ω_{RF} corresponds to a rotation in the opposite sense relative to the laboratory frame, such that $\theta = -\omega_{RF}t$ in Eq. (3.29). Because $\hat{\epsilon}^*_{\sigma+}\cdot\hat{b} = 0$, Eq. (3.29) yields

$$(\boldsymbol{\mathcal{B}}'_{\mathrm{RF}})_{\sigma+} = (\boldsymbol{\mathcal{B}}_{\mathrm{RF}}(t))_{\sigma+}\cos(\omega_{RF}t) - \hat{b}\times(\boldsymbol{\mathcal{B}}_{\mathrm{RF}}(t))_{\sigma+}\sin(\omega_{RF}t)$$

Using $\hat{b} \times \hat{\epsilon}_{\sigma\pm} = \mp i\hat{\epsilon}_{\sigma\pm}$ and substituting Eq. (3.28), we obtain

$$\begin{aligned}
(\boldsymbol{\mathcal{B}}'_{\mathrm{RF}})_{\sigma+} &= \Re\left[\left(\boldsymbol{\mathcal{B}}_0 \cdot \hat{\epsilon}_{\sigma+}\right) e^{-i(\omega_{RF}t+\phi)} \left(\hat{\epsilon}_{\sigma+}\cos(\omega_{RF}t) + i\hat{\epsilon}_{\sigma+}\sin(\omega_{RF}t)\right)\right] \\
&= \Re\left[\left(\boldsymbol{\mathcal{B}}_0 \cdot \hat{\epsilon}_{\sigma+}\right)\hat{\epsilon}_{\sigma+} e^{-i\phi}\right]
\end{aligned}$$

Thus the σ^+ component becomes time-independent in this frame, and varying the phase offset ϕ rotates the stationary component by the same angle.

The rotation of the stationary component in the rotating frame modifies the Rabi lineshape in a manner analogous to the static heading error in Larmor precession. In Fig. 3.7, as $(\boldsymbol{\mathcal{B}}_{RF})_{\sigma+}$ rotates, the angle between $(\boldsymbol{\mathcal{B}}_{RF})_{\sigma+}$ and the optically pumped spin polarization, $\langle \mathbf{F} \rangle$ varies from $90°$ (Fig. 3.7b) to $\sim 90° - \beta$ (Fig. 3.7d) and $\sim 90° + \beta$ (Fig. 3.7e), respectively, where β is the polar angle of the DC magnetic field in the laboratory frame. Because the RF field couples to multiple Zeeman transitions, the changing angle modifies their relative strengths. The resulting redistribution of Rabi peak amplitudes modifies the Rabi lineshape, leading to shifts in the overall measured σ^+-driven Rabi frequency, $\Omega_{\sigma+}$. The same mechanism also applies to σ^- driving, but the fewer number of adjacent transitions in the $F = 1$ manifold reduces the resulting shift in $\Omega_{\sigma-}$.

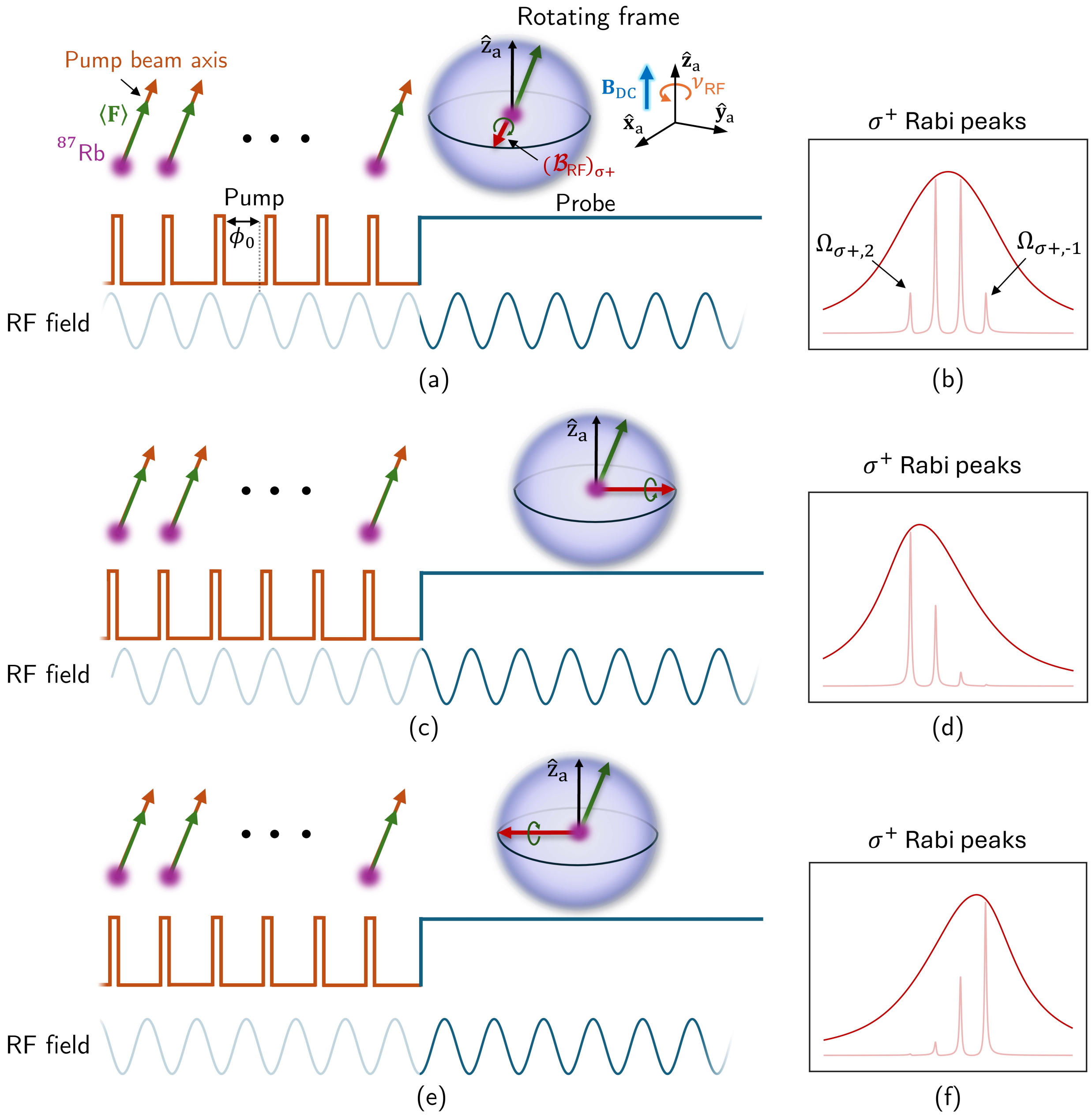

Figure 3.7: Origin of dynamic heading error systematic in Zeeman Rabi frequencies. During synchronous pumping, pump pulses are phase locked to the RF oscillator, while the atoms experience the RF field only during the probing sequence. (a,c,e) show a schematic of the pump-probe sequence and the RF field with relative phases, ϕ_0 at (a) 90°, (b) 0° and (c) 180°, respectively between the pump pulse train and the RF waveform. (b,d,f) display the corresponding σ^+ Rabi spectra for $T_2 = 50$ ms (light red) and $T_2 = 2$ ms (dark red). In the rotating frame, Rabi dynamics correspond to precession about $(\boldsymbol{\mathcal{B}}_{\mathrm{RF}})_{\sigma+}$. Analogous to static heading error (Fig. 2.3), the relative peak amplitudes depend on the angle between the $\langle \mathbf{F} \rangle$ and the stationary $(\boldsymbol{\mathcal{B}}_{\mathrm{RF}})_{\sigma+}$. This angle varies with the phase, ϕ_0, thus producing phase-dependent shifts, in the inferred Rabi frequency. The frequency and the separation of the Rabi peaks depends on the PE structure, the DC magnetic field and the RF frequency.

We can characterize this systematic experimentally by varying the initial phase of the driving RF field. Fig. 3.8 shows the variation of $\Omega_{\sigma+}$ as a function of the applied RF phase, ϕ for $\boldsymbol{\mathcal{B}}_{\mathrm{RF}}(t) \sim 9.1\cos(\omega_{RF}t + \phi + \phi')\,\mu\mathrm{T}\,\hat{x}$. Here ϕ' denotes technical phase shifts introduced by the RF electronics, while $t = 0$ marks the transition from optical pumping to probing. Here $\phi' + \phi$ defines the relative phase between the pump pulses and the driving field. Here the measured $\Omega_{\sigma+}$ exhibits a sinusoidal dependence that is characteristic of a heading error. The peak-to-peak magnitude of the Rabi frequency modulation in Fig. 3.8 depends on β, because the rotation of $(\boldsymbol{\mathcal{B}}_{RF})_{\sigma+}$ sweeps the angle between $\langle \mathbf{F} \rangle$ and $(\boldsymbol{\mathcal{B}}_{RF})_{\sigma+}$ between $90° - \beta$ and $90° - \beta$. As β gets closer to zero, the angular sweep decreases, and the corresponding phase-dependent variation of the Rabi frequency decreases. This behaviour is analogous to the static case, where the heading error vanishes when the magnetic field is orthogonal to the spin polarization.

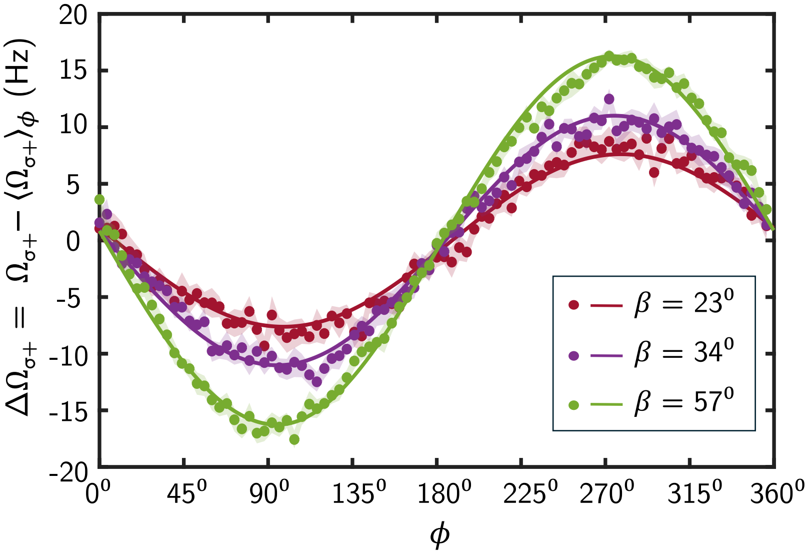

Figure 3.8: Dynamic heading error measurements. Variation of measured $\Omega_{\sigma+}$ with the RF phase, ϕ for three polar angles. $\alpha = 0$ for all three directions. $\langle\Omega_{\sigma+}\rangle_\phi$ denotes the Rabi frequency variation averaged over the entire phase. Solid lines show results of the model (Eq. (3.30)) accounting for dynamic heading errors in the PE, $\boldsymbol{\mathcal{B}}_{\mathrm{RF}} \sim 9.1\cos(\omega_{RF}t + \phi' + \phi)\hat{x}\ \mu\mathrm{T}$ with technical offset phase, $\phi' \sim 232°$.

To model this systematic, we compute the weighted contributions of the individual

Rabi frequencies for a given RF phase based on this initial optically pumped state. The atomic dynamics during optical pumping are evaluated using the optical pumping model described in Sec. 2.3. If ρ_0 denotes the density matrix after the pumping sequence, we can simulate the Faraday rotation signal, $\theta_f(t)$

$$\theta_f(t) = \mathrm{Tr}\left(e^{-i\widetilde{H}_F t/\hbar}\rho_0 e^{i\widetilde{H}_F t/\hbar}\Theta_f\right)$$

where Θ_f is the Faraday rotation operator given in Eq. (2.31) and Tr(..) denotes the trace operation. Expressed in the Floquet eigenbasis, $\{|q_{F,m_F;m}\rangle\}$, this equation yields a sum over coherences oscillating at frequencies given by differences of the Floquet quasienergies,

$$\theta_f(t) = \sum_{m_F,m'_F,m,m'} \left\langle q_{F,m_F;m}\middle|\rho_0\middle|q_{F,m'_F;m'}\right\rangle \left\langle q_{F,m'_F;m'}\middle|\Theta_f\middle|q_{F,m_F;m}\right\rangle \exp\left(-\frac{i\big(q_{F,m'_F;m'} - q_{F,m_F;m}\big)t}{\hbar}\right)$$

As ρ_0 and Θ_f are time-independent, transformation to the expanded Floquet Hilbert space is simple.

$$\begin{aligned}\langle F, m'_F; n'|\rho_0|F, m_F; n\rangle &= \langle F, m'_F|\rho_0|F, m_F\rangle \\ \langle F, m'_F; n'|\Theta_f|F, m_F; n\rangle &= \langle F, m'_F|\Theta_f|F, m_F\rangle\end{aligned}$$

The Rabi peaks measured in the Fourier spectrum of $\theta_f(t)$ at the frequency $\Omega_{\sigma\pm,m}$ have the amplitudes, $A_{\sigma\pm,m}$ given by magnitudes of the corresponding matrix elements (Eq. (3.27)),

$$A_{\sigma\pm,m} = \left|\left\langle q_{F^\pm,m;-m}\middle|\rho_0\middle|q_{F^\pm,(m-1);-(m-1)}\right\rangle \left\langle q_{F^\pm,m;-m}\middle|\Theta_f\middle|q_{F^\pm,(m-1);-(m-1)}\right\rangle\right|$$

The effective Rabi frequency, $\Omega_{\sigma\pm}$ can then be modeled as a weighted average over $\Omega_{\sigma\pm,m}$

$$\Omega_{\sigma\pm} = \frac{\sum_m A_{\sigma\pm,m}\Omega_{\sigma\pm,m}}{\sum_m A_{\sigma\pm,m}} \tag{3.30}$$

where $m \in \{-1, 0, 1, 2\}$ for $\Omega_{\sigma+}$, and $m \in \{0, 1\}$ for $\Omega_{\sigma-}$. Solid lines in Fig. 3.8 show that Eq. (3.30) captures the modulation of $\Omega_{\sigma+}$ with RF phase in excellent agreement with measurements to within $\sim$3 Hz using a pumping rate, $R_{OP} = 0.7$ MHz.

In this chapter, we developed a comprehensive theoretical description of RF-driven Zeeman Rabi dynamics in the ground state of ^{87}Rb at geomagnetic field strengths. We showed that Zeeman Rabi oscillations in alkali vapors cannot be treated as an ideal two-level problem when operating at finite RF amplitudes. While the RWA offers physical intuition and correctly identifies the dominant resonant terms, accurate vector magnetometry requires additional corrections. In particular, counter-rotating contributions and nonlinear Zeeman shifts lead to systematic modifications to the effective Rabi frequencies that depend on both RF parameters and the field orientation. These corrections modify both the magnitude and angular dependence of the Rabi frequencies, and therefore directly influence the inferred magnetic field direction. By incorporating these effects into a single time-independent framework, we established a mapping that connects the applied RF PE to the measured Rabi frequencies with high accuracy. This model forms the foundation for calibration protocols and vector measurements presented in the following chapters.

Chapter 4

Apparatus for Zeeman Rabi Vector Magnetometry

This chapter describes the experimental apparatus developed to implement Zeeman Rabi vector magnetometry. The apparatus is designed for the preparation, manipulation and measurement of atomic spin dynamics in a microfabricated ^{87}Rb vapor cell. Achieving reliable vector magnetometry requires accurate control of both the DC magnetic field that defines the quantization axis, and the time-dependent RF fields that drive Zeeman transitions, as well as sensitive optical techniques for detecting the resulting spin evolution. The apparatus therefore integrates optical pumping and Faraday rotation measurements with dedicated magnetic field generation systems and synchronized electronic control.

The following sections describe the major components of this apparatus. Section 4.1 provides a schematic overview of the apparatus, including the optical systems used for spin preparation and detection. Section 4.2 discusses the microfabricated vapor cell and the optical heating approach used to control its temperature. Section 4.3 presents the DC and RF magnetic field generation and control systems along with their associated electronics. Section 4.4 describes the procedures used to analyze the measured Faraday rotation signals and extract the Rabi and Larmor frequencies.

4.1 Overview of the Experimental Setup

A schematic overview of the apparatus is shown in Fig. 4.1. The rubidium atoms are contained in a microfabricated vapor cell that defines the interaction volume for all measurements. The cell is mounted inside an alumina resonator, which supports stable mounting and efficient thermal coupling. The cell and the resonator are heated up to 100°C with a high optical power heating laser in order to increase the vapor density, according to Eq. (1.2). Two separate triaxial coil systems provide magnetic field control at the cell. A DC coil system generates 50 μT fields in arbitrary directions and an independent RF coil system produces the RF fields used to drive Zeeman Rabi oscillations. To suppress magnetic field noise from the environment, the coil systems, the resonator and the vapor cell are placed inside a four-layer μ-metal shield. The shield is a Twinleaf MS2 system with a nominal shielding factor of 10^6 [142].

Atomic state preparation and readout are performed optically using two separate lasers. A 795 nm laser propagating along the laboratory frame Z axis, with an optical power of 400 mW, is tuned to resonance with the D_1 transition and used to transfer population into the $|2,2\rangle$ stretched state through optical pumping. As described in Sec. 2.3, high spin polarization is achieved using a synchronous pumping protocol in which the pump intensity is amplitude-modulated at a frequency $\omega_{RF}/2\pi \approx \nu_L$. This modulation is implemented using an Acousto-Optic Modulator (AOM) placed in the path of the beam, with the experiment using the first-order diffracted beam. The AOM is driven by a 110 MHz RF tone whose amplitude is modulated with a square wave having an 8% duty cycle, thereby producing the sequence of optical pumping pulses. The modulation is phase-locked to the RF oscillator generating the RF fields driving Zeeman Rabi oscillations in order to maintain a fixed phase relation between the optical pumping sequence and driven spin dynamics. Optical pumping to the $F = 2$ manifold yields substantially higher σ^+ Rabi signals and therefore provides a higher signal-to-noise ratio in the measurements. For this reason, nearly all Rabi frequency measurements presented in the dissertation correspond to $\Omega_{\sigma+}$. Measurements of $\Omega_{\sigma-}$ require population transfer to $F = 1$ via a microwave adiabatic rapid passage pulse or a microwave π-pulse and is briefly discussed in Sec. 6.4.

Spin polarization is measured optically using a quantum non-demolition measurement based on Faraday rotation (Sec. 2.4). A linearly polarized probe beam at 780 nm with an optical power of 0.8 mW co-propagates with the pump beam through the vapor cell. The probe is detuned by approximately 100 GHz from the D_2 resonance in order to suppress absorption and minimize perturbation of the atomic state. The Faraday rotation, θ_f, is measured using balanced photodetection following a polarizing beamsplitter, providing a sensitive and low-noise readout of the atomic spin projection [106, 127]. Fig. 4.2 shows examples of Faraday rotation measurements of a Zeeman Rabi oscillation, Larmor spin precession, and hyperfine Rabi oscillation.

A LabVIEW-based control program coordinates the overall operation of the experiment. Experimental timing is implemented through a Data AcQuisition (DAQ) system that synchronizes digital timing signals with analog voltage outputs. A programmable NI DAQ generates TTL signals that define the sequence of the measurement cycle. These pulses trigger the optical pumping sequence, gate the RF driving fields, and define the acquisition window for the probe signal. The same DAQ also provides analog voltage outputs used to control the pump and probe laser powers. Optical signals from the balanced photodetector are digitized using a 16-bit Alazar ATS9462 Analog-to-Digital Converter (ADC) operated at a sampling rate of 10 MS/s. Additionally, the control program also communicates with external instruments through serial commands. These commands program the DC current controller and the RF oscillator, which set the DC magnetic field and the RF polarization ellipses to drive the Rabi oscllations, respectively.

4.2 Microfabricated Vapor cell

The core sensing element of the experiment is a $3\times3\times2$ mm^3 microfabricated rubidium vapor cell manufactured by Fieldline Industries (Fig. 4.3). Unlike conventional glass-blown vapor cells, microfabricated cells are produced using wafer-level processing, which enables batch fabrication and supports compact packaging. A typical process begins with lithographic patterning of a silicon wafer to define the vapor cavity [47]. After cavity formation,

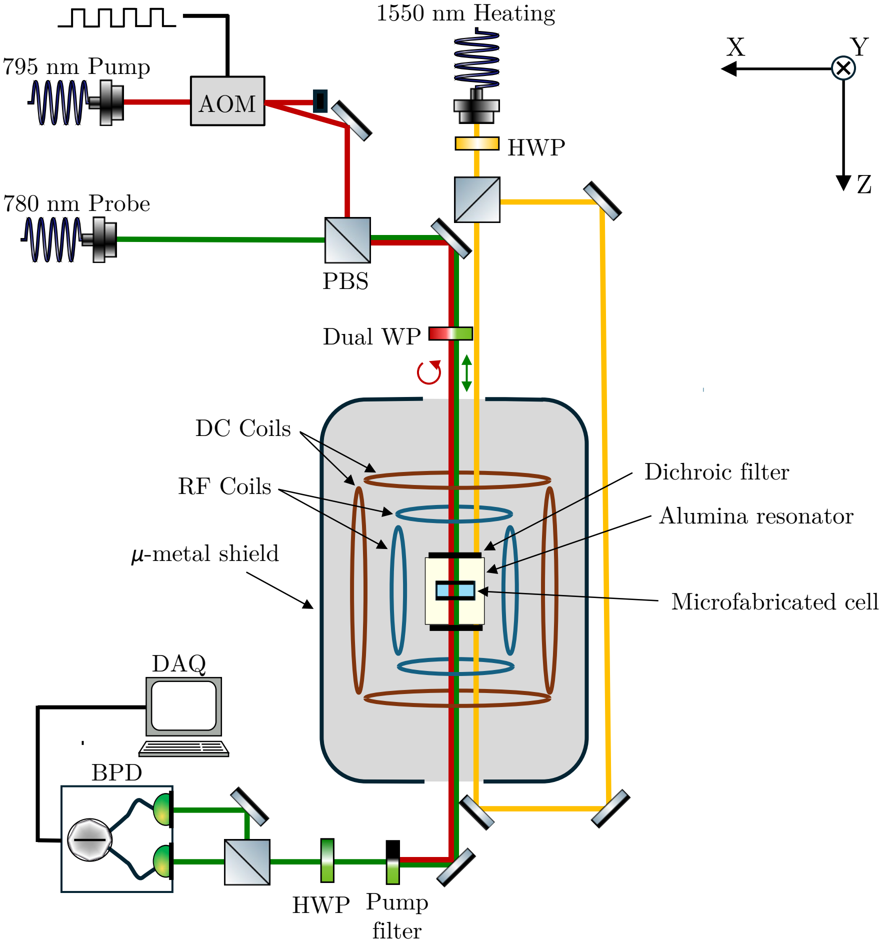

Figure 4.1: Schematic overview of the experimental setup for Zeeman Rabi vector magnetometry. List of acronyms: AOM: Acousto-Optical Modulator HWP: Half-Wave Plate, Dual WP: Dual wavelength Wave Plate (HWP for 780 nm probe and Quarter-Wave Plate (QWP) for 795 nm pump), PBS: Polarizing Beam Splitter, BPD: Balanced PhotoDetector; DAQ: Data AcQuisition system.

the silicon wafer is bonded to borosilicate glass windows using anodic bonding, which provides hermetic sealing and optical access. Rubidium is introduced during fabrication prior to the final sealing, and a buffer gas such as N_2 is added during the bonding process to promote quenching of spontaneous emission from rubidium atoms and suppress relaxation via cell wall collisions. The wafer is then diced into individual cells.

The atomic number density of rubidium vapor is determined primarily by the cell temperature. Our cell is typically operated at 100°C, which provides a number density

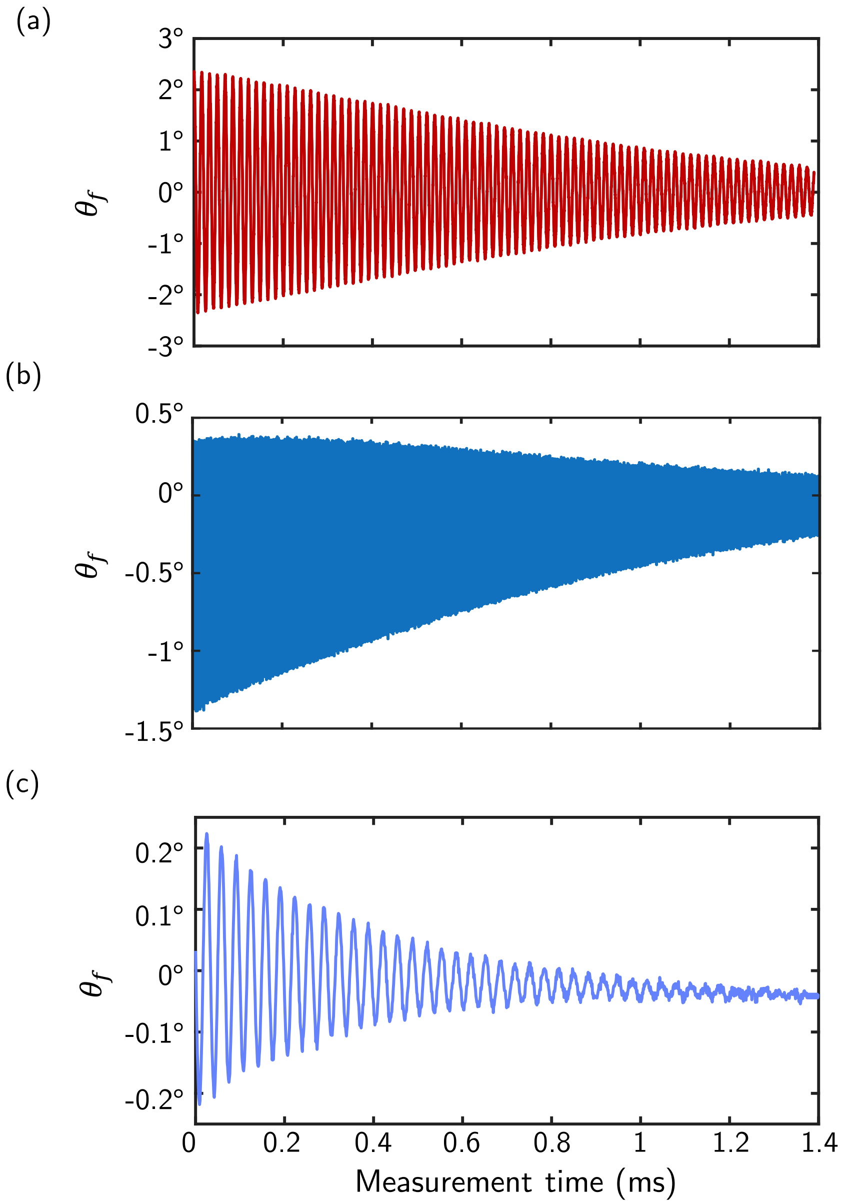

Figure 4.2: Faraday rotation measurements illustrating (a) Zeeman Rabi oscillations, (b) Larmor precession, and (c) Hyperfine Rabi oscillations between ground state manifolds. Due to substantially greater spin-exchange decoherence for hyperfine Rabi oscillations, T_2 of Zeeman Rabi oscillation is roughly twice that for hyperfine Rabi oscillations.

(5×10^9 mm^{-3}) suitable for high signal-to-noise measurements while keeping collisional decoherence within an acceptable range. As mentioned earlier, heating of the vapor cell is implemented using an optical approach. A heating laser at 1550 nm is used together with

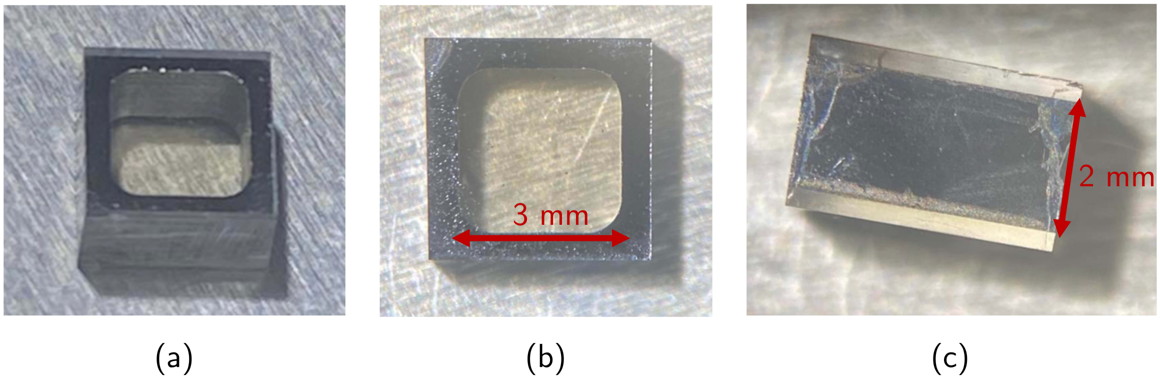

Figure 4.3: Photographs of the microfabricated ^{87}Rb vapor cell used in the experiment with dimensions labeled.

two dichroic filters fabricated from Schott RG9 glass. These filters are bonded to opposite faces of the 12.5 mm alumina microwave resonator cube that encloses the cell along the optical axis, as shown in Fig. 4.4a and Fig. 4.4b. These filters transmit about 90% of pump and probe light, while strongly absorbing the heating light and transmitting only about 4% (Fig. 4.4c). The heating laser, with an optical power of 2 W, is split into equal parts using a polarizing beam splitter, which is then incident on the two filters from opposite sides of the cell. The absorbed light produces heat in the filters that is transferred to the vapor cell through the alumina structure. This optical approach [143] avoids the use of resistive heaters or other conductive or magnetic elements near the sensing region. The thermal mass of the alumina enclosure provides passive stabilization of the cell temperature and promotes a uniform temperature distribution across the cell.

Our cell also contains N_2 at a buffer gas pressure of 350 Torr, which in addition to reducing rubidium wall collisions and quenching spontaneously emitted photons, also produces substantial pressure broadening and a frequency shift of optical transitions. At our operating temperature of 100°C, the broadened D_1 line has a full-width-half-maximum of $\sim$ 6 GHz, and is shifted by $\sim$ 3 GHz. The broadened transition enables efficient optical pumping into the stretched state without requiring an additional repumping laser.

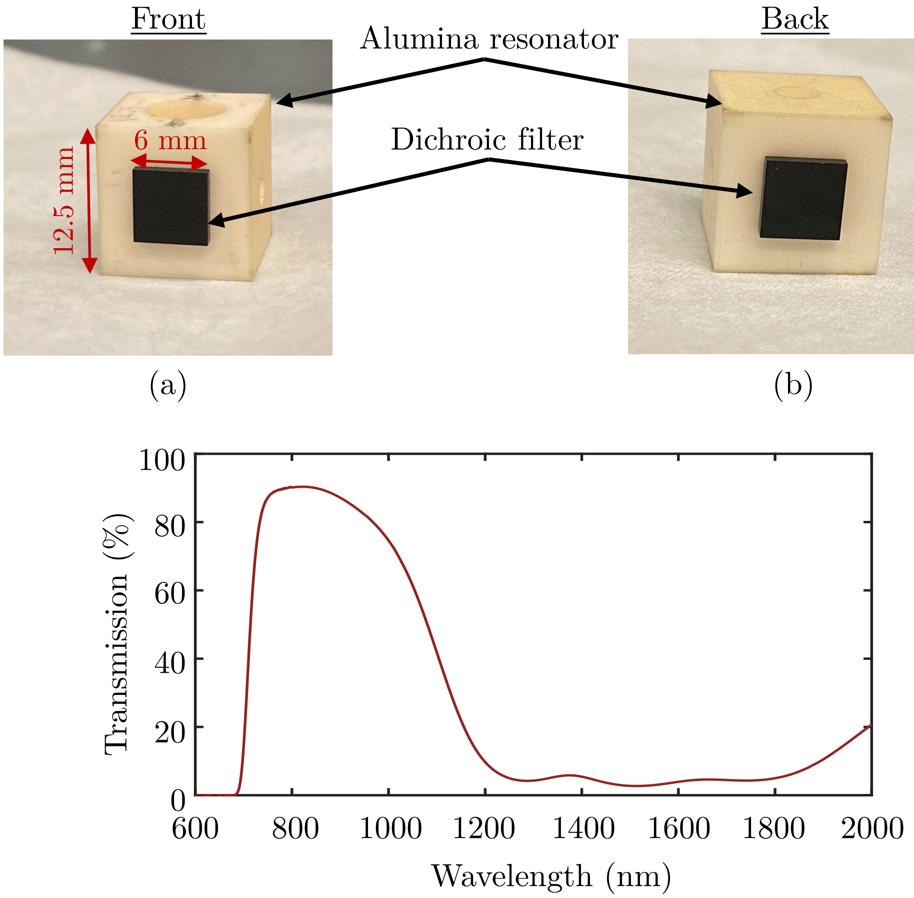

(a)

(b)

(c)

Figure 4.4: Optical heating of the vapor cell. (a) Front face of the alumina resonator facing the pump and probe beams with a 1 mm thick Schott RG9 dichroic filter bonded to the surface. (b) Back face of the resonator with the corresponding filter. (c) Measured transmission of the filter as a function of wavelength. Measurements were obtained with an Agilent Cary-5000 UV-VIS-NIR spectrophotometer.

Furthermore, the small dimensions of the microfabricated cell reduce sensitivity to magnetic field and thermal gradients. The small vapor volume limits the spatial variation of the magnetic field and the temperature experienced by the atoms compared to a larger glass-blown vapor cell. For a given gradient, the spread in Larmor frequency across the ensemble decreases with the cell length, which reduces inhomogenous broadening of Zeeman Rabi resonances.

The performance of the atoms in the microfabricated cell is ultimately determined by the quality of the magnetic field environment in which it operates. Accurate and stable control of DC and RF magnetic fields is essential for minimizing gradients, suppressing systematic effects and ensuring consistency with theoretical models. The following section describes the design and characterization of the magnetic field generation and control system developed for this work.

4.3 Magnetic field Generation and Control

Coil systems are widely used in atomic physics experiments because they offer a precise and practical approach for generating magnetic fields. For a fixed coil geometry, the magnetic field scales linearly with the applied current while enabling continuous tuning of the field magnitude with good reproducibility. This is particularly essential for accurate magnetometry, where precise control of the DC field is required for calibration and for identifying systematic shifts.

With triaxial coil systems, coils further enable precise vector control of the magnetic field. By arranging coils along three orthogonal axes, the Cartesian components of the field can be adjusted independently, allowing the field direction to be varied continuously and reproducibly over the full solid angle. This configuration allows controlled rotations of the magnetic field direction while maintaining an approximately constant magnitude. In contrast to the use of permanent magnets or ambient geomagnetic fields, coil systems provide electronic control of both orientation and amplitude of DC magnetic fields without mechanical motion.

In addition to DC fields, coils also provide a convenient method to generate time-dependent magnetic fields. When driven with sinusoidal currents near the Zeeman resonance, coils produce oscillatory fields with controlled amplitude, frequency and phase, driving Zeeman Rabi oscillations. Furthermore, the magnetic field produced by a coil can be computed from its geometry using the Biot-Savart law [144] and compared with measurements, providing a systematic mapping between the applied currents and the resulting PEs.

4.3.1 DC Magnetic field System

4.3.1.1 First Generation DC Coils

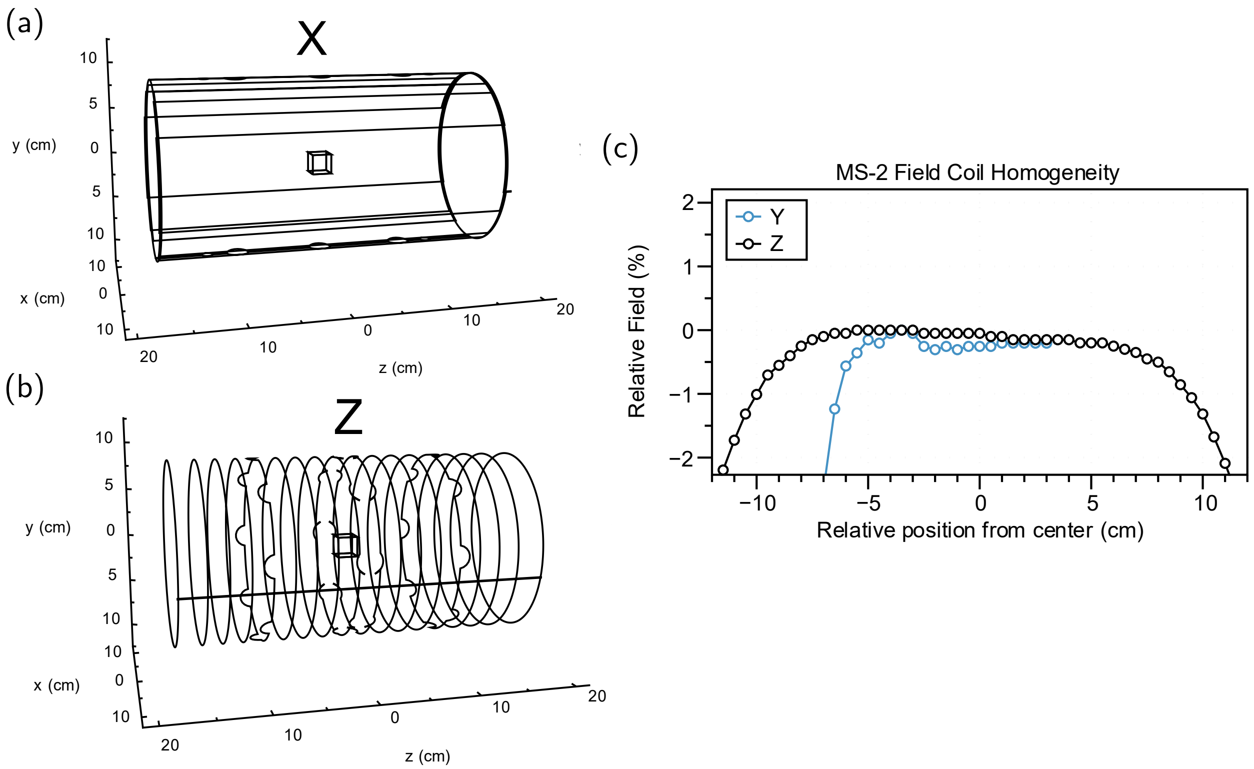

Figure 4.5: First generation DC coil system. (a) Wireframe diagram of Cosine θ coil geometry used for producing magnetic fields along the laboratory X axis. An identical configuration is also used for the Y axis. (b) Solenoidal coil geometry produces magnetic fields along Z axis. (c) Gradients associated with coil-produced magnetic fields. Plots adapted from Ref. [142].

The first generation of experiments was performed using the coil system integrated into the Twinleaf MS2 magnetic shield, shown in Fig. 4.5. The transverse X and Y coils implement a cosine θ geometry [145], while the Z component is produced by a solenoid. These geometries provide improved field uniformity compared with a Helmholtz configuration. As shown in Fig. 4.5c, the measured field variation is $\lesssim 0.1\%$ over 15 cm, which corresponds to 1 nT across the vapor cell in a 50 μT magnetic field. This variation produces a Larmor frequency spread of $\Delta\nu_L \sim 7$ Hz, implying an inhomogeneous dephasing time, $T_2^* \approx 1/(2\Delta\nu_L) \sim$ 70 ms. Because the measured coherence time in the cell is limited by other relaxation mechanisms and is substantially shorter than this estimate, gradients from the shield coils do not significantly contribute to the spin decay.

Despite the promising field uniformity, we ultimately transitioned to a different coil system because the coil factors (current-to-magnetic field conversion) of the shield coils were relatively small. The X and Y coils had a coil factor of 57.6 μT/A while that for the Z coil was 150 μT/A. Therefore, generating 50 μT fields required currents approaching 1 A on the transverse coils. Operation at these currents leads to considerable resistive heating. Additionally, in the same current range, our homebuilt DC current controllers exhibited nonlinearities in their current output, as discussed in Sec. 4.3.1.3. As a result, we replaced the shield coils with a coil system that achieves the same field strengths at lower currents.

4.3.1.2 Second Generation DC Coils

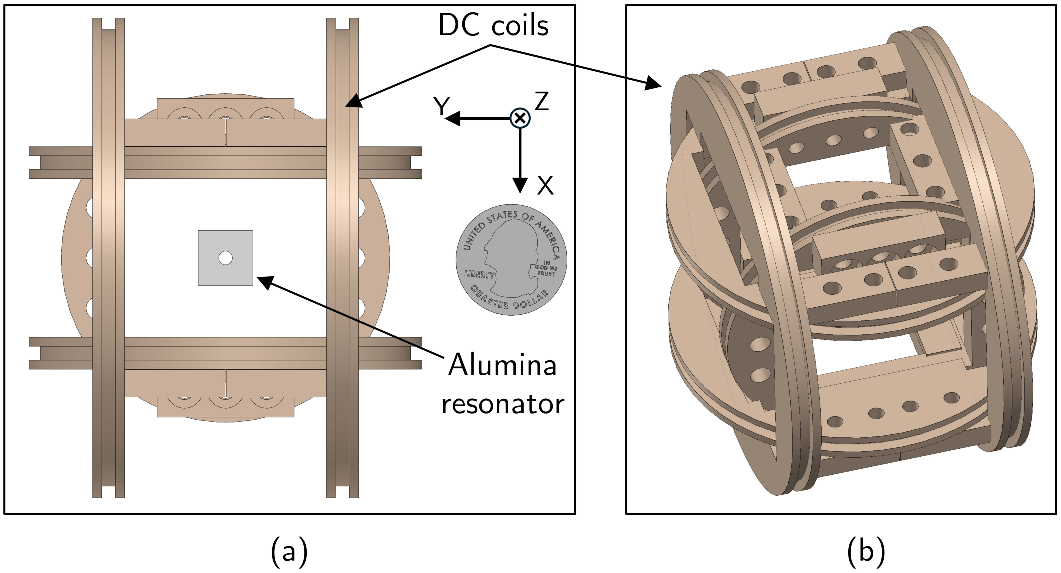

Figure 4.6: Second generation DC coil system used in the experiment. CAD model of triaxial coil system in Helmholtz configuration. US quarter included for scale. Coil parameters are listed in Table 4.1.

This coil system was originally implemented to generate the RF magnetic fields applied to the vapor cell. As the experiment evolved, the RF drive was transferred to a separate set of coils with lower inductance in order to improve bandwidth and reduce impedance at the Zeeman resonance frequency of ~ 350 kHz. The present system is therefore dedicated to the generation of DC magnetic fields.

The system consists of three nominally orthogonal coil pairs arranged in a Helmholtz configuration, as shown in Fig. 4.6. The relevant geometric and magnetic field parameters of the coils are summarized in Table. 4.1. Although the coil diameters differ to accomodate mechanical constraints, the number of turns in each pair was chosen to yield comparable coil factors. The coils are mounted on a 3D-printed Nylon 12 frame that provides mechanical rigidity and minimizes distortions due to the thermal expansion. The dielectric resonator and the vapor cell are located at the geometric center of the structure so that the atoms experience the superposition of the three orthogonal field components in a region of maximum uniformity. According to Table 4.1, the largest gradients arise from the coil pair aligned nominally along the X axis, with a gradient of roughly 30 nT/cm. Over the length of the cell, these gradients correspond to a variation of 9 nT and a Larmor frequency spread of $\Delta\nu_L \sim 63$ Hz , yielding an estimated dephasing time of $T_2^* \sim 8$ ms. While this value is considerably longer than the measured $T_2 \sim 1$ ms of Rabi-Larmor oscillations, it is significantly shorter than that of the shield coils described above.

	X	Y	Z
Number of turns	40	43	48
Diameter	67 mm	100 mm	81 mm
Coil Factor (measured)	1.08 μT/mA	0.85 μT/mA	0.97 μT/mA
Gradient (calculated)	30 nT/cm	14 nT/cm	21 nT/cm

Table 4.1: DC coil system parameters. X, Y, and Z labels indicate coil pairs whose axes are nominally oriented along laboratory X, Y, Z, axes respectively.

Accurate knowledge of the magnetic field direction at the atoms is essential for both the PE calibration procedure and for benchmarking the vector magnetometer. In the calibration procedure, the applied field provides the reference directions at which Rabi frequencies are measured to determine the PE parameters. In benchmarking, the field direction inferred from the measured Rabi frequencies is directly compared to the applied direction, so any uncertainty in the applied field propagates into the inferred angular accuracy.

As a result, it is necessary to model and characterize any nonidealities in the DC coil system. These include drifts in the coil factors, deviations from orthogonality among the coil axes, and the presence of residual background magnetic fields within the shield. These nonidealities modify the relationship between currents in the respective coil pairs and the resulting magnetic fields, producing systematic errors in the field direction. To account for their contributions, we perform scalar calibration of the DC coil system based solely on Larmor spin precession measurements [87, 105, 146], and establish an accurate mapping between the applied currents and the magnetic field,

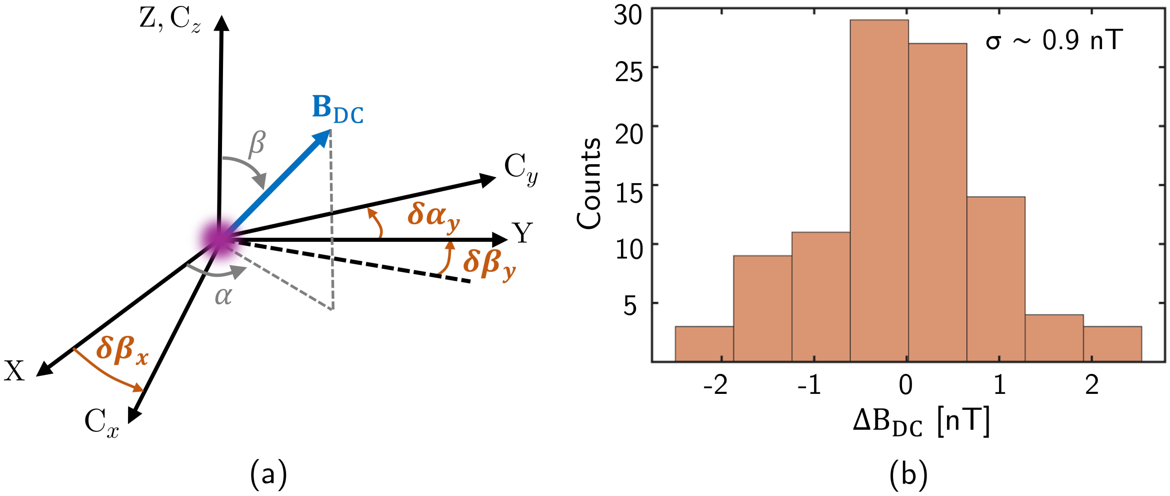

Figure 4.7: Scalar calibration of the DC coil system. (a) Coil frame coordinate system C_x-C_y-C_z, and orthogonalized laboratory frame coordinate system X-Y-Z, with $\{\delta\beta_x, \delta\beta_y, \delta\alpha_y\}$ denoting small angular deviations of the coil frame from the laboratory frame. (b) Residuals from calibration based on Larmor frequency measurements for 100 random magnetic field directions.

We model the DC magnetic field produced by each coil pair as

$$(\widetilde{\mathbf{B}}_{\mathrm{DC}})_j = a_j I_j \, \hat{c}_j, \; j \in \{x, y, z\} \tag{4.1}$$

where a_j is the coil factor, I_j is the applied current and $\hat{c}_j$ denotes the effective field axis of the corresponding coil pair (Fig. 4.7a). In an ideal triaxial system, $\hat{c}_j$ form an orthonormal basis. In practice, small mechanical misalignments may lead to deviations from orthogonality. We express these deviations from a Cartesian coordinate system as small angular perturbations in the following manner

$$\begin{aligned}
&\hat{c}_z = \hat{z} \\
&\hat{c}_x = R_y(\pi/2 + \delta\beta_x)\hat{z} \\
&\hat{c}_y = R_z(\pi/2 + \delta\alpha_y)R_y(\pi/2 + \delta\beta_y)\hat{z}
\end{aligned}$$

Here, $\hat{z}$ is defined to be oriented along $\hat{c}_z$, and $R_x(\theta)$ and $R_y(\theta)$ are standard rotation matrices about the $\hat{x}$ and $\hat{y}$ directions in the laboratory frame. The small angles $\delta\beta_x$, $\delta\alpha_y$, $\delta\beta_y$ quantify the misalignment of the X and Y coils with respect to the nominal orthogonal frame, as illustrated in Fig. 4.7.

Residual magnetic fields within the shield are included through a background field, $\mathbf{B}_{\text{bg}}$. This term accounts for imperfect shielding, remanent magnetization of nearby materials, and residual currents through the coils, even when the applied currents are nominally zero. The total magnetic field is therefore given by

$$\widetilde{\mathbf{B}}_{\text{DC}}(I_x, I_y, I_z; \{U\}) = \Sigma_j a_j I_j \, \hat{c}_j + \mathbf{B}_{\text{bg}} \tag{4.2}$$

with the full set of calibration parameters denoted by $\{U\} = \{a_x, a_y, a_z, \delta\beta_x, \delta\alpha_y, \delta\beta_y, \mathbf{B}_{\text{bg}}\}$

We determine $\{U\}$ by fitting the model prediction for the field magnitude to values extracted from Larmor precession [87, 105, 146]. For the i^{th} applied field direction, the scalar value $\mathrm{B}_{\mathrm{DC,i}}$ is obtained from the measured Larmor frequency $\nu_{L,i}$ using the procedure described later in Sec. 4.4. The scalar calibration is performed by minimizing the cost function

$$\mathcal{C}\left(\{U\}\right) = \sum_i \left| \widetilde{\mathrm{B}}_{\mathrm{DC}}\Big(I_{x,i}, I_{y,i}, I_{z,i}; \{U\}\Big) - \mathrm{B}_{\mathrm{DC,i}} - \delta\mathrm{B}_{\mathrm{he}}\left(\rho_0, \beta_{\mathrm{nom,i}}\right) \right|^2$$

Here, a limited static heading error correction, $\delta\mathrm{B}_{\mathrm{he}}\left(\rho_0, \beta_{\mathrm{nom,i}}\right)$ is applied using the initial density matrix, ρ_0 and at the polar angle, β_{nom}. The nominal polar angle is computed assuming an orthogonal coil system with nominal coil factors. To compute $\delta\mathrm{B}_{\mathrm{he}}\left(\rho_0, \beta_{\mathrm{nom,i}}\right)$, we simulate the Faraday rotation signal of a Larmor precession in the presence of a magnetic field oriented at $\beta_{\mathrm{nom,i}}$ (heading error depends only on the polar angle [56, 103]). The simulation is based on the master equation (Eq. (2.17)) with the time-independent Hamiltonian, H_0 from Eq. (2.8) governing spin evolution in a DC magnetic field. We then extract an apparent field magnitude from the simulated Larmor precession signal using the same procedure applied to experimental data. $\delta\mathrm{B}_{\mathrm{he}}\left(\rho_0, \beta_{\mathrm{nom,i}}\right)$ is then computed from the difference between the applied field strength in the simulation and the magnitude inferred from the simulated signal [103].

The resulting calibration residuals for 100 different magnetic field directions at 50 µT are shown in Fig. 4.7b. The residuals exhibit a standard deviation of ~ 0.9 nT, which is substantially larger than the statistical noise floor of the Larmor measurements, suggesting the presence of systematic errors unaccounted for in the total field model. These systematic contributions may arise from residual heading errors, light leakage from the pump beam or other higher-order geometric errors, such as non-parallel coil planes, which introduce deviations that are not represented in the linear misalignment model. For 50 µT fields, the residual level corresponds to an effective angular accuracy of approximately $0.9\,\mathrm{nT}/50\,\mu\mathrm{T} \sim 20\,\mu\mathrm{rad}$.

4.3.1.3 Homebuilt DC current controller

While the coil geometry establishes the relationship between current and magnetic field, and the uniformity of the applied magnetic field, the stability and accuracy of that field are ultimately set by the current controller. It is therefore essential to maintain low-noise, high stability and accurate control of the coil currents for PE calibration and vector magnetometry.

For the shield coil system described in Sec. 4.3.1.1, fields near 50 μT required currents of approximately 1 A in each of the three channels. Therefore, to remain compatible with both generations of DC coil systems, the current controller was required to provide at least 1 A. Additionally, the magnetic field had to rapidly change between predefined field orientations for calibration and measurement sequences, and thus programmable current control was necessary to enable automated operation. Sufficient current resolution was also necessary to allow fine control of the magnetic field during measurements. Finally, the controller was required to exhibit low current noise, as current fluctuations couple directly to magnetic field fluctuations at the vapor cell.

Satisfying these requirements, a programmable current controller based on the Howland current source topology was implemented [147], as shown in Fig. 4.8. In this approach, a stable programmed voltage is converted into a controlled output current using an op amp and a matched resistor network, realizing a bidirectional current source. The setpoint voltage is provided by an AD5791Z 20-bit digital-to-analog converter referenced to an ultrastable LT6655 voltage reference to improve long-term stability. The voltage is programmed by a FreeSoC2 microcontroller that communicates with the experiment control software to set the desired output current.

The output noise of the homebuilt current controller is shown in Fig. 4.9a. We measure the noise with an SRS SR780 FFT analyzer, while the current controller delivers 200 mA of current through a 25 Ω resistor. The measured noise floor is approximately 5 $\mathrm{nA}/\sqrt{\mathrm{Hz}}$.

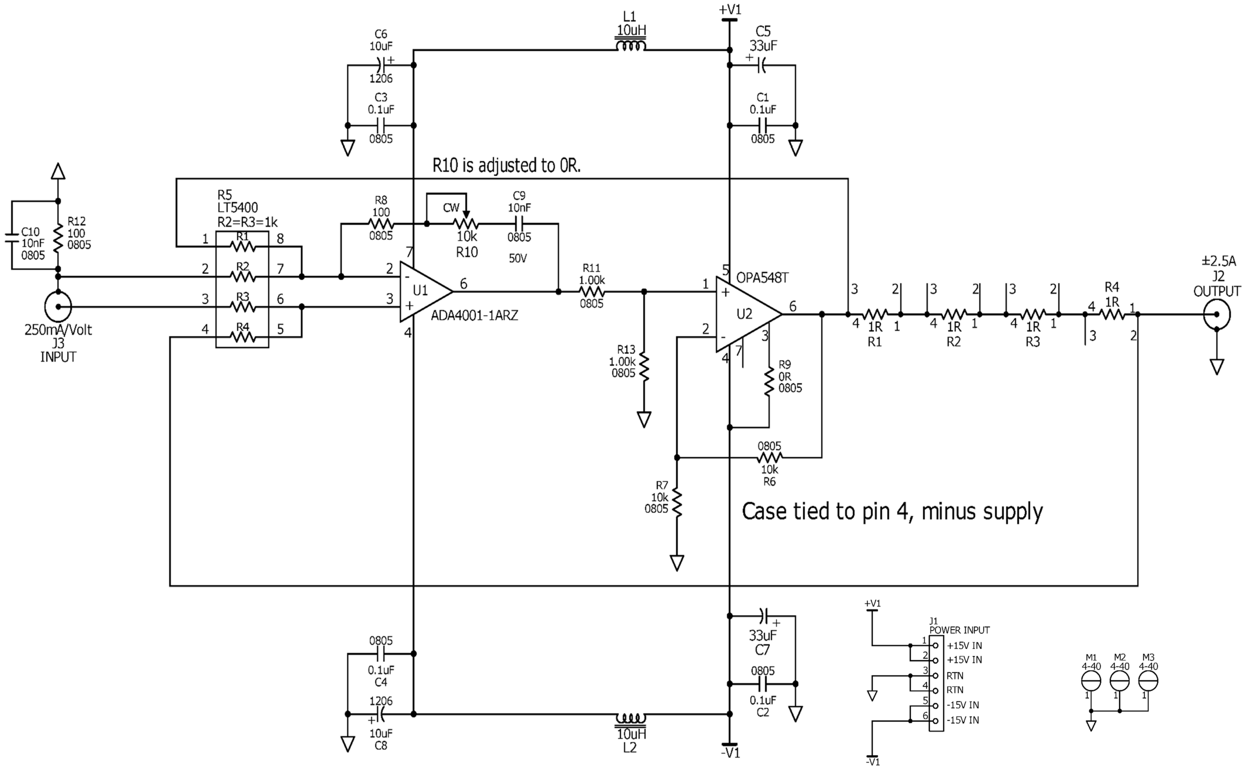

Figure 4.8: Circuit diagram of the homebuilt DC current controller. Circuit was designed by Terry Brown in collaboration with Tobias Thiele.

This level corresponds to a magnetic field noise floor of roughly 300 fT/$\sqrt{\text{Hz}}$ for the first generation shield coil system, and roughly 5 pT/$\sqrt{\text{Hz}}$ for the second generation Helmholtz coil system, reflecting the difference in coil factors between the two configurations.

A primary limitation of the homebuilt controller is a nonlinear relationship between the programmed set current and the delivered current, which motivated the transition to an alternative controller. Fig. 4.9b shows the magnetic field magnitude inferred from Larmor frequency measurements as the programmed currents are swept linearly from -1 A to +1 A. The field is applied along the coil axis nominally aligned with the Laboratory X axis, thus the measured Larmor frequency is not limited by static heading error. We fit the measured field magnitude to a linear model independently for positive and negative currents, and evaluate the residuals as a function of setpoint current. These residuals reveal a nonlinearity at the level of approximately 100 ppm near 50 μT. The physical origin of this effect remains unclear. By comparing independent measurements of the DAC output and the transconductance stage, we find that the nonlinearity is associated with the Howland current source rather than with the voltage reference or digital programming interface. The nonlinear behaviour also drifts over time, which challenges attempts to correct the output through a fixed precalibration curve. Reports of similar nonlinear behaviour in Howland current sources are limited in the literature [148] (thanks to Dr. Ivan Ryger for finding this), and despite further investigation, we were not able to identify any modification of the circuit that eliminated this nonlinearity.

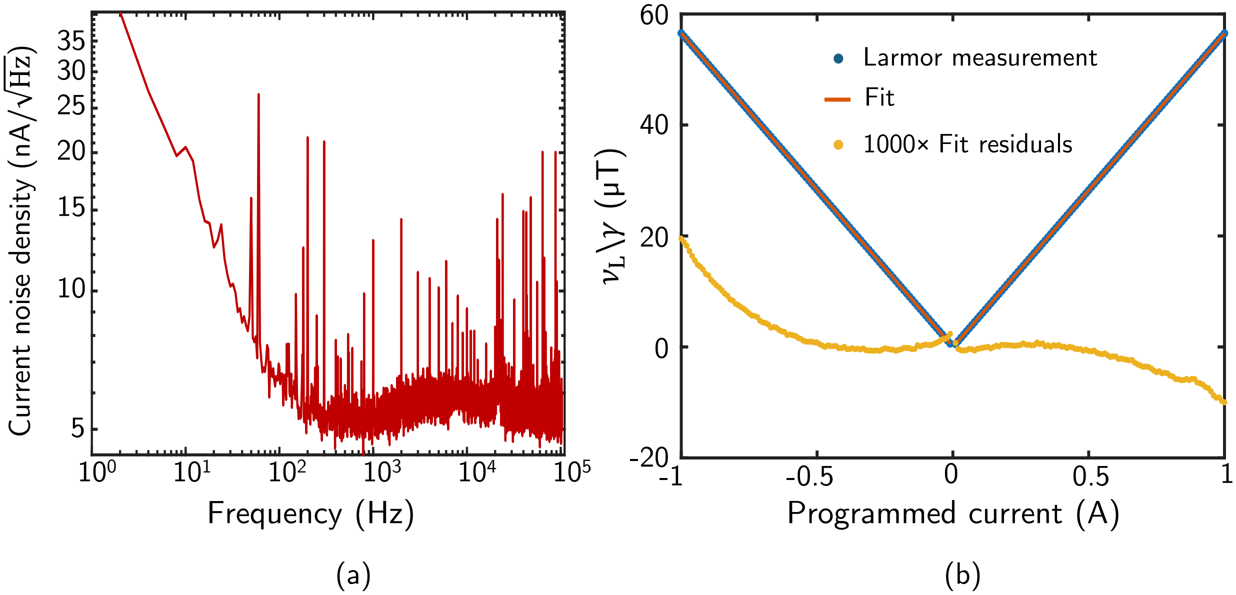

Figure 4.9: Homebuilt DC controller characterization. (a) Current noise density measured at 200 mA current using an SRS780 FFT analyzer across a 25 Ω resistor. (b) Magnetic field strength inferred from Larmor precession measurements as a function of programmed current. Measurements are compared to linear fit and residuals are scaled to highlight nonlinearities.

4.3.1.4 Twinleaf CSB3 current controller

As a result of the nonlinearity in the output current of the homebuilt controller, we transitioned to the commercial Twinleaf CSB3 controller. Based on the manufacturer specifications, the current noise level is comparable to or lower than that of the homebuilt controller, as shown in Fig. 4.10a. We also do not observe measurable nonlinearity in the output current (Fig. 4.10b). A limitation of the CSB3 is its reduced dynamic range of ±250 mA, which restricts its use to the second generation DC coil system with larger coil factors. These coil factors helps apply 50 μT with fields with lower currents, helping the long-term stability of DC magnetic field generated. Fig. 4.10c plots repeated Larmor measurements of a 50μT magnetic field over 500 s. The magnetic field is oriented at $(45°, 45°)$ so it's sensitive to cross-drifts along all three coil pairs. The standard deviation of the variations is ~ 200 pT, which shows great stability.

The CSB3 also provides programmable current control with 20-bit resolution, supporting automated magnetic field sequences. The controller also incorporates a 16 Hz RC filter on the control voltage to suppress high frequency noise in the output current. This filter however reduces the bandwidth of the current control loop and increases the settling time following a step change in the current set point. In our experiment, we apply a delay of 0.85 s after a magnetic field direction change to allow the currents to settle within 10 ppm of its final value. As a result, this settling time increases the duration of calibration sequences that require repeated field direction changes.

4.3.2 RF PE Generation

4.3.2.1 RF coil system

Although both the DC and RF coil systems generate magnetic fields at the vapor cell, their design requirements differ significantly. The DC coil system is optimized to provide a spatially uniform magnetic field with long-term stability. In contrast, the RF coil system must produce a time-dependent magnetic field with a stable amplitude and phase at the Zeeman resonance frequency, which is ~ 350 kHz at a 50 μT magnetic field. At these frequencies, an important consideration in RF coil design is the frequency-dependent impedance of the

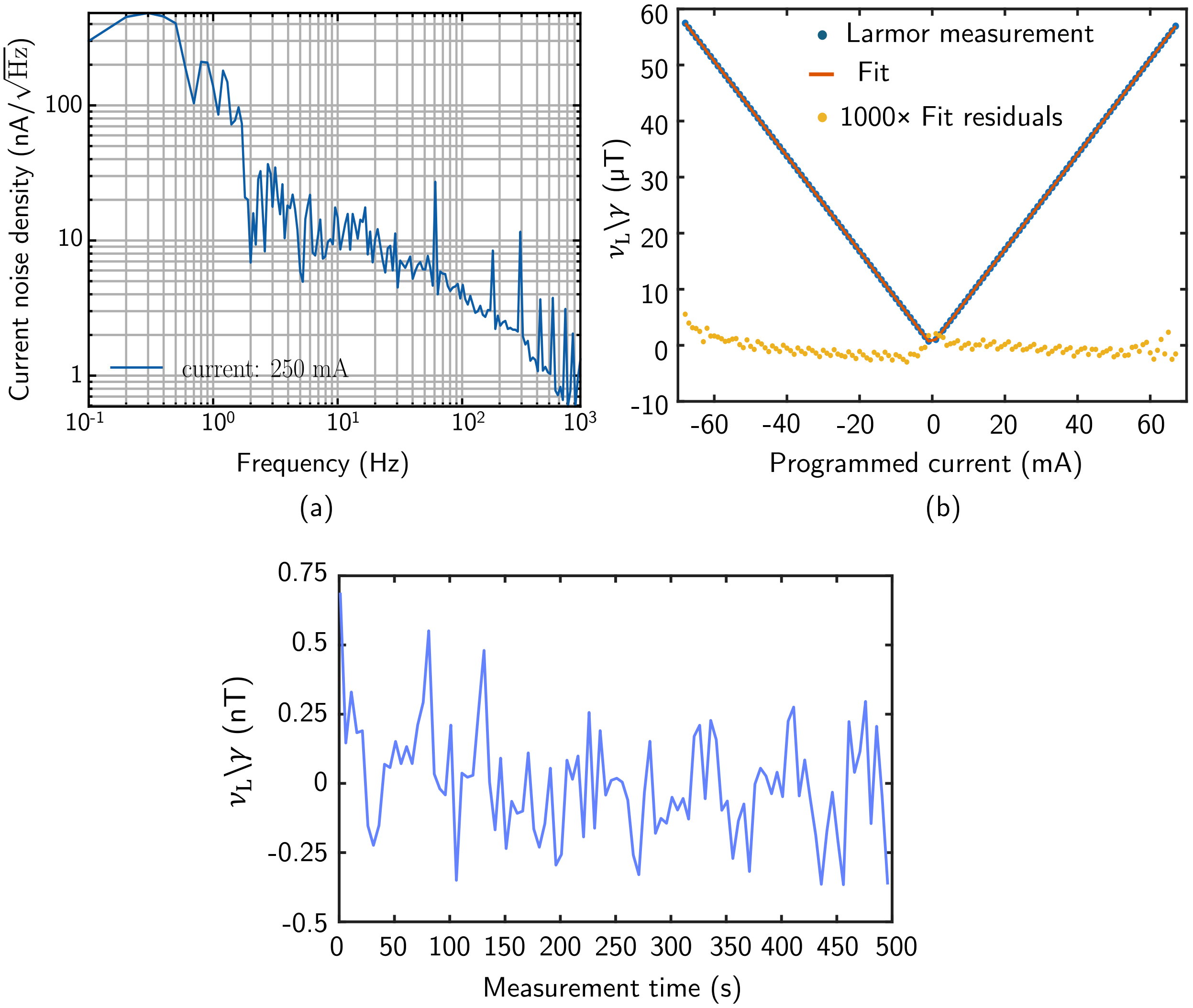

(a)

(b)

(c)

Figure 4.10: Twinleaf controller characterization. (a) Current noise density measured at 250 mA (adapted from Ref. [149]). (b) Magnetic field obtained from Larmor measurements as a function of programmed current. Measurements are fit with a linear model, and scaled residuals are plotted. (c) Magnetic fluctuations extracted from Larmor measurements fluctuations sampled every 5 s for 500 s.

coil. The inductance of the coils combines with the parasitic capacitance between turns and the resistance of the coil wire to form a complex impedance. This impedance determines both the magnitude and the phase of the magnetic field for a given current, and define the self-resonance frequency of the coil. Near resonance, small changes in frequency or load can produce significant variations in amplitude and phase, thus degrading control of the applied

RF magnetic field. Furthermore, the interaction between the RF coil and the surrounding conductive elements is more pronounced than in the DC case. Time-varying magnetic fields can induce eddy currents in nearby metallic components, which alter the effective field amplitude and phase at the atoms.

	X	Y	Z
Diameter	38 mm	28 mm	46 mm
Inductance (measured)	55 μH	39 μH	64 μH
Coil Factor (measured)	0.76 μT/mA	0.95 μT/mA	0.59 μT/mA
Self-resonance frequency (measured)	8 MHz	5.9 MHz	4.7 MHz

Table 4.2: RF coil system parameters. X, Y, and Z labels indicate coil pairs whose axes is nominally oriented along laboratory X, Y, Z, respectively.

For these reasons, the RF coil system was designed with a lower inductance than the DC coils. Since the inductance of a coil pair scales approximately as $L \propto N^2R^2$, where N and R are the number of turns and the radius of the coil, respectively, we implemented a smaller triaxial Helmholtz geometry with fewer turns than in the DC system to improve RF performance (Fig. 4.11). The coil mount was 3D printed with the same glass-bead-filled Nylon 12 material employed for the DC coil mount to ensure mechanical stability, low thermal expansion and electrical insulation, minimizing eddy currents. The RF coil parameters are summarized in Table 4.2. Each coil pair consists of 16 turns. As shown in Fig. 4.11, the RF coils are designed to be concentric with the DC coils so that both systems share a common center at the vapor cell location, thus ensuring that uniform RF and DC magnetic fields overlap spatially and the atoms experience a combined field. Moreover, the RF frequency of 350 kHz lies well below the self-resonance frequency of the coil pairs. As a result, the impedance remains dominated by the inductive component and the resulting RF PE remains stable with minimal amplitude or phase distortion.

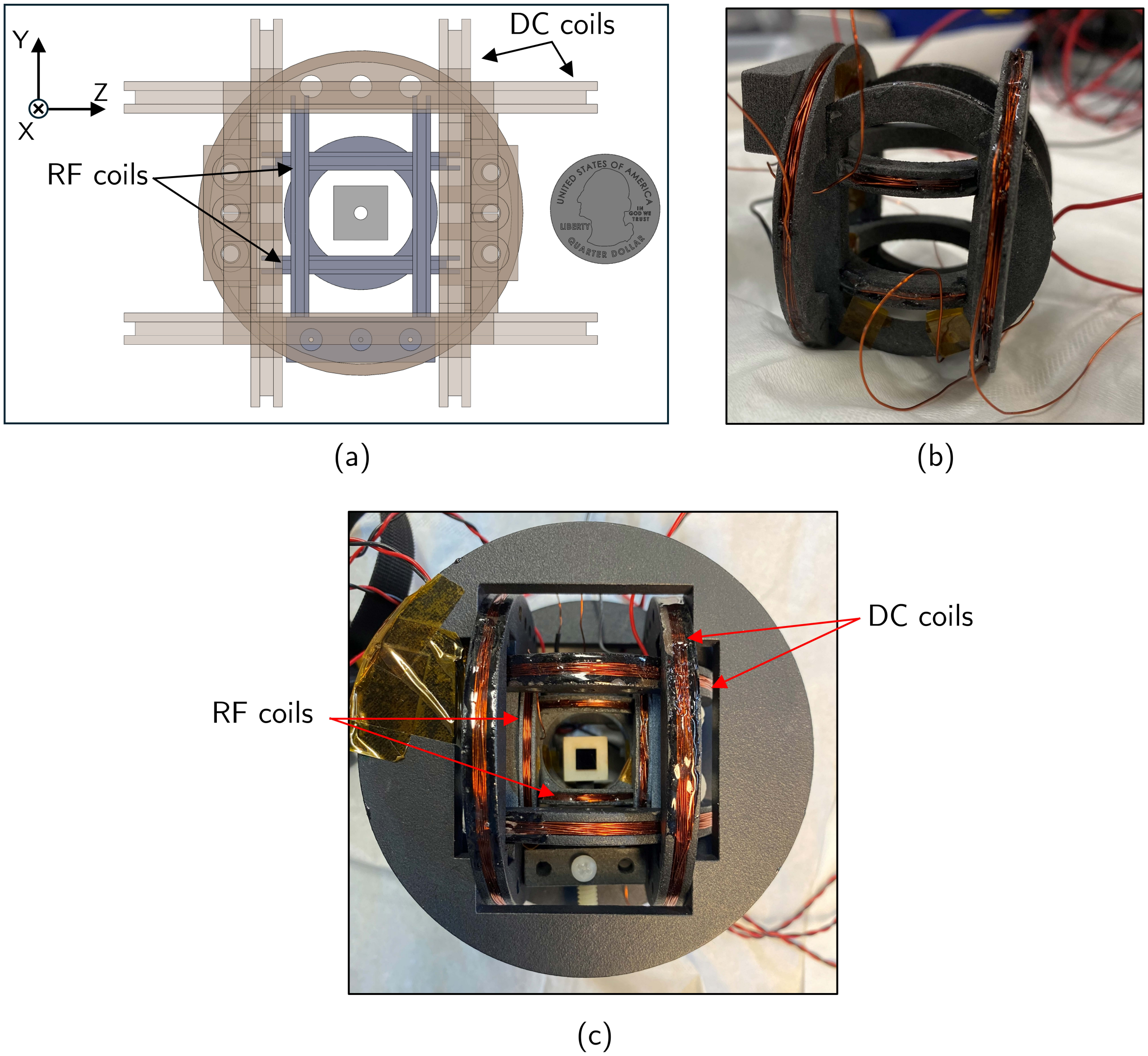

Figure 4.11: (a) CAD model of the RF Helmholtz coil system (grey) with respect to the DC coil system (semi-transparent bleach white). (b) Photograph of the triaxial coil system. (c) Photograph of the assembled DC and RF coil systems along with the alumina resonator. The microfabricated ^{87}Rb cell is located inside the resonator.

4.3.2.2 RF Current Controller

Generation of RF PEs also requires the ability to deliver stable oscillatory current to the RF coil at sufficient amplitudes. As mentioned earlier, unlike the DC controller, the RF controller must operate at frequencies near 350 kHz, where the coil presents an inductive impedance. As a result, the driving circuit must provide a substantially higher

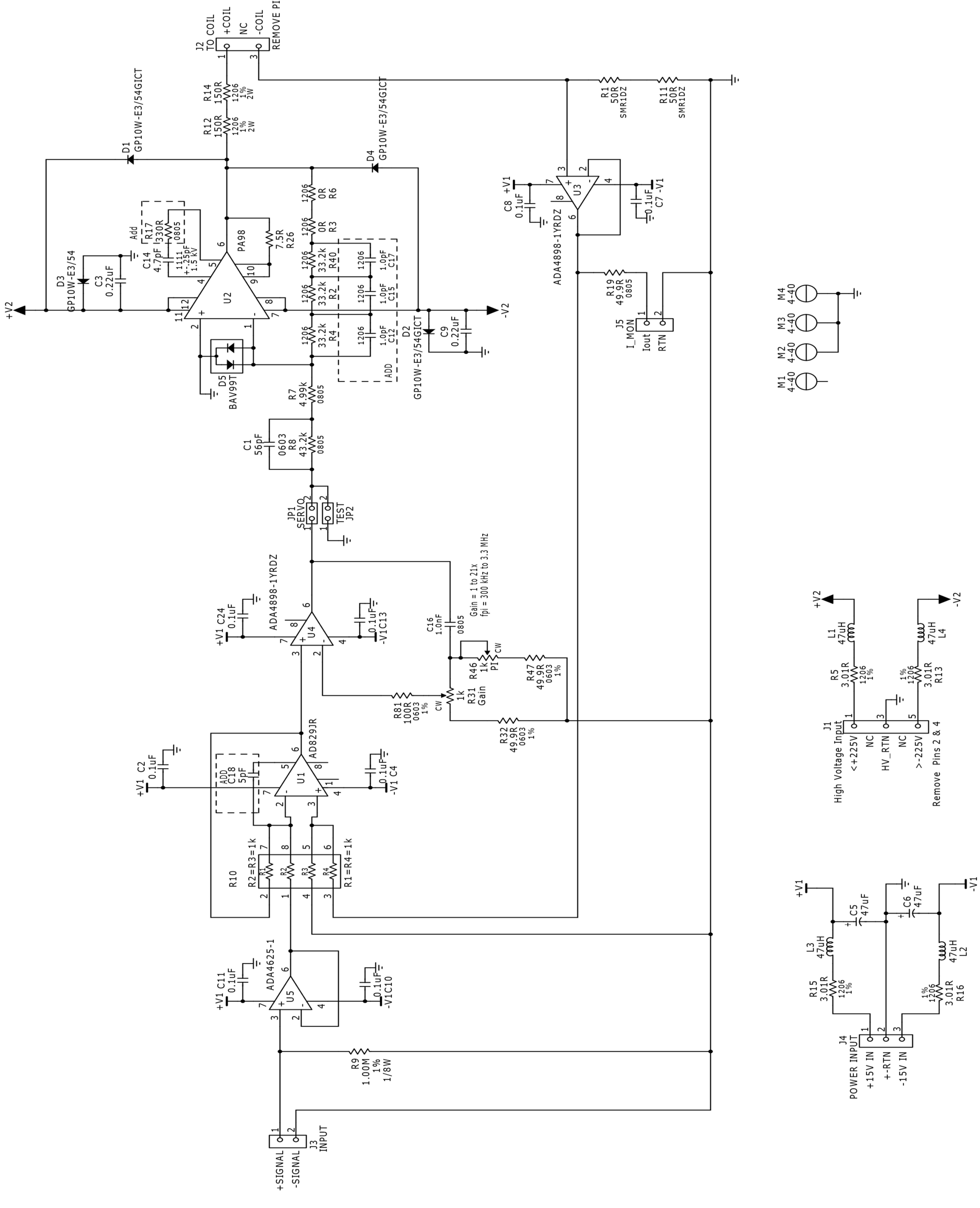

Figure 4.12: Circuit diagram of the RF current controller used in the experiment. Circuit was designed by Terry Brown.

bandwidth and voltage compliance to maintain the desired current amplitude. To meet these requirements, the JILA electronics shop developed a dedicated RF current controller, whose circuit diagram is shown in Fig. 4.12. The circuit accepts a differential reference voltage and converts it into a RF current and regulates that current through a feedback loop. Input buffering reduces loading of the reference input, and frequency compensation is incorporated to maintain stability when driving the coil at 350 kHz. A separate current sensing stage also allows monitoring of the output RF current.

4.3.2.3 RF Signal Conditioning

The experiment requires precise control of the RF currents applied to each pair. During optical pumping and during Larmor measurements, the RF fields must be disabled to prevent Rabi driving. Moreover, as we will discuss later, selective excitations of various combinations of coil pairs helps vary the polarization ellipse and this requires independent switching control of each coil pair. Finally, to control and calibrate the effects of dynamic heading error (Sec. 3.5), the Rabi driving must always begin at the same RF phase relative to the synchronous pumping pulse sequence.

To implement these requirements, the RF and pump modulation signals are generated using a set of synchronized function generators. The RF sinewaves are produced using three channels from two separate Siglent 2042X function generators. A third Siglent 2042X function generator produces pump modulation waveform for synchronous pumping, and produces an additional 350 kHz sync signal. We will discuss the pump modulation in greater detail in the following section. All function generators are locked to a SRS FS780 10 MHz rubidium reference. By sharing a common reference, the relative phase between the RF channels and the pump modulation remains fixed and controllable.

This phase relationship between RF waveform and pumping does not extend to the timing of the experiment sequence. As mentioned earlier in Sec. 4.1, our control program generates the TTL signals that trigger the optical pumping pulses and gates the RF excitation.

This program, however, does not maintain identical timing between successive experimental cycles. Small variations arise because the program waits for responses from instruments and transfers recorded data from hardware buffers to the control computer. These delays change the time at which the TTL signal ends pumping and begins the Rabi driving/probing sequence relative to the RF waveform. As a result, the RF phase at the onset of Rabi driving differs between runs (Fig. 4.13a), introducing fluctuations in the dynamic heading error.

Therefore the TTL pulses must be synchronized with the phase of RF waveform to ensure consistent timing of the experiment. This synchronization is realized using a reference sync signal. The sync signal consists of a 5V square wave with a duty cycle of 50%, and is phase-locked to the RF waveform and the pump modulation. With the help of a D flip-flop, it serves as a phase reference that links this waveform to the digital timing signals that control the experiment sequence. The sync signal is applied to the clock input of a D flip flop (Fig. 4.13b), while one of the TTL signals that initiates the RF excitation is connected to the data input pin of the flip-flop. The output of the flip-flop controls a high-speed RF switch (Mini Circuits ZASWA-2-50DRA+) that gates the RF signal to the atoms. The flip-flop updates its output only on the rising edge of the sync signal. Because the sync signal is phase-locked to the RF waveform, the rising edge always coincides with the same RF phase. As a result, the command from the control computer is also transferred to the RF switch at the same phase. The RF switch therefore turns on at a fixed phase of the RF waveform so that the atoms experience the same RF phase at the beginning of each Rabi driving sequence.

A second RF switch is placed earlier in the signal chain (RF switch I in Fig. 4.13b) and is controlled directly by a separate TTL signal from the control program. This switch provides additional isolation of the atoms from unwanted RF leakage, which is particularly important during the Larmor precession stage, when the residual RF field can perturb the spin evolution. A bias-tee is also included to remove any residual DC component that could otherwise leak into the RF current controller.

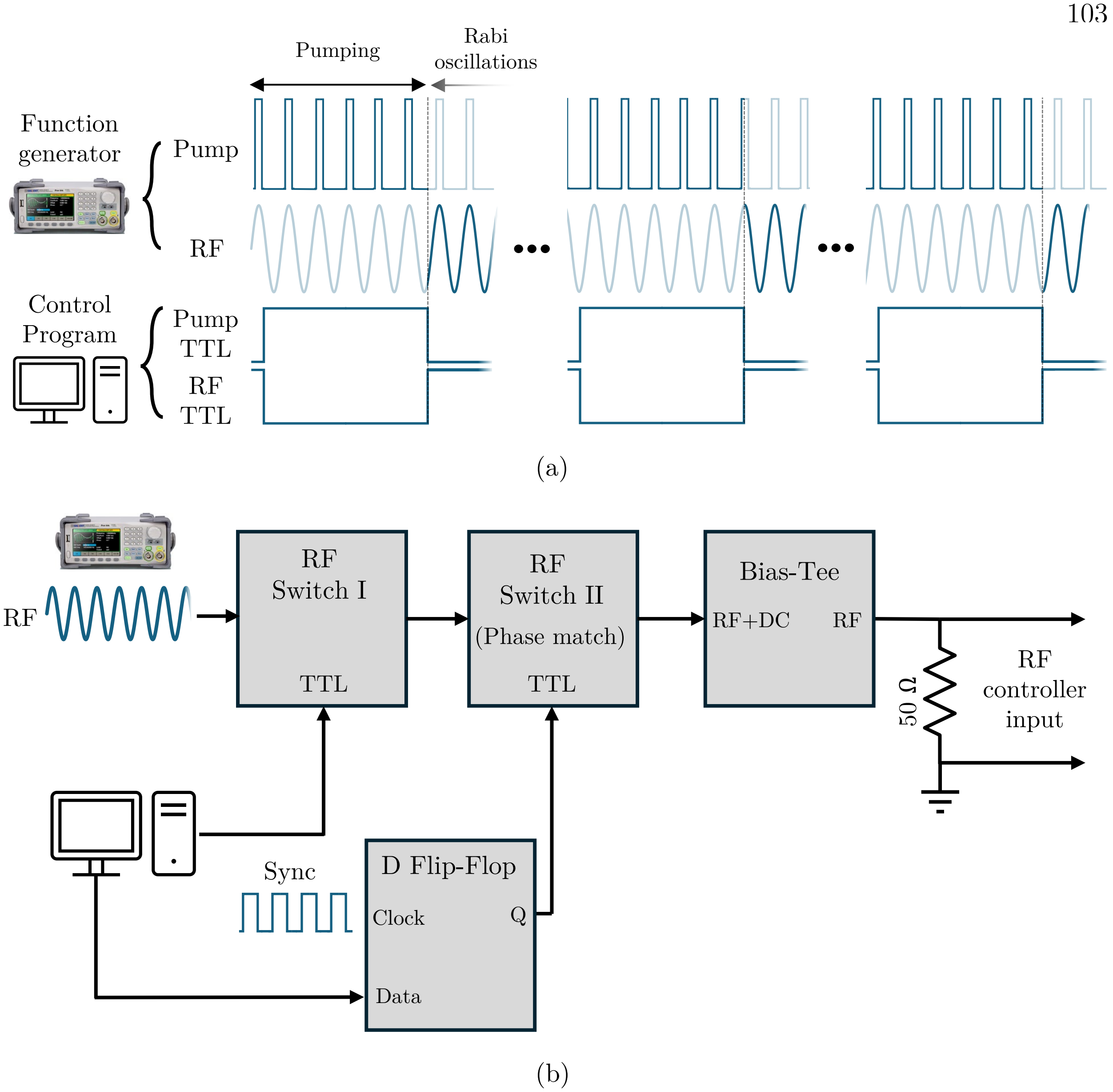

Figure 4.13: Schematic overview of RF signal conditioning. (a) Function generator produces phase-locked pump modulation and RF signals for synchronous pumping and for exciting Rabi oscillations, respectively. However, the experiment control program gates these signals asynchronously with respect to the RF waveform, so the initial RF phase and the time delay from the last pump pulse vary between experimental runs, introducing dynamic heading error variations. (b) Block diagram of the RF switching and synchronization chain before the RF controller input.

The RF switches allow the PE that is used to drive the Zeeman Rabi oscillations to be changed during the measurement sequence. Employing a series of PEs for vector measurements is useful as each one has a distinct angular dependence of the Rabi frequency, as illustrated in Fig. 4.14. Magnetic field directions for which one PE results in a small Rabi frequency are often complemented by another one that yields a larger Rabi frequency. Combining Rabi measurements from multiple PEs therefore suppresses the fractional systematic errors associated with the small Rabi frequencies and improves the overall angular accuracy. It also makes the angular gradient of the Rabi frequency more uniform over the full solid angle, which enhances angular resolution and supports deadzone-free operation. Here, the PEs are generated by selectively driving one, two or all three coil pairs simultaneously, giving the X (PE1), Y (PE2), Z (PE3), X+Y (PE4), X+Z (PE5), and X+Y+Z (PE6) PEs in the laboratory frame (Fig. 4.14). The '+' here denotes simultaneous excitation of the corresponding coil pairs. The Y+Z PE was not included because it provided negligible additional vector information and yielded no improvement in performance while increasing the total measurement time.

We also examine the short-term fluctuations of the Rabi frequency, shown in Fig. 4.15a. In this measurement, the Rabi frequency is sampled every 2 ms over 600 ms, and the deviation, $\Delta\Omega_{\sigma+}$ from the mean value of 56.089 kHz is plotted. Here, the observed Rabi fluctuations are directly related to fluctuations in the RF magnetic field. In particular, variations associated with dynamic heading error between successive measurements are largely removed. Because the measured Rabi oscillations are driven using PE6 with all three RF coil pairs excited, the extracted frequency is sensitive to RF fluctuations in each channel.

The same approach also allows us to examine long-term drifts in RF field. In contrast to the DC magnetic field, which remains stable over comparatively long timescales, the RF field exhibits noticeable drift. This behaviour likely arises from the larger number of thermally sensitive components in the RF setup. For instance, the voltage reference for the RF current controller is supplied by a function generator rather than by a low-drift reference, and the signal path also includes multiple RF switches as well as a bias-tee before the controller. Additional drift may arise within the current controller itself as it drives

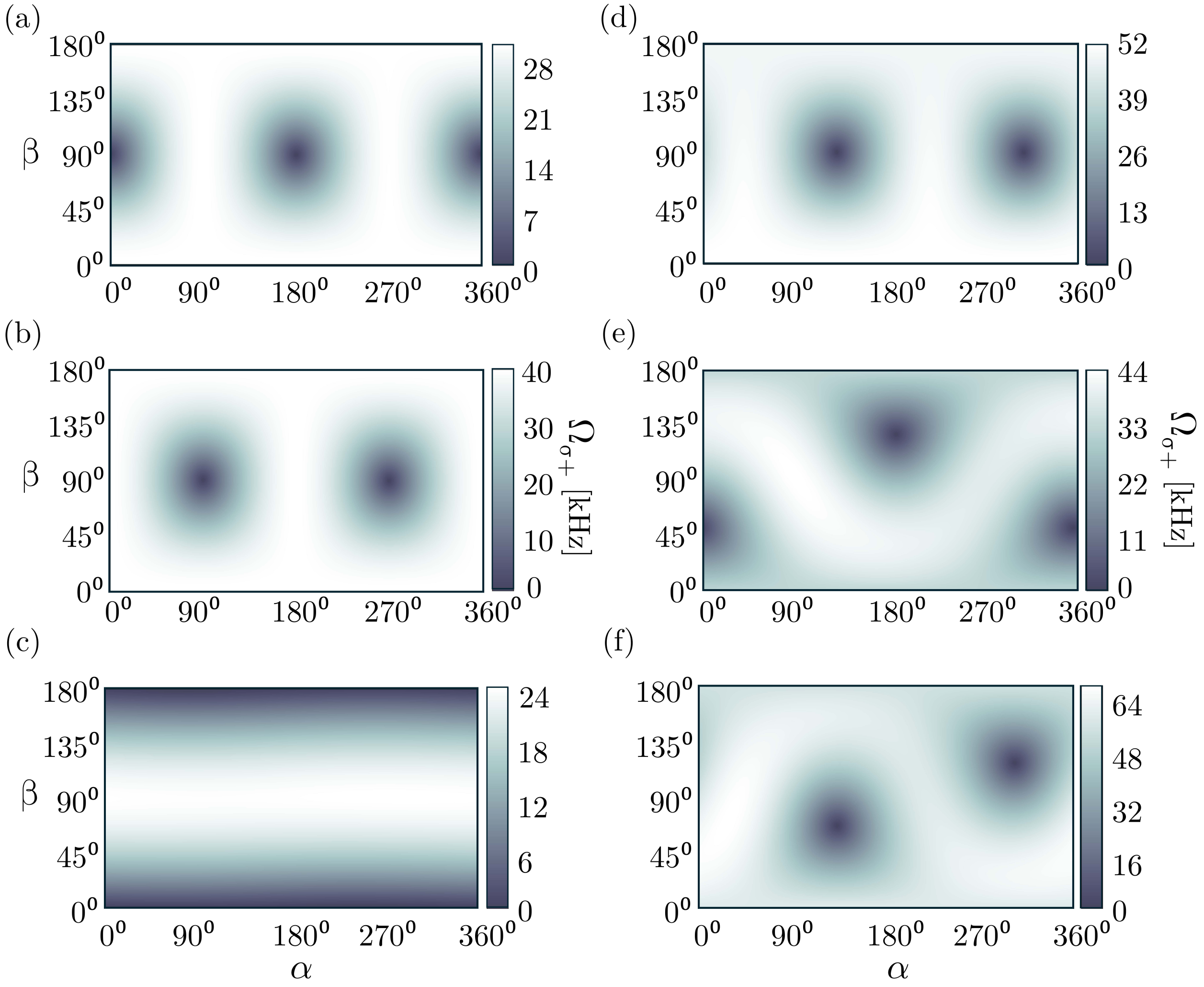

Figure 4.14: Angular dependence of the σ^+ Rabi frequencies for different PEs. Panels show the Rabi frequency as a function of the DC magnetic field orientation (α, β) for (a) PE1 (X), (b) PE2 (Y) (c) PE3 (Z) (d) PE4 (X+Y) (e) PE5 (X+Z) (f) PE6 (X+Y+Z). Labels in parentheses indicate the coil pairs driven simultaneously to produce the corresponding PE.

current into an inductive load, while the compact coil geometry may reduce the efficiency of heat dissipation. Fig. 4.15b shows Rabi frequency measurements sampled every 5 s over 500 s. Over this interval, the total drift is approximately 35 Hz, corresponding to a fractional change of about 0.06%. As in the short-term measurement, all three coil pairs are driven simultaneously, so the observed drift reflects the combined thermal drift of the full RF system.

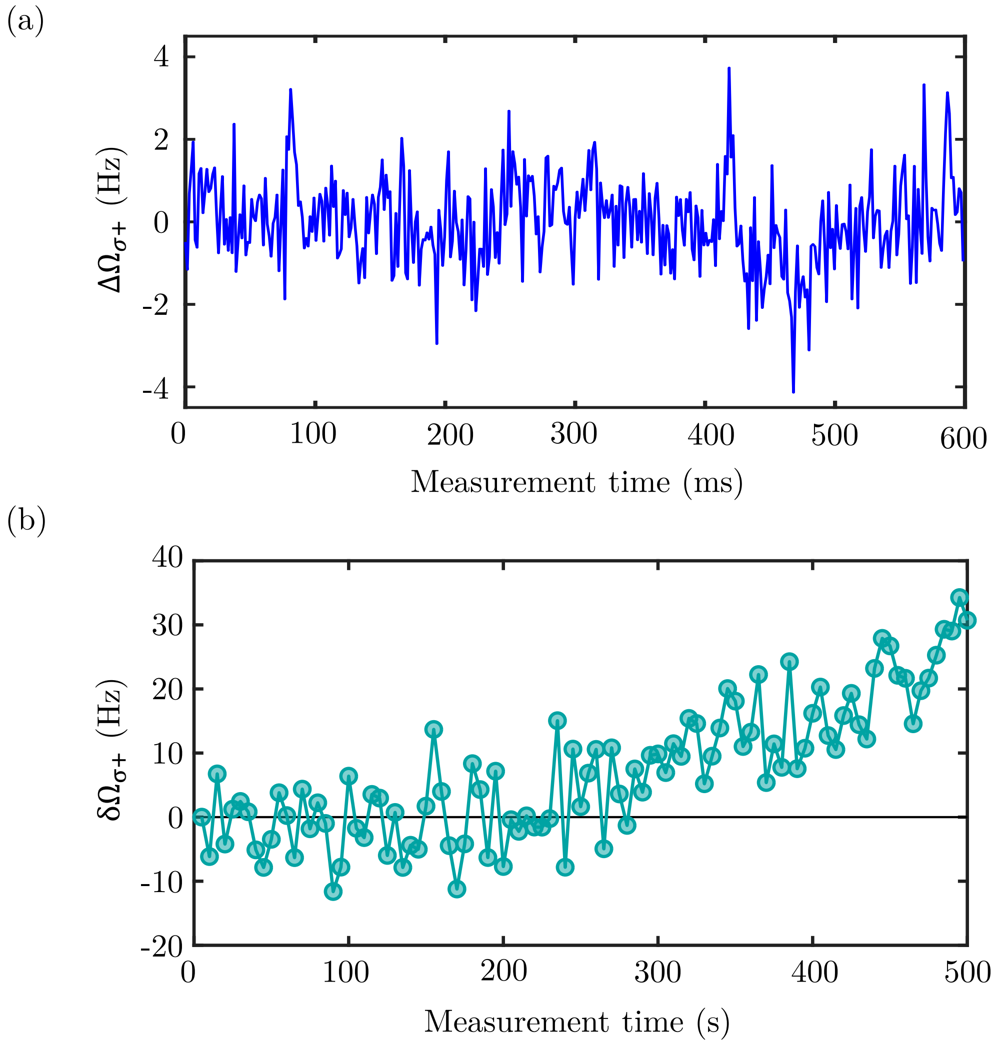

Figure 4.15: Measurements of Rabi frequency noise and drift. (a) Rabi frequencies are measured every 1.5 ms for 600 ms and $\Delta\Omega_{\sigma+} = \Omega_{\sigma+} - \langle\Omega_{\sigma+}\rangle$ is shown with a standard deviation of 1 Hz. (b) Long-term drift obtained from Rabi frequency measurements taken every 5 s for 500 s, plotted as, $\delta\Omega_{\sigma+} = \Omega_{\sigma+} - \Omega_{\sigma+,0}$, where $\Omega_{\sigma+,0}$ is the initial measurement.

The coil systems and controllers described in this section provide the ability to generate controlled DC and RF magnetic fields at the vapor cell. Together with the optical pumping and probing techniques described earlier, these fields produce the atomic spin dynamics that are observed through the Faraday rotation signals. In order to implement vector magnetometry using the spin dynamics, it is essential to determine the corresponding Rabi and Larmor frequencies. The following section therefore describes the analysis procedure used to obtain these frequencies from the measured Faraday rotation data.

4.4 Extraction of Rabi and Larmor Frequencies

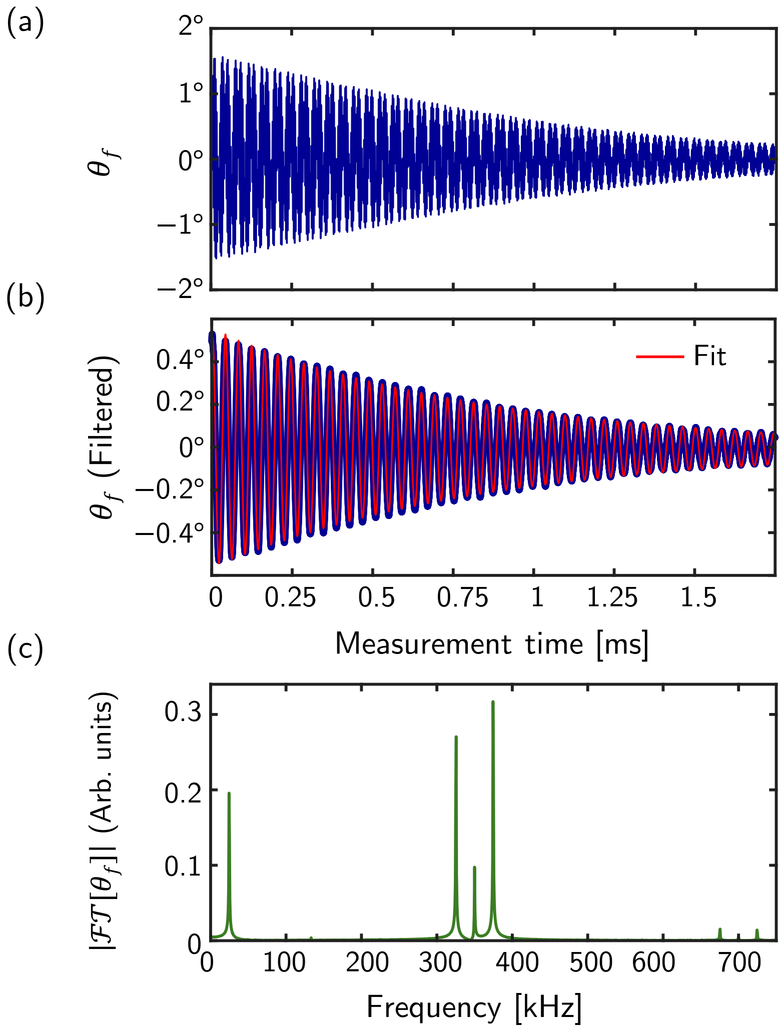

Figure 4.16: Extraction of Rabi frequencies from Faraday rotation measurements. Raw Faraday rotation signal showing Zeeman Rabi oscillations for PE1 with the magnetic field oriented at (α, β)=$(228°, 71.84°)$. (b) Low-pass filtered signal with a fitted model used to determine $\Omega_{\sigma+}$. (c) Fourier spectrum of the raw signal showing peaks at $\Omega_{\sigma+}$, $\nu_{RF} \pm \Omega_{\sigma+}$, and weaker components at $2\nu_{RF} \pm 2\Omega_{\sigma+}$.

In general, the Faraday rotation signal measured for σ^+-driven Rabi oscillations contains both the oscillation at $\Omega_{\sigma+}$ and the rapidly oscillating components associated with the RF field (Fig. 4.16). To remove the high-frequency components, the measured $\theta_f(t)$ is passed through a digital low pass filter with a 3 dB cutoff frequency of 170 kHz. This filtering removes components at $\nu = \nu_{RF}, \nu_{RF} \pm \Omega_{\sigma+}$, while preserving the Rabi oscillation at $\Omega_{\sigma+}$. The Rabi frequency is then obtained by fitting the filtered signal to the function [87, 106]:

$$\theta_f(t) = A_0 + A_{11}e^{-t/T_{11}} + A_{12}e^{-t/T_{12}} + A_2 e^{-t/T_2} \sin(2\pi\Omega_{\sigma+}t + \varphi)$$

The double exponential decay of the background signal arises from spin-exchange collisions that cause the spin-decay of the ensemble [106].

To measure Larmor precession, the RF fields are switched off after optical pumping so that the spin-polarized atoms evolve only under the DC magnetic field. The resulting Faraday rotation signal is then analyzed in the frequency domain to determine the field magnitude. We compute the complex Fourier spectrum using a zero-padded discrete Fourier transform of the measured signal. The purpose of zero padding is to sample the spectrum more finely in frequency, which facilitates fitting of the resonance lineshape. The real and imaginary parts of the complex spectrum are fit simultaneously to a model consisting of two Lorentzian resonances corresponding to the $F = 2$ and $F = 1$ hyperfine manifolds centered at their respective Larmor frequencies:

$$\mathcal{FT}[\theta_f]\,(\nu) = A_0 + (\mathcal{L}(\nu))_{F=2} + (\mathcal{L}(\nu))_{F=1}$$

Here, each resonance is described by

$$\mathcal{L}(\nu; A_1, \nu_0, \Gamma, \varphi) = A_1 e^{-i\varphi} \frac{\Gamma/2 + i(\nu - \nu_0)}{(\nu - \nu_0)^2 + (\Gamma/2)^2}$$

In this model, the resonance frequencies of the two hyperfine manifolds are jointly constrained by the Breit-Rabi formula (Sec. 2.1.2), so that both resonances are determined by a single fitted value of the DC magnetic field strength [56].

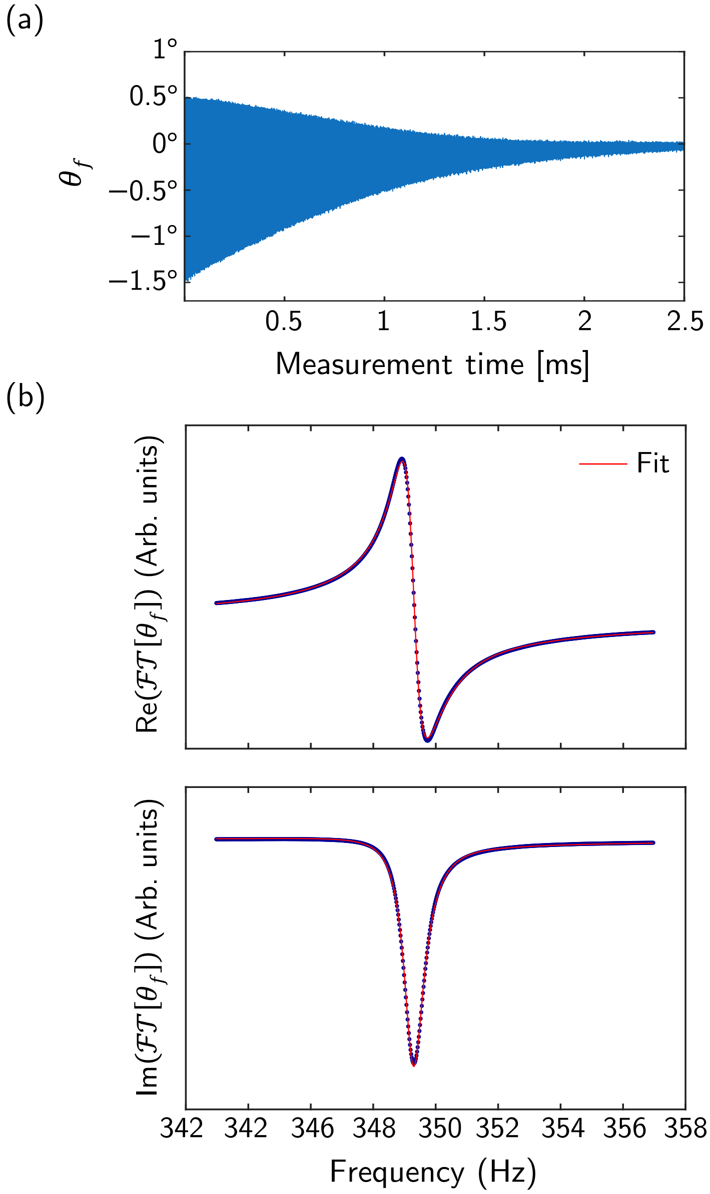

Figure 4.17: Extraction of the magnetic field from Larmor precession measurements. (a) Raw Faraday rotation signal of a Larmor precession. (b) Real and imaginary parts of the Fourier transform of the Faraday rotation signal fitted to a double-Lorentzian model corresponding to Larmor frequencies in the $F = 2$ and $F = 1$ hyperfine manifolds.

The experimental apparatus described in this chapter provides a stable and versatile platform for studying atomic spin dynamics and implementing Zeeman Rabi vector magnetometry. The microfabricated vapor cell, together with the DC and RF magnetic field generation systems and synchronized electronic control, provides a controlled environment in which Rabi and Larmor frequencies can be measured accurately. With this platform established, the following chapter describes how these capabilities are used to perform vector magnetometry.

Chapter 5

Vector Magnetometry with Zeeman Rabi oscillations

In previous chapters, we have developed the components necessary to realize vector magnetometry in an alkali vapor cell. We started with a theoretical model of atomic spin dynamics and its coupling to the magnetic field. We then expanded this picture to include RF-driven Zeeman Rabi oscillations, where we discussed various systematics arising from counter-rotating components and the nonlinear Zeeman effect. Next we described the experimental setup in detail, including the vapor cell, the optical setup, and the magnetic field system, and also the signal processing methods that are used to infer the relevant frequencies from the measured Faraday rotation signals.

With these pieces in place, in this chapter, we will focus on how this idea is implemented in practice. We begin by describing the experiment sequence used to prepare, drive and probe the ^{87}Rb atoms in the microfabricated vapor cell. This sequence sets the length of each stage of the sequence, including the optical pumping of the spin polarization, applying a series of resonant PEs to drive Zeeman Rabi oscillations, and the optical measurement of Faraday rotation signals used for inferring the Rabi frequencies. As discussed earlier, one important advantage of this system is that it is fundamentally based on frequency measurements, which can be made with high precision and long-term stability, compared to similar amplitude-based measurements [150].

We then describe the calibration procedure that determines the PE parameters and establish the vector reference relative to which magnetic field direction is inferred. The calibration is performed by applying controlled rotations of the magnetic field and measuring the corresponding Rabi frequencies for each PE. Following calibration, we use these PEs to measure magnetic fields over a wide range of directions. By relying on several PEs with differing angular sensitivity, a PE that exhibits poor sensitivity for a given magnetic field direction is generally compensated by another with a stronger sensitivity. Thus combining multiple Rabi measurements help maintain nonzero sensitivity over the full solid angle. We then characterize the performance of the magnetometer through measurments of a variety of metrics such as angular accuracy, consistency and noise density. The chapter concludes by examining the factors that limit performance. These include residual systematics in the time-independent model, and slow drifts in the apparatus over time, resulting in residuals in calibration. From these results, we can evaluate how well the vector magnetometer works in practice and identify the main sources of error.

5.1 Experiment Sequence

We begin by describing the timing sequence used in the experiment. For each measurement, a magnetic field of 50 μT is programmed to a desired direction (α, β) by setting the corresponding currents in the three DC coil pairs. These currents are supplied by an ultra-stable current controller, as described in Sec. 4.3.1.4. However, the controller output is filtered by a 16 Hz RC stage to reduce high-frequency current noise at the coils. Although this filtering improves the current stability, and hence the field stability during the measurement, the presence of this filter causes the current to approach its final value gradually rather than instantaneously. To ensure that all measurements are performed only after the field has stabilized, we introduce a delay of 0.85 s between programming the new field direction and initiating the measurement sequence, as shown in Fig. 5.1a. This delay corresponds to the time required for the currents to reach within 10 ppm of their final programmed values. Waiting for the fields to settle is important for avoiding systematic errors associated with transient coil currents and for ensuring that repeated measurements at a given field direction are performed under the same conditions.

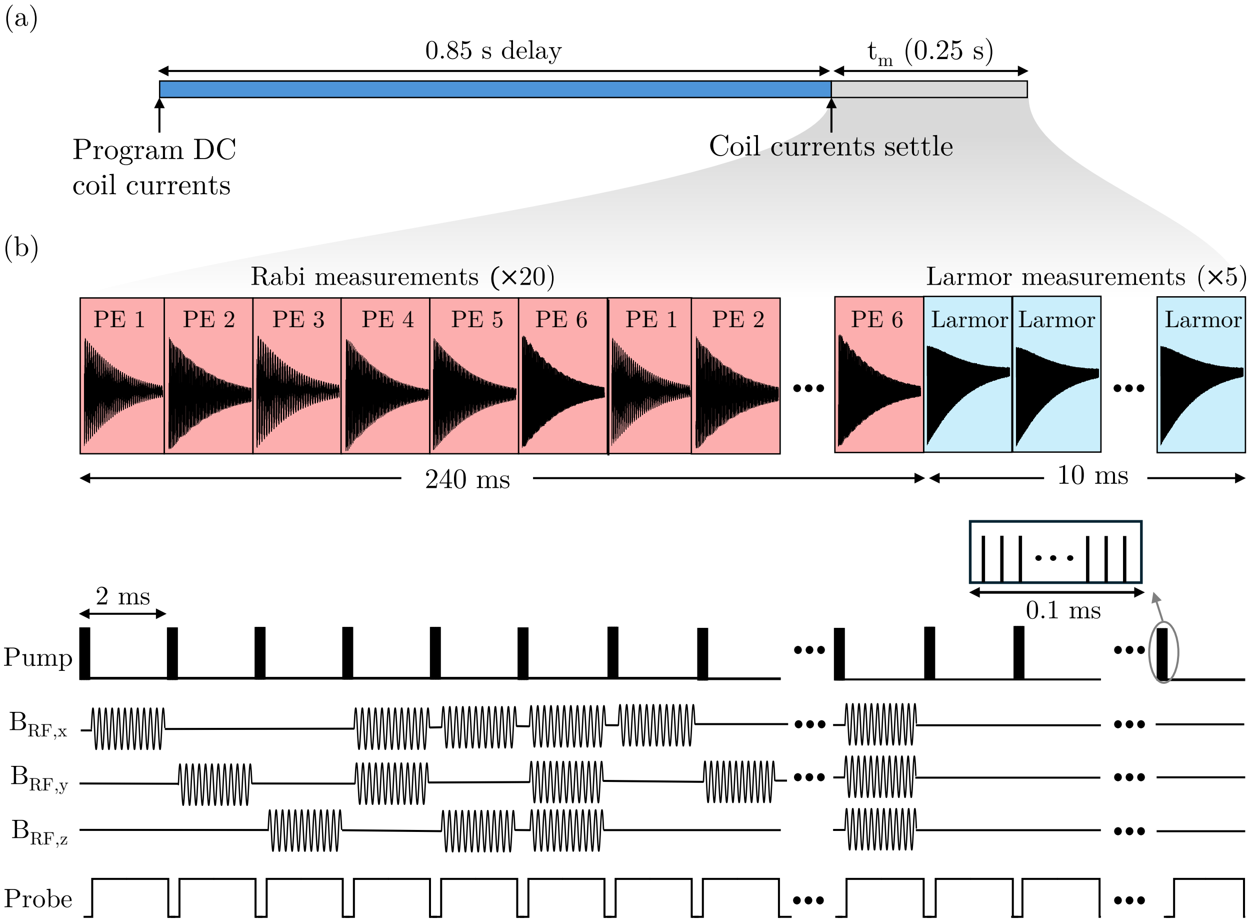

Figure 5.1: Experiment timing sequence. (a) After the new DC coil currents are programmed, we wait 0.85 s for the currents to settle and the DC field to stabilize before acquiring data. (b) Each cycle begins with 0.1 ms of synchronous optical pumping to prepare spin polarization. Following the pumping stage, the atoms are interrogated using six PEs generated by distinct combinations of RF pulses applied to the RF coil system. $B_{RF,i}, i \in \{x, y, z\}$ denotes the RF signals applied to the corresponding coil pair. Rabi measurements are averaged over 20 repetitions, while each Larmor measurement is averaged over 5 repetitions.

Once the magnetic field has settled, the atoms are interrogated using a repeated pulse sequence (Fig. 5.1b). Each measurement begins with 0.1 ms of synchronous optical pumping with the 400 mW pump laser, which prepares a spin-polarized atomic state with a well-defined phase relation to the applied RF driving field. This pumping stage is followed by a 1.9 ms probe laser pulse. During Rabi measurements, an RF pulse is applied during this interval to one or more coil pairs, thereby driving Zeeman Rabi oscillations whose frequency depends on the applied polarization ellipse and the magnetic field direction. During Larmor measurements, the RF fields remain off for the same duration so that the polarized atoms evolve only under the DC magnetic field. In both cases, the transmitted probe light is monitored through its Faraday rotation, and the resulting Rabi and Larmor frequencies are extracted from the measured signals by least squares fitting (Sec. 4.4). For each magnetic field orientation, Rabi oscillations are measured for six distinct PEs: PE1 (X), PE2 (Y), PE3 (Z), PE4 (X+Y), PE5 (X+Z), PE6 (X+Y+Z), produced by applying currents to different combinations of the coil pairs. For each PE, the Rabi measurement is repeated 20 times to reduce frequency uncertainty arising from technical fluctuations, while Larmor measurements are repeated 5 times for the same reason.

5.2 PE Calibration

The first step in mapping the measured Rabi frequencies to sense an unknown magnetic field direction is the calibration of all six PEs. The calibration determines the parameters of each PE in the laboratory frame. Once these parameters are known, the Rabi frequency measurements can be interpreted using the theoretical model developed in the previous chapters. As discussed earlier, only $\Omega_{\sigma+}$ measurements are utilized in the experiment and in the corresponding models. As optical pumping transfers nearly all the atomic population into the $F = 2$ hyperfine manifold, Rabi oscillations associated with this manifold dominate the Faraday rotation signal. By focusing on $\Omega_{\sigma+}$, we make use of the transition that carries the highest signal-to-noise ratio.

To perform the calibration, $\Omega_{\sigma+}$ is measured for each of the six PEs at thirty randomly selected but predefined magnetic field directions, denoted by $(\alpha_{ci}, \beta_{ci})$ in Fig. 5.2. These calibration directions are distributed over the full solid angle and allow the angular dependence of each PE to be sampled over a broad range of field directions. The use of thirty calibration directions provides an overconstrained determination of the six parameters associated with each PE. This ensures that the calibrated parameters account not only for the nominal programmed RF current amplitudes and phases, but also for experimental nonidealities such as coil imbalance, phase delays in the RF electronics, and potential distortions of the applied field at the vapor cell.

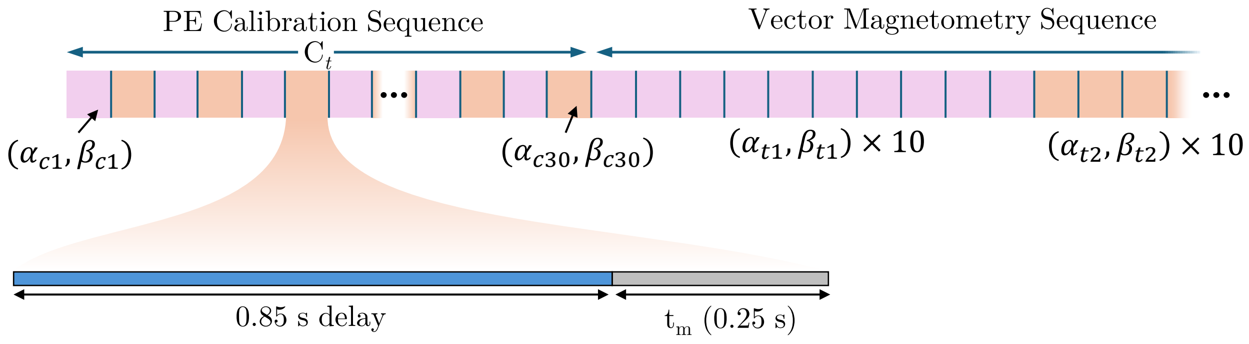

Figure 5.2: Schematic of calibration and vector magnetometry sequences. $(\alpha_{ci}, \beta_{ci})$ and $(\alpha_{ti}, \beta_{ti})$ denote calibration and test magnetic field directions, respectively.

For a given PE, the 30 measured Rabi frequencies are then compared with the predictions of the Floquet-based theoretical model introduced in Eqns. (3.27) and (3.30). The PE parameters are obtained by minimizing the cost function [87]

$$\mathcal{C}(\boldsymbol{\mathcal{B}}_0) = \sum_{j=1}^{30} \left[\widetilde{\Omega}_{\sigma+} \left(\boldsymbol{\mathcal{B}}_0, (\alpha, \beta)_j \right) - \left(\Omega_{\sigma+} \right)_j \right]^2 \tag{5.1}$$

Here, $\widetilde{\Omega}_{\sigma+} \left(\boldsymbol{\mathcal{B}}_0, (\alpha, \beta)_j \right)$ denotes the Rabi frequency predicted by the model for the j^{th} magnetic field orientation. Namely,

$$\widetilde{\Omega}_{\sigma+} = \frac{\sum_m A_{\sigma+,m} \Omega_{\sigma+,m}}{\sum_m A_{\sigma+,m}}$$

where,

$$\begin{aligned} A_{\sigma+,m} &= \left| \left\langle q_{F^+,m;-m} \middle| \rho_0 \middle| q_{F^+,(m-1);-(m-1)} \right\rangle \left\langle q_{F^+,m;-m} \middle| \Theta_f \middle| q_{F^+,(m-1);-(m-1)} \right\rangle \right| \\ \Omega_{\sigma+,m} &= \frac{q_{F^+,m;-m} - q_{F^+,(m-1);-(m-1)}}{h} \end{aligned} \tag{5.2}$$

Here $q_{F^+,m;n}$ and $|q_{F^+,m;n}\rangle$ are the eigenvalues and eigenstates of the Floquet Hamiltonian, $\widetilde{H}_F$ given in Eq. (3.26), and ρ_0 and Θ_f are the initial pumped density matrix and the Faraday rotation operator, respectively.

In Eq. (5.1), $(\Omega_{\sigma+})_j$ denotes the Rabi frequency measurement at the j^{th} magnetic field direction. $\boldsymbol{\mathcal{B}}_0$ consists of the three amplitudes and three phases in the laboratory frame. It is written as

$$\boldsymbol{\mathcal{B}}_0 = \sum_{j \in \{x,y,z\}} (\mathcal{B}_0)_j \; e^{-i\phi_j} \, \hat{j}$$

so that the applied full time-dependent field can be represented as $\mathbf{B}_{\mathrm{RF}}(\mathrm{t}) = \boldsymbol{\mathcal{B}}_0 e^{-i\omega_{RF} t}$. In addition, because the model includes the dynamic heading error term of Eq. (3.30), the fit also determines the initial phase of the RF field relative to the pump modulation pulses during the pumping stage. The calibrated field parameters, denoted by $\boldsymbol{\mathcal{B}}_{0,\mathrm{cal}}$, are found by nonlinear least squares minimization of $\mathcal{C}(\boldsymbol{\mathcal{B}}_0)$ using the Levenberg-Marquardt algorithm. This minimization is carried out independently for each of the six PEs, producing a complete set of calibrated RF parameters for subsequent vector sensing. The nominal set of calibrated RF parameters are given in Table 5.1. Errors in the calibration parameters were estimated using a bootstrapping procedure. For each PE, the predefined magnetic field directions were resampled with replacement to generate synthetic calibration datasets, and the calibration fit was repeated for each dataset. The resulting distribution of the fitted parameters was used to estimate the errors given in Table 5.2.

The full calibration sequence for all six PEs presently requires a duration, $\mathbf{C}_t$ of approximately 30 s. This time is determined primarily by the dead time associated with

	$(\mathcal{B}_0)_x$	$(\mathcal{B}_0)_y$	$(\mathcal{B}_0)_z$	ϕ_x	ϕ_y	ϕ_z
PE1	9.093 μT	97 nT	56 nT	349°	176.1°	145.4°
PE2	124 nT	11.438 μT	77 nT	358.3°	2°	177.2°
PE3	49 nT	123 nT	7.115 μT	118.9°	160.8°	345°
PE4	8.967 μT	11.529 μT	34 nT	277°	101°	308°
PE5	9.113 μT	52 nT	7.162 μT	252°	194.9°	64°
PE6	8.994 μT	11.411 μT	7.082 μT	149°	333°	321°

Table 5.1: Nominal calibration parameters for the PEs used in the experiment.

	$\delta\left(\mathcal{B}_0\right)_x$	$\delta\left(\mathcal{B}_0\right)_y$	$\delta\left(\mathcal{B}_0\right)_z$	$\delta\phi_x$	$\delta\phi_y$	$\delta\phi_z$
PE1	0.2 nT	0.2 nT	0.3 nT	1.2°	0.2°	0.2°
PE2	0.3 nT	0.2 μT	0.4 nT	0.5°	0.9°	0.2°
PE3	0.2 nT	0.3 nT	0.1 nT	0.2°	0.2°	1.3°
PE4	0.6 nT	0.5 nT	0.3 nT	0.8°	0.8°	0.8°
PE5	0.5 nT	0.1 nT	0.5 nT	0.9°	0.5°	1.3°
PE6	0.5 nT	0.8 nT	0.5 nT	0.4°	1.6°	1.6°

Table 5.2: Parameter errors for Table 5.1

reprogramming the DC magnetic field between successive calibration points. If the current control bandwidth were increased so that the settling delay could be reduced to approximately 0.05 s, the full calibration time would decrease to about 9 s. Such an improvement would make the calibration procedure more practical for applications that require frequent recalibration to compensate for drift in the RF parameters.

The quality of the calibration can be assessed from the residual differences between the measured Rabi frequencies and the model prediction, which remain small over the full calibration set. Fig. 5.3 shows the residuals, $\sqrt{\mathcal{C}(\boldsymbol{\mathcal{B}}_{0,\mathrm{cal}})}$ of the calibration procedure, for the six PEs. The calibration results in root mean square residuals ranging from 1 Hz (0.2 nT) to 3.5 Hz (0.7 nT) across the six PEs.

The observed residuals arise from several sources. One contribution comes from slow drifts in the RF system during the calibration sequence. Although the DC magnetic field system remains stable over repeated measurements, the RF coil system and the associated electronics undergo drifts over the duration of the calibration, $\mathbf{C}_t$. As mentioned above, in the present implementation, the total calibration time is extended mainly by the delays required to allow the DC coil currents to settle after a change in the magnetic field orientation. These delays increase the time between successive measurements and make the RF system more susceptible to drifts during the acquisition of the calibration data.

In addition to technical drifts, part of the residuals also arises from systematic effects that are not incorporated in our theoretical models. In particular, spin-exchange collisions and residual population in the $F = 1$ hyperfine manifold produce small corrections to the measured Rabi frequencies. These effects couple to the σ^- component of the applied PEs and shift the effective Rabi frequency measured in the experiment. Because these contributions are not included in the fitting model, they appear as residual disagreement between the measured data and the calibrated prediction. The resulting deviations can reach a few Hz, which is consistent with the scale of the residuals shown in Fig. 5.3. These drifts and systematics are further discussed in Sec. 5.4.

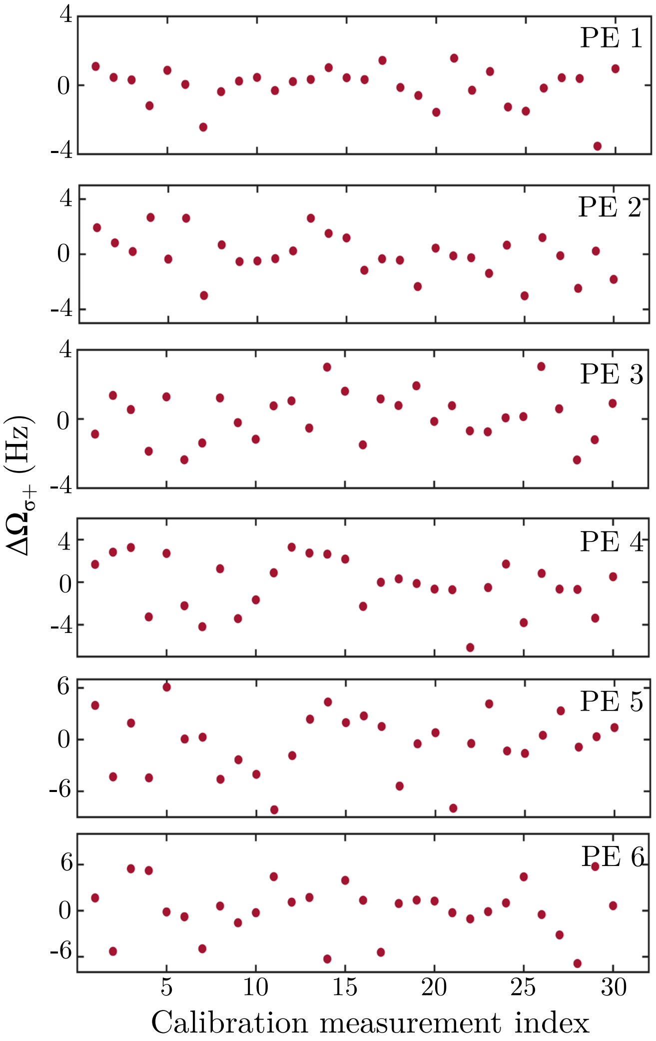

Figure 5.3: For each PE, we plot residuals, $\Delta\Omega_{\sigma+} = \widetilde{\Omega}_{\sigma+}\left(\boldsymbol{\mathcal{B}}_{0,\mathrm{cal}},\, \alpha_{ci}, \beta_{ci}\right) - \left(\Omega_{\sigma+}\right)_i$, at the calibration direction $i \in \{1, 2, ..., 30\}$. RMS value of residuals ranges from 1 Hz (PE1) to 3.5 Hz (PE5).

The small size of the residuals indicates that the calibration captures the dominant features of the angular dependence of the Rabi frequencies for all six PEs. At the same time, the calibration residuals provide an indicator of the level at which slow drifts and “unmodeled” atomic physics affect the calibration accuracy, and hence the performance of the magnetometer.

5.3 Vector Magnetometry

Once the six PEs have been calibrated, they can be used to determine an unknown magnetic field direction. The magnitude of the magnetic field is independently obtained from Larmor frequency measurements. This step effectively inverts the calibration procedure. During calibration, the magnetic field direction is known and the measured Rabi frequencies are used to determine the parameters describing the PEs. In the vector magnetometry stage, the calibrated PEs are assumed to be fixed and the measured Rabi frequencies are used to infer the magnetic field direction.

For a given magnetic field, each of the six calibration PEs drive Zeeman Rabi oscillations, and the corresponding Rabi frequency is extracted from the measured Faraday rotation signal. The unknown direction is then obtained by comparing the measured Rabi frequencies with the values predicted by the theoretical model. This is best expressed through the cost function [87]

$$\mathcal{C}(\alpha, \beta) = \sum_{i=1}^{6} \left[\widetilde{\Omega}_{\sigma+} \left(\left(\boldsymbol{\mathcal{B}}_{0,\mathrm{cal}}\right)_i , \alpha, \beta \right) - \left(\Omega_{\sigma+}\right)_i \right]^2 \tag{5.3}$$

where $\widetilde{\Omega}_{\sigma+}$ is the Rabi frequency predicted by the theoretical model of Eqs. (3.20) and (3.30) for the i^{th} calibrated PE $\left(\boldsymbol{\mathcal{B}}_{0,\mathrm{cal}}\right)_i$, and $\left(\Omega_{\sigma+}\right)_i$ is the corresponding measured mean value of the 20 Rabi repetitions for each PE. As in the calibration procedure, the minimum of $\mathcal{C}(\alpha, \beta)$ is found using a nonlinear least squares algorithm (Levenberg-Marquardt), which yields the best fit field direction, (α^*, β^*). These angles are reported in the laboratory frame established by the DC coil system after scalar calibration. It is important to note, however, that for practical applications, the DC coil system serves only to define the reference frame during calibration. Once the PEs have been calibrated, the direction measurement no longer depends on the generation of known magnetic fields by the DC coil system. The DC coil system is not part of the measurement process itself. This separation between frame definition and field measurement is important because it allows the sensor to function as an independent vector magnetometer after calibration.

To benchmark the performance of our vector magnetometer, however, the DC coil system is used to generate magnetic fields of known direction. We evaluate the performance of the magnetometer by comparing the reconstructed field direction, (α^*, β^*) with the applied magnetic field direction [87, 89, 151]. From this comparison, we determine both the angular accuracy and noise density. To evaluate the magnetometer over the full solid angle, 50 μT was applied along 342 randomly chosen directions. Recalibration measurements were interleaved throughout the dataset approximately every 50 test directions. For each applied direction, the Rabi frequencies associated with the six PEs were measured, and the corresponding field direction (α^*, β^*) was obtained using the procedure described above. In addition, the full Rabi and Larmor measurement cycle was repeated 10 times for each direction, as shown in Fig. 5.2.

To compare the results with those reported for other vector magnetometer platforms, we express the directional error in terms of transverse field component errors, $(\delta\mathrm{B}_x, \delta\mathrm{B}_y)$ defined relative to the applied field direction. This representation is useful because it provides a uniform description of vector error over the full sphere. By contrast, an error expressed directly in terms of the azimuthal and polar angles becomes awkward near the poles, where the azimuthal angle, α becomes ill-defined as $\beta \to 0°$, 180°. Following the procedure introduced in Ref. [87], we rotate the measured magnetic field vector into a coordinate system in which the applied DC coil system field lies along the Z axis

$$(\delta\mathrm{B}_\mathrm{x}, \delta\mathrm{B}_\mathrm{y}, \mathrm{B}_\mathrm{z}) = R_y(-\beta)R_z(-\alpha)\mathbf{B}_\mathrm{m}$$

Here $\mathbf{B}_\mathrm{m}$ denotes the measured magnetic field vector oriented along the measured direction, (α^*, β^*), and R_y and R_z denote the Cartesian rotation matrices for the laboratory frame Y and Z axes, respectively. In this rotated frame, the quantities, $\delta\mathrm{B}_x$ and $\delta\mathrm{B}_y$ represent components of the vector error perpendicular to the true field direction, while B_z corresponds

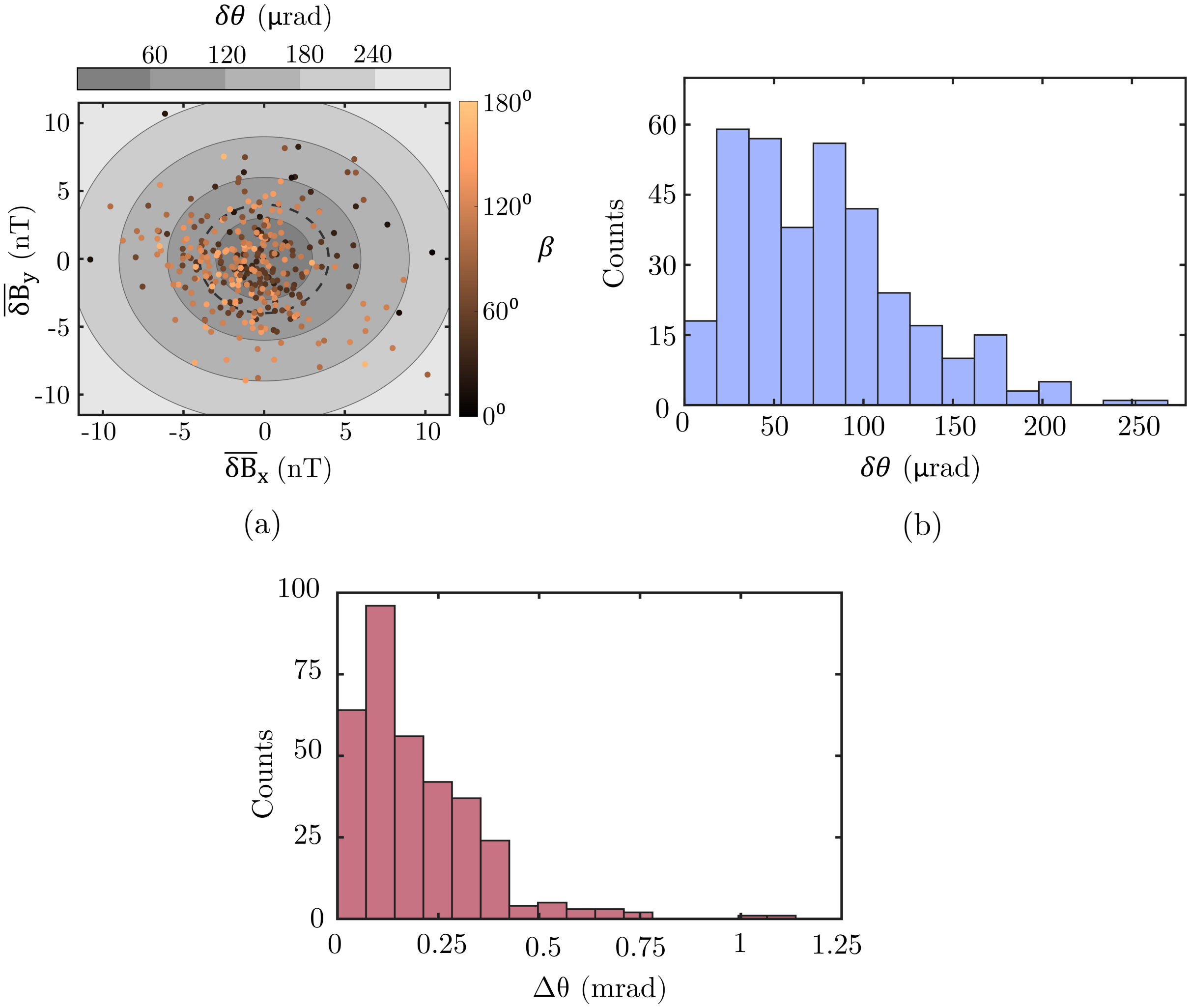

(a) (b)

(c)

Figure 5.4: (a) Transverse component errors, $\overline{\delta B_x}$, $\overline{\delta B_y}$ for 342 applied field orientations, with points color coded by the polar angle, β. Gray contours denote boundaries of constant angular accuracy, $\delta\theta$, and dashed line indicate the mean angular accuracy (80 µrad) over the test directions. (b) Angular accuracy, $\delta\theta$ for the same data in (a) is shown in a histogram plot. (c) Histogram of the relative angular error, $\Delta\theta$ between vectors inferred from two disjoint PE sets.

to the component parallel to the direction. The transverse component errors are useful because they isolate the directional error from any error in the field magnitude.

We define the angular accuracy in terms of the mean transverse component errors according to,

$$\delta\theta = \tan^{-1}\left(\sqrt{\overline{\delta \mathrm{B}}_{\mathrm{x}}^{2} + \overline{\delta \mathrm{B}}_{\mathrm{y}}^{2}}/\mathrm{B}_{\mathrm{m}}\right)$$

where $\overline{\delta \mathrm{B}}_{\mathrm{x}}$ and $\overline{\delta \mathrm{B}}_{\mathrm{y}}$, are obtained by averaging transverse component errors over 10 repetitions for each direction, and $\mathrm{B}_{\mathrm{m}} = |\mathbf{B}_{\mathrm{m}}|$. Averaged over all 342 field orientations, the magnetometer yields a mean angular accuracy of $\langle\delta\theta\rangle = 80\,\mu\mathrm{rad}$, corresponding to a transverse field accuracy of 4 nT, as shown in Fig. 5.4a and Fig. 5.4b. This measured angular accuracy is consistent with the magnitude of the residual errors obtained in the calibration of the six PEs.

The analysis above evaluates the vector accuracy of the magnetometer with respect to the magnetic field applied by the DC coil system. It is also useful to evaluate an internal measure of consistency that does not rely on an external coil system by comparing independent reconstructions of the same magnetic field. To do so, we divide the six PEs into two disjoint subsets, {PE1, PE2, PE6} and {PE3, PE4, PE5}, and obtain the field direction separately using each subset. These two subsets were chosen so that their average Rabi frequencies are comparable over the set of measured field directions, ensuring that both PE subsets experience similar levels of fractional systematic errors.

Using a smaller PE subset generally reduces the quality of the vector reconstruction. Because each direction measurement is measured by half the number of PEs compared to the earlier accuracy measurement, the resulting estimates generally exhibit reduced angular precision and accuracy. With fewer measurements, the direction inferred from the Rabi frequencies becomes more sensitive to angular regions in which the Rabi frequency gradients are small, and systematic effects associated with small Rabi frequencies can play a larger role. Nevertheless this comparison provides a useful consistency check since both reconstructions are derived entirely from Rabi measurements, and therefore this comparison does not depend on the scalar calibration of the DC coil system. We define the relative angular error between the two measured vectors as

$$\Delta\theta = \cos^{-1}\left(\frac{\overline{\mathbf{B}}_{\mathrm{m1}} \cdot \overline{\mathbf{B}}_{\mathrm{m2}}}{\mathrm{B}_{\mathrm{m}}^{2}}\right) \tag{5.4}$$

The vectors, $\overline{\mathbf{B}}_{\mathrm{m1}}$ and $\overline{\mathbf{B}}_{\mathrm{m2}}$ are obtained by averaging the ten repeated measurements using the subsets {PE1, PE2, PE6} and {PE3, PE4, PE5}, respectively. The relative angular error was calculated for the same field directions used in Fig. 5.4a. The resulting distribution is shown in Fig. 5.4c and yields a mean value of $\langle\Delta\theta\rangle = 197\,\mu\mathrm{rad}$. This value is larger than the accuracy obtained when all six PEs are used together, as expected from the reduced amount of vector information available in each subset.

The discrepancy between the two vector reconstructions can primarily be attributed to systematic effects that are not fully described by our Floquet-based model and that influence the two PE subsets differently for a given field direction. Because the two subsets contain different combinations of PEs, they do not sample model imperfections in the same way. The impact of these effects becomes more significant when the reconstruction relies on a smaller number of PEs. Additional differences may also arise from relative amplitude and phase drifts between the PEs, particularly for those formed from superpositions of fields along multiple coil axes.

To measure the angular sensitivity of the magnetometer, we determine the angular noise density from the fluctuations of the measured transverse component errors over the ten repeated measurements at each magnetic field orientation. To convert these fluctuations into a noise density, the finite measurement bandwidth must be taken into account. Assuming white noise, the noise density associated with the transverse component is

$$\mathrm{S}_{\mathrm{B_j}} = \sigma_{B_j}\sqrt{2t_m}$$

where σ_{B_j} is the standard deviation of δB_j over the ten repetitions and t_m is the measurement time required for one complete direction estimate. This measurement time includes the acquisition of the six Rabi measurements and the corresponding Larmor measurements. It

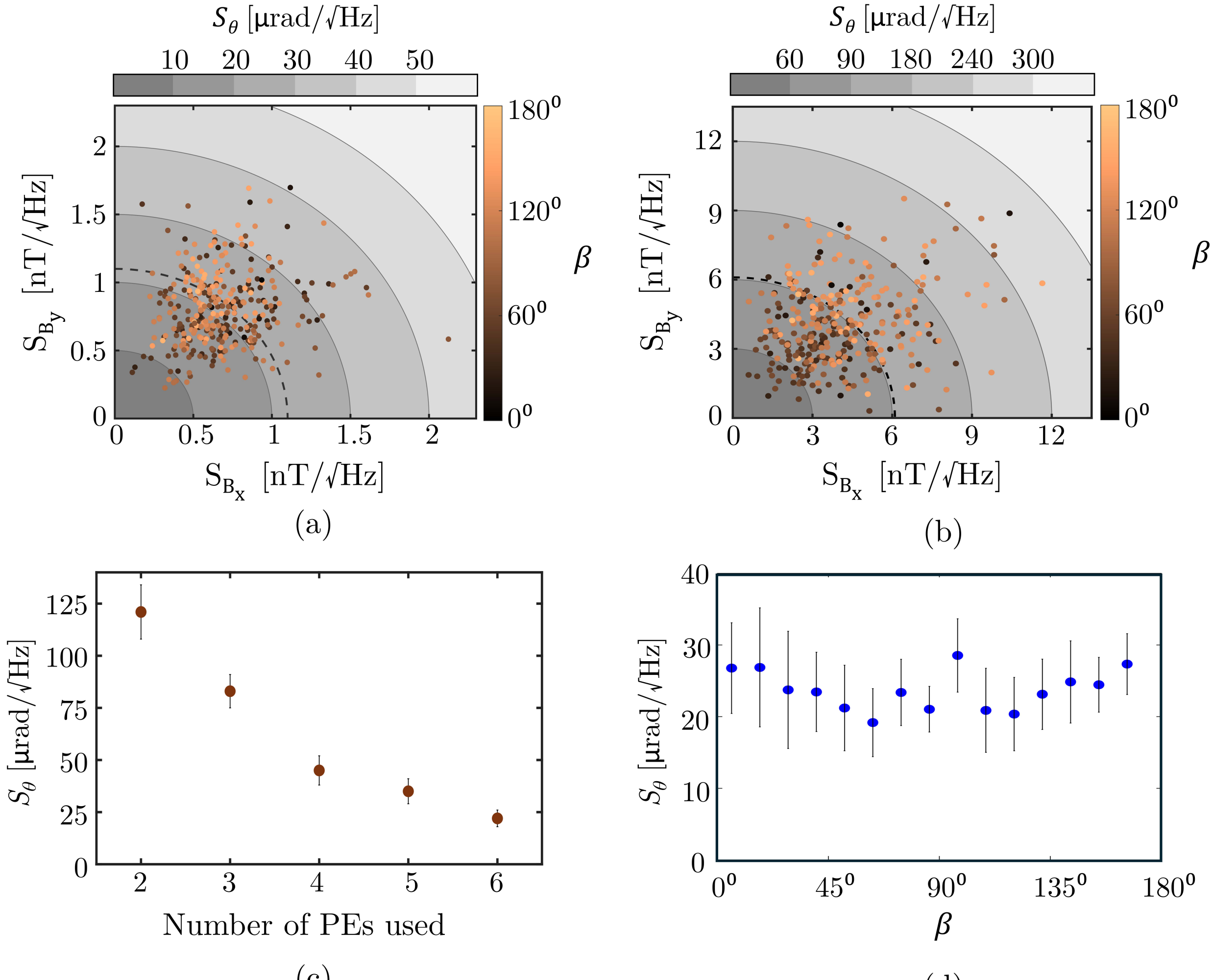

(a)

(b)

(c)

(d)

Figure 5.5: Transverse component noise densities S_{B_x}, S_{B_y} evaluated for 342 test magnetic field orientations using (a) two PEs (PE1 and PE2) and (b) all six PEs. Gray contours denote boundaries of constant angular noise density, S_θ. Dashed lines indicate the mean values $\langle S_\theta \rangle$ 120 µrad/$\sqrt{\text{Hz}}$ (a) and and 22 µrad/$\sqrt{\text{Hz}}$ (b). (c) Angular noise density for 342 applied direction as function of the number of PEs used to infer the direction. (d) Angular noise density, S_θ binned as a function of the polar angle, β, illustrating the variation of noise with magnetic field orientation.

does not include the additional 0.85 s delay applied before the start of the measurement, since that interval reflects technical settling time of the programmed currents rather than the bandwidth of the measurement itself.

The transverse component noise densities can be converted to an angular noise density according to [87]

$$S_\theta = \tan^{-1}\left(\frac{\sqrt{\mathrm{S}^2_{\mathrm{B_x}} + \mathrm{S}^2_{\mathrm{B_y}}}}{\mathrm{B_m}}\right)$$

The transverse component densities along with the 342 test directions around the full solid angle are shown in Fig. 5.5a. Over the full set of measured directions, the angular noise densities reaches a minimum value of 8 μrad/$\sqrt{\mathrm{Hz}}$ at $(\alpha, \beta) = (65.57°, 49.68°)$. Averaged over all measured directions, the mean value is $\langle S_\theta \rangle = 22\,\mu$rad/$\sqrt{\mathrm{Hz}}$. At the field magnitude of 50 μT, this corresponds to a transverse component density of 1.1 nT/$\sqrt{\mathrm{Hz}}$.

The six calibrated PEs do not provide uniform sensitivity over the full angular range, the angular noise density is therefore direction-dependent. This dependence arises from the angular gradients of the corresponding Rabi frequencies. The Rabi-frequency gradients vary strongly with (α, β). Along directions where these gradients are large, fluctuations in Rabi frequency produce only a small error in the inferred direction. In contrast, where the gradients are weak, the same level of fluctuations lead to a larger directional uncertainity.

The use of six PEs plays an important role in improving the angular noise density. Each PE provides a different dependence of the Rabi frequency on the field direction, and therefore contributes a distinct sensitivity to angular variations. When all six PEs are used together, the effective sensitivity is determined by an average over these gradients. In directions where one PE exhibits a weak gradient and therefore provides limited directional information, another PE exhibits a stronger gradient along that same direction. This averaging over complementary sensitivities reduces the overall noise in the direction obtained from the Rabi frequencies. If a smaller number of PEs are used, this averaging is reduced and the reconstruction becomes more sensitive to directions in which the available PEs have weak gradients. Fig. 5.5b plots the transverse component noise densities for reconstructed directions obtained by using two PEs, PE1 and PE2. In this case, the mean angular noise density was measured to be 122 μrad/$\sqrt{\mathrm{Hz}}$, substantially higher than the angular noise density measured using six PEs. Fig. 5.5c further illustrates this dependence. As the number of PEs included in the vector measurement increases, the angular noise density decreases, indicating that the additional vector information provided by the larger PE set outweighs the increase in total measurement time.

The measured performance is comparable to that of other single-axis vector magnetometers demonstrated at geomagnetic field strengths [71, 83, 87], accounting for the smaller atomic volume in our system. At the same time, lower noise floors have been reported in architectures that employ multiple sensing axes [73] or active compensation to operate the atoms in an effective zero-field environment [69]. In our case, the dominant contribution to the noise appears to arise from shot-to-shot residual amplitude variations in the applied RF fields. These variations can be attributed to short-term thermal drifts as well amplitude fluctuations in the function generator and in the RF switches used in the RF delivery system. A calculation of the fundamental photon shot noise limit gives an angular noise density of 0.4 $\mu\text{rad}/\sqrt{\text{Hz}}$ for our 18 mm^3 vapor cell. This value is substantially below the measured noise floor, indicating that the performance is limited by technical noise sources, rather than by fundamental optical or spin noise.

Single-optical-axis magnetometers are often susceptible to deadzones, for particular orientations of the magnetic field relative to this axis. This can be understood from the symmetry of the measurement, where the optical axis may define the only preferred direction, and the signal becomes weak when the magnetic field is oriented such that the spin dynamics have minimal projection onto this axis. The use of RF-driven PEs mitigates this limitation by introducing additional effective axes through controlled superpositions of RF fields, which produce Rabi dynamics with different angular dependencies and produce sensitivity to field directions that otherwise correspond to a weak signal. We evaluate the angular dependence of the measured noise density by binning S_θ into bins of polar angle, β with a width of approximately 12°. For each bin, we calculate the angular noise density as shown in Fig. 5.5d. The error bars represent 1σ variation of noise density within each bin. Across the range of polar angles, S_θ shows only a modest dependence on β, with the mean values remaining between 19-27 μrad/$\sqrt{\text{Hz}}$. In particular, no divergence in the noise is observed for any field orientation, indicating deadzone-free vector operation. This result once again reflects the advantage of combining measurements from six calibrated PEs. The different PEs provide complementary angular sensitivities, and therefore avoid the loss of sensitivity that would otherwise be expected in a single-optical-axis system. A natural extension of this approach would be to employ a larger set of calibrated PEs with a wider range of relative phases among the three coil pairs in order to further suppress angular variation in the noise density and improve precision.

5.4 Systematic Effects and Technical Limitations

The performance of the vector magnetometer is ultimately limited by a combination of technical imperfections in the experimental implementation and by systematic deviations that are not fully captured by the idealized theoretical model. The Floquet-based time-independent model of the Rabi dynamics used to interpret the measurements neglects several effects, including deviations arising from imperfect pumping and distortions of the Rabi response. In addition, slow drifts in the RF system and imperfections in the applied fields introduce further errors that accumulate over the course of the measurement. In this section, we examine these contributions using both numerical simulations and experimental measurements, and assess their impact on the inferred field direction.

Table 5.3: Angular accuracy budget

Source of error	Estimated contribution
Residual modeling systematics (Sec. 5.4.1)	$\sim 30\,\mu$rad
Technical drifts (Sec. 5.4.2)	$\sim 30\,\mu$rad
Scalar calibration of DC coil system (Sec. 4.3.1.2)	$\sim 20\,\mu$rad

Table 5.3 summarizes the estimated contributions to the overall angular accuracy of the magnetometer. The values listed here should be considered to be order-of-magnitude

estimates, as they are inferred from a combination of theoretical modeling and measurements. However they still provide a useful picture of the dominant sources of error.

5.4.1 Residual Modeling Systematics

To estimate the contribution of residual systematics, we compare the time-independent model used for calibration and inferring direction with numerical simulations based on the full atomic dynamics. The simulated Faraday rotation signals are obtained by numerically solving the full time-dependent Hamiltonian, $H(t)$ given in Eq. (3.1). Relaxation processes are incorporated through the Lindblad master equation in Eq. (2.17), which includes the effects of spin-exchange collisions, wall collisions, and spin-destruction collisions. In this simulation, RF Stark shifts and systematics associated with the nonlinear Zeeman effect are naturally included in the simulated Faraday rotation. This direct simulation of the Rabi dynamics is computationally feasible because the applied RF field lies at a relatively low frequency. As a result, the time evolution can be resolved with a manageable numerical time-step over the 1.9 ms long Faraday rotation signal. On the other hand, an analogous simulation for microwave-driven hyperfine transitions would be far more demanding, since a 6.8 GHz driving frequency would require much finer time-step to resolve the dynamics. Simulating a Faraday rotation signal for a hyperfine Rabi oscillation over millisecond timescales would therefore become computationally prohibitive. Rabi frequencies are then extracted from the simulated signals using the same analysis procedure applied to the experimental data, as described in Sec. 4.4. This ensures that the comparison accounts for not only the Hamiltonian model itself, but also any bias introduced by the frequency extraction procedure.

The residual systematics are quantified by comparing the Rabi frequencies extracted from the numerical simulations with those predicted by the time-independent model. In this way, the comparison isolates discrepanices associated with the limitations of the time-independent description. It does not include additional technical contributions that are present in the experiment such as RF drifts or other time-dependent sources of error. Fig. 5.6

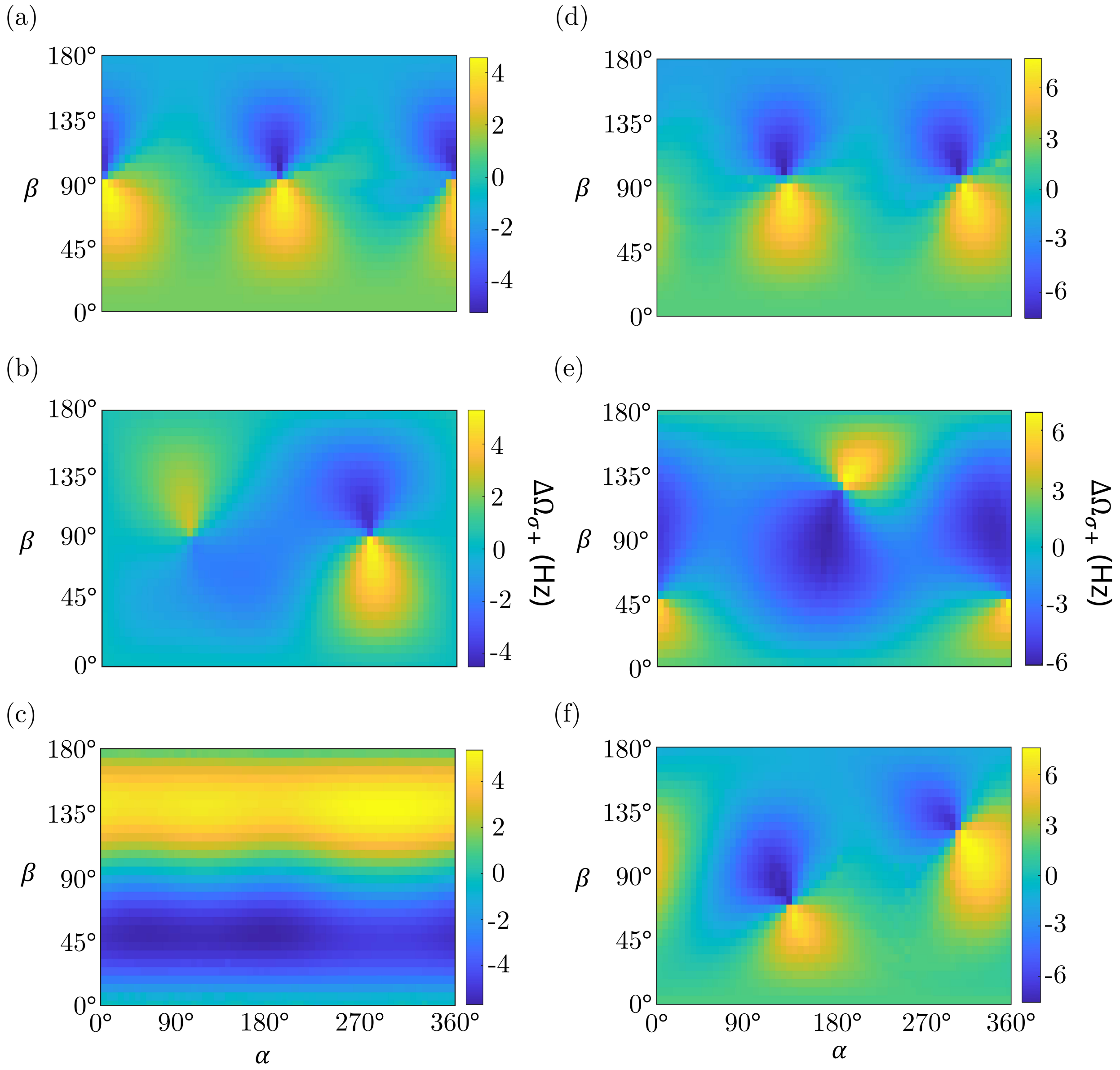

Figure 5.6: $\Delta\Omega_{\sigma+}$ denotes the difference between Rabi frequencies obtained from the numerical simulation of the time-dependent Hamiltonian, $H(t)$ with the Lindblad master equation, incorporating various decoherence mechanisms, and those predicted by our time-independent model for (a) PE1, (b) PE2, (c) PE3, (d) PE4, (e) PE5, and (f) PE6

shows the resulting frequency difference $\Delta\Omega_{\sigma+}$ over the full solid angle. These results show that these systematics depend sensitively on field direction as well as the PE itself. To determine the effect of these systematics on the inferred field direction, we propagate them into an error using

$$\delta\theta \approx \sqrt{(\sin(\beta)\delta\alpha)^2 + (\delta\beta)^2}$$

where $\delta\alpha = \sum_i \Delta\Omega/(\partial\Omega/\partial\alpha)$ and $\delta\beta = \sum_i \Delta\Omega/(\partial\Omega/\partial\beta)$, and i denotes the PE index. When averaged over the full solid angle, these residual systematics are found to contribute approximately $\langle\delta\theta\rangle \sim 30\,\mu\text{rad}$ to the mean vector accuracy.

One contribution to this discrepancy arises from imperfect optical pumping, which leaves a small residual population in the $F = 1$ hyperfine manifold. This population can couple to the σ^- component of the PE and drive Rabi oscillations between adjacent Zeeman sublevels in the $F = 1$ manifold at the frequency $\Omega_{\sigma-}$. These oscillations are not accounted for in the Rabi frequency extraction procedure, which assumes that the measured signal only contains the σ^+-driven Rabi oscillations. Therefore this additional signal can lead to a systematic offset in the fitted Rabi frequency. Its effect is reduced, however, because the Faraday rotation signal associated with the $F = 1$ manifold is half that from $F = 2$, reflecting the smaller spin projection $\langle F = 1\rangle_Z$. Another source of error arises from the

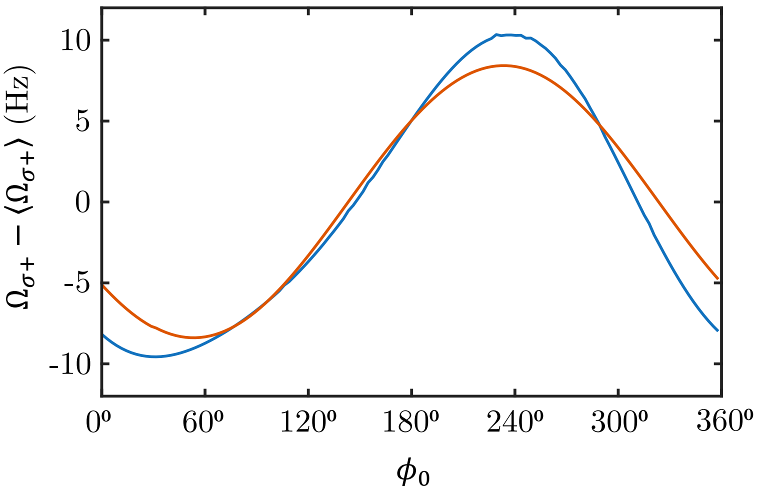

Figure 5.7: Dynamic heading error systematics beyond the time-independent model. $\Omega_{\sigma+} - \langle\Omega_{\sigma+}\rangle$ as a function of RF phase, ϕ_0 for the PE, $\{\boldsymbol{\mathcal{B}}_0, \phi\} = \{(11\ \mu\text{T}, 45^\circ + \phi_0)_x, (5\ \mu\text{T}, 180^\circ + \phi_0)_y, (7\ \mu\text{T}, \phi_0)_z\}$. The numerical simulation (blue) shows a distorted phase response relative to the prediction of Eq. 3.30 (orange).

distortion of the Rabi lineshape by the dynamic heading error effects. Within the $F = 2$ manifold, the Rabi oscillations consist of four frequency components, $\Omega_{\sigma+,m}$ with $m \in \{2, 1, 0, -1\}$ (Eq. (3.27)). These components contribute overlapping Lorentzian features whose amplitudes are determined by A_m. The measured Rabi signal therefore reflects the superposition of several nearby contributions rather than a single idealized oscillation. This multicomponent signal can distort the effective lineshape and shift the fitted Rabi frequency away from the simple amplitude-weighted average predicted by the model in Eq. (3.30), as illustrated in Fig. 5.7. This effect becomes more pronounced as the decoherence rate increases, because the individual Lorentzians broaden and overlap more strongly.

Spin-exchange collisions represent another source of residual error not captured in the time-independent model. Apart from being a source of relaxation, spin-exchange can also induce shifts in the Zeeman energies through short-range interactions between atoms in different spin states. These shifts modify the effective transition frequencies and therefore perturb the Rabi frequencies in a manner that depends on both the instantaneous spin polarization and population distribution across the Zeeman sublevels. Because these can vary with the PE and magnetic field direction, the resulting shifts, on the order of 100s of pT [56], can introduce orientation-dependent shifts in the extracted Rabi frequency.

5.4.2 Systematics from Technical Drifts

The performance of the vector magnetometer depends substantially on the stability of the PEs driving the Rabi oscillations. Therefore slow drifts in the RF system present an important limitation in the magnetometer. The PEs are generated from superpositions of RF fields applied along multiple coil axes, with well-defined amplitudes and phases. Over time, these parameters drift, leading to systematics in the calibration of the PEs. Because the field direction is obtained by comparing Rabi frequencies using the calibrated PE parameters, this introduces systematic errors in the reconstructed direction as well.

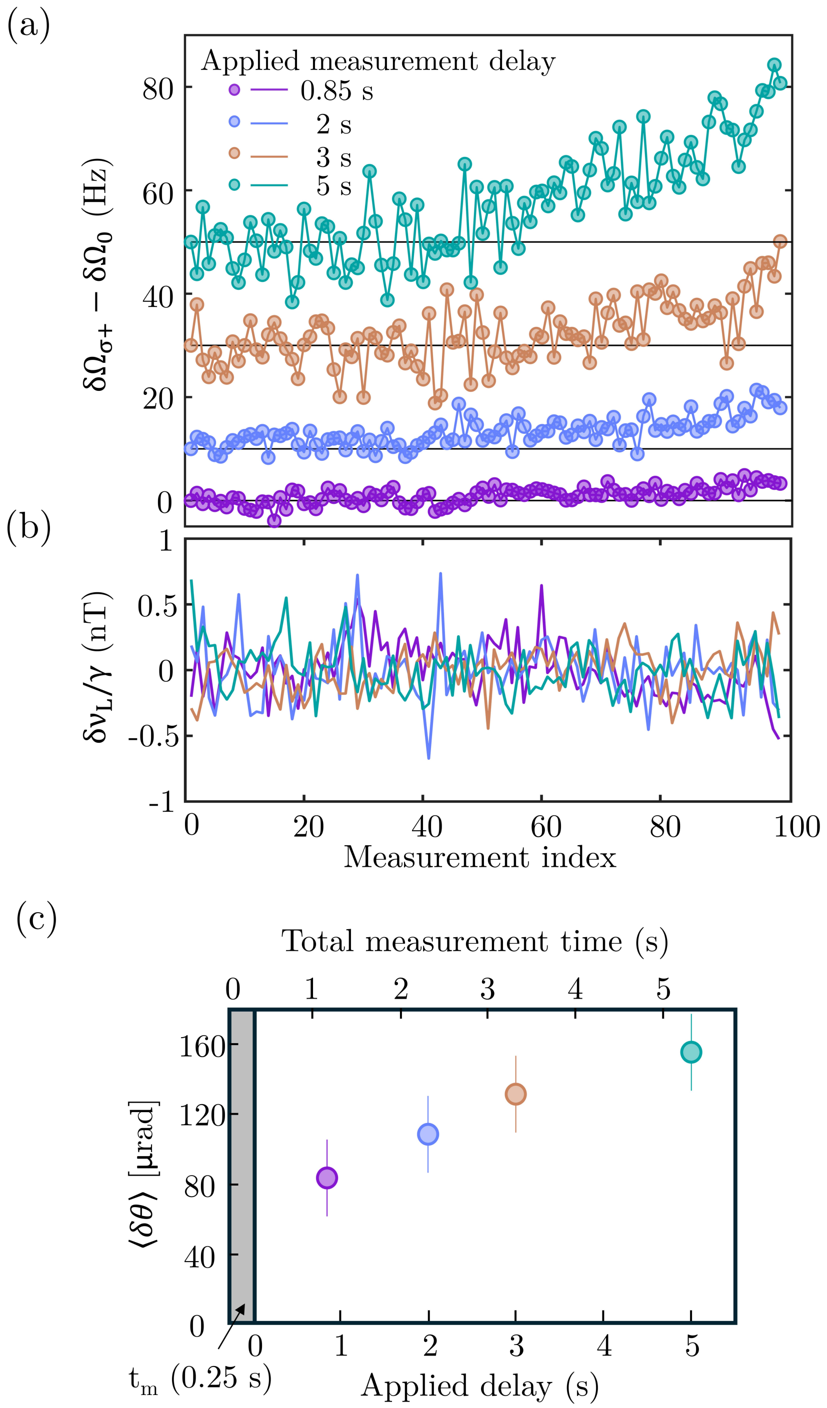

Figure 5.8: Effect of measurement delay on Rabi frequency drift and vector performance. (a) Rabi frequency drift for PE6, $\delta\Omega_{\sigma+}[n] = \Omega_{\sigma+}[n] - \Omega_{\sigma+}[1]$ for several applied delays. For clarity, the Rabi frequency time series are vertically offset by an arbitrary reference $\delta\Omega_0$, indicated by horizontal black lines. (b) Corresponding Larmor frequency drift, $\delta\nu_L[n]/\gamma = (\nu_L[n] - \nu_L[1])/\gamma$. The average Rabi frequency, $\langle\Omega_{\sigma+}\rangle$ is 56.089 kHz across the 100 repeated measurements. (c) Average angular accuracy, $\langle\delta\theta\rangle$ measured for over 340 applied field directions versus applied delay.

As we mentioned earlier, in the measurement sequence, a delay of 0.85 s is inserted before the start of each atomic measurement. The delay ensures that the atoms are interrogated only after the DC currents, and hence the field, has reached steady state. This delay is essential, as any residual transient in the DC field would lead directly to an error in the extracted Rabi and Larmor frequencies. The delay thus improves the reproducibility of the programmed field direction, but it also increases the total time required to complete a calibration sequence, $\mathbf{C}_t$, thus allowing drifts to accumulate. As discussed in Sec. 4.3.2.3, the dominant drifts in the RF system arise from gradual thermal changes in the RF coils and in the associated electronics. The RF system involves a larger number of thermally sensitive components compared to the DC current system, including RF switches and voltage reference for each coil axis provided by a function generator.

To investigate how these drifts influence vector performance, we vary the applied delay and measure the Rabi frequency as a function of time. Delays of 0.85 s, 2 s, 3 s, and 5 s are applied, and the Rabi frequency is measured repeatedly for PE6 at the fixed magnetic field $(\alpha, \beta) = (45°, 45°)$, as shown in Fig. 5.8a. The interval between successive measurements is given by the measurement time, t_m of 250 ms in addition to the applied delay. PE6 was chosen for this test because it consists of a superposition of RF fields along three coil axes, and is therefore sensitive to drift in the amplitudes and phases of all three RF channels. In this way, PE6 serves as a probe of the overall stability of the RF system. In Fig. 5.8a, the cumulative drift in the Rabi frequency is observed to increase monotonically with the applied delay, although the dependence is not strictly linear. This is also accompanied by a rise in the shot-to-shot variation of the measured Rabi frequency at longer applied delays. A comparison with the corresponding Larmor frequency measurements shows that the dominant drift originates in the RF system rather than in the DC magnetic field. As shown in Fig. 5.8b, the measured Larmor frequencies remain comparatively stable, with a variation of 1 nT over the 100 measurements.

To determine the impact of this behaviour on the vector measurements, we also evaluate the angular accuracy for the same 342 random field directions used in the previous section while varying the applied delay, as shown in Fig. 5.8c. The mean accuracy improves as the delay is reduced, which is consistent with the reduction of drifts over shorter sequences. Extrapolating the trend to zero yields an estimated mean angular accuracy of $\sim$ 50 µrad, indicating the scale of contribution of the drifts to the performance.

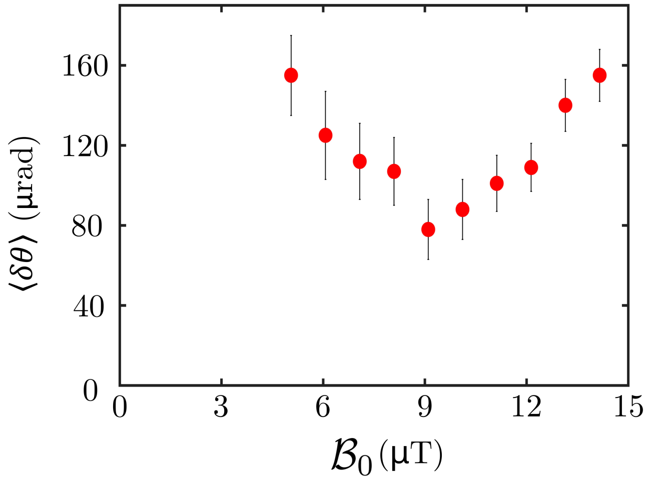

Figure 5.9: Variation of mean angular accuracy with amplitude of the RF field. Because of unequal coil factors, the RF field amplitudes are $\mathcal{B}_0$, $1.25\,\mathcal{B}_0$ and $0.77\,\mathcal{B}_0$ for the X, Y and Z RF coil axes, respectively.

We also explore the angular accuracy dependence on the amplitude of the RF field by measuring accuracy for 100 random DC field directions, as shown in Fig. 5.9. The observed trend in angular accuracy reflects competing effects at small and large RF amplitudes. The accuracy gets worse at larger RF amplitudes, which is consistent with higher thermal loading of the RF coil and the associated electronics, increasing drifts in the applied PEs over the course of the calibration sequence. Additionally, the waveform from the RF controller gets increasingly distorted as the controller nears its compliance voltage while driving the inductive coils. At lower RF amplitudes, the accuracy degrades for a different reason. In this regime, smaller Rabi frequencies reduce the size of the angular gradient, thus increasing the effects of the residual systematic shifts and uncertainty in the frequency obtained from the fits to the Faraday rotation signal. The amplitude dependence of the accuracy is therefore a result of a tradeoff between the increased drifts at large RF amplitudes, and smaller angular gradients with greater fractional errors at small RF amplitudes.

In this chapter, we have developed a picture of how Zeeman Rabi oscillations can be used to extract magnetic field direction in a single-axis geometry. In this picture, the Rabi frequencies measured from a series of resonant PEs carry information about the magnetic field vector, and a calibrated model translates these frequencies to obtain the field direction. The results show that this approach is effective over the full angular range and is capable of accurate and sensitive vector measurements. The present implementation is primarily limited by the calibration time and slow drifts in the RF system, as well as residual systematics from $\Omega_{\sigma-}$ contributions from $F = 1$. These limitations also point to natural directions for improvement. Faster calibration with a higher bandwidth current controller and active temperature control of the RF electronics would reduce the drift accumulated during the calibration sequence. Additionally, a more complete treatment of σ^--driven dynamics in our time-independent model would further reduce the residual errors. One approach is to directly measure σ^- and incorporate it in this model together with $\Omega_{\sigma+}$. In the next chapter, we explore measurements in this direction by using microwave population transfer to transfer atoms to $F = 1$ and measure $\Omega_{\sigma-}$ directly.

Chapter 6

Microwave Delivery and Control Using Alumina Resonator

In this chapter, we extend the capabilities of the platform to include microwave-driven interactions enabled by the alumina resonator. In the previous chapters, vector magnetometry was performed using RF-driven Zeeman Rabi oscillations, where the measurement relied on the angular dependence of the Zeeman Rabi frequency. Here we add microwave control as a tool for driving the atomic system. This approach allows access to hyperfine transitions, providing complementary information about the magnetic field. We describe the implementation of the alumina resonator and the coupling of microwave fields into the vapor cell. These capabilities are then used to drive hyperfine Rabi transitions as well as perform basic RF-based $\Omega_{\sigma-}$ measurements in the same platform. This chapter illustrates the flexibility of the platform and motivates the integration of microwave and RF techniques for improving magnetometer performance.

6.1 Alumina Resonator Context

Metallic microwave cavities have been widely used for delivering resonant microwave fields for exciting hyperfine transitions in atoms [99, 152]. For microwave-driven Rabi vector magnetometry experiments [87], a copper cavity of size $76 \times 76 \times 40\,\mathrm{mm}^3$ (Fig. 6.1a) was used to generate the resonant 6.8 GHz microwave PEs required for driving Rabi oscillations across the hyperfine manifolds of ^{87}Rb. Copper is chosen due to its high electrical conductivity, enabling confinement of microwave fields and high quality factors, allowing strong coupling of the resonant fields to the atoms. However, using conductive materials introduces several limitations in the context of vector magnetometry. Changes in the applied magnetic field direction induce eddy currents in the cavity walls, leading to slow magnetic transients. The presence of these transients constrains the speed at which the magnetic fields are changed and successive measurements can be taken, as the system must reach a steady state before Rabi frequencies can be measured.

These effects impact the performance of microwave-driven Rabi vector magnetometry. Similar to Zeeman Rabi techniques, this method also relies on the calibration of microwave PEs by applying magnetic fields in various known directions and measuring the resulting Rabi frequencies. The presence of eddy current transients increases the calibration duration, as measurements over many magnetic field orientations require long settling times. Furthermore, eddy currents in conducting structures also contribute to the magnetic field noise through thermal fluctuations. These currents arise from Johnson noise currents in the conductor and produce field noise at the atoms that decay inversely with the distance from the conductor [153]. Proximity of the copper in the cavity to the microfabricated cell contributes to the noise [154], and further motivates coupling microwave fields to the atoms using non-conductive materials. At the same time, thermal drifts in the cavity modify both the amplitude and phase of the microwave field, leading to slow drifts in the microwave PE. Obtaining the magnetic field direction relies on an accurate and stable calibration of the PE, and therefore such drifts introduce systematic errors in the inferred direction.

To address these challenges, dielectric resonators are a promising alternative. These resonators have been used in spin resonance experiments to generate resonant microwave fields and to probe interactions between spins and cavity electromagnetic modes [155]. They have also been employed in NV center experiments for controlling spin qubits, demonstrating their ability to support stable microwave fields [156].

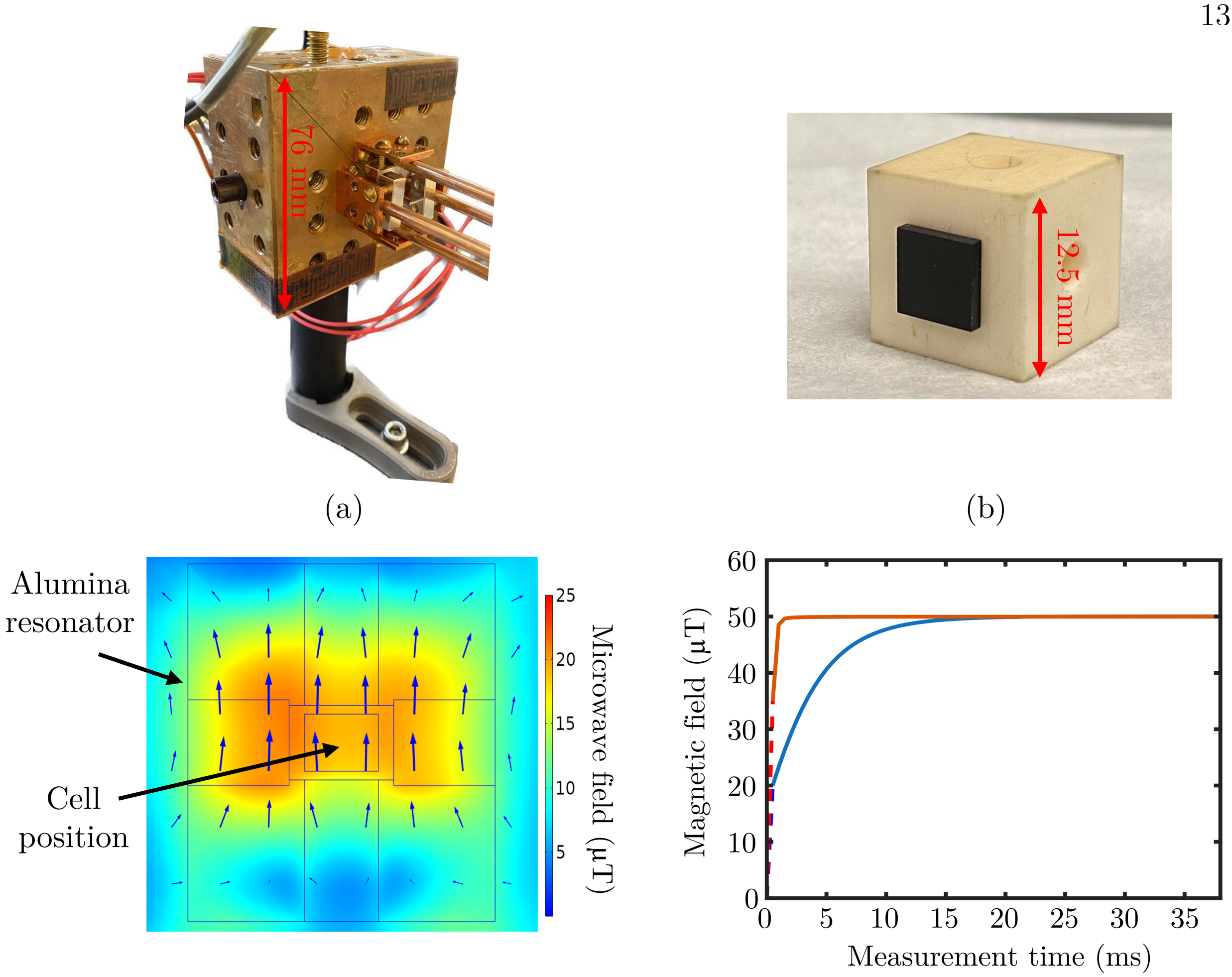

(a) (b)

(c) (d)

Figure 6.1: Compact alumina resonator for microwave delivery. (a) Copper cavity ($76 \times 76 \times 40$ mm^3) used for driving ^{87}Rb hyperfine Rabi oscillations. (b) Alumina resonator ($12.5 \times 12.5 \times 12.5$ mm^3) tuned to the hyperfine splitting frequency. Bonded dichroic filters on the faces enable optical heating of the vapor cell to 100°C (Sec. 4.2). (c) COMSOL simulation of the resonant microwave mode and field distribution at the vapor cell. (d) Larmor frequency measurements of the magnetic field after a DC field step from 0 μT to 50 μT. Here the vapor cell is placed inside the alumina resonator (orange) and the copper cavity (blue). Eddy currents in the copper cavity slow the rise of the magnetic field to the final value, leading to a dead time before Rabi measurements.

In dielectric resonators, electromagnetic fields are confined within non-conductive materials with high relative permittivity. The contrast between the dielectric constant of the resonator material and the surrounding medium leads to confinement of the microwave field within the dielectric. In metallic cavities, boundary conditions imposed by the conductive walls result in vanishing tangential electric fields, leading to confinement through reflection at the cavity surface. Dielectric resonators, on the other hand, rely on partial reflection and refraction at the interface between different materials, resulting in resonant modes that are concentrated within the dielectric but extend evanescently into the surrounding medium, which in our case is air. As the dielectric constant increases, the wavelength of the field inside the material decreases, resulting in a smaller resonant mode size. Thus larger dielectric constants allow a given microwave frequency to be resonant in a smaller physical volume.

In this work, alumina is chosen as the dielectric material for the resonator due to its relatively high dielectric constant value of 9.8, which enables strong confinement and compact resonator dimensions (Fig. 6.1b). It also possesses a low dielectric loss tangent, allowing microwave fields to persist with little dissipation. Additionally, alumina is thermally conductive, which helps maintain a stable uniform temperature distribution within the resonator (Sec. 4.2). Furthermore, as Fig. 6.1 shows, the absence of any electrical conductivity eliminates eddy currents and therefore suppresses the transient current effects described above.

6.2 Excitation of Resonator Modes with Loop antennas

Microwaves are coupled into the alumina resonator through multiple loop antennas. Here, a small conducting loop is placed close to the resonator and excites the resonant mode through inductive coupling. The coupling strength is determined by the overlap between the magnetic field from the loop and the spatial distribution of the field in the resonator mode. The loop antenna itself supports a resonance when its circumference is comparable to the microwave wavelength. To first-order, the resonance condition can be written as

$$2\pi r \approx \lambda$$

where r is the loop radius and λ is the free space wavelength. This condition determines the frequency at which the loop couples to the resonator most efficiently. This method of

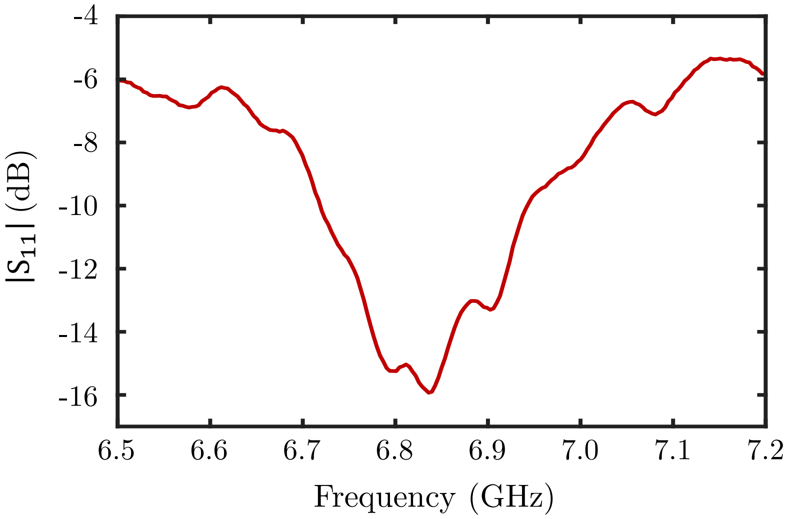

Figure 6.2: Measured magnitude of the reflection coefficient, $|S_{11}|$ for the Alumina resonator coupled to a loop antenna, showing the resonant dip associated with the coupled mode. Measurements were performed with an Agilent E8358A vector network analyzer.

coupling preferentially excites modes with the dominant magnetic field component aligned with the loop orientation. Fig. 6.2 shows the measured S_{11} response of the loop antenna-alumina resonator system. The resonance is centered near $\sim$ 6.83 GHz with a Q $\sim$ 50. The relatively low Q is similar to that of the copper microwave cavity. This ensures that the frequency dependence of the resonator remains small over the $\sigma^{\pm}$, π transitions and they see nearly the same microwave PE, even though the transitions differ by $\sim$ 2 MHz in frequency.

By driving multiple loop antennas simultaneously, we can excite multiple modes within the alumina resonator. Fig. 6.3a shows the three loop antennas arranged along the three axes, with each antenna coupling to a different mode. The vapor cell is located at the center of the dielectric resonator, where microwave fields from the different modes overlap. Each mode results in a microwave field with a distinct field distribution and phase at the atoms. By varying the relative amplitudes and phases of the microwave signals applied to the three loop antennas, we can realize different superpositions of the resonator modes. Therefore, we can generate arbitrary microwave PEs, each with its own distinct angular dependence of the Rabi frequency. Unlike the copper microwave cavity, where microwave PEs were confined to a plane defined by the cavity dimensions, the alumina resonator allows 3D control of the microwave PE.

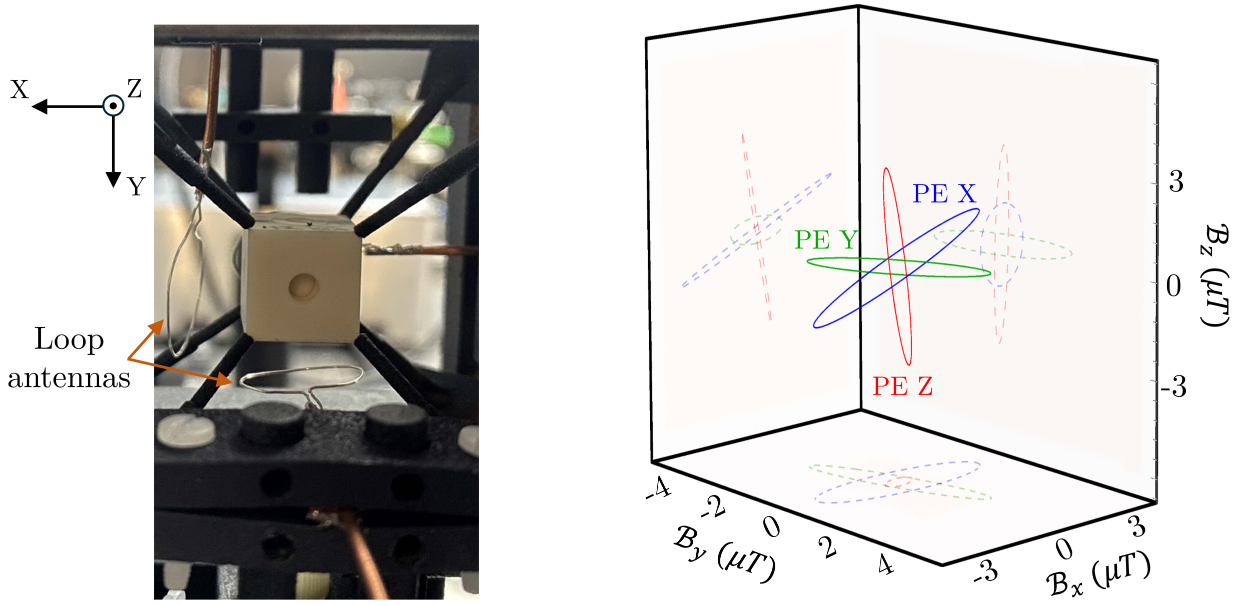

(a) (b)

Figure 6.3: (a) Photograph of the three loop antennas arranged to excite 3 independent resonator modes in the alumina resonator. (b) The microwave PEs excited by loop antennas along X, Y, and Z axes in the laboratory frame.

6.3 Driving Hyperfine Rabi Oscillations

Now that we have established microwave control with the alumina resonator, we drive ground state hyperfine Rabi oscillations in the ^{87}Rb microfabricated vapor cell. Fig. 6.5a shows the measured Rabi frequencies as a function of the magnetic field direction (α, β) for σ^+-driven transitions between $|2,2\rangle$ and $|1,1\rangle$. For these measurements, the microwave frequency is tuned near the σ^+ resonance frequency at 6.83592 GHz. The angular dependence of $\Omega^{\mu w}_{\sigma+}$ reflects the variation of the σ^+ component of the microwave PE and demonstrates that the resonator can drive coherent hyperfine Rabi oscillations over a wide range of field directions. This angular dependence forms the basis for extracting the magnetic field direction from Rabi measurements [87]. Furthermore, as previously demonstrated with the copper

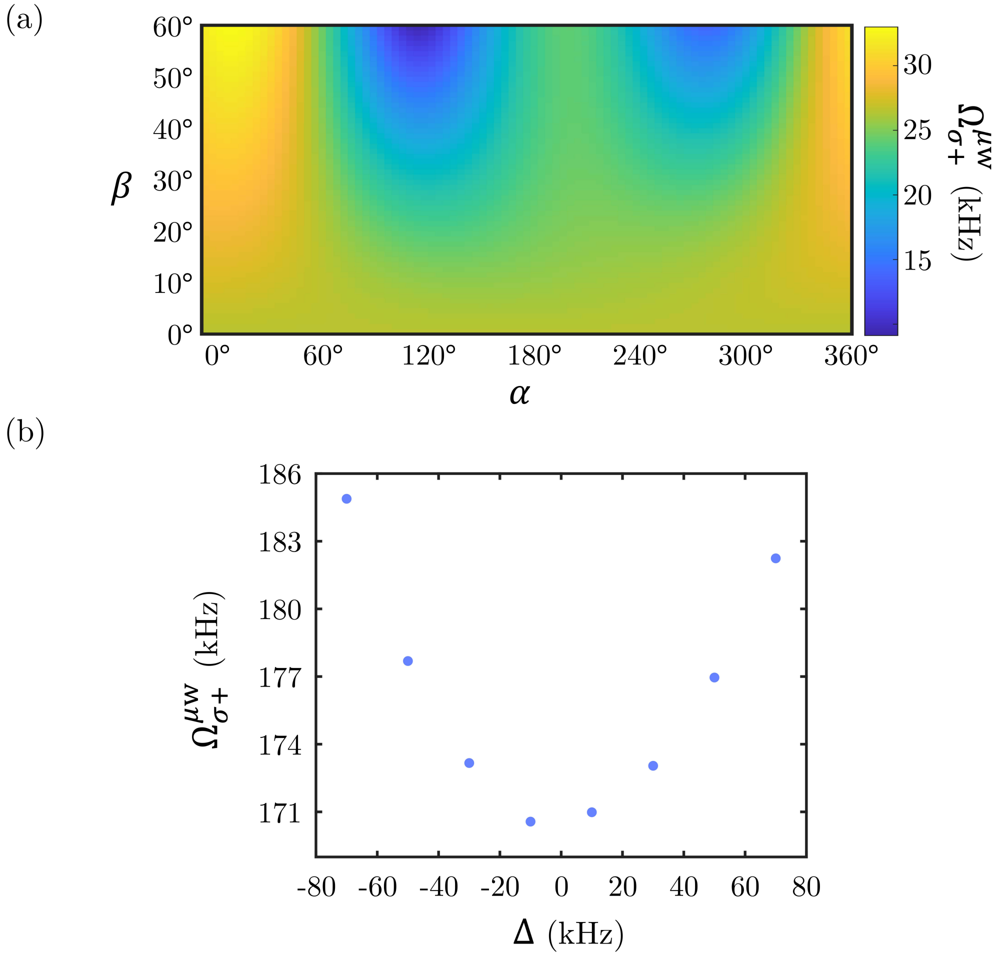

Figure 6.4: Hyperfine Rabi oscillations excited with alumina resonator. (a) Angular dependence of hyperfine Rabi frequency, $\Omega_{\sigma+}^{\mu w}$ measured for microwave PE Y over the magnetic field direction, (α, β). (b) Rabi frequency measured as a function of detuning, Δ from $|2,2\rangle \leftrightarrow |1,1\rangle$ hyperfine resonance.

cavity setup [56], the frequency dependence of $\Omega_{\sigma+}^{\mu w}$ can be used to determine the magnetic field strength. Fig. 6.4b shows this frequency dependence, which allows a heading-error-free scalar measurement as the microwaves are addressing a pair of individual Zeeman sublevels. At the same time, the hyperfine Rabi measurements also revealed an important drawback of the alumina resonator. Fig. 6.5b compares two Faraday rotation signals measured with the alumina resonator and with the copper cavity with similar microwave amplitudes and Rabi frequencies. The signal obtained with the resonator shows a substantially smaller T_2 compared to the corresponding signal with the copper cavity. This is in large part a result of

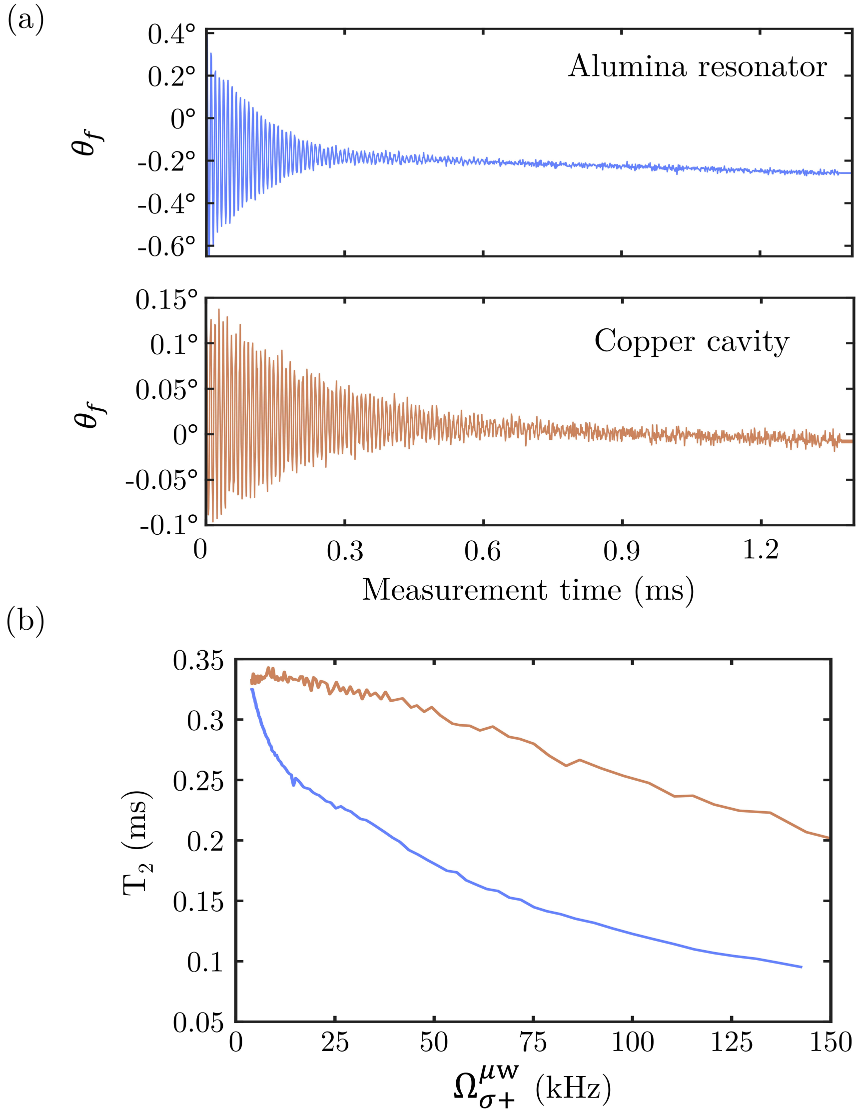

Figure 6.5: (a) Faraday rotation signals of hyperfine Rabi oscillations with the same $\Omega_{\sigma+}^{\mu w}$ for the alumina resonator (blue) and copper cavity (brown), showing distinct coherence times. (b) T_2 extracted from hyperfine Rabi oscillations as a function of Rabi frequency for the copper cavity (brown) and the alumina resonator (blue). The difference in T_2 becomes larger with increasing microwave amplitude, consistent with stronger microwave inhomogeneity.

the larger microwave inhomogeneity from the small size of the resonator. As the resonator mode is confined to a smaller volume, the spatial variation of the microwave field over the cell becomes larger. This results in a distribution of local Rabi frequencies, reducing the coherence time of the averaged Rabi oscillation signal. This difference in resonator and cavity

T_2 becomes larger at higher Rabi frequencies, as shown in Fig. 6.5b.

6.4 σ^- Zeeman Rabi Measurements via Microwave Population Transfer

In Chapter 5, vector magnetometry was implemented using only $\Omega_{\sigma+}$ Zeeman Rabi measurements. This was primarily because the synchronous optical pumping procedure drives atoms towards the stretched state $|2,2\rangle$, so that a substantial fraction of the population resides in the $F = 2$ manifold. Because the population remaining in the $F = 1$ manifold is small, the corresponding $\Omega_{\sigma-}$ measurements have a substantially lower signal-to-noise ratio.

Nevertheless, measuring $\Omega_{\sigma-}$ would offer several important advantages. It would provide additional independent angular information on the magnetic field direction. As we described in Chapter 5, combining Zeeman Rabi measurements from PEs with complementary angular dependencies improves the performance of the vector magnetometer, as this reduces the impact of regions in which a given PE has poor angular gradients. Incorporating $\Omega_{\sigma-}$ measurements would extend this approach by adding another set of constraints on the inferred magnetic field direction. This additional information can be obtained without increasing the total measurement time, as both $\Omega_{\sigma\pm}$ can be extracted simultaneously from the Faraday rotation signal. This also increases the redundancy in the Rabi information extracted from the PEs. Furthermore, as we discussed in Sec. 5.4.1, part of the residual systematics in $\Omega_{\sigma+}$ Rabi measurements arise from unintended σ^- contributions due to the small residual population in the $F = 1$ manifold. By measuring both $\Omega_{\sigma\pm}$ explicitly, these contributions can be accounted for and separated, thus reducing the corresponding systematic errors.

In the previous sections of this chapter, we discussed additional microwave capabilities enabled by the alumina resonator. These capabilities can now be used to perform measurements of $\Omega_{\sigma-}$. As noted earlier, a sufficient signal-to-noise ratio for the σ^- transition requires a spin-polarized population in the $F = 1$ manifold. This is achieved by first optically pumping the atoms into the $|2,2\rangle$ as usual. Population is then transferred to the $|1,1\rangle$ state

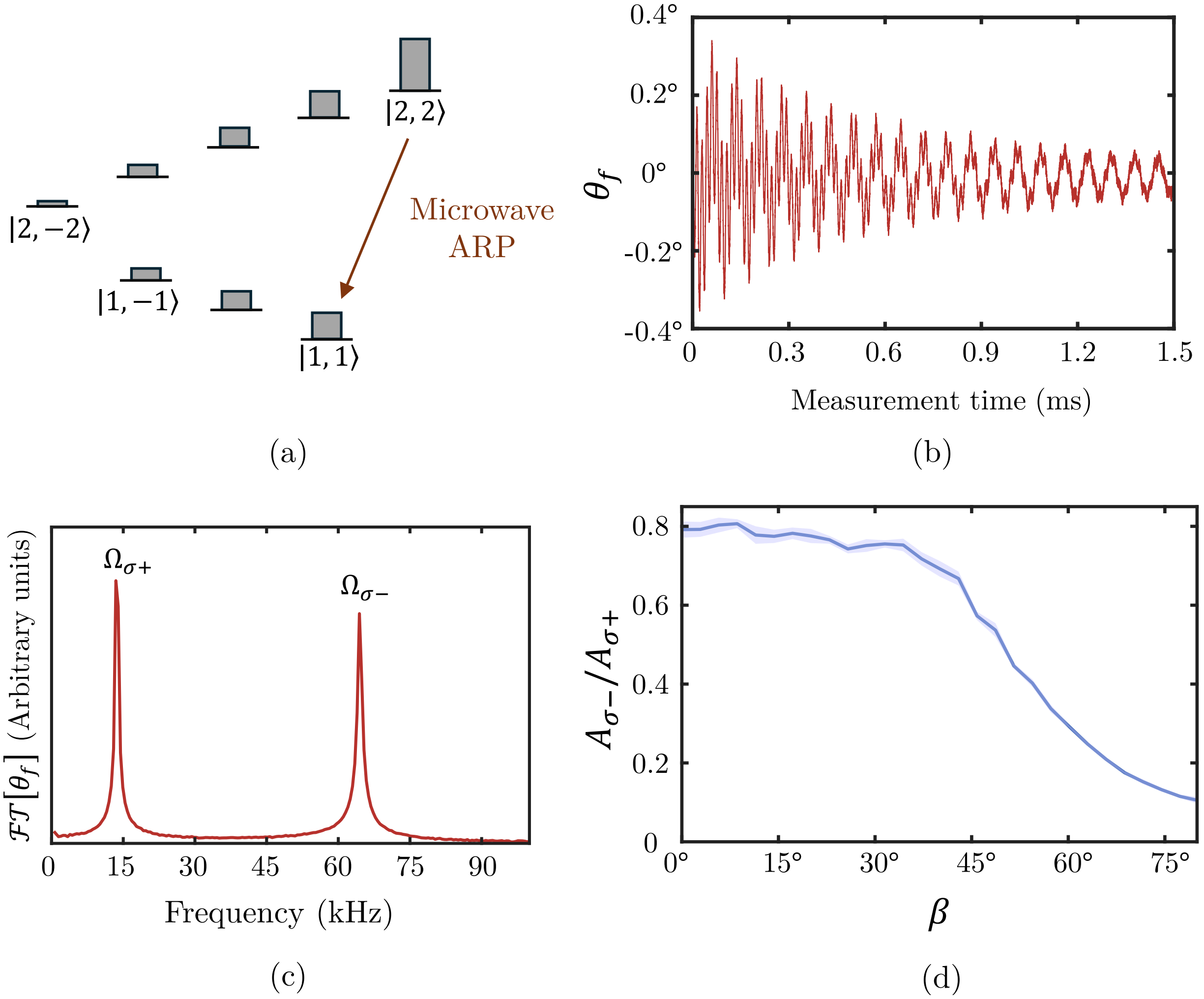

(a) (b)

(c) (d)

Figure 6.6: Measurement of σ^--driven Zeeman Rabi oscillations. (a) Level schematic illustrating microwave Adiabatic Rapid Passage (ARP) across the hyperfine transition $|2,2\rangle \leftrightarrow |1,1\rangle$ to transfer population from the $F = 2$ manifold to the $F = 1$ manifold. (b) Faraday rotation signal and (c) the corresponding Fourier transform of RF-driven Zeeman Rabi oscillations after a microwave ARP. (d) Amplitude ratio of $\Omega_{\sigma-}$ and $\Omega_{\sigma+}$ Rabi oscillations as a function of the polar angle, β. As the hyperfine Rabi frequency drops, the adiabatic condition becomes harder to satisfy, reducing ARP efficiency.

using a microwave adiabatic rapid passage pulse applied across the $|2,2\rangle \leftrightarrow |1,1\rangle$ transition, as shown in Fig. 6.6a. In this sequence, the atoms are pumped for 50 μs, after which a 50 μs microwave chirp pulse is applied. The chirp signal sweeps 400 kHz across the resonance frequency and prepares spin polarization in $F = 1$ for $\Omega_{\sigma-}$ measurements.

Fig. 6.6b shows the Faraday rotation signal measured after the microwave chirp, and

Fig. 6.6c shows the corresponding Fourier transform. Two distinct peaks are visible in the Fourier spectrum, corresponding to $\Omega_{\sigma+}$ and $\Omega_{\sigma-}$. Despite the smaller population in $F = 2$, their contribution to the Faraday rotation signal is nearly twice that of the $F = 1$ manifold because of their larger total angular momentum. This residual $F = 2$ population is useful because it enables both Rabi frequencies to be measured within the same measurement. This allows $\Omega_{\sigma+}$ and $\Omega_{\sigma-}$ to be resolved and fit from a single Faraday rotation signal, thus reducing residual systematics from unintentional $\Omega_{\sigma-}$ contributions. We can also see that the peak associated with $\Omega_{\sigma-}$ is broader than that corresponding to $\Omega_{\sigma+}$. The broader linewidth is consistent with the stronger influence of spin-exchange decoherence in the $F = 1$ manifold [106].

This ARP procedure does not universally work for all magnetic field directions, however. Adiabatic transfer requires the detuning sweep rate, $\dot{\Delta}$ to remain small, satisfying

$$\dot{\Delta} \ll (\Omega^{\mu w}_{\sigma+})^2$$

where $\Omega^{\mu w}_{\sigma+}$ denotes the microwave Rabi frequency for the hyperfine transition, $|2,2\rangle \leftrightarrow |1,1\rangle$. Because this microwave Rabi frequency varies with direction, this requirement is not satisfied uniformly as the same set of ARP parameters is used for every measurement. In regions where the microwave Rabi frequency is reduced, the sweep becomes too fast, and the adiabatic condition is no longer satisfied. In practice, it is observed that the efficiency of the microwave ARP falls off as $\beta \to 90^\circ$, as shown in Fig. 6.6d, and reflects the failure of the adiabatic condition in these regions.

In this chapter, we explored how the addition of microwave control with the combination of the alumina resonator and the loop antennas extended the capabilities of the setup beyond RF-driven Zeeman Rabi measurements. By exciting additional transitions and exploiting their distinct angular and frequency dependencies, we can extract heading-error-free scalar and vector information from the same atomic ensemble. The performance of these measurements is limited in the current implementation by spatial inhomogeneities of the microwave field and sensitivity to the direction-dependent microwave Rabi frequencies for ARP protocols. The techniques discussed in this chapter therefore provide a foundation for future implementations that combine microwave and RF approaches in a single compact sensor.

Chapter 7

Conclusion

Accurate measurement of the magnetic field direction remains an important challenge for quantum sensing. OPMs are intrinsically scalar magnetic field sensors, as they fundamentally measure the Zeeman splitting that depends on the magnetic field strength. As a result, measuring vector information requires coupling the atoms to an external vector reference frame that links the measured atomic signals to the magnetic field direction in this frame. The performance of the OPM vector magnetometer hence relies on the mathematical modeling of the measured atomic signals to the magnetic field direction, as well as on the long-term stability of the vector reference.

Towards this goal, over Chapters 2 and 3, we discussed the theoretical framework that describes the atomic interaction with both the DC and RF magnetic fields. Chapter 2 set the foundation for this description, introducing the ground state structure of ^{87}Rb, Larmor precession, optical pumping, relaxation processes, and measurements of spin dynamics through Faraday rotation. Chapter 3 then extended this description to RF-driven Zeeman Rabi oscillations. Here, the measured Rabi oscillations are influenced by several systematic effects, including Bloch-Siegert shifts arising from counter-rotating terms, and dynamic heading error effects associated with the nonlinear Zeeman effect that depend on the phase of the applied RF field with respect to the pump modulations. By accounting for these effects through a Floquet-based description, we establish a model linking the applied RF fields and DC magnetic field to the measured atomic signals with Hz-level accuracy.

The next step was realizing an apparatus for implementing this technique. Chapter 4 described the experimental setup, including the microfabricated ^{87}Rb vapor cell, synchronous optical pumping, and Faraday rotation measurement in a single-axis configuration. We discussed the design of the magnetic field system, which allowed DC magnetic fields to be applied with an angular accuracy of 20 µrad at 50 µT after scalar calibration. The chapter also discussed techniques used to synchronize the six resonant RF PEs generated by the RF coil system with the optical pumping sequence, which was important for modeling RF phase-dependent systematics associated with nonlinear Zeeman effects.

We brought the theoretical and experimental parts together in Chapter 5 to realize vector magnetometry based on RF-driven Zeeman Rabi oscillations. The first step in this measurement is the calibration of the six PEs by measuring Rabi frequencies using a set of known magnetic field directions. The magnetic field direction was obtained by combining Rabi measurements from six calibrated PEs, each offering a distinct angular dependence of the Rabi frequency, while simultaneous Larmor measurements yielded the field magnitude. We evaluated the performance of the vector magnetometer across more than 340 random applied field directions all over the unit sphere, measuring sub-100 µrad angular accuracies at 50 µT fields and noise densities down to 8 µrad/$\sqrt{\text{Hz}}$. Using the complementary angular dependencies of the six PEs, we observed a relatively weak variation of the noise with angles relative to the optical axis, demonstrating deadzone-free vector operation in a single-optical-axis configuration.

Chapter 5 also discussed how the performance of the magnetometer is limited by the same two requirements outlined above, namely the accuracy of the mathematical model relating atomic signals to magnetic field direction and the stability of the vector reference. Residual systematics between the measured Rabi frequencies and the Floquet-based time-independent model led to direction-dependent errors in the inferred direction. We also saw how slow drifts in the RF system degrade the stability of the PEs over the calibration interval and limit the quality of calibration. These technical drifts can be reduced by using a faster current control bandwidth to update the magnetic field direction quicker, thus reducing the calibration duration, $\mathbf{C}_t$.

In Chapter 6, we changed gears and examined additional capabilities of this apparatus offered by the alumina resonator. We described how we could incorporate microwave-driven hyperfine Rabi oscillations in the same setup and realize a heading-error-free, vector-scalar magnetometer. Additionally, we also showed how this system enables measurements of $\Omega_{\sigma-}$ Rabi frequencies, providing additional constraints on the inferred magnetic field direction.

7.1 Prospects for π-driven Rabi oscillations

One limitation of this technique, when compared to microwave-driven hyperfine Rabi vector magnetometry, is the absence of π transitions in the ground state Zeeman structure. In the microwave case, the hyperfine manifold contains independent $\sigma^{\pm}, \pi$ transitions, which completely characterizes the PE in the atomic frame. In contrast, for the ground state Zeeman structure, the PE still decomposes into $\sigma^{\pm}$ and π components with respect to the quantization axis defined by the DC field, but only the $\sigma^{\pm}$ components couple to allowed transitions. This limits the information available from the measurements about the PE, and in turn limits the information from the PE that can be used to infer the field direction.

Incorporating Ω_π measurements would offer several advantages for the Zeeman Rabi approach. In the microwave case, it was shown that Rabi measurements using $\sigma^{\pm}$ and π transitions can be exploited, not only to reconstruct the PE, but also to test the consistency in the inferred direction and to detect PE drift [87]. For instance, Rabi frequencies, $\Omega_{\sigma\pm}$ could be used to infer the direction while the difference between the expected and measured Ω_π at the same magnetic field direction indicate drifts in the setup.

While single-photon Zeeman transitions do not couple to the π component, this component can be measured through two-photon $\sigma^+ - \pi$ Zeeman transitions (Fig. 7.1a). These transitions are resonant near $\nu_L/2 \approx 175$ kHz for 50 μT DC fields. These two-photon Rabi oscillations can also be measured using Faraday rotation measurements of a linearly po-

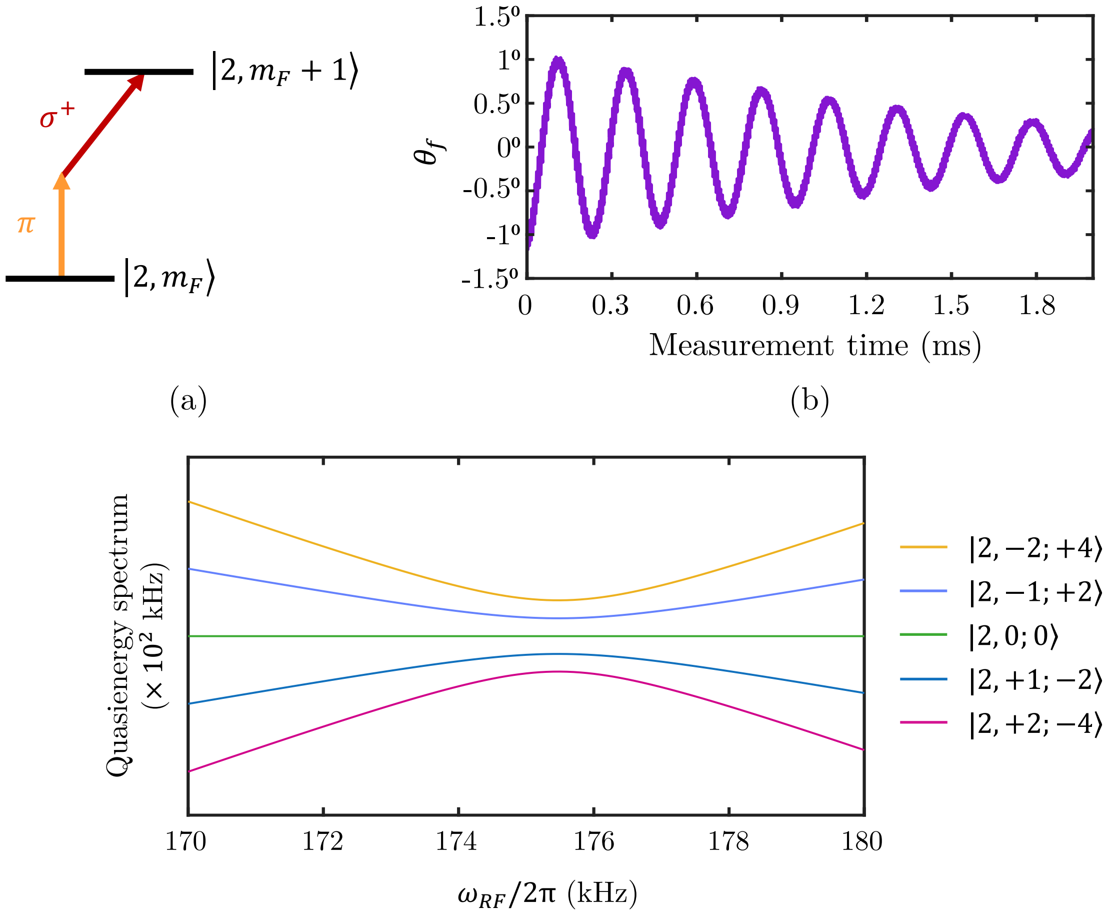

(a)

(b)

(c)

Figure 7.1: Driving two-photon Zeeman Rabi oscillations. (a) Level schematic illustrating transition between $|2, m_F\rangle$ and $|2, m_F + 1\rangle$ via a two-photon process involving π and σ^+ polarization components. (b) Faraday rotation signal showing two-photon Rabi oscillations. (c) Floquet quasienergies for $|F, m_F; n\rangle$ as a function of $\omega_{RF}/2\pi$ showing the avoided crossing at the two-photon resonance.

larized probe beam, as shown in Fig. 7.1b. Furthermore, they can be modeled within the Floquet formalism developed in Chapter 3, as the corresponding dressed state splittings appear in the quasienergy spectrum at the two photon resonance frequency. Therefore, the same formalism used to calculate Rabi frequencies for $\sigma^\pm$ transitions can be extended to include $\Omega^{(2)}_{\sigma+,\pi}$, where the superscript (2) denotes the two photon process. Furthermore, Rabi frequencies can be modeled using the same Floquet-based formalism that we have developed in Chapter 3. The quasienergy spectrum shown in Fig. 7.1c shows dressed state splittings near 175 kHz resulting from these transitions.

Measuring $\Omega_{\sigma\pm,\pi}$ signals provides more information than $\Omega_{\sigma\pm}$ alone. Measurements at several field orientations contain information about both the field direction and the PE. As shown in Ref. [105], this can be visualized as an overconstrained problem where the PE and the experimental imperfections are determined simultaneously from a set of Rabi measurements. In this picture, the atoms probe the RF field in a self-consistent way, with the transition strengths determined by atomic constants. This approach does not require prior knowledge of the magnetic field directions that are applied. Both the field orientation and the PE parameters are obtained from the Rabi measurements, thus leading to a self-calibrating scheme where the vector reference is defined by the atomic response itself, allowing slow drifts and misalignments to be absorbed into the calibration and improving the long-term stability.

However, there are some technical issues that would have to be addressed before this approach can be used for vector magnetometry. The main challenge is that the PE would have to be frequency-independent. A frequency jump from ν_L to $\nu_L/2$ is large enough that the relative amplitudes and phases of the RF field can change appreciably due to overall frequency dependence of the RF electronics. So, the PE at the two-photon frequency may not be identical to the one calibrated with single-photon transitions. This is important because exploiting the measurement of all three polarization components for drift monitoring or self-calibration relies on the measurements referring to the same PE. A second issue that would have to be addressed is that the two-photon RF field would need to be synchronized differently to the pump modulation sequence, which may introduce additional phase-dependent systematics through the nonlinear Zeeman effect. These systematics have to be accounted for in the dynamic heading error model before $\Omega^{(2)}_{\sigma+,\pi}$ transitions can be used in the measurement protocol.

7.2 Comparison and Outlook for Vector Magnetometry Techniques

To extend OPM operation to vector magnetometry, a variety of techniques have been explored. These approaches differ in their definition of a vector reference, how directional information is extracted from the atomic signals, how they perform calibration and treat systematics. In this thesis, we have shown that both the accuracy of the mathematical model and the stability of the vector reference play a role in determining the angular accuracy of the vector magnetometer. Comparing these techniques is not very straightforward, because benchmarking vector accuracy can be challenging and is often not reported consistently in the literature. In most cases, the performance is described only in terms of sensitivity and systematic error estimates, without an evaluation of accuracy or the long-term stability of the vector references. Therefore, we present a comparison table of vector OPMs (Table 7.1) that focuses on a subset of techniques for which accuracy has been measured, and calibration procedures and dominant systematics have been described. In addition to results reported in the literature, the table also includes extrapolated information based on the basic operating principles of each technique and on issues observed in related implementations. These extrapolations are intended to help in comparing these techniques, particularly where corresponding accuracy or calibration description is not available.

As mentioned in Chapter 1, calibration approaches based on physical sensor rotations or based on rotations of the magnetic field link the measured atomic signals to a vector reference. These two approaches differ in how this reference is established. With sensor rotations, the magnetometer is physically rotated with respect to a fixed, stable magnetic field, so that the atomic signals are measured as a function of orientation. This approach does not require control of the magnetic field, but generally introduces mechanical complexity and is often slower as the whole sensor body must be carefully rotated either manually or with motors. For instance, Ref. [71] reports $\mathbf{C}_t \sim 3$ hours for their sensor rotation-based calibration. The fixed magnetic field must therefore remain stable throughout the calibration time. In contrast, calibration based on field rotations defines the reference through stable externally-applied magnetic fields generated by a calibrated coil system. The sensor remains fixed while the magnetic field direction is changed, which simplifies the experimental setup, is generally more compatible with compact implementations, and typically significantly faster. However, this approach requires accurate calibration and long-term stability of the applied fields. As a result, the choice between these approaches results in a trade-off between mechanical complexity and calibration time, with precise control of applied magnetic fields.

The table also compares implementations based on alkali atoms and those based on metastable ^{4}He atoms. Metastable helium has zero nuclear spin and thus results in the absence of hyperfine structure. The simple atomic structure of ^{4}He thus eliminates the nonlinear Zeeman effect and associated heading error systematics, and reduces sensitivity to additional couplings, such as σ^- or π that lead to additional systematics. However, helium-based implementations generally require larger discharge-based cells and are not compatible with microfabricated vapor cells. In contrast, alkali atom-based magnetometers can be implemented in batch-fabricated microfabricated vapor cells and have access to a larger set of transitions that can extract additional information from the atomic signals, and enable drift monitoring and self-calibration [87, 105]. However, this additional flexibility comes at the cost of increased systematic effects.

Table 7.1: Comparison of angular accuracies and calibration procedures of several vector OPMs. All implementations considered here use a single-optical-axis configuration. Reported values are taken from the literature when available. Red text indicates extrapolated performance based on operating principles and expected limitations. Green text highlights future directions and possible improvements.

Atomic Species	**Calibration procedure**	
	Sensor rotation	**Field rotation**
	• Longer calibration time • Mechanically complex implementation	• Requires low-noise DC coil system for calibration
	Zeeman Rabi • Dead-zone-free vector measurement	
Alkali Atoms	• Dynamic heading error must be corrected from vector in situ. • ^{39}K may enable peak resolution and reduced dynamic heading error due to its substantially larger nonlinear Zeeman effect [157] • Measurements of Rabi frequencies sensitive to $\sigma^{\pm}$ and π[1] PE components enable self-monitoring of drift and self-calibration	
	• Drifts further limit accuracy due to longer calibration time	• Reported angular accuracy of 80 µrad [107] • Accuracy limited by residual systematics from Ω_{σ^-}, nonlinear Zeeman effect in ^{87}Rb, and drifts [107]
Metastable ^{4}He	• Drifts further limit accuracy due to longer calibration time	• Minimal residual systematics due to lack of Ω_{σ^-}; nonlinear Zeeman effect absent

---

[1] via two-photon process

Atomic Species	**Calibration procedure**	
	Sensor rotation	**Field rotation**
	Coil Modulation • Deadzones exist when Larmor precession signal is lost	
Alkali Atoms	• Heading error must be corrected from vector in situ	
	• Expected to exhibit similar performance limits as metastable ^{4}He if heading error systematics are corrected.	• DC coil noise is amplified through the modulation, with reported amplification of order 10^3 for SWARM [71]. This places additional requirements on DC field stability relative to other approaches.
Metastable ^{4}He	• Reported accuracy of 10 µrad [71] • Accuracy currently limited by drifts [65]	
	Hyperfine Rabi • Dead-zone-free measurement with Simultaneous Precession and Rabi (SPaR) technique [87] • Heading-error-free	
Alkali Atoms	• Drifts further limit accuracy due to longer calibration time	• Reported 460 µrad angular accuracy [87] • Self-monitors drift and also allows self-calibration [87]
Metastable ^{4}He	• No hyperfine structure	
	EIT • Dead-zone-free vector measurement • Heading-error-free	

Atomic Species	**Calibration procedure**	
	Sensor rotation	**Field rotation**
Alkali Atoms	• Limited by modeling systematics that persist under sensor rotations	• Reported ∼ 17 mrad angular accuracy [89]
Metastable ^{4}He	• No hyperfine structure	

Comparison between the four techniques - Zeeman Rabi, coil modulation, hyperfine Rabi, and EIT, reveals several fascinating trends. The coil modulation technique here specifically refers to methods in which small low-frequency modulations are applied along each coil pair of a triaxial coil system, and the vector components are inferred from the corresponding modulation amplitudes in the Larmor precession signal [71]. Among the techniques considered here, alkali atom implementations based on Zeeman coherences, such as the coil modulation and the Zeeman Rabi techniques, are affected by heading error effects because the relevant transitions occur within each hyperfine manifold. As a result, in the ESA SWARM mission, metastable ^{4}He was instead used due to its absence of heading error. It may be possible to correct these effects in alkali atoms but doing so requires calibration and modeling as we have performed in this thesis. On the other hand, hyperfine Rabi and EIT-based techniques probe transitions between specific Zeeman sublevels and therefore avoid these systematics.

The table also highlights an important difference in calibration for these implementations. Calibration for most of the implementations considered here is based on controlled rotations of the applied magnetic field with the sensor fixed in space. As outlined above, this is generally easier to implement than rotating the sensor itself, especially in compact systems. However, coil modulation techniques are more difficult to calibrate in this way because fluctuations in the applied DC field map onto the measured modulation amplitudes [71]. This noise is amplified onto the vector signals by a factor of B_0/B_{mod}, where B_0 and

B_{mod} are the ambient and modulation field strengths, respectively, making field rotation-based calibration more challenging compared to the other methods, which instead rely on frequency measurements.

The comparison in Table. 7.1 suggests that further improvements to Zeeman Rabi vector magnetometers can be achieved by extending this technique to other atomic species. One approach is to use metastable ^{4}He with its simpler atomic structure. As described earlier, as it has no hyperfine structure, the nonlinear Zeeman effect and thus dynamic heading error issues do not exist. Furthermore, here, Zeeman Rabi oscillations would be driven only by the σ^+ component of the applied RF field, which would eliminate residual σ^- contributions and simplify the modeling of the measured signal. Using ^{4}He may therefore improve accuracy by reducing sensitivity to modeling systematics.

An alternative route is to exploit, rather than suppress, nonlinear Zeeman effects. For example, ^{39}K exhibits a significantly larger nonlinear Zeeman splitting between adjacent Zeeman resonances than other alkali atoms at the same magnetic fields. At geomagnetic fields, this splitting can be large enough to resolve individual Zeeman peaks and address individual $\Delta m_F = 1$ transitions, rather than measuring an average over several overlapping transitions [157]. By addressing a single transition, contributions from neighbouring resonances are reduced, which reduces the influence of dynamic heading error systematics. At the same time, the atomic structure of ^{39}K allows measurement of $\sigma^{\pm}$, π Rabi frequencies and thus would provide redundant information for self-calibration or self-monitoring drift in this system.

7.3 Applications beyond Vector Magnetometry

Beyond DC vector magnetometry, the PE calibration protocol developed in this thesis can be repurposed as an atom-based tool for RF metrology. In our approach, the local RF magnetic field at the vapor cell is treated as a complex PE with three amplitudes and phases. By combining PE calibration via controlled DC field rotations with the Floquet-based model of Zeeman Rabi dynamics, Rabi frequency measurements can be used to infer the unknown amplitude, polarization and phase of an unknown RF magnetic field. As discussed earlier, a key advantage of this approach is that it relies on frequency measurements, which are inherently more robust than measuring signal amplitudes. This is especially useful in RF metrology, where conventional antenna-based measurements are often limited by calibration uncertainties. By contrast, atom-based sensors offer a self-referencing standard tied to fundamental atomic constants, enabling absolute calibration of RF fields [158, 159]. In contrast to Rydberg atom-based sensors, which primarily measure electric fields at microwave frequencies and above, this method probes magnetic fields in the kHz-MHz regime. This technique also avoids the complications typically associated with high principal quantum number atomic states. Additionally, this technique is compatible with standard wafer-based microfabricated vapor cells, whereas Rydberg measurements can be more sensitive to surface effects and stray electric fields from charges on nearby cell surfaces.

One potential application of this approach is magnetic induction tomography, where low-frequency RF fields are used to probe the conductivity and permeability of materials [95, 160]. Here a primary RF field induces eddy currents in a target, and the resulting secondary field carries information about the material properties. Tomographic reconstruction of these properties requires accurate determination of the RF field amplitude, phase, and also the spatial variation of the induced RF field. The calibration protocol, combined with the Floquet-based model, enables precise determination of the PE associated with the RF field. This allows the secondary field to be inferred with high accuracy from the measured atomic response. Because the Floquet framework accounts for strong driving effects beyond RWA, this approach reduces systematic errors and reliably reconstructs the material parameters [161–163].

Another important application is in ultralow-frequency RF communication, which is used in scenarios where large wavelengths are required for signal penetration, such as communication through seawater, underground, or dense structures. These wavelengths can be too large for efficient pickup through antennas, and communication instead relies on near-field coupling of local oscillating magnetic fields, rather than propagating waves. Recent work has demonstrated low-frequency magnetic communication using OPMs in this regime. Gerginov *et al.* used phase-sensitive detection with spread-spectrum techniques (BPSK modulation with pseudorandom code) to enable communication based on amplitude and phase measurements of a known RF field [53]. Fan *et al.* extended this approach by encoding information in the helicity of the RF field and measuring this with a dual channel OPM sensitive to opposite circular polarizations [164]. Both approaches, however, implicitly assume that part of the RF PE is already known, while the signal is encoded in the remaining unknown degree of freedom. By contrast, the PE calibration approach reconstructs the full RF field at the atoms, including amplitude, phase, and of course, the polarization with the same Rabi measurements. This approach can separate the true modulation signal from distortions associated with spurious couplings from the environment or coil imperfections. As a result, the present approach in principle enables encoding schemes that extend beyond binary phase or helicity modulation. Access to all PE parameters allows encoding of information in multiple degrees of freedom of the RF field. Multi-parameter encoding increases the information carried by the signal and allows operation in environments with distorted RF fields at the atoms.

Bibliography

[1] P. Sharma, Magnetic method applied to mineral exploration, Ore Geology Reviews **2**, 323 (1987).

[2] D. Stevenson, Planetary magnetic fields, Reports on Progress in Physics **46**, 555 (1983).

[3] H.-F. Liu, Z.-C. Luo, Z.-K. Hu, S.-Q. Yang, L.-C. Tu, Z.-B. Zhou, and M. Kraft, A review of high-performance MEMS sensors for resource exploration and geophysical applications, Petroleum Science **19**, 2631 (2022).

[4] A. Canciani and J. Raquet, Absolute positioning using the earth's magnetic anomaly field, NAVIGATION: Journal of the Institute of Navigation **63**, 111 (2016).

[5] A. J. Canciani and C. J. Brennan, An analysis of the benefits and difficulties of aerial magnetic vector navigation, IEEE Transactions on Aerospace and Electronic Systems **56**, 4161 (2020).

[6] M. Romalis, W. Griffith, J. Jacobs, and E. Fortson, New limit on the permanent electric dipole moment of ^{199}Hg, Physical Review Letters **86**, 2505 (2001).

[7] D. F. Jackson Kimball, D. Budker, T. E. Chupp, A. A. Geraci, S. Kolkowitz, J. T. Singh, and A. O. Sushkov, Probing fundamental physics with spin-based quantum sensors, Physical Review A **108**, 010101 (2023).

[8] L. Cong, W. Ji, P. Fadeev, F. Ficek, M. Jiang, V. V. Flambaum, H. Guan, D. F. Jackson Kimball, M. G. Kozlov, Y. V. Stadnik, *et al.*, Spin-dependent exotic interactions, Reviews of Modern Physics **97**, 025005 (2025).

[9] S. Pustelny, D. F. Jackson Kimball, C. Pankow, M. P. Ledbetter, P. Wlodarczyk, P. Wcislo, M. Pospelov, J. R. Smith, J. Read, W. Gawlik, *et al.*, The Global Network of Optical Magnetometers for Exotic physics (GNOME): A novel scheme to search for physics beyond the Standard Model, Annalen der Physik **525**, 659 (2013).

[10] D. J. Kimball, S. Lamoreaux, and T. Chupp, Tests of fundamental physics with optical magnetometers, Optical Magnetometry , 339 (2013).

[11] A. Fabricant, I. Novikova, and G. Bison, How to build a magnetometer with thermal atomic vapor: a tutorial, New Journal of Physics **25**, 025001 (2023).

[12] H. Xia, A. Ben-Amar Baranga, D. Hoffman, and M. Romalis, Magnetoencephalography with an atomic magnetometer, Applied Physics Letters **89** (2006).

[13] A. Borna, T. R. Carter, J. D. Goldberg, A. P. Colombo, Y.-Y. Jau, C. Berry, J. McKay, J. Stephen, M. Weisend, and P. D. Schwindt, A 20-channel magnetoencephalography system based on optically pumped magnetometers, Physics in Medicine & Biology **62**, 8909 (2017).

[14] N. Nardelli, A. Perry, S. Krzyzewski, and S. Knappe, A conformal array of microfabricated optically-pumped first-order gradiometers for magnetoencephalography, EPJ Quantum Technology **7**, 11 (2020).

[15] M. Limes, E. Foley, T. Kornack, S. Caliga, S. McBride, A. Braun, W. Lee, V. Lucivero, and M. Romalis, Portable magnetometry for detection of biomagnetism in ambient environments, Physical Review Applied **14**, 011002 (2020).

[16] J. Sheng, S. Wan, Y. Sun, R. Dou, Y. Guo, K. Wei, K. He, J. Qin, and J.-H. Gao, Magnetoencephalography with a Cs-based high-sensitivity compact atomic magnetometer, Review of Scientific Instruments **88** (2017).

[17] A. Weis, G. Bison, and R. Wynands, Mapping of human heart beat dynamics by atomic magnetometers, in *AIP Conference Proceedings*, Vol. 770 (American Institute of Physics, 2005) pp. 373–380.

[18] G. Bison, R. Wynands, and A. Weis, A laser-pumped magnetometer for the mapping of human cardiomagnetic fields, Applied Physics B **76**, 325 (2003).

[19] G. Bison, R. Wynands, and A. Weis, Optimization and performance of an optical cardiomagnetometer, Journal of the Optical Society of America B **22**, 77 (2005).

[20] R. Fenici, G. Bison, R. Wynands, D. Brisinda, A. M. Meloni, A. Weis, *et al.*, Comparison of magnetocardiographic mapping with squid-based and laser-pumped magnetometers in normal subjects, Biomed. Tech **48**, 192 (2004).

[21] G. Bison, R. Wynands, and A. Weis, Dynamical mapping of the human cardiomagnetic field with a room-temperature, laser-optical sensor, Optics Express **11**, 904 (2003).

[22] N. Gusev, P. Vetoshko, A. Kuzmichev, D. Chepurnova, E. Samoilova, A. Zvezdin, A. Korotaeva, and V. Belotelov, Ultra-sensitive vector magnetometer for magnetocardiographic mapping, Biomedical Engineering **51**, 157 (2017).

[23] V. K. Shah and R. T. Wakai, A compact, high performance atomic magnetometer for biomedical applications, Physics in medicine and biology **58**, 8153 (2013).

[24] W. Li and J. Wang, Magnetic sensors for navigation applications: an overview, The Journal of navigation **67**, 263 (2014).

[25] J. Lenz and S. Edelstein, Magnetic sensors and their applications, IEEE Sensors journal **6**, 631 (2006).

[26] M. Dougherty, S. Kellock, D. Southwood, A. Balogh, E. Smith, B. Tsurutani, B. Gerlach, K.-H. Glassmeier, F. Gleim, C. Russell, *et al.*, The Cassini magnetic field investigation, Space Science Reviews **114**, 331 (2004).

[27] J. Connerney, M. Benn, J. Bjarno, T. Denver, J. Espley, J. Jorgensen, P. Jorgensen, P. Lawton, A. Malinnikova, J. Merayo, *et al.*, The Juno magnetic field investigation, Space Science Reviews **213**, 39 (2017).

[28] R. Kleiner, D. Koelle, F. Ludwig, and J. Clarke, Superconducting quantum interference devices: State of the art and applications, Proceedings of the IEEE **92**, 1534 (2004).

[29] S. Wei, X. Liao, H. Zhang, J. Pang, and Y. Zhou, Recent progress of fluxgate magnetic sensors: Basic research and application, Sensors **21**, 1500 (2021).

[30] L. Rondin, J.-P. Tetienne, T. Hingant, J.-F. Roch, P. Maletinsky, and V. Jacques, Magnetometry with nitrogen-vacancy defects in diamond, Reports on progress in physics **77**, 056503 (2014).

[31] G. Boero, M. Demierre, R. Popovic, *et al.*, Micro-Hall devices: performance, technologies and applications, Sensors and Actuators A: Physical **106**, 314 (2003).

[32] D. Budker and M. Romalis, Optical magnetometry, Nature physics **3**, 227 (2007).

[33] J. Allred, R. Lyman, T. Kornack, and M. V. Romalis, High-sensitivity atomic magnetometer unaffected by spin-exchange relaxation, Physical Review Letters **89**, 130801 (2002).

[34] A. J. Kox, The discovery of the electron: II. The Zeeman effect, European journal of physics **18**, 139 (1997).

[35] W. Happer, Optical pumping, Reviews of modern physics **44**, 169 (1972).

[36] F. Riehle, Optical atomic clocks could redefine unit of time, Physics **5**, 126 (2012).

[37] D. A. Steck, *Rubidium 87 D line data* (2025).

[38] P. Oreto, Y.-Y. Jau, A. Post, N. Kuzma, and W. Happer, Buffer-gas-induced shift and broadening of hyperfine resonances in alkali-metal vapors, Physical Review A **69**, 042716 (2004).

[39] J. Vanier, R. Kunski, N. Cyr, J. Savard, and M. Têtu, On hyperfine frequency shifts caused by buffer gases: Application to the optically pumped passive rubidium frequency standard, Journal of Applied Physics **53**, 5387 (1982).

[40] M. Balabas, K. Jensen, W. Wasilewski, H. Krauter, L. Madsen, J. Müller, T. Fernholz, and E. Polzik, High quality anti-relaxation coating material for alkali atom vapor cells, Optics express **18**, 5825 (2010).

[41] M. Balabas, T. Karaulanov, M. Ledbetter, and D. Budker, Polarized alkali-metal vapor with minute-long transverse spin-relaxation time, Physical Review Letters **105**, 070801 (2010).

[42] S. Knappe, V. Gerginov, P. Schwindt, V. Shah, H. Robinson, L. Hollberg, and J. Kitching, Atomic vapor cells for chip-scale atomic clocks with improved long-term frequency stability, Optics letters **30**, 2351 (2005).

[43] M. Hashimoto and M. Ohtsu, Experiments on a semiconductor laser pumped rubidium atomic clock, IEEE journal of quantum electronics **23**, 446 (2003).

[44] L.-A. Liew, S. Knappe, J. Moreland, H. Robinson, L. Hollberg, and J. Kitching, Microfabricated alkali atom vapor cells, Applied Physics Letters **84**, 2694 (2004).

[45] J. Kitching, S. Knappe, and L. Hollberg, Miniature vapor-cell atomic-frequency references, Applied Physics Letters **81**, 553 (2002).

[46] P. D. Schwindt, S. Knappe, V. Shah, L. Hollberg, J. Kitching, L.-A. Liew, and J. Moreland, Chip-scale atomic magnetometer, Applied Physics Letters **85**, 6409 (2004).

[47] J. Kitching, Chip-scale atomic devices, Applied Physics Reviews **5** (2018).

[48] X. Wang, M. Ye, F. Lu, Y. Mao, H. Tian, and J. Li, Recent progress on micro-fabricated alkali metal vapor cells, Biosensors **12**, 165 (2022).

[49] E. B. Aleksandrov and A. K. Vershovskii, Modern radio-optical methods in quantum magnetometry, Physics-Uspekhi **52**, 573 (2009).

[50] E. Alexandrov and A. Vershovskiy, Mx and mz magnetometers, Optical Magnetometry **1**, 60 (2013).

[51] P. D. Schwindt, B. Lindseth, S. Knappe, V. Shah, J. Kitching, and L.-A. Liew, Chip-scale atomic magnetometer with improved sensitivity by use of the mx technique, Applied Physics Letters **90** (2007).

[52] R. Jiménez-Martínez, W. C. Griffith, Y.-J. Wang, S. Knappe, J. Kitching, K. Smith, and M. D. Prouty, Sensitivity comparison of Mx and frequency-modulated Bell–Bloom Cs magnetometers in a microfabricated cell, IEEE Transactions on Instrumentation and Measurement **59**, 372 (2009).

[53] V. Gerginov, F. Da Silva, and D. Howe, Prospects for magnetic field communications and location using quantum sensors, Review of Scientific Instruments **88**, 125005 (2017).

[54] V. Gerginov, M. Pomponio, and S. Knappe, Scalar magnetometry below 100 $\mathrm{fT}/\sqrt{\mathrm{Hz}}$ in a microfabricated cell, IEEE sensors journal **20**, 12684 (2020).

[55] W. E. Bell and A. L. Bloom, Optically driven spin precession, Physical Review Letters **6**, 280 (1961).

[56] C. Kiehl, T. S. Menon, D. P. Hewatt, S. Knappe, T. Thiele, and C. A. Regal, Correcting heading errors in optically pumped magnetometers through microwave interrogation, Physical Review Applied **22**, 014005 (2024).

[57] A. Pollinger, R. Lammegger, W. Magnes, C. Hagen, M. Ellmeier, I. Jernej, M. Leichtfried, C. Kürbisch, R. Maierhofer, R. Wallner, *et al.*, Coupled dark state magnetometer for the china seismo-electromagnetic satellite, Measurement Science and Technology **29**, 095103 (2018).

[58] H.-G. Hong, S. E. Park, S.-B. Lee, M.-S. Heo, J. Park, T. H. Kim, H. Y. Kim, and T. Y. Kwon, Chip-scale ultra-low field atomic magnetometer based on coherent population trapping, Sensors **21**, 1517 (2021).

[59] H. Liu, H. Dong, J. Ge, and Z. Liu, An overview of sensing platform-technological aspects for vector magnetic measurement: A case study of the application in different scenarios, Measurement **187**, 110352 (2022).

[60] Y. Lu, T. Zhao, W. Zhu, L. Liu, X. Zhuang, G. Fang, and X. Zhang, Recent progress of atomic magnetometers for geomagnetic applications, Sensors **23**, 5318 (2023).

[61] M. D. Prouty and M. Tchernychev, *Real-time threat detection using magnetometer arrays*, Vol. 9825 (2016) p. 49.

[62] B. Patton, A. Brown, R. Slocum, and E. Smith, Space magnetometry, Optical Magnetometry , 285 (2013).

[63] M. H. Acuna, The MAGSAT precision vector magnetometer, Johns Hopkins APL Technical Digest **1**, 210 (1980).

[64] L. A. Mount, *Navigation using Vector and Tensor Measurements of the Earth's Magnetic Anomaly Field*, Master's thesis, Air Force Institute of Technology (2018).

[65] J.-M. Léger, T. Jager, F. Bertrand, G. Hulot, L. Brocco, P. Vigneron, X. Lalanne, A. Chulliat, and I. Fratter, In-flight performance of the absolute scalar magnetometer vector mode on board the swarm satellites, Earth Planets Space **67**, 57 (2015).

[66] A. Vershovskii, M. Balabas, A. Ivanov, V. Kulyasov, A. Pazgalev, and E. Aleksandrov, Fast three-component magnetometer-variometer based on a cesium sensor, Technical Physics **51**, 112 (2006).

[67] E. Alexandrov, M. Balabas, V. Kulyasov, A. Ivanov, A. Pazgalev, J. Rasson, A. Vershovski, and N. Yakobson, Three-component variometer based on a scalar potassium sensor, Measurement Science and Technology **15**, 918 (2004).

[68] M. C. Tayler, K. Mouloudakis, R. Zetter, D. Hunter, V. G. Lucivero, S. Bodenstedt, L. Parkkonen, and M. W. Mitchell, Miniature biplanar coils for alkali-metal-vapor magnetometry, Physical Review Applied **18**, 014036 (2022).

[69] F. Bertrand, T. Jager, A. Boness, W. Fourcault, G. Le Gal, A. Palacios-Laloy, J. Paulet, and J.-M. Leger, A ^{4}He vector zero-field optically pumped magnetometer operated in the earth-field, Review of Scientific Instruments **92** (2021).

[70] J.-M. Leger, F. Bertrand, T. Jager, M. Le Prado, I. Fratter, and J.-C. Lalaurie, Swarm absolute scalar and vector magnetometer based on helium 4 optical pumping, Procedia Chemistry **1**, 634 (2009).

[71] O. Gravrand, A. Khokhlov, L. M. JL, and L. JM, On the calibration of a vectorial ^{4}He pumped magnetometer, Earth, planets and space **53**, 949 (2001).

[72] T. Pyragius, H. M. Florez, and T. Fernholz, Voigt-effect-based three-dimensional vector magnetometer, Physical Review A **100**, 023416 (2019).

[73] T. Wang, W. Lee, M. Limes, T. Kornack, E. Foley, and M. Romalis, Pulsed vector atomic magnetometer using an alternating fast-rotating field, Nature Communications **16**, 1374 (2025).

[74] G. Bison, V. Bondar, P. Schmidt-Wellenburg, A. Schnabel, and J. Voigt, Sensitive and stable vector magnetometer for operation in zero and finite fields, Optics express **26**, 17350 (2018).

[75] S. Afach, G. Ban, G. Bison, K. Bodek, Z. Chowdhuri, Z. Grujić, L. Hayen, V. Hélaine, M. Kasprzak, K. Kirch, *et al.*, Highly stable atomic vector magnetometer based on free spin precession, Optics express **23**, 22108 (2015).

[76] H. Huang, H. Dong, X. Hu, L. Chen, and Y. Gao, Three-axis atomic magnetometer based on spin precession modulation, Applied Physics Letters **107** (2015).

[77] B. Cai, C.-P. Hao, Z.-R. Qiu, Q.-Q. Yu, W. Xiao, and D. Sheng, Herriott-cavity-assisted all-optical atomic vector magnetometer, Physical Review A **101**, 053436 (2020).

[78] B. Patton, E. Zhivun, D. Hovde, and D. Budker, All-optical vector atomic magnetometer, Physical Review Letters **113**, 013001 (2014).

[79] R. Zhang, R. Mhaskar, K. Smith, E. Balasubramaniam, and M. Prouty, Vector measurements using all optical scalar atomic magnetometers, Journal of Applied Physics **129** (2021).

[80] S. Pustelny, W. Gawlik, S. Rochester, D. J. Kimball, V. Yashchuk, and D. Budker, Nonlinear magneto-optical rotation with modulated light in tilted magnetic fields, Physical Review A **74**, 063420 (2006).

[81] H. Lee, M. Fleischhauer, and M. O. Scully, Sensitive detection of magnetic fields including their orientation with a magnetometer based on atomic phase coherence, Physical Review A **58**, 2587 (1998).

[82] V. Yudin, A. Taichenachev, Y. Dudin, V. Velichansky, A. Zibrov, and S. Zibrov, Vector magnetometry based on electromagnetically induced transparency in linearly polarized light, Physical Review A **82**, 033807 (2010).

[83] K. Cox, V. I. Yudin, A. V. Taichenachev, I. Novikova, and E. E. Mikhailov, Measurements of the magnetic field vector using multiple electromagnetically induced transparency resonances in Rb vapor, Physical Review A **83**, 015801 (2011).

[84] O. Rollins, E. E. Mikhailov, and I. Novikova, Magnetic field direction detection using electromagnetically induced transparency with a vector vortex beam, Optics Letters **51**, 961 (2026).

[85] X. Meng, Y. Zhang, X. Zhang, S. Jin, T. Wang, L. Jiang, L. Xiao, S. Jia, and Y. Xiao, Machine learning assisted vector atomic magnetometry, Nature Communications **14**, 6105 (2023).

[86] L. Lenci, A. Auyuanet, S. Barreiro, P. Valente, A. Lezama, and H. Failache, Vectorial atomic magnetometer based on coherent transients of laser absorption in Rb vapor, Physical Review A **89**, 043836 (2014).

[87] C. Kiehl, T. S. Menon, S. Knappe, T. Thiele, and C. A. Regal, Accurate vector optically pumped magnetometer with microwave-driven Rabi frequency measurements, Optica **12**, 77 (2025).

[88] T. Schönau, T. Scholtes, F. Wittkämper, A. Sekels, S. Hiebel, G. Oelsner, and R. Stolz, Optically pumped vector magnetometer using a strong bias magnetic field, Physical Review Applied **23**, 024006 (2025).

[89] J. A. McKelvy, I. Novikova, E. E. Mikhailov, M. A. Maldonado, I. Fan, Y. Li, Y.-J. Wang, J. Kitching, and A. B. Matsko, Application of kernel principal component analysis for optical vector atomic magnetometry, Machine learning: science and technology **4**, 045048 (2023).

[90] N. Olsen, L. T. Clausen, T. J. Sabaka, P. Brauer, J. M. Merayo, J. L. Jørgensen, J.-M. Léger, O. V. Nielsen, F. Primdahl, and T. Risbo, Calibration of the ørsted vector magnetometer, Earth, planets and space **55**, 11 (2003).

[91] C. Kiehl, *Microwave-driven Rabi Magnetometry Implemented in Hot Atomic Vapor*, Ph.D. thesis, University of Colorado Boulder (2024).

[92] A. Ben-Kish and M. Romalis, Dead-zone-free atomic magnetometry with simultaneous excitation of orientation and alignment resonances, Physical Review Letters **105**, 193601 (2010).

[93] Q.-Q. Yu, S.-Q. Liu, C.-Q. Yuan, and D. Sheng, Light-shift-free and dead-zone-free atomic-orientation-based scalar magnetometry using a single amplitude-modulated beam, Physical Review Applied **18**, 014015 (2022).

[94] M. Koschorreck, M. Napolitano, B. Dubost, and M. Mitchell, Sub-projection-noise sensitivity in broadband atomic magnetometry, Physical Review Letters **104**, 093602 (2010).

[95] C. Deans, Y. Cohen, H. Yao, B. Maddox, A. Vigilante, and F. Renzoni, Electromagnetic induction imaging with a scanning radio frequency atomic magnetometer, Applied Physics Letters **119** (2021).

[96] A. Horsley, G.-X. Du, and P. Treutlein, Widefield microwave imaging in alkali vapor cells with sub-100 μm resolution, New Journal of Physics **17**, 112002 (2015).

[97] A. Horsley and P. Treutlein, Frequency-tunable microwave field detection in an atomic vapor cell, Applied Physics Letters **108** (2016).

[98] P. Böhi and P. Treutlein, Simple microwave field imaging technique using hot atomic vapor cells, Applied Physics Letters **101** (2012).

[99] C. Affolderbach, G.-X. Du, T. Bandi, A. Horsley, P. Treutlein, and G. Mileti, Imaging microwave and dc magnetic fields in a vapor-cell Rb atomic clock, IEEE Transactions on Instrumentation and Measurement **64**, 3629 (2015).

[100] J. M. Brown and T. G. Walker, Perspective: Practical atom-based quantum sensors, Physical Review A **112**, 040102 (2025).

[101] J. H. Shirley, Solution of the schrödinger equation with a hamiltonian periodic in time, Physical Review **138**, B979 (1965).

[102] H. M. Florez and T. Pyragius, Floquet description of optically pumped magnetometers, Physical Review A **103**, 033113 (2021).

[103] W. Lee, V. Lucivero, M. Romalis, M. Limes, E. Foley, and T. Kornack, Heading errors in all-optical alkali-metal-vapor magnetometers in geomagnetic fields, Physical Review A **103**, 063103 (2021).

[104] G. Bao, A. Wickenbrock, S. Rochester, W. Zhang, and D. Budker, Suppression of the nonlinear Zeeman effect and heading error in earth-field-range alkali-vapor magnetometers, Physical Review Letters **120**, 033202 (2018).

[105] T. Thiele, Y. Lin, M. O. Brown, and C. A. Regal, Self-calibrating vector atomic magnetometry through microwave polarization reconstruction, Physical Review Letters **121**, 153202 (2018).

[106] C. Kiehl, D. Wagner, T.-W. Hsu, S. Knappe, C. A. Regal, and T. Thiele, Coherence of Rabi oscillations with spin exchange, Physical Review Research **5**, L012002 (2023).

[107] T. S. Menon, D. P. Hewatt, C. Kiehl, M. Ellmeier, S. Knappe, and C. A. Regal, An accurate vector magnetometer via Zeeman Rabi oscillations, arXiv preprint arXiv:2603.08594 (2026).

[108] J. J. Sakurai and J. Napolitano, *Modern quantum mechanics* (Cambridge University Press, 2020).

[109] C. Guttin, J. Leger, and F. Stoeckel, An isotropic earth field scalar magnetometer using optically pumped helium 4, Le Journal de Physique IV **4**, 655 (1994).

[110] M. Auzinsh, D. Budker, and S. Rochester, *Optically polarized atoms: understanding light-atom interactions* (Oxford University Press, 2010).

[111] D. Hewatt, M. Ellmeier, C. Kiehl, T. Menon, J. Pollock, C. Regal, and S. Knappe, Investigating the hyperfine systematic error and relative phase in low-spin-polarization alkali-metal free-induction-decay magnetometers, Physical Review A **111**, 033106 (2025).

[112] J. Vanier and C. Audoin, *The Quantum Physics of Atomic Frequency Standards*, Vol. 2 (1989).

[113] S. Appelt, A. B.-A. Baranga, C. Erickson, M. Romalis, A. Young, and W. Happer, Theory of spin-exchange optical pumping of ^{3}He and ^{129}Xe, Physical Review A **58**, 1412 (1998).

[114] S. Micalizio, A. Godone, F. Levi, and J. Vanier, Spin-exchange frequency shift in alkali-metal-vapor cell frequency standards, Physical Review A **73**, 033414 (2006).

[115] A. B.-A. Baranga, S. Appelt, M. Romalis, C. Erickson, A. Young, G. Cates, and W. Happer, Polarization of ^{3}He by spin exchange with optically pumped Rb and K vapors, Physical Review Letters **80**, 2801 (1998).

[116] P. Berman, Collisional decay and revival of the grating stimulated echo, Physical Review A **49**, 2922 (1994).

[117] Y. Chang and J. Qin, Wall-collision effect on optically polarized atoms in small and hot vapor cells, Physical Review A **109**, 023113 (2024).

[118] H. M. Gibbs and R. J. Hull, Spin-exchange cross sections for Rb 87-Rb 87 and Rb 87-Cs 133 collisions, Physical Review **153**, 132 (1967).

[119] M. Wagshul and T. Chupp, Optical pumping of high-density Rb with a broadband dye laser and GaAlAs diode laser arrays: Application to ^{3}He polarization, Physical Review A **40**, 4447 (1989).

[120] A. Pouliot, G. Carlse, H. Beica, T. Vacheresse, A. Kumarakrishnan, U. Shim, S. Cahn, A. Turlapov, and T. Sleator, Accurate determination of an alkali-vapor–inert-gas diffusion coefficient using coherent transient emission from a density grating, Physical Review A **103**, 023112 (2021).

[121] D. Hunter, S. Piccolomo, J. Pritchard, N. Brockie, T. Dyer, and E. Riis, Free-induction-decay magnetometer based on a microfabricated Cs vapor cell, Physical Review Applied **10**, 014002 (2018).

[122] E. Hrycyshyn and L. Krause, Inelastic collisions between excited alkali atoms and molecules. vii. sensitized fluorescence and quenching in mixtures of rubidium with H_2, HD, D_2, N_2, CH_4, CD_4, C_2H_4, and $C_2.H_6$, Canadian Journal of Physics **48**, 2761 (1970).

[123] M. Hernández Ruiz, Y. Ma, H. Medhat, C. Mazzinghi, V. G. Lucivero, and M. W. Mitchell, Cavity-enhanced detection of spin polarization in a microfabricated atomic vapor cell, Physical Review Applied **21**, 064014 (2024).

[124] V. Acosta, M. Ledbetter, S. Rochester, D. Budker, D. Jackson Kimball, D. Hovde, W. Gawlik, S. Pustelny, J. Zachorowski, and V. Yashchuk, Nonlinear magneto-optical rotation with frequency-modulated light in the geophysical field range, Physical Review A **73**, 053404 (2006).

[125] W. Gawlik, L. Krzemień, S. Pustelny, D. Sangla, J. Zachorowski, M. Graf, A. Sushkov, and D. Budker, Nonlinear magneto-optical rotation with amplitude modulated light, Applied Physics Letters **88** (2006).

[126] Z. D. Grujić and A. Weis, Atomic magnetic resonance induced by amplitude-, frequency-, or polarization-modulated light, Physical Review A **88**, 012508 (2013).

[127] S. J. Seltzer, *Developments in alkali-metal atomic magnetometry*, Ph.D. thesis, Princeton University (2008).

[128] G. A. Smith, S. Chaudhury, A. Silberfarb, I. H. Deutsch, and P. S. Jessen, Continuous weak measurement and nonlinear dynamics in a cold spin ensemble, Physical Review Letters **93**, 163602 (2004).

[129] V. Shah, G. Vasilakis, and M. Romalis, High bandwidth atomic magnetometery with continuous quantum nondemolition measurements, Physical Review Letters **104**, 013601 (2010).

[130] C. J. Foot, *Atomic physics*, Vol. 7 (Oxford university press, 2005).

[131] F. Bloch and A. Siegert, Magnetic resonance for nonrotating fields, Physical Review **57**, 522 (1940).

[132] J. Sudyka, Limitations of rotating-wave approximation in magnetic resonance: characterization and elimination of the bloch–siegert shift in magneto-optics, New Journal of Physics **21**, 023024 (2019).

[133] C. A. R. Almeida, *Continuous Measurement Quantum State Tomography of Atomic Ensembles*, Ph.D. thesis, The University of New Mexico (2011).

[134] B. Hall, *Lie Groups, Lie Algebras, and Representations: An Elementary Introduction*, Graduate Texts in Mathematics (Springer International Publishing, 2015).

[135] J. Tuorila, M. Silveri, M. Sillanpää, E. Thuneberg, Y. Makhlin, and P. Hakonen, Stark effect and generalized Bloch–Siegert shift in a strongly driven two-level system, Physical Review Letters **105**, 257003 (2010).

[136] P. Forn-Díaz, J. Lisenfeld, D. Marcos, J. J. Garcia-Ripoll, E. Solano, C. Harmans, and J. Mooij, Observation of the Bloch–Siegert shift in a qubit-oscillator system in the ultrastrong coupling regime, Physical Review Letters **105**, 237001 (2010).

[137] T. Shi, G. Jin, and S. Zou, High-order magnetic resonance in the presence of strong longitudinal radio-frequency magnetic field based on atomic alignment states, Physical Review A **109**, 043117 (2024).

[138] Y. Sun, Y. Xu, and Z. Wang, The multi-RF photon transition driven by strong RF field in optical magnetic resonance of atoms, Optics & Laser Technology **145**, 107488 (2022).

[139] M. Sato and T. N. Ikeda, Floquet theory and applications in open quantum and classical systems, Journal of the Physical Society of Japan **94**, 111007 (2025).

[140] L. Huang, J. Luneau, J. Schirk, F. Wallner, C. M. Schneider, S. Filipp, K. Liegener, and P. Rabl, Theory of multi-photon processes for applications in quantum control, arXiv preprint arXiv:2509.16074 (2025).

[141] E. Piña, Rotations with Rodrigues' vector, European journal of physics **32**, 1171 (2011).

[142] Twinleaf LLC, MS-2 magnetic shield system, `https://twinleaf.com/shield/MS-2/` (2026).

[143] R. Mhaskar, S. Knappe, and J. Kitching, A low-power, high-sensitivity micromachined optical magnetometer, Applied Physics Letters **101** (2012).

[144] J. Jackson, *Classical Electrodynamics* (Wiley, 1999).

[145] N. Amemiya, H. Miyahara, T. Ogitsu, and T. Kurusu, Design of a cosine-theta dipole magnet wound with coated conductors considering their deformation at coil ends during winding process, Physics Procedia **67**, 776 (2015).

[146] J. M. Merayo, P. Brauer, F. Primdahl, J. R. Petersen, and O. V. Nielsen, Scalar calibration of vector magnetometers, Measurement science and technology **11**, 120 (2000).

[147] P. Bertemes-Filho, F. Alexandre, and V. C. Vincence, High accurate howland current source: Output constraints analysis, Circuits and Systems **4**, 451 (2013).

[148] D. S. Batista, F. Granziera Jr, M. C. Tosin, and L. F. de Melo, Analysis and practical implementation of a high-power howland current source, Measurement **207**, 112404 (2023).

[149] Twinleaf LLC, CSB3 current supply, https://twinleaf.com/current/CSB3/ (2026).

[150] D. Plankensteiner, J. Schachenmayer, H. Ritsch, and C. Genes, Laser noise imposed limitations of ensemble quantum metrology, Journal of Physics B: Atomic, Molecular and Optical Physics **49**, 245501 (2016).

[151] C. Amtmann, A. Pollinger, M. Ellmeier, M. Dougherty, P. Brown, R. Lammegger, A. Betzler, M. Agú, C. Hagen, I. Jernej, J. Wilfinger, R. Baughen, A. Strickland, and W. Magnes, Accuracy of the scalar magnetometer aboard ESA's JUICE mission, Geosci. Instrum. Methods Data Syst. **13**, 177.

[152] W. Culver, The Maser: A Molecular Amplifier for Microwave Radiation, Science **126**, 810 (1957).

[153] S.-K. Lee and M. Romalis, Calculation of magnetic field noise from high-permeability magnetic shields and conducting objects with simple geometry, Journal of Applied Physics **103** (2008).

[154] C. T. Munger Jr, Magnetic johnson noise constraints on electron electric dipole moment experiments, Physical Review A—Atomic, Molecular, and Optical Physics **72**, 012506 (2005).

[155] G. Annino, M. Cassettari, I. Longo, and M. Martinelli, Dielectric resonators in ESR: overview, comments and perspectives, Applied Magnetic Resonance **16**, 45 (1999).

[156] H. H. Vallabhapurapu, J. P. Slack-Smith, V. K. Sewani, C. Adambukulam, A. Morello, J. J. Pla, and A. Laucht, Fast coherent control of a nitrogen-vacancy-center spin ensemble using a $KTaO_3$ dielectric resonator at cryogenic temperatures, Physical Review Applied **16**, 044051 (2021).

[157] Y. Ding, R. Zhang, J. Zheng, J. Chen, X. Peng, T. Wu, and H. Guo, Active stabilization of terrestrial magnetic field with potassium atomic magnetometer, Rev. Sci. Instrum. **93**, 015003 (2022).

[158] J. Kitching, J. P. Shaffer, and D. Budker, Atom-based quantum sensing of electromagnetic fields, Optica **12**, 2008 (2025).

[159] C. Motamedi and K. Sauer, Magnetic Jones vector detection with RF atomic magnetometers, Physical Review Applied **20**, 014006 (2023).

[160] B. Maddox and F. Renzoni, Two-photon electromagnetic induction imaging with an atomic magnetometer, Applied Physics Letters **122**, 144001 (2023).

[161] L. Marmugi and F. Renzoni, Optical magnetic induction tomography of the heart, Scientific reports **6**, 23962 (2016).

[162] L. Rushton, T. Pyragius, A. Meraki, L. Elson, and K. Jensen, Unshielded portable optically pumped magnetometer for the remote detection of conductive objects using eddy current measurements, Review of Scientific Instruments **93**, 125103 (2022).

[163] L. Rushton, L. Ellis, J. Zipfel, P. Bevington, and W. Chalupczak, Polarization of radio-frequency magnetic fields in magnetic induction measurements with an atomic magnetometer, Physical Review Applied **22**, 014002 (2024).

[164] I. Fan, S. Knappe, and V. Gerginov, Magnetic communication by polarization helicity modulation using atomic magnetometers, Review of Scientific Instruments **93**, 053004 (2022)